Mathematical Models of Influenza A Virus Infection: Multiplicity of Infection and Its Impact on Co-Infection and Virus Production

Dissertation

zur Erlangung des akademischen Grades

Doktoringenieur
(Dr.-Ing.)

von: Daniel Rüdiger, M. Sc.

geboren am: 24. Juli 1989 in Magdeburg

genehmigt durch die Fakultät für Verfahrens- und Systemtechnik

der Otto-von-Guericke-Universität Magdeburg

Promotionskommission: Prof. Dr.-Ing. habil. Evangelos Tsotsas

Prof. Dr.-Ing. Udo Reichl

Prof. Dr. John Yin

Prof. Dr. Carmen Molina-París

eingereicht am: 30. November 2021

Promotionskolloquium am: 02. März 2022

A theory that explains everything,

explains nothing.

Karl Popper

__Abstract__

Influenza A viruses (IAV) are pathogens that infect up to 20% of the human population in seasonal epidemics inducing a contagious respiratory disease, which can lead to more than half a million deaths each year. Besides their annual impact on public health and the economy, the outbreak of major pandemics like the "Spanish flu" caused by emerging virus strains may threaten millions of lives. For the development and improvement of prevention and treatment strategies for IAV infections, it is critical to understand the exact mechanisms during virus infection and spreading on the cellular, human and global level.

In this thesis, we aim to establish mathematical models of IAV infection that can describe and predict virus replication and spreading dynamics in a wide range of infection conditions relevant for vaccine production. In particular, we focus on the impact of the number of infecting virus particles per cell, i.e., the multiplicity of infection (MOI), and the impact of defective interfering particles (DIPs) on the infection dynamics. These two factors strongly influence virus yields during cell culture-based vaccine production. In addition, DIPs show great promise for antiviral application.

In the first part of this thesis, we develop a mathematical multiscale model of IAV infection in animal cell culture that closely captures replication and propagation dynamics on the intracellular and cell population level for high MOI infections. Using the same model parameters, the model was able to reproduce infectious and total virus titers in low MOI conditions. The key difference between high and low MOI conditions was the percentage of infectious virions among the total virus particles released. Furthermore, we find that the time until cells are detected as apoptotic after IAV infection is normally distributed, which can be described closely using a logistic function for the rate of apoptosis. Overall, the multiscale model of IAV infection provides an ideal framework for the prediction and optimization of IAV manufacturing in animal cell culture.

Cell culture-derived DIPs, which cannot replicate on their own, are considered for antiviral therapy, because they can inhibit IAV production during co-infection and enhance the innate immune response in the host. The second part of this work covers

a mathematical multiscale model of IAV and DIP co-infection that reproduces intracellular and cell population dynamics closely for a wide range of infection conditions. To describe these different scenarios of competition between the two types of virus particles with a single set of parameters, various regulatory mechanisms of viral ribonucleic acid (RNA) synthesis had to be considered. We observe a reduction of the levels of viral messenger RNAs (vmRNAs) related to proteins of the viral polymerase. Furthermore, we find that the accumulation of vmRNA in cells infected only by a specific DIP, which cannot produce the viral polymerase required for replication, can be described by incorporating the primary transcription of vmRNA mediated solely by the parental viral polymerase bound to the viral genome. Additionally, the levels of viral genomic RNA (vRNA) can only be captured if the ratio between the MOI and the number of DIPs per cell, i.e., the multiplicity of DIPs (MODIP), is considered during intracellular virus replication. Overall, the co-infection model supports a comprehensive understanding of the interactions between IAVs and DIPs during co-infection and enables the prediction and optimization of DIP production for therapeutic use.

In the last part of this thesis, we use the two developed multiscale models for simulation studies and model prediction. Simulations performed with the model of IAV infection suggest that for high MOIs the infection is driven only by multiple-hit infections of the seed virus. In low MOI conditions, infections are induced almost exclusively by progeny virus particles shifting from single- to multiple-hit infections over time. The model of IAV and DIP co-infection predicts that the concentration of DIPs should be at least 10^4 times higher than that of regular IAV particles to prevent the spread of an infection. Furthermore, model simulations suggest a nearly equimolar concentration of IAVs and DIPs as the optimal initial conditions for cell culture-derived production of DIPs for antiviral therapy.

Taken together, the multiscale models developed in this thesis provide a systems-level understanding of IAV infection dynamics and how this dynamics is impacted by the initially provided MOI and MODIP. These detailed mathematical models successfully describe infection dynamics on the intracellular and cell population level for a wide range of conditions using a single set of parameters and enable meaningful model predictions. Such models, thus, support the fight against influenza and could facilitate

a deeper understanding of infection processes for other virus species, in particular regarding the impact of the MOI and potential interactions with DIPs.

Kurzfassung

Influenza-A-Viren (IAV) sind Krankheitserreger, die bis zu 20% der Weltbevölkerung in saisonalen Epidemien infizieren. Solche Infektionen rufen eine ansteckende Lungenwegserkrankung hervor, umgangssprachlich auch als Grippe bezeichnet, welche zu mehr als einer halben Million Todesfällen pro Jahr führen kann. Neben den jährlichen Schäden für die Bevölkerung und die Wirtschaft ist eine weitere Gefahr der Ausbruch von Influenza-Pandemien, wie z.B. der sogenannten „Spanischen Grippe", ausgelöst durch mutierte Virenstämme. Um Strategien zur Bekämpfung und Prävention von Grippeinfektionen zu entwickeln und zu verbessern, ist das Verstehen der zugrundeliegenden Mechanismen einer Virusinfektion ein wichtiger Faktor.

Das Ziel dieser Doktorarbeit war die Entwicklung mathematischer Modelle, welche die Dynamik von IAV-Infektionen für verschiedene impfstoffproduktionsrelevante Infektionsbedingungen beschreiben und vorhersagen können. Dabei wird der Fokus auf die Anzahl der infizierenden Viruspartikel pro Zelle, bezeichnet als Multiplizität der Infektion (MOI), und die Interaktion mit defekten interferierenden Viruspartikeln (DIPs) gelegt. Diese beiden Faktoren zeigen einen starken Einfluss auf die zellkulturbasierte Impfstoffproduktion. Zudem werden DIPs für eine Nutzung als antivirales Medikament in Erwägung gezogen.

Im ersten Teil dieser Arbeit wird ein mathematisches Multiskalenmodell der IAV-Infektion in tierischen Zellkulturen entwickelt, welches die virale Replikations- und Ausbreitungsdynamik auf intrazellulärer Ebene und auf Ebene der Zellpopulationen für Infektionen mit einer hohen MOI beschreibt. Mit den für dieses Szenario bestimmten Modellparametern konnte das Modell die infektiösen und gesamten Virustiter unter niedrigen MOI-Bedingungen reproduzieren. Der Hauptunterschied zwischen hohen und niedrigen MOI-Bedingungen war der prozentuale Anteil der infektiösen Virionen an der gesamten Viruspartikelfreisetzung. Darüber hinaus stellen wir fest, dass die vergangene Zeit, nach welcher infizierte Zellen als apoptotisch detektiert werden können, normal verteilt ist. Dies ließ mit einer logistischen Funktion für die Apoptoserate gut beschreiben. Insgesamt bietet das Multiskalenmodell der IAV-

Infektion eine ideale Grundlage für die Vorhersage und Optimierung der IAV-Herstellung in Zellkulturen.

Aus Zellkulturen gewonnene DIPs, die sich nicht selbst replizieren können, werden für die antivirale Therapie in Betracht gezogen, da sie die IAV-Produktion während einer Koinfektion hemmen und die angeborene Immunantwort von Zellen verstärken können. Der zweite Teil dieser Arbeit befasst sich mit einem mathematischen Multiskalenmodell der IAV- und DIP-Koinfektion, welches die Dynamik auf der intrazellulären und der Zellpopulations-Ebene für eine Vielzahl von Infektionsbedingungen genau beschreibt. Um diese verschiedenen Szenarien der Interaktion zwischen den beiden Arten von Viruspartikeln mit einem einzigen Parametersatz zu beschreiben, mussten verschiedene Regulationsmechanismen der Synthese von viralen Ribonukleinsäuren (RNA) berücksichtigt werden. Dabei stellt sich heraus, dass die Konzentrationen viraler Boten-RNAs (vmRNAs), welche zur Produktion der Proteine der viralen Polymerase genutzt werden, deutlich reduziert sind. Darüber hinaus stellen wir fest, dass die Ansammlung von vmRNA in Zellen, die nur mit einem DIP infiziert sind, welches die virale Polymerase nicht produzieren kann, durch die Einbeziehung der primären Transkription von vmRNA durch parentale virale Polymerasen beschrieben werden kann. Zudem können die Mengen an viraler genomischer RNA (vRNA) nur erfasst werden, wenn das Verhältnis zwischen der MOI und der Anzahl der DIPs pro Zelle, bezeichnet als Multiplizität der DIPs (MODIP), während der intrazellulären Virusreplikation berücksichtigt wird. Somit unterstützt das Koinfektionsmodell ein umfassendes Verständnis der Wechselwirkungen zwischen IAVs und DIPs während der Koinfektion und ermöglicht die Vorhersage und Optimierung der DIP-Produktion für den therapeutischen Einsatz.

Im letzten Teil dieser Arbeit verwenden wir die beiden Multiskalenmodelle für Simulationsstudien und Modellvorhersagen. Simulationen, die mit dem Modell der IAV-Infektion durchgeführt wurden, deuten darauf hin, dass bei einer hohen MOI Zellen immer durch mehrere Viruspartikel, welche aus dem Saatvirus stammen, infiziert werden. Unter niedrigen MOI-Bedingungen werden Infektionen fast ausschließlich durch neu produzierte Viruspartikel ausgelöst, wobei Zellen anfangs von einzelnen und später von mehreren Viruspartikeln infiziert werden. Modellprädiktionen der Koinfektion von IAVs und DIPs sagen voraus, dass die Konzentration von DIPs

mindestens 10^4-mal höher sein sollte als die von normalen IAV-Partikeln, um die Ausbreitung einer Infektion zu verhindern. Darüber hinaus deuten Modellsimulationen darauf hin, dass eine nahezu äquimolare Konzentration von IAVs und DIPs die optimalen Anfangsbedingungen für die Produktion von DIPs in Zellkulturen für die antivirale Therapie darstellen.

Zusammengenommen bieten die in dieser Arbeit entwickelten Multiskalen-Modelle ein Verständnis der IAV-Infektionsdynamik auf Systemebene und zeigen, wie diese Dynamik durch die eingesetzten MOIs und MODIPs beeinflusst wird. Diese detaillierten mathematischen Modelle beschreiben die Infektionsdynamik für ein breites Spektrum von Bedingungen auf intrazellulärer und Zellpopulations-Ebene unter Verwendung eines einzigen Parametersatzes und ermöglichen Modellvorhersagen. Solche Modelle unterstützen somit den Kampf gegen die Grippe und könnten ein tieferes Verständnis der Infektionsprozesse bei anderen Virusarten ermöglichen, insbesondere hinsichtlich der Auswirkungen der MOI und möglicher Wechselwirkungen mit DIPs.

Contents

List of Abbreviations

AIC	Akaike information criterion
COVID-19	Coronavirus disease 2019
CRM1	cellular receptor chromosome region maintenance 1 protein
cRNA	complementary RNA
cRNP	complementary ribonucleoprotein
DDE	delay differential equation
DI	defective interfering
DI244	well characterized IAV with a large deletion in genome segment 1
DIP	defective interfering particle
ER	endoplasmic reticulum
FIVR	fraction of infectious virions released
FL	full-length
HA	hemagglutinin
HBV	hepatitis B virus
HCV	hepatitis C virus
HIV	human immunodeficiency virus
IAV	Influenza A virus
hpi	hours post infection
IFN	interferon
L3	MOI 10^{-3} and MODIP 3
L30	MOI 10^{-3} and MODIP 30
M1	matrix protein 1
M2	matrix protein 2
MDCK	Madin-Darby Canine Kidney
MDCKadh	adherent Madin-Darby Canine Kidney
MDCKsus	suspension Madin-Darby Canine Kidney
MODIP	multiplicity of DIPs
MOI	multiplicity of infection
mRNA	messenger ribonucleic acid

NA	neuraminidase
NEP	nuclear export protein
NIBSC	National Institute for Biological Standards and Control
NLS	nuclear localization signal
NP	nucleoprotein
NS1	nonstructural protein 1
ODE	ordinary differential equation
PA	polymerase acidic protein
PB1	polymerase basic protein 1
PB2	polymerase basic protein 2
PFU	plaque forming unit
Pol II	cellular RNA polymerase II
PR	Puerto Rico
RdRp	RNA-dependent RNA polymerase
RKI	Robert Koch Institute
RNA	ribonucleic acid
RT-qPCR	quantitative reverse transcription polymerase chain reaction
SA	sialic acid
SARS-CoV2	severe acute respiratory syndrome coronavirus 2
SIE	superinfection exclusion
SSR	sum of squared residuals
STV	standard virus particle
TCID$_{50}$	50% tissue culture infective dose
vmRNA	viral messenger ribonucleic acid
vRNA	viral genomic RNA
vRNP	viral ribonucleoprotein complexes
VSV	vesicular stomatitis virus

List of Symbols

Symbol	Unit	Description
α	–	significance level
β	ml/(virion · h)	virus infection rate
δ	h^{-1}	death rate of infected cells
$\hat{\varepsilon}_i$	–	residuals estimated from a fitted model
θ	–	parameter vector
μ	h^{-1}	specific growth rate of target cells
μ_{Max}	h^{-1}	maximum specific growth rate of target cells
ν_1	–	factor connecting the MODIP-to-MOI ratio to the reduction of vRNA synthesis
ν_2	–	exponent connecting the MODIP-to-MOI ratio to the reduction of vRNA synthesis
ν_{Apo}	h^{-1}	distribution factor of the virus-induced apoptosis rate
σ	–	standard deviation
σ_i	–	standard deviation of measurement at time point i
σ_s	–	maximum value of species s
$\hat{\sigma}^2$	–	maximum likelihood estimator
τ	h	infection age
τ_{Apo}	h	time after cell infection at which the rate of virus-induced apoptosis reaches its half-maximum
τ_{SIE}	h	infection age after which STV-only infected cells cannot become re-infected by a DIP
AIC	–	Akaike information criterion
B_{Hi}	site or sites/ml	number of free high-affinity binding sites
B_{Lo}	site or sites/ml	number of free low-affinity binding sites
B_{Hi}^{D}	site or sites/ml	number of free high-affinity binding sites on cells susceptible to DIP infection
B_{Lo}^{D}	site or sites/ml	number of free low-affinity binding sites on cells susceptible to DIP infection
$B_{\text{Hi}}^{\text{Tot}}$	site or sites/cell	total number of high-affinity binding sites
$B_{\text{Lo}}^{\text{Tot}}$	site or sites/cell	total number of low-affinity binding sites
B_{Hi}^{V}	site or sites/ml	number of free high-affinity binding sites on cells susceptible to STV infection
B_{Lo}^{V}	site or sites/ml	number of free low-affinity binding sites on cells susceptible to STV infection
c	h^{-1}	clearance rate of virions
C_{Tot}	cells/ml	total number of viable cells
Cp	molecules/cell	number of (nuclear) cRNPs
Cp_{i}	molecules/cell	number of (nuclear) cRNPs of segment i

Symbol	Unit	Description
d	h^{-1}	death rate of uninfected target cells
D	virions/ml	concentration of defective interfering particles
D_{Rib}	nucleotides	distance between two adjacent ribosomes on an mRNA
D_{Hi}^{Att}	virions/cell	DIPs attached to high-affinity binding site
D_{Lo}^{Att}	virions/cell	DIPs attached to low-affinity binding site
D^{Cyt}	molecules/cell	complex of parental vRNPs in the cytoplasm containing one DI vRNP
D_{Cplx}^{Cyt}	molecules/cell	complex of progeny vRNPs in the cytoplasm containing one DI vRNP
D^{En}	virions/cell	number of DIPs in endosomes
D^{Ex}	virions/cell	number of DIPs in the extracellular medium
D^{Rel}	virions/cell	number of progeny DIPs
D_{Tot}^{Rel}	virions/cell	total number of released DIPs
f_{μ}	–	cell growth reduction factor
F_{μ}	–	cell growth reduction in very high virus concentrations
F_{Adv}	–	replication advantage of a DI RNA
$f_{D,V}$	–	MODIP-to-MOI ratio
F_{Fus}	–	fraction of fusion-competent virions
F_{Inf}	cells/virion	infection efficiency
f_{M}	–	reduction factor for RdRp-related vmRNA synthesis
F_{M}	–	reduction of RdRp-related vmRNA synthesis
F_{MODIP}	virions/cell	threshold MODIP for vRNA synthesis reduction
F_{Par}	–	fraction of infectious virions released
F_{Spl7}	–	fraction of M2-encoding vmRNAs
F_{Spl8}	–	fraction of NEP-encoding vmRNAs
I	cells/ml	concentration of infected cells
I_{A}	cells/ml	concentration of apoptotic infected cells
I_{CO}	cells/ml	concentration of co-infected cells
I_{DIP}	cells/ml	concentration of DIP-infected cells
I_{STV}	cells/ml	concentration of STV-infected cells
K	–	number of model parameters
K_{I}	h^{-1}	maximum virus-induced apoptosis rate
K_{R}	molecules/cell	vmRNA synthesis inhibition constant
K_{V}	h^{-1}	maximum vRNA synthesis rate
$K_{V^{Rel}}$	virions	influence of protein concentration on virus release

Symbol	Unit	Description
$k_{\text{I}}^{\text{Apo}}$	h^{-1}	apoptosis rate of infected cells
$k_{\text{T}}^{\text{Apo}}$	h^{-1}	apoptosis rate of uninfected target cells
$k_{\text{c,Hi}}^{\text{Att}}$	ml/(site $\cdot$ h)	attachment rate to high-affinity binding sites
$k_{\text{c,Lo}}^{\text{Att}}$	ml/(site $\cdot$ h)	attachment rate to low-affinity binding sites
$k_{\text{Hi}}^{\text{Att}}$	(site $\cdot$ h)$^{-1}$	attachment rate to high-affinity binding sites
$k_{\text{Lo}}^{\text{Att}}$	(site $\cdot$ h)$^{-1}$	attachment rate to low-affinity binding sites
$k_{\text{M1}}^{\text{Bind}}$	(molecule $\cdot$ h)$^{-1}$	binding rate of M1 to nuclear vRNPs
$k_{\text{NP}}^{\text{Bind}}$	(molecule $\cdot$ h)$^{-1}$	binding rate of NP to RdRp-RNA complexes
$k_{\text{RdRp}}^{\text{Bind}}$	(molecule $\cdot$ h)$^{-1}$	binding rate of RdRp complexes to vRNA/cRNA
k^{Cplx}	molecule$^{-7} \cdot$ h^{-1}	formation rate of complexes containing eight vRNPs
$k_{\text{M}}^{\text{Deg}}$	h^{-1}	degradation rate of vmRNAs
$k_{\text{R}}^{\text{Deg}}$	h^{-1}	degradation rate of naked cRNA/vRNA
$k_{\text{Rnp}}^{\text{Deg}}$	h^{-1}	degradation rate of RNPs
$k_{\text{RRdRp}}^{\text{Deg}}$	h^{-1}	degradation rate of RdRp-RNA complexes
$k_{\text{V}}^{\text{Deg}}$	h^{-1}	degradation rate of infectious virions
$k_{\text{Ven}}^{\text{Deg}}$	h^{-1}	degradation rate of virions in lysosomes
$k_{\text{Hi}}^{\text{Dis}}$	h^{-1}	detachment rate from high-affinity binding sites
$k_{\text{Lo}}^{\text{Dis}}$	h^{-1}	detachment rate from low-affinity binding sites
k^{En}	h^{-1}	endocytosis rate
$k_{\text{c,Hi}}^{\text{Eq}}$	ml/site	equilibrium constant of high-affinity binding sites
$k_{\text{c,Lo}}^{\text{Eq}}$	ml/site	equilibrium constant of low-affinity binding sites
$k_{\text{Hi}}^{\text{Eq}}$	site^{-1}	equilibrium constant of high-affinity binding sites
$k_{\text{Lo}}^{\text{Eq}}$	site^{-1}	equilibrium constant of low-affinity binding sites
k^{Exp}	(molecule $\cdot$ h)$^{-1}$	rate of NEP binding and nuclear export
k^{Fus}	h^{-1}	fusion rate
k^{Imp}	h^{-1}	nuclear import rate
k^{Lys}	h^{-1}	lysis rate of apoptotic cells
k^{RdRp}	molecules$^{-2} \cdot$ h^{-1}	formation rate of polymerase complexes
k^{Rel}	virions/(molecule $\cdot$ h)	virus release rate
$k_{\text{Red}}^{\text{Rel}}$	–	decrease of the fraction of infectious virus particle released
$k_{\text{C}}^{\text{Syn}}$	h^{-1}	cRNA synthesis rate
$k_{\text{M}}^{\text{Syn}}$	nucleotides/h	vmRNA synthesis rate
$k_{\text{P}}^{\text{Syn}}$	nucleotides/h	protein synthesis rate
$k_{\text{V}}^{\text{Syn}}$	h^{-1}	vRNA synthesis rate

Symbol	Unit	Description
L_i	nucleotides	length of the vmRNA of segment i
L_V	nucleotides	average length of a vRNA
$L_{V,i}$	nucleotides	length of the vRNA of segment i
$\log(L(\hat{\theta}\vert\text{data}))$	−	log-likelihood function
$M(\gamma)$	−	characteristic of the system output γ
N_c	−	number of experimental conditions
N_d	−	number of available individual measurements
N_j	molecules/virion	number of proteins of type j in a virus particle
N_s	−	number of measured species
N_t	−	number of measured time points
N_{M1}^{Nuc}	nucleotides	number of nucleotides bound by on M1 molecule
N_{NEP}^{Nuc}	nucleotides	number of nucleotides bound by on NEP molecule
N_{NP}^{Nuc}	nucleotides	number of nucleotides bound by on NP molecule
p	virions/(cells · h)	rate of virus production
P_j	molecules/cell	number of proteins of type j
P^{Rel}	virions/cell	total number of progeny virions
P_{Tot}^{Rel}	virions/cell	total number of released virus particles
R^C	molecules/cell	number of naked cRNAs
R_i^C	molecules/cell	number of naked cRNAs of segment i
R_{RdRp}^C	molecules/cell	number of RdRp-cRNA complexes
r^{Inf}	h^{-1}	infection rate of target cells
r_{DIP}^{Inf}	h^{-1}	DIP infection rate of target cells
r_{STV}^{Inf}	h^{-1}	STV infection rate of target cells
r^{Lys}	h^{-1}	lysis rate of apoptotic cells
r_{DIP}^{Lys}	h^{-1}	lysis rate of apoptotic cells susceptible to DIP infection
r_{STV}^{Lys}	h^{-1}	lysis rate of apoptotic cells susceptible to STV infection
R_i^M	molecules/cell	number of vmRNA of segment i
$R_{i,DIP}^M$	molecules/cell	number of vmRNA of segment i in DIP-only infected cells
r_{DIP}^{Rel}	virions/(cells · h)	release rate of infectious DIPs
$r_{DIP,I_{CO}}^{Rel}$	virions/(cells · h)	release rate of infectious DIPs from co-infected cells
$r_{DIP,I_{STV}}^{Rel}$	virions/(cells · h)	release rate of infectious DIPs from STV-only infected cells

Symbol	Unit	Description
$r_{\text{DIP,Tot}}^{\text{Rel}}$	virions/(cells $\cdot$ h)	total release rate of DIPs
$r_{\text{Inf}}^{\text{Rel}}$	virions/(cells $\cdot$ h)	release rate of infectious virus particles
$r_{\text{Par}}^{\text{Rel}}$	virions/(cells $\cdot$ h)	release rate of non-infectious virus particles
$r_{\text{STV}}^{\text{Rel}}$	virions/(cells $\cdot$ h)	release rate of infectious STVs
$r_{\text{STV,I}_{\text{CO}}}^{\text{Rel}}$	virions/(cells $\cdot$ h)	release rate of infectious STV from co-infected cells
$r_{\text{STV,I}_{\text{STV}}}^{\text{Rel}}$	virions/(cells $\cdot$ h)	release rate of infectious STV from STV-only infected cells
$r_{\text{STV,Tot}}^{\text{Rel}}$	virions/(cells $\cdot$ h)	total release rate of STV
R^{V}	molecules/cell	number of naked vRNAs
$R_{\text{RdRp}}^{\text{V}}$	molecules/cell	number of RdRp-vRNA complexes
$R_{\text{RdRp,i}}^{\text{V}}$	molecules/cell	number of RdRp-vRNA complexes of segment i
s	h^{-1}	growth rate of uninfected target cells
S_{θ}^{M}	–	sensitivity coefficient
t	h	time
t_{I}	h	time of cell infection
T	cells/ml	concentration of uninfected target cells
T_{0}	cells/ml	initial target cell concentration
T_{A}	cells/ml	concentration of apoptotic uninfected cells
T_{Max}	cells/ml	maximum target cell concentration
V	virions/ml	concentration of virus particles
$V_{\text{Hi}}^{\text{Att}}$	virions/cell	STV attached to high-affinity binding site
$V_{\text{Lo}}^{\text{Att}}$	virions/cell	STV attached to low-affinity binding site
V^{Cyt}	molecules/cell	complex of eight parental vRNPs in the cytoplasm
$V_{\text{Cplx}}^{\text{Cyt}}$	molecules/cell	complex of eight progeny vRNPs in the cytoplasm
V^{En}	virions/(cell or ml)	number of virions in endosomes
V^{Ex}	virions/cell	number of virions in the extracellular medium
V^{Rel}	virions/cell	number of infectious progeny virions
$V_{\text{Tot}}^{\text{Rel}}$	virions/cell	total number of released infectious virions
Vp^{Cyt}	molecules/cell	number of cytoplasmic vRNPs
$Vp_{\text{i}}^{\text{Cyt}}$	molecules/cell	number of cytoplasmic vRNPs of segment i
$Vp_{\text{M1}}^{\text{Cyt}}$	molecules/cell	number of cytoplasmic M1-NEP-vRNP complexes
$Vp_{\text{M1,i}}^{\text{Cyt}}$	molecules/cell	number of cytoplasmic M1-NEP-vRNP complexes of segment i
Vp^{Nuc}	molecules/cell	number of nuclear vRNPs

Symbol	Unit	Description
Vp_i^{Nuc}	molecules/cell	number of nuclear vRNPs of segment i
Vp_{M1}^{Nuc}	molecules/cell	number of nuclear M1-vRNP complexes
$Vp_{M1,i}^{Nuc}$	molecules/cell	nuclear M1-vRNP complexes of segment i
w_i	−	model probability of model i
x	−	realization of the state vector of a stochastic model
x_i	−	measurement value at time point t_i
y	−	vector of experimental observations
$y_{s,c}$	−	model output of species s at condition c

1. Introduction

Infectious diseases affect almost all organisms and are responsible for roughly 17% of human deaths [1]. A large portion of these infections is caused by viruses, which are non-cellular life forms that hijack the reproductive system of their host cells to generate progeny virus particles. When virus infections spread rapidly among populations on a global level, they induce pandemics, which can have hazardous impacts. The currently ongoing Coronavirus disease 2019 (COVID-19) pandemic, which has so far claimed more than 5.1 million human lives [2], shifted a large part of the attention towards coronaviruses. However, influenza viruses were responsible for most of the major pandemic outbreaks since the beginning of the 20th century [3]. The Spanish flu claimed around 50 million lives and more recent influenza pandemics caused up to a million deaths each [4, 5]. Based on historical data, influenza pandemics are expected to occur at least once every 60 years [6]. However, wildlife markets and the expansion of industrial livestock production may contribute to an even higher frequency of pandemic outbreaks in the future, if no countermeasures are taken [7].

Due to the high mutation rate of the influenza genome, which has been estimated between 2×10^{-6} to 2×10^{-4} mutations per site per round of genome replication, and the potential reassortment with strains from other hosts, influenza viruses can evolve rapidly [8]. This enables influenza viruses to infect a variety of species, e.g., poultry, horses, pigs, and humans [9]. However, their natural reservoirs are wild aquatic birds, which normally do not become severely sick following an infection [10]. When infecting humans, influenza viruses predominantly target epithelial cells in the upper respiratory tract inducing a contagious disease. General symptoms include fever, rhinitis, sore throat, headache, muscle pain, and fatigue. Severe influenza virus infections may also induce pneumonia, meningitis or encephalitis and lead to the death of the host. In adult patients with a functioning immune system, seasonal influenza strains generally cause mild to moderate symptoms [11]. However, children, the elderly or immunocompromised individuals carry a larger risk for severe infections and mortality. In most cases, the immune system of a host is able to prevent or reduce the severity of an infection by the same pathogen after surviving a disease. The reassortment with

other strains and the adaptation to their hosts allow influenza viruses to escape or mitigate the host immune response by carrying slight variations in their genome [8]. This enables the re-infection of former hosts and results in annual epidemic outbreaks, which generally occur during the winter season, as the virus spreads through populations with reduced immunity. However, a baseline immune response is usually retained against seasonal influenza virus strains and the immune system is not completely naive, as compared to pandemic virus strains. Nevertheless, seasonal influenza outbreaks can cause up to five million severe infections and 650,000 deaths each year [12].

To reduce the impact of seasonal influenza epidemics, annual vaccinations are administered worldwide. However, vaccination rates can vary greatly between countries and the composition of the vaccine has to be updated if the currently prevalent virus strains change [13]. During a pandemic outbreak, influenza vaccines for a newly emerged pandemic strain could be developed with a certain delay, i.e., at least 5–6 months after the initial detection [14], but would not be available immediately. For the application during early phases of seasonal epidemics, pandemic outbreaks and the general treatment of influenza virus infections, antiviral drugs can be administered. Typically, such drugs interfere with the viral life cycle reducing symptoms and supporting viral clearance. However, antivirals can become ineffective if viruses acquire resistances to specific drugs via genetic shifts [15, 16]. To ensure successful prevention and treatment of influenza virus infection on a global scale, the optimization of vaccine production processes and the discovery of potent antivirals is highly important.

Defective interfering particles (DIPs) are considered as promising candidates for antiviral therapy due to their capability to interfere with virus replication [17]. They are structurally similar to their corresponding standard virus particle (STV), replication-incompetent on their own, reduce STV titers during co-infection and can enhance the innate immune response of cells. With the advent of powerful analytical methods in recent years, DIP composition and production could be investigated thoroughly. However, various aspects of DIP *de novo* generation and their interference mechanism remain largely unknown. Different animal studies confirmed their therapeutic potential for prevention and mitigation of influenza A virus (IAV) infections [18, 19]. In these

studies, a high ratio of DIPs to STVs was required for DIPs to show significant impacts on animal survival.

The number of infecting virus particles per cell, i.e., the multiplicity of infection (MOI) and the multiplicity of DIPs (MODIP), do not only affect DIP interference, but also strongly impact regular infection dynamics. During natural influenza infections, which typically occur via airborne transmission, the MOI is an indicator for the chance of a breakthrough infection. Individual virus particles can fail during infection, but larger virus populations have a much higher chance for successful propagation. Furthermore, during influenza vaccine production, the initial MOI is a tightly controlled parameter and the production process is initiated at very low MOIs. In contrast, high MOI conditions support the production of DIPs. Understanding the complex roles of MOI and MODIP, i.e., their impact on infection dynamics, on vaccine and DIP production, and their dynamics changes during an infection could greatly benefit the prevention or treatment of influenza virus infections.

The underlying mechanisms of complex biological systems, e.g., virus-host cell interactions and virus spreading in cell populations, remained elusive for a long time due to a scarcity of measurements. However, advances in various disciplines, e.g., analytical methods, computational processing power and systems biology, enabled the collection of large amounts of data and the development of sophisticated mathematical models. These models were employed to test existing hypotheses, to generate new hypotheses that could be evaluated experimentally, and to predict system behavior. In particular, model-based studies describing the global spread of infections were developed to guide public health strategies in response to pandemic outbreaks, e.g., for influenza [20] and COVID-19 [21]. Furthermore, models were used to study the infection dynamics of various viruses inside hosts, such as humans or animals, or even in single cells. These kinds of studies support the understanding of immune responses, the development of novel antivirals and the optimization of vaccine production. The vast majority of models focused on virus-host interactions on individual scales, i.e., on the single-cell, within-host, between-host or global level. More recently, multiscale models that study the interplay between these different levels have been developed to uncover previously unknown interactions and mechanisms.

The aim of this thesis was to develop a mathematical multiscale model of STV and DIP co-infection for IAV that can be used to predict intracellular virus replication dynamics and infection spreading on the cell population level. Using this model, we intended to assess the impact of the MOI and the MODIP on viral titers, evaluate their dynamic behavior during an infection and study mechanisms of DIP interference. This could support the optimization of vaccine and DIP production, improve the understanding of STV and DIP interactions in general, and enable the estimation of an optimal DIP dose for therapeutic application. As the interaction of STVs and DIPs on the intracellular level strongly affects virus propagation on the cell population level and vice versa, a multiscale approach is required to represent the complexity of the underlying mechanisms. Thus, three main objectives were defined for this thesis: (i) the development of a multiscale model of STV and DIP co-infection, (ii) the explicit consideration of the impact of MOI and MODIP conditions on infection dynamics in the model, and (iii) the determination of a parametrization, ideally a single set of parameters, allowing the description of a large range of infection conditions to enable reliable model predictions.

Following this introduction, we highlight general properties of IAVs and DIPs, outline the influence of the MOI and the MODIP on virus infections and discuss mathematical modeling in virology (Chapter 2). In Chapter 3, we define the multiscale models developed to describe IAV infection dynamics in different MOI conditions and for the co-infection of STVs and DIPs. Then, we present the results of model construction, simulation and prediction for the two different models, which were calibrated to intracellular and cell population measurements from infection experiments (Chapter 4). Lastly, we provide a general conclusion and an outlook for this thesis in Chapter 5 and 6, respectively.

2. Theoretical background

In the first section of this chapter, an overview of influenza virus structure, the viral replication cycle and defective interfering particles is provided. Then, the impact of the MOI and the MODIP on infection dynamics as well as on the competition between STVs and DIPs is outlined. Finally, mathematical modeling approaches and theoretical tools for model analysis are highlighted.
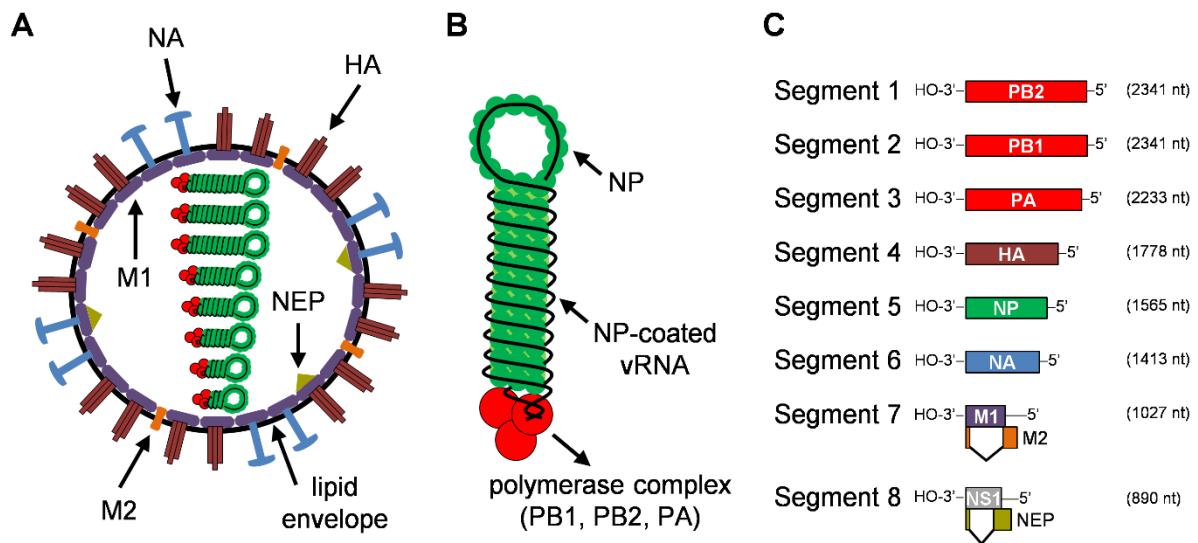
2.1 Influenza A virus

Influenza viruses are members of the family of *Orthomyxoviridae*, which are negative-sense ribonucleic acid (RNA) viruses. Currently, four genera of influenza viruses are known, i.e., influenza virus A, B, C and D, with the last one discovered just recently [22, 23]. Influenza epidemics are primarily caused by the types A and B, which induce an infectious respiratory disease in humans. However, the major pathogen is IAV, which is also able to infect birds and has caused severe pandemic outbreaks in the past. Therefore, we focus on IAV for the rest of this work.

Due to the high mutation rate of the viral genome, a large variety of IAV strains has been discovered. The different strains are characterized by their genus, place of isolation, isolate number, year of isolation, and the subtype of their surface proteins, i.e., hemagglutinin (HA) and neuraminidase (NA). The IAV strain A/PR/8/34 (H1N1) [24], which is widely used for infection experiments, was isolate number 8 obtained in Puerto Rico (PR) in the year 1934 and contains HA and NA of subtype 1.

2.1.1 Morphology

IAV spreads between hosts via spherical (diameter of 80-120 nm) or elongated, filamentous (up to 1 µm long) virus particles, also referred to as virions [25, 26]. The general composition of an IAV particle is presented in Figure 2.1.

Figure 2.1.: Influenza virus particle and genome structure. (A) Scheme of a spherical IAV particle. (B) Schematic depiction of an influenza viral ribonucleoprotein. (C) Overview of the eight genome segments of the influenza A/PR/8/34 strain. Boxes represent the encoded proteins for each segment, respectively. For segments 7 and 8, introns of the spliced messenger RNAs (mRNAs) are indicated by V-shapes. PB1/PB2 = polymerase basic protein 1 or 2, PA = polymerase acidic protein, HA = hemagglutinin, NP = nucleoprotein, NA = neuraminidase, M1/M2 = matrix protein 1 or 2, NS1 = nonstructural protein 1, NEP = nuclear export protein. Figure adapted from [27].

Virions of IAV are enveloped by a lipid bilayer, which originates from the membrane of the host cell and carries the viral ion channel matrix protein 2 (M2) and the viral surface proteins HA and NA. The viral matrix protein 1 (M1) is coating the envelope from the inside separating it from the core of the virion. In the core, the nuclear export protein (NEP) and the viral genome are located. The IAV genome is segmented and comprises eight individual genomic viral RNAs (vRNAs). In a virus particle, these vRNAs occur as viral ribonucleoprotein complexes (vRNPs), which are formed by the vRNA binding to one RNA-dependent RNA polymerase (RdRp) and multiple nucleoproteins (NPs). Additionally, vRNPs interact with M1 proteins in the core of the virus particle. The RdRp consists of three subunits, i.e., polymerase basic proteins 1 and 2 (PB1 and PB2) and polymerase acidic protein (PA) [28-30]. Furthermore, the unspecific incorporation of various host cell factors has been observed [31].

2.1.2 Viral genome and proteins

IAV particles possess a segmented, negative-sense, single-stranded genome that consists of eight vRNPs. The genome segments form rod-shaped complexes and contain 890 to 2341 nucleotides (for reference strain A/PR/8/34) resulting in a length of 30 to 120 nm [32]. Although the genome is single-stranded, it is configured in a double-helical structure with the RdRp bound to both ends of the RNA (5' and 3'), which is intertwined and forms a helix with itself. Inside the virion, the eight genome segments adopt a "7+1" configuration with one core vRNP and the other seven segments forming a ring around it [33, 34].

Each genome segment provides the genetic information for at least one specific viral protein, with currently 18 different proteins described for IAV [35]. The polymerase subunits PB2, PB1 and PA are located on segments 1 to 3, respectively. Segment 4 and 6 encode for the viral surface proteins HA and NA, respectively, and NP is provided by segment 5. Segment 7 encodes for M1 and, by using alternative RNA splicing, can also generate M2. The same applies to segment 8, which encodes for non-structural protein 1 (NS1) and can additionally provide NEP using alternative splicing [36]. Further viral proteins can be generated using alternative reading frames (for segment 2) and ribosomal frameshifting (for segment 3). However, these proteins were only detected in a few virus strains or in cell culture experiments suggesting they are non-essential or serve a highly specialized function [35, 37].

2.1.3 Intracellular replication cycle

IAV replication occurs in the nucleus of its host cell, which is rare for RNA viruses. Therefore, the genomic information of the virus has to be transferred to the nucleus and, after progeny vRNP production, back to the cell membrane for virus particle release (Figure 2.2).
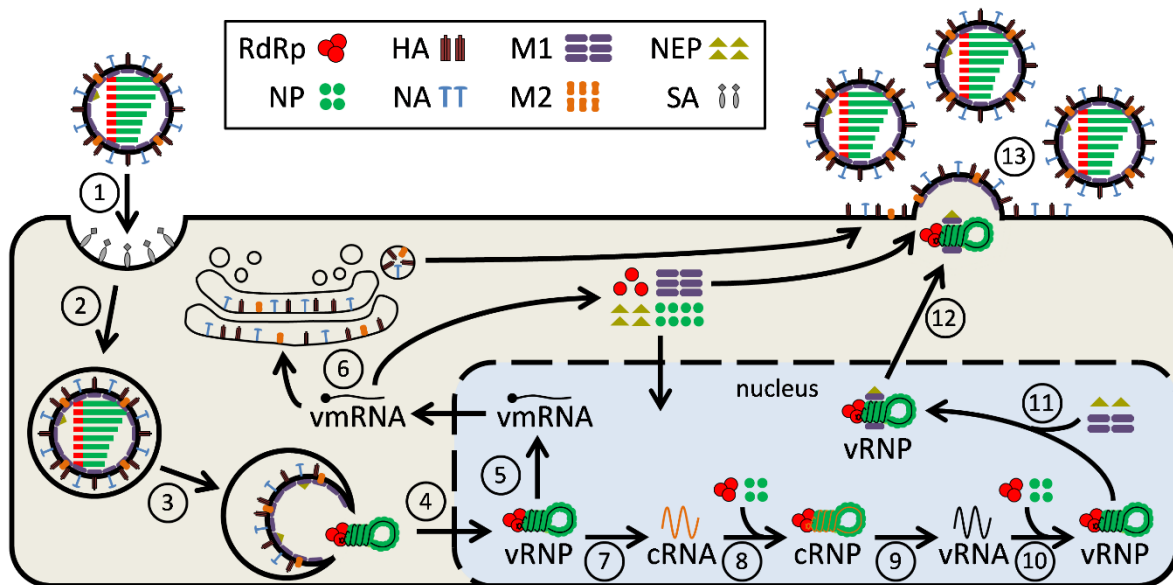
Figure 2.2.: Schematic depiction of the intracellular IAV life cycle. Outside of the virus particle, only one of the eight virus genome segments is shown to represent the others and NS1 is not shown. The steps of intracellular infection are marked by the numbers as following: 1 - attachment to sialic acids, 2 - endocytosis, 3 - fusion in late endosomes, 4 - nuclear import, 5 - transcription, 6 - protein translation, 7 - cRNA synthesis, 8 - cRNA encapsidation, 9 - vRNA synthesis, 10 - vRNA encapsidation, 11 - M1 and NEP binding, 12 - nuclear export, 13 - virus assembly and budding. Figure adapted from [38].

Virus entry and nuclear import

The initial step of IAV infection is the binding of the HA on the surface of the virus particle to sialic acids (SA), which are located on the apical surface of the polarized cell membrane. Then, IAV particles enter the cell via receptor-mediated endocytosis and are transported towards the cellular nucleus in endosomes. Late endosomes are subject to an acidification process, which induces two important changes to the virus particle. M2 proteins assume their function as ion channels and mediate the import of protons, which triggers the dissociation of vRNPs from M1 proteins, a process referred to as uncoating (reviewed in [22, 39, 40]). Additionally, HA proteins on the virion surface undergo conformational changes leading to the fusion of the viral envelope to the endosomal membrane, which enables vRNPs to enter the cytoplasm.

Due to these events, M1-free vRNPs enter the cytoplasm and travel to the nucleus, where they utilize an energy-driven cellular import mechanism relying on nuclear transport receptors [41-43]. This is enabled by nuclear localization signals (NLSs), which have been detected on all vRNP-related proteins, with the NLS on NP being suggested as crucial for the process. These NLSs interact with the nuclear transport receptors facilitating vRNP import. However, binding of M1 can disable the NLS preventing nuclear import [44]. Thus, M1 acts as a regulator controlling the entry of vRNPs into the nucleus. After uncoating, parental vRNPs are not bound by M1 and can enter the nucleus. In contrast, progeny vRNPs carry M1 proteins when they are exported from the nucleus and, thus, are not re-imported [45-47]. This prevents the accumulation of progeny vRNPs in the nucleus and facilitates virus particle release.

Viral mRNA transcription and protein translation

After reaching the nucleus, the primary function of vRNPs is to act as separate entities that perform the transcription of viral mRNA (vmRNA) for their respective genome segment [48]. From here on, mRNA of viral origin will be referred to as "vmRNA" and mRNA of cellular origin will be explicitly labelled "cellular mRNA". To perform its intended function, the vmRNA takes advantage of multiple cellular mechanisms which requires it to disguise itself as a cellular mRNA [29, 49]. Therefore, vmRNA transcription by vRNPs occurs as a primer-dependent process, which utilizes precursors of cellular mRNAs produced by the host cell. These precursors, which consist of a 5' cap and 10-13 nucleotides, are obtained from cellular RNA polymerase II (Pol II) in a process called "cap-snatching" [22, 30, 50, 51]. To that end, the vRNP-associated RdRp binds to Pol II, cleaves the cap and uses it as the basis for vmRNA transcription. The RdRp acts in *cis* for transcription in a 3'->5' direction using the vRNA as a template. At the 5' end, it encounters a steric hindrance causing it to stutter and produce a series of five to seven uridine residues [52, 53]. This leads to a polyadenylation and the formation of a poly(A) tail. Thus, the vmRNA emulates the structure of cellular mRNAs by having a cap at the 5' end and a poly(A) tail at the 3' end. This enables the exploitation of the mechanism used for the nuclear export of cellular mRNAs, which, thereby, can be used by vmRNAs to enter the cytoplasm [29, 54].

The translation of viral proteins is performed by cellular ribosomes in the cytoplasm. IAV vmRNAs have developed various mechanisms to preferentially access these ribosomes and outcompete cellular mRNAs [55]. Newly synthesized viral proteins can either enter the nucleus via their NLS to support virus replication and nuclear export of vRNPs, or relocate to the cell membrane for virus particle assembly [43, 56, 57]. Additionally, some viral proteins, i.e., HA, NA and M2, undergo post-translational processing in the endoplasmic reticulum (ER) and the Golgi apparatus [23]. Subsequently, these proteins travel to the cell membrane. NA proteins are expressed on the cell surface, where they cleave SA. This prevents the accumulation of progeny virus particles at the cell membrane after release. Additionally, it reduces the chance of superinfection by other virus particles, which require SAs to successfully enter the cell [58].

Various experimental studies have also revealed that some viral proteins are accumulating much earlier than others, which may be crucial for the regulation of different phases of infection [59, 60]. In particular, high NS1 and NP levels were observed early during infection, while HA, NA and M1 appeared significantly later. This may also affect superinfection exclusion (SIE) mediated by NA, resulting in a window of superinfection until enough NA is produced. Therefore, the temporal control of viral protein synthesis adds an additional layer of regulation and could enable optimal virus yields by controlling the transition between different stages of infection.

Primary transcription and vmRNA regulation

In the initial phase of infection, i.e., until around 1 hour post infection (hpi), vmRNAs of all eight segments are produced in equimolar amounts [60-62]. This process is often referred to as "primary transcription", which is only mediated by the initially provided viral genomes and proteins. Subsequently, viral proteins and the first progeny vRNPs are generated, which initiates the transition towards the secondary phase of vmRNA transcription. In this phase, vmRNAs originating from segment 1 to 3, which encode for subunits of RdRp, are produced in much lower amounts than the other segments resulting in up to ten times higher levels for non-RdRp segment vmRNAs. This could also be closely related to the differentiation between early and late viral proteins adding an additional layer of viral RNA regulation [59].

After reaching peak concentrations around 4 hpi in high MOI infections, vmRNA is degraded rapidly despite large amounts of vRNPs present in the nucleus [63, 64]. Recent studies have suggested that newly synthesized RdRp could play a role in preventing a longer period of vmRNA accumulation. It was shown that RdRp has two different mechanisms of interaction with Pol II [65, 66]. When RdRp carries a copy of the viral genome, i.e., when it is part of a complete vRNP complex, binding to Pol II induces vmRNA synthesis. However, the binding of free RdRp to Pol II leads to the specific degradation of Pol II. The reduction of Pol II levels impedes vmRNA transcription and could lead to a shutdown as observed in [59].

Viral genome replication

The secondary function of vRNPs in the nucleus is the initiation of viral genome replication, in which numerous copies are produced. The vmRNA transcribed from vRNP is not suitable as the basis for progeny vRNA generation, because it contains a cap, a poly(A) tail and is shorter than the complete genome segment. Therefore, an additional RNA species is utilized, the so-called complementary RNA (cRNA). This positive-sense cRNA is synthesized by RdRp from vRNA in a primer-independent process and contains the complete genomic information (reviewed in [22, 30, 67]). Similar to the vRNA, the cRNA is encapsidated with one RdRp and multiple NPs to from a complementary ribonucleoprotein complex (cRNP). In the next step, vRNA is synthesized by RdRp using the cRNP as a template, which ultimately leads to the formation of negative-sense vRNPs after subsequent encapsidation [22].

Nuclear export of vRNPs

Following replication, progeny vRNPs can remain in the nucleus to continue viral transcription and replication processes or leave the nucleus to form viral particles. The nuclear export of vRNP is an important process in the viral life cycle as it balances a continued amplification of the viral genome with the release of virus particles from the host cell. The exact procedure and order of events involved in the nuclear export is still elusive. However, the viral proteins M1 and NEP, and the cellular receptor chromosome region maintenance 1 protein (CRM1) were shown to play major roles during this process (reviewed in [22, 23, 42, 43]).

One proposed mechanism describes a "daisy chain" model, in which NEP is connected to the vRNP via M1 and recruits CRM1 using a nuclear export signal [68-70]. The initial step, i.e., the binding of M1 to vRNP, has been theorized to switch vRNP from an active to an inactive state preventing further viral replication and preparing it for the export [71-76]. Then, the CRM1 mediates the export of vRNP in an energy-driven transport process. In a different hypothesis, NEP binds directly to the vRNP-associated RdRp and mediates the binding of M1 to the vRNP. Furthermore, NEP is required for M1 to suppress replication activity of vRNP [77, 78]. While the two models suggest different functions for M1 and NEP, their interaction seems to be crucial for the nuclear export process. As mentioned previously, M1 and NEP are considered as late proteins, which suggests an additional layer of temporal regulation that prevents vRNP export before sufficient virus replication could occur.

Viral genome packaging and virion release

To produce progeny virus particles, all required components accumulate at the cellular membrane to form virions. The necessary proteins, i.e., NA, HA, M1 and M2, are either directed to lipid rafts on the membrane by the ER and the Golgi apparatus or associate with raft boundaries [22, 79-81]. The transport of vRNPs to the membrane is mediated by the cellular microtubule network, which is accessed using a marker for recycling endosomes (Rab11) and assisted by other host cell factors [82, 83]. At the membrane, vRNPs are recruited by M1 and form a complex containing eight vRNPs. For the generation of replication-competent virus particles, a complete set of viral genomes, i.e., one copy of each of the eight different vRNPs, is required. This is ensured by segment-specific packaging signals, which are non-coding regions located at both ends of the vRNA [84, 85]. Additionally, inter-segment interactions (RNA-RNA) contribute to this process and are responsible for the organization in the aforementioned "7+1" configuration [33, 34, 86-88]. Despite these regulatory mechanisms, significant amounts of IAV particles were shown to contain less than the required eight viral genomes (discussed in section 2.1.4) [89].

During virion budding, a curvature in the cell membrane is introduced to form virus particles. The viral proteins HA, NA, M1 and M2 are assumed to contribute to this process [22, 41, 51, 90, 91]. A key role is played by M1, which oligomerizes at the

membrane and forms curved structures [23]. In the growing bud, membrane-associated M1 also interacts with the vRNPs linking them to the membrane and establishing the core of the virion. The last steps of budding are performed by M2, which forms a neck at the bud and, finally, separates the virus particle from the host cell [92].

2.1.4 Subpopulations of IAV particles

IAV particle populations show a large genetic diversity, which stems from the high mutation rate of the genome and errors occurring during virus replication. While most IAV particles theoretically have the chemical characteristics required for infectivity, only up to 10% of particles seem to be capable to induce a productive infection [93]. This high chance of failure can have different reasons, e.g., incomplete virus particles or erroneous replication. Next to fully functional particles, which only represent a small fraction of all virus particles, different kinds of non-infectious particles contribute to pathogenicity and evolutionary fitness (Figure 2.3).

Non-infectious virions and non-productive infections

An IAV particle is considered infectious when it is capable to generate fully functional progeny virions. Most IAV particles can enter cells using their viral surface proteins, however, when they cannot induce the production of infectious progeny virions, they are referred to as replication-incompetent or non-infectious [93].

IAV particles can be rendered non-infectious when they have a defect in or are missing one of their eight genome segments. This can be caused by mutations in the genome or errors during particle packaging. Each genome segment encodes for different viral proteins required for successful virus replication. Therefore, the alteration or loss of genome segments prevents the production of functional proteins inducing non-productive infections. DIPs, which are covered in section 2.1.5, represent a special case of genome deletions that are actively interfering with regular replication [17, 94, 95]. Additionally, IAV particles can carry other defects that could prevent productive infections, e.g., non-functional viral proteins impeding virus entry or replication. Lastly, deformed, broken or empty virus particles were also observed during IAV infection [64].
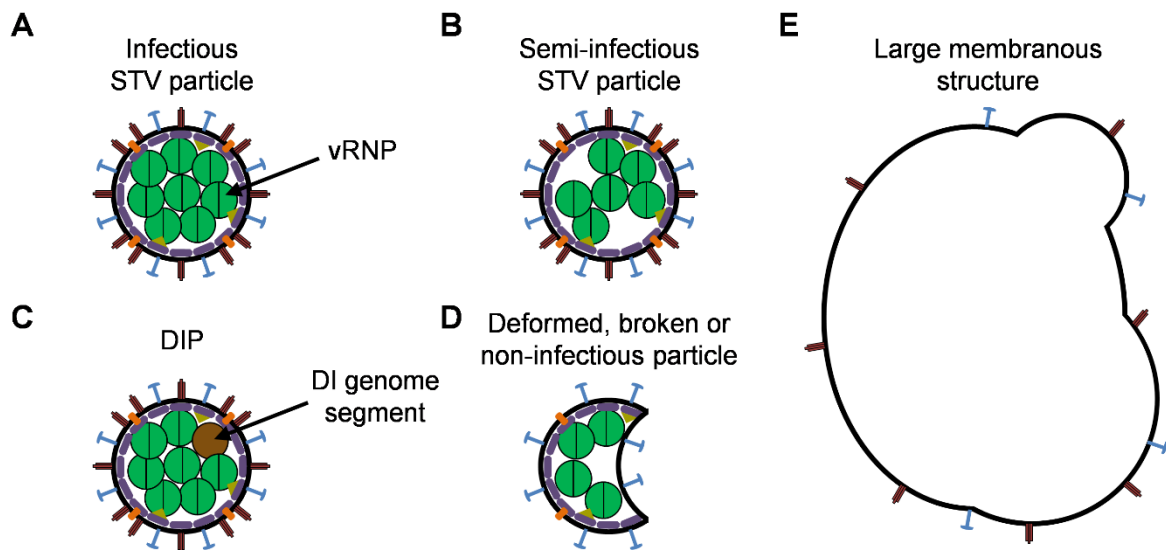
Figure 2.3: Overview of different infectious and non-infectious influenza virus particles. (A) Top view of a fully infectious virus particle showing the "7+1" configuration of vRNPs. (B-C) Top views of virus particles containing less than the eight influenza virus genomes or a defective interfering genome. (D-E) Non-infectious virus particles that may contribute to measured total virus titers, but do not show any infection activity. Depictions based on transmission electron microscopy results [64, 89].

These are predominantly generated during late stages of infection and do not have the typical spherical shape of IAV particles. They can still carry viral proteins on their surface, which induces virus-like responses in host systems, e.g., the activation of the immune system.

However, even fully functional virus particles can fail to induce a productive infection due to stochastic noise during virus entry, replication and packaging [27, 96]. At every step of the viral life cycle, a non-zero chance of failure of molecule reactions and interactions exists. These effects are exacerbated at specific steps of the life cycle relying on small molecule numbers during early infection. For instance, it was shown that only around 50% of virus particles fused successfully with the endosomal membrane during transport to the nucleus [97, 98]. Failure during this step leads to the degradation of virions in lysosomes preventing progeny virion production. Additionally, right after nuclear import of vRNPs, IAV is susceptible to the loss of individual genome segments. If a vRNP is degraded before its genomic information could be transcribed

to a cRNA, the respective segment is lost and cannot be incorporated into progeny virus particles.

The chance of non-productive infections is most prominent in low MOI conditions when largely single-hit infections occur [99]. Increasing the amount of virus particles entering a cell also elevates the number of initial genome segments available in the nucleus, which reduces the impact of endosomal fusion failure and genome degradation. Furthermore, multiple-hit infections by non-infectious virus particle could theoretically induce productive infections assuming that in combination all genome segments required for replication are provided. Therefore, non-infectious virus particles have also been referred to as semi-infectious [100-103].

Quantification of IAV subpopulations

IAV titers can be determined using different experimental approaches, e.g., standard dilution methods and real-time reverse transcription quantitative polymerase chain reaction (RT-qPCR) [63, 104, 105]. These methods examine different aspects of virus particles, which enables the evaluation of IAV subpopulations.

The HA assay detects particles that carry HA proteins on their surface [106]. As this includes all particles presenting HA, regardless of virion shape or content, it can be employed to measure the total amount of infectious and non-infectious particles. The total amount of virus particles can also be determined using RT-qPCR, which measures viral RNA levels [63]. These RNA levels can be related to the total virion count by assuming every particle carries the viral RNAs. An advantage of RT-qPCR is the capability of detecting specific RNA sequences, which supports the quantification of virions containing specific mutations in the genome. This is especially relevant to measure DIP concentrations, which are challenging to quantify using other methods.

The 50% tissue culture infective dose (TCID$_{50}$) [107] and the plaque assay rely on virus propagation, which cannot be performed by non-infectious virus particles, to quantify virus titers. Therefore, they can be used to detect levels of infectious virions. Generally, TCID$_{50}$ measurements are 10–100 times lower than HA assay results when measuring virus titers during early virus production stages, which supports that around 10% of produced IAV particles are infectious. In later stages of infection, TCID$_{50}$ results can be up to 100,000 times lower than HA titers as virus particles lose their infectivity over

time. Furthermore, experimental data obtained via plaque assay are slightly lower than TCID$_{50}$ measurements.

2.1.5 Defective interfering particles

DIPs occupy a unique position among non- or semi-infectious particles. While they are not capable of productively infecting a cell on their own, they can interfere with STV replication during co-infection. DIPs were initially discovered in experimental studies by Henle and Henle in 1943, which observed that "inactive" influenza virus particles could interfere with the replication of regular influenza virions [108]. One decade later, von Magnus observed the reduction of the ratio of infectious to non-infectious virus particles during the successive passaging of influenza viruses in eggs using high MOIs [109]. This phenomenon became known as the "von Magnus effect" and he hypothesized that it was connected to the generation of "incomplete" virions [110]. The term "defective interfering" (DI) particle was later proposed by Huang and Baltimore, which also provided the first description of its properties [94]. Following their identification in experiments under laboratory conditions, DIPs were also detected *in vivo* [17, 111]. DIP generation was observed for nearly all viruses [95, 112, 113], which indicates that their emergence is closely connected to the general viral life cycle. Furthermore, DIPs likely affect biotechnological processes, e.g., vaccine production [114, 115]. In the following, influenza virus DIPs will be the focus.

Based on the current understanding, DIPs can be described as (i) composed similarly to their homologous STV, (ii) propagation-incompetent on their own, (iii) capable of propagation when missing viral proteins are provided, and (iv) interfering with the intracellular replication of their homologous STV during co-infection.

Structure and emergence of DI RNAs

The composition of an influenza DIP is closely related to the homologous STV it originates from [17, 95, 112, 113]. The surfaces of DIPs and STVs are practically identical making their distinction challenging. However, DIPs are defective in one or more of the eight genome segments containing the genetic information. This renders DIPs propagation-incompetent on their own, because they are incapable to produce

the complete set of viral proteins. Commonly, such defects are induced by a large internal deletion in the DI RNA retaining a varying amount of nucleotides at both ends of the genetic sequence. The essential parts for replication and release, i.e., promotors, the bundling signal and the packaging signal, are located at the 5' and 3' ends of the RNA [84, 95, 116] (Figure 2.4). Due to their internal deletions, which can vary significantly in length and span from less than 100 to over 2000 nucleotides, DI RNAs are shorter than RNAs of their corresponding full-length (FL) segment [114, 117]. DIPs can possess deletions in more than one segment, but most commonly only contain a single defective RNA. Segments 1–3, which encode for sub-units of RdRp, represent the vast majority of naturally occurring DI RNAs [18, 111, 118-120]. Furthermore, the application of novel techniques to characterize genomes has demonstrated that a large variety of RNAs containing internal deletions is accumulating when infecting cells in batch as well as continuous cultivations [118, 121]. However, it is not clear if all of these defective RNAs show interfering capabilities.

The large internal deletion in the middle of a DI RNA is caused by an erroneous virus replication process [95]. It was suggested that the RdRp might detach from the viral template during replication and translocate to an incorrect position on the RNA. Then, it continues replication skipping a large part of the genome. Due to the double-helical structure of the vRNP (Figure 2.4), distant parts of the RNA sequence can be located directly next to each other. Additionally, the majority of detected internal deletions are nearly symmetrical, which further supports this hypothesis [118, 121].

In addition to deletions, defects in the genome segment can also be induced by other factors. In a recent study, an IAV particle with multiple point mutations in the RNA sequence of segment 7, which encodes for the proteins M1 and M2, was characterized and showed interfering characteristics similar to DIPs [122]. Moreover, DI RNAs that have parts of their sequence copied in reverse complement ("hairpin" and "panhandle" DI genomes) and that have multiple non-adjacent sections joined together ("mosaic" DI genomes) were discovered [17, 123, 124]. For the rest of this thesis, DIPs with an internal deletion in one genome segment will be the focus.
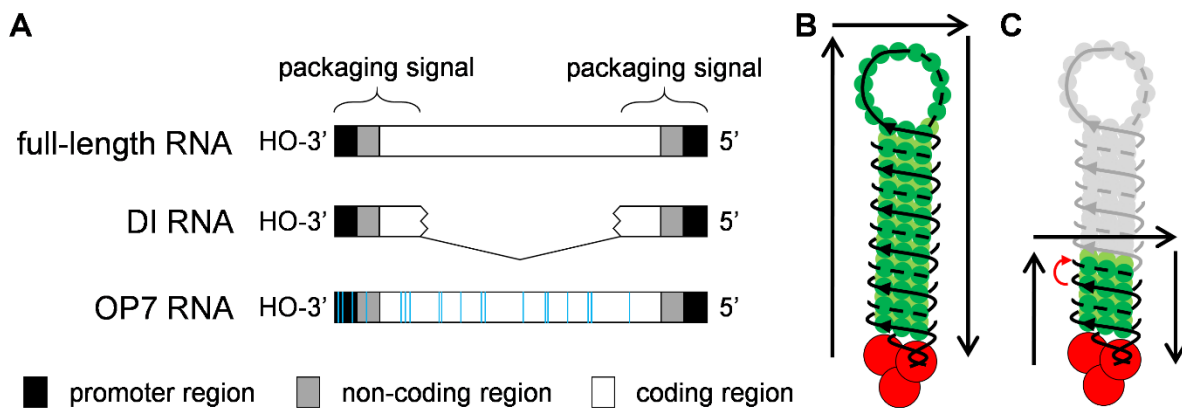
Figure 2.4.: Scheme of DI RNA structure and *de novo* generation. (A) Structure of full-length, regular DI and OP7 RNA. The promoter, non-coding and parts of the coding region form the packaging signal required for genome assembly. DI RNAs normally contain a large internal deletion in the coding region indicated by the V-shape. The OP7 RNA contains multiple nucleotide substitutions exemplified by blue vertical lines. For the exact positions of substitutions the reader is referred to the original publication on OP7 [122]. (B) Regular reading sequence for the generation of full-length RNAs by RdRp. (C) Potential underlying mechanism for the *de novo* generation of DI RNAs. The viral polymerase is hypothesized to translocate erroneously from the forward-moving strand to an RNA region close to the end of the genome sequence. Due to the double-helical structure of the RNA, these regions are closely associated promoting such an event. Thus, the large part in the middle of the RNA would not be transcribed. Figure adapted from [27].

DIP propagation and replication advantage

DIPs can propagate successfully when a complete set of viral proteins is available. During a natural infection, this is mainly achieved by co-infection with a STV, which acts as a helper virus and provides the genetic information to produce the missing protein(s). Because DI vRNAs still possess the required promotors, the RdRp recognizes them enabling DI cRNA and progeny DI vRNP generation. Furthermore, the bundling and packaging signals are retained in the DI RNA facilitating virion release. The transcription of DI vmRNA has also been observed [125, 126]. However, proteins potentially synthesized from DI vmRNA containing an internal deletion would likely either show no or non-regular activity. Moreover, a strategy to enable DIP

propagation in the absence of its STV, which relies on a modified cell line to produce influenza virus proteins, has been developed recently (discussed in section 2.1.6).

During STV and DIP co-infection, DI RNAs typically accumulate to higher levels than their FL RNA counterparts and infected cells mostly release progeny DIPs. Different mechanisms were proposed to contribute to these effects. A replication advantage of DI RNA over the FL RNA has been suggested as a major factor, because the preferential amplification of subgenomic RNAs has been observed in infections affected by DIPs [113, 127, 128]. In particular, an advantage during the DI cRNA synthesis was proposed by Odagiri *et al.* [129]. The significantly shorter length of DI RNAs was identified as a likely cause for faster replication assuming the RdRp operates at a constant rate of transcription. This would result in a higher number of DI RNA copies produced per minute allowing it to overgrow their corresponding FL RNA due to the autocatalytic mechanism of viral RNA replication. Experiments using two competing influenza virus-like RNAs showed that the shorter RNA could outperform the longer one, which supports this hypothesis [130]. However, a direct relation between DI RNA length and interference potential could not be established. During the propagation of STVs and DIPs in a semi-continuous production system, the length of strongly accumulating DI RNAs was distributed around a seemingly optimal length value [121]. Furthermore, not all subgenomic RNAs interfere with the STV and accumulate to high levels in co-infections [128]. Additionally, most naturally occurring DI RNAs are related to the longer segments 1–3 suggesting that other factors also play an important role. An additional mechanism that could result in an advantage for DI RNAs during replication is the incorporation of a "superpromotor".

A specific type of DIP containing various point mutations on segment 7, but no deletions, was shown to feature a "superpromotor" resulting in the enhanced synthesis of vRNA, vmRNA and viral proteins related to this segment [122]. Ultimately, this led to the strong suppression of STV replication while the DIP could propagate. Lastly, some co-infection studies also proposed that DI RNAs might be packed preferentially into virus particles [128, 131, 132]. The ratio of DI to FL RNA in released virions was shown to be higher than inside the cell. This suggests that the choice of incorporating a DI or FL RNA into progeny virus particle may not be random, but DI RNAs may be packaged more efficiently. As a result, co-infected cells almost exclusively released

DIPs despite sufficient amounts of available FL RNA. Thus, specific interactions during the packaging of progeny virions may also contribute to the advantage of DIPs over STVs during propagation.

Interference with the STV replication

Due to their overall replication advantage during co-infection, DIPs can strongly interfere with STV production reducing infectious viral titers by multiple orders of magnitude. The main factor for interference is likely the competition for viral and cellular resources [113]. In particular, the RdRp, which facilitates the key steps during replication, is considered a limiting factor. DI and FL RNAs of vesicular stomatitis virus (VSV) have been shown to compete for their viral polymerase [130, 133]. Similar results were shown for influenza virus-like RNAs, whose replication was found to depend on the availability of RdRp [127, 134]. This competition combined with the accumulation of DI RNAs to higher levels, which enables them to occupy a larger fraction of available RdRp, would severely reduce the ability of FL RNAs to replicate. Other viral proteins, which are necessary for vRNP stabilization and nuclear export, could also be the target of competition. To transport progeny vRNPs to the cell membrane, the combined function of RdRp, NP, M1 and NEP is required. Due to their higher numbers, DI RNAs could also induce a reduced availability of these components hampering FL vRNP production. In addition to viral proteins, cellular resources like Pol II may further contribute to the disturbance of FL RNA replication.

Next to resource competition, the aforementioned advantage of DIPs during packaging could also contribute to interference with the STV release. If DI vRNPs were preferentially packaged, e.g., due to their smaller size or increased binding affinities, this would further reduce STV propagation [128, 131, 132]. Furthermore, experiments have shown that peptides produced from DI RNAs can assume biological functions and contribute to influenza virus pathogenicity [135]. Therefore, these peptides could also influence the balance between DI and FL RNA by affecting specific steps of virus replication and release.

Another factor impairing STV propagation is the impact of STV and DIP co-infection on the amount of genome segments provided by the infecting virions. In a regular single-hit infection by a complete STV, all eight FL vRNPs are provided and replication

starts from an equal amount of templates. While the balance between the amounts of vRNPs may change during the infection, they initially have a similar chance to replicate, i.e., one in eight or 12.5% (neglecting potential segment-specific differences during replication). However, if we assume a co-infection of a STV and a DIP containing a DI vRNP of genome segment 1, this balance changes. Initially, one segment 1 DI vRNP, one segment 1 FL vRNP and two of each of the other seven vRNPs would be available. This translates to an initial chance of one in 16 or 6.25% for the segment 1 DI and FL vRNP to replicate, while the other segments are more likely to succeed. The segment 1 DI RNA can overcome this disadvantage due to its replication advantage. For segment 1 FL RNA, however, it is more likely that accumulation is severely impacted and levels of progeny segment 1 FL vRNP are low. As this FL vRNP is required for the generation of progeny STVs, this would further reduce STV titers. For the DI RNA this also has the additional benefit that the levels of is corresponding FL RNA are reduced specifically, which improves its own chance to be packaged into progeny virions.

The interference of DIPs with the STV can also have negative effects for the propagation of the DIPs themselves. This effect is called "self-interference" and refers to a severe suppression of STV replication leading to reduced DIP production. If large amounts of DIPs are co-infecting cells with the STV, reduced DIP levels were observed for VSV [136, 137]. Additionally, vRNA levels of influenza DIPs were reduced when a high MODIP of 30 was used for infections [125]. Thus, a very strong interference with the STV replication may reduce DIP titers and a more moderate reduction of STV titers may be optimal for DIP propagation.

Interestingly, a reduction of STV production could also be beneficial for viruses themselves. Lower STV levels could reduce overall lethality enabling a longer lifetime of the host resulting in prolonged virus replication. Supporting this hypothesis, a study of severe influenza virus infections has shown a reduction of DIP levels suggesting they are connected to virus pathogenicity [138]. Also, infections subject to DIP interference could induce milder symptoms increasing the chance of the host to spread the infection to new targets, which was shown for Dengue virus [139].

DIPs as antivirals

Due to their ability to inhibit virus production, DIPs are considered as promising candidates for antiviral therapy. The initial studies on the effect of DIPs on IAV infections in mice and chicken eggs showed their capability to reduce infectious titers [108-110]. Over the years, various animal studies demonstrated that the administration of DIPs could successfully prevent and treat IAV infections in mice and ferrets [17-19, 140, 141]. Additionally, DIPs derived from IAV have been shown to induce antiviral activity against other viruses, e.g., influenza B virus [142], pneumovirus [143] and severe acute respiratory syndrome coronavirus 2 (SARS-CoV-2) [144]. Currently available antivirals for treatment of IAV infection, i.e., neuraminidase inhibitors (oseltamivir, zanamivir and peramivir [145]) and a recently approved cap-dependent endonuclease inhibitor (baloxavir [146]), target an individual biochemical reaction or viral protein. In contrast, DIPs interfere with the whole virus replication process, which could provide benefits regarding the treatment of a wide range of virus infections and the development of antiviral resistances [17].

DIP co-infections have also been shown to result in an enhanced innate immune response from infected host cells [124, 147, 148]. Experimental studies demonstrated that the retinoic acid inducible gene I (RIG-I) protein, which induces interferon (IFN) activity, preferentially binds to the shorter DI RNAs [149, 150]. Thus, DI RNAs can lead to an increased activation of the IFN system. This enhanced innate immune response was proposed to contribute to the antiviral effect of IAV-derived DIPs against influenza infection [18, 143]. However, mini vRNAs, which are very short aberrant RNAs (56–125 nt) generated by the RdRp during viral replication, were reported to induce a larger stimulation of IFN expression than DI RNAs [151]. Additionally, these mini vRNAs were produced preferentially when viral RNA replication was dysregulated [151]. As mentioned above, DIPs compete with the STV for cellular and viral resources, especially for RdRp, which leads to a dysregulated viral replication. Therefore, DIPs may induce an enhanced innate immune response indirectly, i.e., by supporting the accumulation of mini vRNAs that lead to an increased expression of IFN. The individual significance of the DIP-induced effects i.e., the interference with the STV replication and the enhanced expression of IFN, to combat influenza infections, or if both are necessary for successful treatment, is not fully understood.

However, the increased innate immune response has been proposed as a key factor for the induction of antiviral activity against non-influenza viruses [152].

2.1.6 Influenza vaccine and DIP production

The main strategy to combat severe influenza virus infections is mediated by annual vaccination. While for the treatment of acute infections antivirals can be employed, the most efficient and reliable results are achieved by the prevention of infections. The first influenza vaccine candidates were developed in the 1930s and became broadly available soon after due to their successful application [153-155]. Throughout the last eight decades, these vaccines were mostly based on inactivated or live-attenuated virus particles produced in embryonated chicken eggs. These particles carry the relevant antigens, i.e., HA and NA, on their surface, which can be detected by immune cells to prepare the adaptive immune system for future infections. Additional strategies were developed and licensed, including cell culture-derived recombinant protein-based vaccines [156], split vaccines [157], and sub-unit vaccines [158], but these could not capture the market due to lower efficacy and the low costs of the regular vaccines. A promising approach are mRNA vaccines, which were first proposed in 1989 and saw a breakthrough in 2020 due to the COVID-19 pandemic [159]. The safety and efficacy of mRNA vaccines against the flu were studied in mice and clinical trials [160, 161]. In the near future, they may become readily available for broad application [162].

Due to the limited duration of protection and the high mutation rate of influenza viruses, which can induce structural changes in the HA and NA proteins and enable an antigenic evasion, influenza vaccination has to be repeated annually and the composition of the vaccine must be updated [163]. Current vaccines contain three or four different virus strains, which are recommended by the WHO based on their predominance in the previous season [164]. Therefore, an annual production of influenza virus material for vaccine formulation is required, which should be flexible to react to the emergence of new strains and potential pandemic outbreaks.

Egg-based and cell culture-based vaccine production

The propagation of influenza virus particles in embryonated chicken eggs has been a cornerstone of influenza vaccine production since its initial development. Even today, influenza vaccine production is mainly performed in eggs using a process that has been optimized for over 80 years [165]. Cell culture-based vaccine production processes were developed starting in the 1950s with a polio vaccine manufactured in monkey-derived Vero cells [166]. Later, cell culture-based processes were considered for influenza vaccine production and the first human influenza vaccine derived from cell culture was approved in the European Union in 2001 [167]. Since then, more cell culture-based influenza vaccines have been developed and are becoming a serious alternative to the traditional egg-based vaccines.

Egg- and cell culture-based vaccine production processes offer specific advantages and disadvantages. Influenza vaccine production in embryonated chicken eggs has been refined to the near optimum since its inception making the product cheap and safe. However, it relies on the availability of large amounts of vaccine-grade eggs limiting its flexibility during times of increased demand, e.g., pandemic outbreaks [168, 169]. Cell culture-based vaccine production can be scaled-up readily to supply the required amount of doses. Additionally, it provides a sterile and controlled production process that, in contrast to egg-based production, has no record of introducing mutations to the HA protein during passaging, which reduces vaccine efficacy [163, 170]. Due to the large investments required to establish a cell culture-based production platform and the comparatively harder approval process, the financial burden may still dissuade large vaccine manufacturers. However, one final advantage of cell culture-based vaccine production is the diversity of the available influenza virus-propagating cell lines, which can be a target of optimization for increased product yields.

In addition to the aforementioned Vero cells, a variety of cells have shown the capability to successfully propagate influenza viruses including a cell line of canine origin, i.e., Madin-Darby Canine Kidney cells (MDCK), human and chicken embryonic cells (HEK-293 and PBS-1), and insect cells (Sf9) [164, 171, 172]. Furthermore, the potential of different designer cell lines, i.e., AGE1.CR®, CAP®, EB14®/EB66® and PER.C6®, was evaluated [173-175]. Currently, MDCK cells are the main platform used for cell culture-based influenza vaccine production and related research. Adherent

MDCK (MDCKadh) cells were used to produce the first cell culture-derived human influenza vaccine [167], however, newer cell culture-based vaccines use MDCK suspension (MDCKsus) cells [158, 176, 177]. The advantage of suspension cells is that they can achieve significantly higher cell densities increasing product yield. For the calibration of the mathematical models presented in this thesis, both MDCKadh and MDCKsus cells were used.

DIP production

To facilitate the application of DIPs as antivirals, a safe and cost-efficient production process is required. For the generation of seed virus material for most DIP infection studies and animal experiments, producer systems, e.g., embryonated chicken eggs or cell cultures, were co-infected with STVs and DIPs. The resulting product always contained a mixture of STVs and DIPs, which would require an inactivation for usage in therapy, e.g., by UV irradiation [17, 141]. This negatively affects the interfering efficacy of DIP preparations and would pose a major challenge for regulatory approval. A novel approach for the production of DIPs that does not require a co-infection by STV was developed to overcome these limitations [178]. The general strategy is to supplement a viral protein that cannot be generated by a specific DIP, because it has a defect on the genome segment encoding for this protein. To that end, a modified cell line, which was genetically engineered to express a viral protein, is used. This principle has been used to generate large quantities of purely clonal DIP in a recent study [141]. In particular, an MDCKsus cell expressing PB2 was generated and used to propagate a DIP with a large deletion in genome segment 1. The produced STV-free material was shown to be innocuous and tested successfully in mice underlining the potential of this approach for DIP production.

2.2 Multiplicity of infection

The MOI is generally defined as the number of infecting agents per targets. In case of the infection of cell cultures with IAV, it represents the number of infectious IAV particles per uninfected cells added at the start of infection. However, its interpretation

can change drastically depending on what kind of measurement is used as the basis for calculation. As mentioned above, virus particle concentrations and their infectivity can be determined using various assays, e.g., the focus forming assay, the plaque assay, and the TCID$_{50}$ assay [104, 105, 107]. When comparing experimental results from literature, one has to check the method used to calculate the number of infecting virus particles carefully, because the MOI has a large impact on the time-scales and yields of infection.

Impact on virus replication and spreading

The time course of IAV infections is heavily impacted by the MOI. In particular, the time until maximum virus titers are achieved during production can be more than twice as long when using low MOIs [179]. When few virions are provided initially, only a low number of cells is infected and can produce virus particles. Then, these progeny virions initiate subsequent waves of infection repeating the process. After multiple cycles, all cells are infected and, finally, the maximum titers are reached. By starting the process with a sufficiently high MOI, all cells can be infected in one step and the maximum titers are achieved after a single infection wave [64].

For influenza vaccine manufacturing, the MOI is a tightly controlled process parameter and infections of cell cultures are usually initiated at very low MOIs [175]. This has multiple reasons including the increase of profitability due to the reduced demand for vaccine-grade seed virus material. Additionally, low MOIs were connected to increased virus yields compared to high MOI conditions in multiple studies [179, 180]. The underlying mechanisms leading to higher titers are not completely understood, but were connected to the impact of DIPs or a later induction of apoptosis [179].

In contrast, most laboratory experiments infecting cell cultures have been focusing on high MOI conditions, especially during the early days of influenza virus research. High MOIs have the advantage to induce a single infection wave, which causes virus replication and release to occur in a similar time frame in all infected cells. This enables the identification of distinct infection dynamics compared to the multiple and likely overlapping infection waves in lower MOI conditions. Additionally, very low MOIs could theoretically fail to induce an infection when too few cells are productively infected initially. In a combined laboratory and modeling study, single-cell experiments and a

stochastic model of IAV infection were used to show how the probability of successful infection decreases when using lower MOIs [99]. When applying an MOI of 1, a significant number of infected cells were non-productive compared to an MOI of 10 where most cells produced progeny virions. The inability to produce even a single virus particle was connected to the failure of virion fusion with the endosomal membrane or the loss of individual virus genome segments. These effects introduce a significant amount of noise into experiments with low MOIs making their realization and analysis challenging. However, low MOIs have been studied more rigorously in recent IAV studies [99, 125, 179, 181].

The MOI is also a predictor for more severe infections in host organisms. Larger concentrations of infecting virions are more likely to induce breakthrough infections and induce more severe symptoms. In humans, the airborne infectious dose is estimated to be 0.6 to 3 infectious units [18]. Therefore, low MOIs presumably represent the majority of initial *in vivo* infection scenarios. After the initial infection and the establishment of the virus in the host, the producing cells may create localized spots of high MOIs increasing the chance of further spread in competition with the immune system. Thus, a mixture of low and high MOI conditions likely play a role during IAV propagation and need to be considered for the design of experiments and model development.

Influence on DIP generation and interference

All interactions between STVs and DIPs are also highly dependent on the MOI. Additionally, the MODIP is a critical factor for interference and STV suppression. Typically, STVs represent the majority of virus particles in IAV seeds, but these can also contain varying levels of DIPs. To obtain virus seeds with a strongly depleted DIP content, a serial passaging in low MOI conditions can be performed [121]. Completely DIP-free virus seeds can be generated via reverse genetics [182], but the production of larger quantities would come with a large financial burden.

Assuming that the majority of virions in a virus seed are STVs, cell culture infections performed at low MOIs, i.e., below 10^{-1}, start with the infection of small fraction of the available cells. These would result in mostly single-hit infections (Figure 2.5), which reduces DIP propagation due to the absence of co-infections.
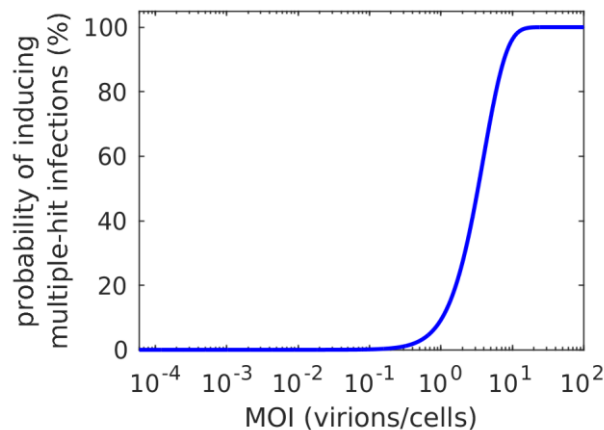
Figure 2.5.: Chance of multiple-hit infections in relation to the MOI. Simulation of the probability that a cell is infected by multiple virions depending on the MOI. Calculated values were determined based on the Poisson distribution.

Then, the progeny STVs produced in this initial wave infect more cells, which may lead to co-infections, but a large portion of the cells is infected only by STVs. Therefore, DIPs can still propagate, but later than the STV resulting in relatively low DIP titers.

If infections are initiated at high MOIs, the chance of co-infections is increased, which supports DIP propagation and may lead to substantial DIP accumulation during production. In such scenarios, a reduction of infectious virus titers can also be observed indicating that the DIPs are able to interfere with the STV propagation. This effect could also be shown in studies on mice, which were subjected to lethal doses of IAV [18, 19]. In particular, the application of DIPs prevented symptoms and protected the mice from virus-induced death if the DIP dose was sufficiently high. Therefore, using high MODIPs can strongly suppress STV propagation, even when substantial amounts of STVs are provided.

The impact of different MOI and MODIP conditions can also be observed using a specific experimental set-up, i.e., during the propagation of IAV in a continuous cell culture [183]. In such a system, uninfected cells are continuously provided from a cell bioreactor to the virus bioreactor while a corresponding volume is removed from the latter. The infection can be initiated at low MOI and MODIP conditions, which support STV propagation. This leads to the increase of virus titers, a high MOI and a larger chance of co-infections. Subsequently, the MODIP increases until high MOI and

MODIP conditions are present. This highly favors DIP production and inhibits STV propagation leading to low MOI and high MODIP conditions. Here, the chance of multiple-hit infections is still high, but most of them are not STV and DIP co-infections. Thus, DIP production is also slowed down. Subsequently, virus titers drop as bioreactor material is removed from the system and fresh cells are provided. Over time, the MOI and MODIP are reduced to low values that enable STV propagation and the whole process starts anew. As shown in multiple studies, this ultimately leads to an oscillation of virus titers [121, 183, 184]. Therefore, a continuous cultivation system can provide a microcosm of STV and DIP interactions in different MOI and MODIP conditions, which can generate substantial insights into their competition.

2.3 Systems biology approaches for virus infections

Biological processes have been studied since the emergence of intelligent life on earth. For a long time, knowledge about these processes, which was derived mostly from observation and reaction to manipulation, was limited by a lack of reliable measurements. However, the development of increasingly sophisticated technologies and experimental methods, especially since the middle of the 20th century, led to the generation of overwhelming amounts of experimental data. The computer-assisted field of bioinformatics was created attempting to handle and interpret these data. This has spawned various sub-disciplines investigating biological interactions including systems biology.

Systems biology is the analysis of complex biological processes using mathematical and computational methods. In that context, mathematical models are used as a theoretical representation of a process to describe and understand underlying mechanisms. They were used with great success to represent chemical reactions, enzyme kinetics or metabolic networks. Such mathematical models have also been widely used to describe virus infections, from the early models of human immunodeficiency virus (HIV) infection to the current models that attempt to predict the dynamics of the COVID-19 pandemic [21, 185].

2.3.1 Mathematical modeling of biological processes

Generally, mathematical models of biological processes consist of state variables and a description of their interactions. Such models are highly flexible regarding their size, complexity and the simulation approach chosen. Models can be divided into various categories, which have significant implications for their applicability to specific problems. Focusing on mathematical models of virus infection, the scale of infection they describe is a key factor for the choice of a fitting modeling approach. Different scales of interest are the interaction dynamics of individual proteins, the kinetics of virus replication in the cellular nucleus, the propagation of virus particles between cells, infection spread in tissues and organs, infections of small human or animal communities and the global spread of infection waves. Depending on the problem that is addressed, a model tailored to the respective process and available experimental data can be employed. To investigate processes during IAV infection and vaccine production, the two most relevant approaches are (i) within-host models that cover the spread of an infection between cells in a host, and (ii) single-cell models that describe the intracellular replication of virus particles. The majority of these models can be classified as deterministic, dynamic and continuous.

Deterministic models

Deterministic models describe a single trajectory of changing state variables over time, uniquely determined by the initial conditions and model parameters. Therefore, the complete dynamics of the respective biological system can be simulated and the abundance of each state variable at a specific time can be calculated. Deterministic models are usually implemented via ordinary differential equation (ODEs), which describe changes of state variables dependent on the system time.

To characterize time-dependent changes to the state variables, e.g., when a cell population is infected by virus particles, dynamic models are employed. For the analysis of biological systems in an equilibrium, static models can be used. However, static models are rarely applied to describe virus infections. In the majority of deterministic models, the state variables are implemented as continuous properties and, therefore, can assume values between two non-negative integers, e.g., 0.5 virus

particles. This can be interpreted as being in the transition between two discrete values or as the average number of virus particles present in the system at this specific time point.

For the application of deterministic models, some key assumptions have to be made. They only describe one unique solution and disregard stochastic effects, which are inherent to biochemical reactions. This can be a disadvantage when simulating biological processes that are heavily impacted by noise, such as gene expression [96, 186]. Especially when low molecule numbers can strongly influence the dynamics, random fluctuations have a large impact. As an example, while zero virus particles cannot infect a cell population, one particle has a certain chance to succeed. However, this single virion can degrade or other random factors may prevent the production of progeny virus particles. This would stop the infection and the probability of such events can be described with a stochastic model. In contrast, if in a deterministic model 0.1 virions were added to a cell population, cells would always become infected and the virus could reproduce over time to infect the whole population. To prevent such misrepresentations of biological processes strongly affected by random fluctuations, deterministic models are generally applied to describe interactions of large populations [187]. By disregarding randomness, deterministic models can be computed significantly faster than stochastic models of similar size. This enables various ways of model analysis that are challenging to apply for stochastic models, e.g., parameter estimation or sensitivity analysis.

Additionally, in the majority of deterministic models it is assumed that the system is well-mixed resulting in a readily available supply of substrates and other required materials for reactions. Therefore, the spatial distribution of components is disregarded and interactions can occur without additional transport processes. Most deterministic models describe reaction dynamics using the law of mass action kinetics. Thus, it is assumed that the rate of a reaction is directly proportional to the product of the concentration of the involved components. Some further assumptions are made specifically for mathematical models of virus infection. To describe the dynamics of virus replication, the kinetics of viral components are uncoupled from host cell kinetics to focus on the former. Additionally, host cell resources required for virus propagation,

e.g., cellular proteins and polymerases, are considered as unlimited to reduce complexity or due to the absence of appropriate measurements quantifying them.

Other modeling approaches

Another large class of models are discrete, stochastic models that consider the inherent randomness in biochemical reactions. When simulating dynamics in these models, state variables change in random time intervals based on their reaction propensities. Using the same initial conditions and model parameters can produce vastly different results as stochastic effects influence the production or degradation of state variables. To obtain a reasonable overview over the dynamics resulting from the models, they can either be solved using the master equation or have to be simulated numerous times to obtain an average time course of events. Although some approaches were developed to solve the master equation for larger models [188, 189], this is highly challenging and currently impossible for more complex implementations. Simulating stochastic models, which is mostly performed using the Gillespie algorithm [190, 191], can take a significant amount of time and computational effort.

Stochastic models also often use discrete state variables that can only assume non-negative integer values and consider exponentially distributed waiting times between events. This is important to represent dynamics with very low concentrations, but can be obstructive when millions of molecules are described. With very high numbers, changes in the concentration occur with very high frequency slowing down simulation even further. This increase in required simulation steps can be handled using different techniques, e.g., tau-leaping [192], but still makes stochastic models unattractive for such biological systems. In cases where both scenarios are relevant, i.e., very high concentrations and large effects of stochastic fluctuations, hybrid models combining deterministic and stochastic approaches can be used [193, 194].

Further theoretical approaches that have been applied to describe virus infections include cellular automata [195-197], agent-based models [198, 199], Boolean frameworks [200], and population balance models [201, 202]. Cellular automata and agent-based models follow similar approaches and act on the spatial level, introducing individual areas of interaction (so-called cells) or agents that act individually based on a defined set of rules.

2.3.2 Models of virus propagation in cell populations

Within-host models of infection mostly focus on the processes inherent to virus infections, i.e., the infection of uninfected target cells, the production of progeny virions and the virus-induced death of infected cells. They can be used to describe infection dynamics in humans, animals and cell cultures with the aim of predicting infection progression or estimate important infection parameters, e.g., the basic reproduction number R_0 [203]. The standard within-host model (Figure 2.6), which represents the simplest implementation of the aforementioned processes [204], can be applied to a large variety of viruses, e.g., HIV, IAV, Hepatitis B and C virus (HBV and HCV), Ebola virus, flaviviruses and SARS-CoV2. It is defined as

$$\frac{dT}{dt} = sT - dT - \beta TV \tag{2.3.1}$$

$$\frac{dI}{dt} = \beta TV - \delta I \tag{2.3.2}$$

$$\frac{dV}{dt} = pI - cV \tag{2.3.3}$$

where T, I and V denote target cells, infected cells and infectious virus particles, respectively. Target cells grow with the rate s and die with the rate d. The infection rate constant β is used to describe the infection of target cells via the law of mass action kinetics. Infected cells die with the rate δ and produce virus particles with the rate p. Infectious virus particles are cleared with the rate c [204].

This model can be expanded to investigate competing hypotheses of infection processes, e.g., regarding the effects of antiviral drugs, the effectivity of different intervention strategies and the evolution of viruses. An additional layer of interaction that can be considered in such a model is the host immune response, which has a large impact on infection dynamics. However, due to sparse experimental data from patients and the complexity of the immune response, modeling of within-host infection dynamics remains challenging.
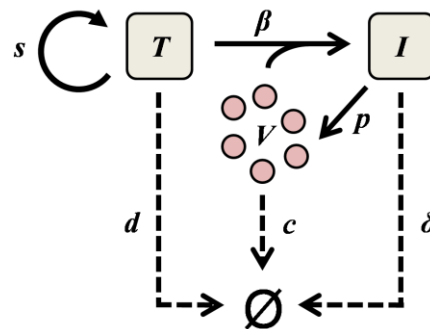
Figure 2.6.: Schematic depiction of the standard model of within-host dynamics of virus infection. Target cells (T) grow and are infected with the rates s and β, respectively. Infected cells (I) produce infectious virions (V) with the rate p. Target and infected cells die with the rates d and δ, respectively, and virions are degraded with the rate c.

Early within-host models

One of the first mathematical models of virus infection was developed by Perelson *et al.* to study HIV infection [205, 206]. They used experimental data from patients treated with an antiviral drug to evaluate its effect on infection kinetics. Their model-based analysis uncovered that HIV would develop resistances to the drug quite fast if it was applied as a monotherapy. Based on these findings, new treatment strategies were developed that use a combination of different antiviral drugs to prevent the emergence of such resistances. But modeling studies of HIV infection did not stop there and over time various aspects were investigated including the host immune response [207, 208], virus persistence [209, 210], and virus evolution [211, 212]. Similarly, models of HBV and HCV infection were developed in the same time frame to study different antivirals and their impact on infection [213, 214]. Overall, these models contributed greatly to improve the general understanding of virus infections and still provide the basic framework for the investigation of newly emerging viruses like Zika virus and SARS-CoV2 [215, 216].

Within-host models of *in vivo* IAV infection

The general structure of mathematical models of IAV infection is similar to the models mentioned above. However, influenza-induced infection processes occur on a very different time scale, i.e., in the span of one to two weeks compared to months or years for HIV, HBV and HCV infections [20, 204]. Therefore, long-term processes like virus evolution, which are relevant for other viruses, are generally neglected. Additionally, this shorter time frame of infection increases the impact of time-dependent processes, e.g., the time delay until infected cells release progeny virions or how long infected cells survive. These delays can be incorporated by using delay differential equations (DDEs) or by separating infected cells into different classes, i.e., considering latent cells and virion-releasing cells. While standard within-host models can describe IAV titers sufficiently well, the consideration of a delayed virus particle release enables a more realistic representation of IAV infection kinetics [217, 218].

Mathematical models of IAV infection were initially established to describe disease propagation in humans and animals [218, 219]. As for HIV, later IAV models were employed to evaluate the host immune response [220-223]. Additionally, the application of various antiviral drugs and different treatment approaches was evaluated [224, 225]. Again, combination therapies were suggested as beneficial for the treatment of influenza infections in light of potential emerging resistances [226, 227]. Furthermore, spatial models, which take the effects of diffusion and advection in the respiratory tract into account, were applied reproducing tissue damage levels reported in patients [228]. However, modeling the complete host immune response to describe all observed infection dynamics remains a challenge [229].

Within-host models of *in vitro* IAV infection

A majority of the model-based studies on IAV infection relied on *in vivo* measurements from sick patients or animal experiments. These data sets often consist of only a few measurement time points and their availability is limited, because they are obtained from small groups of animals or volunteers. Additionally, they can show a high variety between test subjects due to biological noise and large differences in individual immune responses. Furthermore, the time point of infection is rarely known for patient data, which can further affect the comparability between measurements. An additional

approach to investigate IAV infection dynamics are *in vitro* experiments. These can provide high quantities of experimental data in a tightly controlled set-up. Furthermore, experimental conditions can be easily modified to inspect the respective influence on infection kinetics. Due to the large variety of analysis techniques available for cell cultures, e.g., flow cytometry, RT-qPCR and electron microscopy, the dynamics of *in vitro* infections can be observed in detail. Regarding IAV, important steps of infection, such as viral RNA and protein synthesis, host cell apoptosis, and nuclear export processes can be measured in a high resolution [64]. Moreover, there is a large variety of cell lines that can be used to cultivate IAV including human cell lines (discussed in section 2.1.6).

One of the first mathematical models describing an IAV infection of cell cultures was developed by Möhler *et al.*, which applied the standard within-host model to IAV production in MDCKadh cells [230]. In their study, they compared a model implementation with and without time delay between cell infection and virion release, which lead to similar results. Finally, they concluded that the number of available uninfected cells, the rate of virus production, and the rate of infected cell death are the most important factors affecting virus yields. Schulze-Horsel *et al.* expanded this model by introducing the virus-induced apoptosis of cells, which followed an additional time delay [231]. To that end, they measured infection progression and apoptosis induction via flow cytometry, which could provide a detailed look into the dynamics of uninfected, infected and apoptotic cell populations. Furthermore, a differentiation between infectious and non-infectious virus particles was implemented to describe virus titers measured in MDCKadh cells infected by different IAV strains. At the same time, Sidorenko *et al.* developed a stochastic population balance model of IAV infection considering the intracellular and cell population level [232, 233]. The amount of intracellular viral components was linked to virus replication and release, which were compared to experimental data from flow cytometry measurements of viral proteins. Using this stochastic model, they were able to emulate the fluorescence intensity distribution of infected MDCKadh cells at various time points post infection. Later, Müller *et al.* used a deterministic population balance model that could reproduce the fluorescence intensity distribution of NP measured via flow cytometry in a low MOI infection [202]. Thereby, they were able to represent the different waves of the infection

process, i.e., the infection of uninfected cells, the production of viral proteins, virus-induced apoptosis, and cell lysis. Furthermore, a statistical model was employed by Martin and Harris *et al.* to investigate the impact of the MOI on IAV infections in different cell lines [234]. In their study, they concluded that infected cell death rates are independent of the MOI. However, virus production rates were estimated to increase with the MOI in MDCK cells, but not in human A549 cells.

2.3.3 Intracellular virus replication models

Next to the spreading of virus particles between cells in their host system, mathematical models have also been applied to describe the replication of the viral genome inside of cells. Generally, these models cover the viral life cycle during the infection of a single cell, from initial infection to progeny virion release. The level of detail of single-cell models can vary greatly, from simple descriptions of virus genetics to covering the full viral life cycle (Figure 2.2) or even including cellular metabolism. The initial models of intracellular replication were developed for different species of bacteriophages including a single-stranded positive sense RNA phage [235]. The general framework provided by these models was later applied by Dee *et al.* to describe Semliki Forest virus [236] and baculovirus infections [237]. The first model of the complete intracellular life cycle of a virus infecting humans was proposed by Reddy and Yin covering HIV infection [238]. Further single-cell models were developed for VSV, HBV, HCV, poliovirus, herpes simplex virus 1, Dengue virus and IAV (reviewed in [239]). These models mainly focused on improving the understanding of infection dynamics and the discovery of targets for antiviral drugs.

Intracellular models of IAV infection

A comprehensive model of the intracellular replication of IAV was developed by Sidorenko *et al.* aiming to describe vaccine production in MDCK cells [240]. It covered virion attachment, endocytosis, replication in the cellular nucleus, and progeny virus particle release. The model could reproduce general infection dynamics successfully based on literature parameters. To optimize virus yields, various steps of the viral life cycle were analyzed identifying potential bottlenecks during production, e.g., cellular

resources. However, due to a limited availability of experimental data, the model was not calibrated to measurements from an actual vaccine production process. Later, another model of IAV replication in cells was developed by Bazhan *et al.* describing vmRNA transcription, virus genome replication and virion assembly during infection [241]. Based on the initial model by Sidorenko *et al.*, Heldt *et al.* developed an even more detailed representation of intracellular IAV replication [242]. To that end, they implemented highly detailed interactions during virion attachment, viral RNA synthesis and nuclear export of vRNPs. The model was calibrated to experimental data from different experiments, which examined virion fusion and viral RNA dynamics. Additionally, they used the model to compare two hypotheses describing the transition from vmRNA transcription to the replication of the viral genome during IAV infection. Model simulations supported the theory that this transition is mediated by the stabilization of newly generated cRNAs by viral NP. Subsequently, Heldt and Kupke *et al.* translated this model into a stochastic framework to investigate the effects of random fluctuations on IAV infection [99]. Therefore, they considered the segment-specific dynamics of viral RNAs originating from the eight different genome segments. Based on stochastic simulations, they determined that the failure of virion fusion and the random degradation of vRNAs could induce non-productive infections in more than 80% of cells infected by a single virus particle. Thus, their results suggest that IAV can show highly heterogeneous infection dynamics, especially in low MOI conditions.

2.3.4 Multiscale models of infection

While within-host and single-cell models can deliver intriguing insights into the dynamics of virus propagation, they both disregard important aspects of infection. Within-host models cannot describe potential effects of antiviral drugs that interact with viral proteins or intracellular processes on virus propagation. In contrast, single-cell models cannot be used to investigate the emergence of antiviral resistance in response to antiviral treatment or how different MOIs would affect yields during vaccine production. These limitations can be overcome by establishment of multiscale models, which are able to describe the dynamics on the intracellular and cell population level

simultaneously. However, by linking both levels of infection, they can result in complex models that require considerable computational effort for simulation.

The basic framework for multiscale modeling of virus infections was provided by the works of Haseltine *et al.*, which combined the single-cell and cell population levels using population balance equations [201]. Furthermore, they established a modeling approach that led to a significant reduction of the required computational effort for simulation [243]. Specifically, they uncoupled both levels assuming that components on the extracellular level do not affect production rates on the intracellular level. Thus, the intracellular dynamics, which could be calculated beforehand, were applied during the subsequent simulation of the cell population level.

Typically, multiscale models of virus infection combine the intracellular replication and the dynamics on the cell population level. Such a framework is the focus of this thesis. However, other approaches were employed to develop epidemiological models by linking within-host and between-host dynamics [225, 244, 245]. For instance, Handel *et al.* applied such an approach to examine scenarios favoring virus persistence at different within-host temperatures [246]. Future multiscale models of infection could also include the spread of virus infection in different organs or tissues providing a more detailed time scale of infection processes.

Multiscale model of HCV infection

Guedj *et al.* evaluated the effect of a viral protein inhibitor, which affects intracellular virus replication, on HCV propagation in patients [247]. Attempting to reproduce viral load data, they concluded that only a multiscale modeling approach is capable of capturing the observed dynamics. To that end, they considered the infection age of cells, i.e., the time since cells were infected by a virus particle, and included a description of viral genome replication in the model. Using their multiscale model, they concluded that the observed inhibitor affected two distinct steps of virus replication, i.e., viral RNA synthesis and virion assembly, with high effectiveness [248].

Multiscale modeling of IAV infection

To support the discovery of novel antiviral drugs to treat IAV infections, Heldt *et al.* developed a multiscale model of IAV infection based on their aforementioned single-

cell model [38]. To that end, they introduced the cell population level, which considered dynamics of uninfected cells, infected cells, apoptotic cells, and infected apoptotic cells. The intracellular level was linked to these cells in different states via an age-segregated infected cell population, which released virus particles based on the respective infection age. This model was calibrated to measurements from infections of MDCKadh cells, which provided the dynamics of viral RNA synthesis, cell populations in different infection and apoptosis states, and viral titers. The model reproduced infection dynamics on both levels of infection and was subsequently used to examine the effects of potential antivirals that affect intracellular virus replication. Model simulations suggested that drugs interfering with vmRNA and viral protein synthesis, virion assembly and release, and the nuclear export of viral genomes show the most promise to impede IAV infections. Additionally, they concluded that a strong inhibition of vRNA and cRNA synthesis could significantly reduce virus titers. However, a moderate reduction of these two steps of replication could lead to increased virus titers in model simulations, which highlights potential challenges during the development of antiviral therapies against IAV infections.

2.3.5 Models of STV and DIP co-infection

DIPs propagate during co-infection with their homologous STV, but both require the same precursors, viral proteins, and utilize the same replication machinery. Thus, DIPs and STVs compete for replication on the intracellular level. The dynamics of competition of two or more populations has been studied extensively in predator-prey models, which focused mostly on animals [249, 250]. In recent years, the interaction of DIPs and their corresponding STV has emerged as a topic of interest for mathematical modeling. However, due to the limited amount of available experimental data, most model-based studies examined theoretical aspect of DIP interference or attempted to reproduce the reduction of STV titers using literature parameters.

Within-host models of co-infection

Initial theoretical studies on STV and DIP interactions were performed in the 1990s and employed different modeling approaches [251-253]. The authors concluded that

the MOI plays an important role for interference and that the co-infection of STVs and DIPs shows many features of deterministic chaos. Later, Stauffer-Thompson *et al.* developed a model of VSV infection subject to DIP interference to investigate the effects of DIP dosing on virus production [137]. They determined that low DIP doses enable STV and DIP production, while higher DIP regimes lead to the inhibition of production for both species. Furthermore, they predicted the decline of virus levels for serial-passaging using a fixed MOI, but failed to reproduce fluctuations occurring when applying a fixed volume during passaging [254].

Frensing and Heldt *et al.* employed a within-host model of IAV infection of cell cultures to describe vaccine production in a continuous bioreactor [183]. This specific set-up was shown to generate periodic oscillations in viable cell concentration and virus titers. By considering the presence of DIPs in their model, they could reproduce the observed dynamics. Model simulations also predicted that even small amounts of DIPs in the initial seed virus or a very low rate of DIP *de novo* generation would lead to oscillations during continuous cultivations of infected cell cultures. Tapia and Laske *et al.* extended this model by considering non-infectious STVs and limiting which cells can become infected by which type of virion [184]. Using the extended model, they were able to reproduce experimental data from continuous bioreactor cultivations of MDCKsus cells infected with influenza A STV and a well-described DIP. In their experiments, they applied two residence times leading to different oscillation frequencies, which could also be captured by model simulations. Moreover, Liao *et al.* used a mathematical model of IAV and DIP co-infection to examine the validity of a standard experimental method employed to evaluate DIP concentrations based on STV titers [255].

Other co-infection models

A probabilistic model of defective interfering baculoviruses in insect cells was developed by Zwart *et al.* [256]. In their study, they observed irregular oscillations and concluded that chaos must be present in the model dynamics to describe measurements from their serial passaging experiments sufficiently.

Laske and Heldt *et al.* extended the intracellular model of IAV replication developed by Heldt *et al.* to include DIP dynamics [257]. To that end, they considered the viral RNAs related to the eight different genome segments separately, introduced a replication

advantage for DI cRNA, and implemented the assembly of genome segments at the membrane prior to release. Using this mechanistic model, they reproduced experimental data from yield reduction assays and co-infection studies. Furthermore, they showed that the competition for viral protein may be a critical factor for DIP interference. Moreover, their model predicts that DIPs with a deletion in genome segments encoding for subunits of RdRp are more competitive than other DIPs.

Akpinar *et al*. provided two different theoretical approaches to investigate DIP dynamics during VSV infection, i.e., a gamma distribution model [258] and a cellular automaton model [197]. They were able to reproduce patterns of infection spread in a cell monolayer, which was infected by STV and different DIP doses. Based on their studies, they conclude that kinetics of infection and interference quantitatively depend on the DIP concentration. However, they remark that individual cells show a large heterogeneity in STV and DIP production, which is induced by stochastic noise during infection.

Finally, Meir *et al*. developed a mathematical model based on game theory to investigate the competition between DI viruses [259]. Their simulation suggested that a single DIP could reach an equilibrium with its wild type virus, but antagonistic interactions between multiple DIPs could ultimately lead to their extinction.

2.3.6 Model analysis

The complexity of mathematical models ranges from simple descriptions of molecule decomposition to covering interactions of a variety of components on multiple scales. The rate of such interactions is normally quantified by model parameters, which can be taken from literature, determined from experimental observations or calibrated by fitting the model to measurements of process dynamics. The evaluation of model parametrization becomes more challenging the larger models grow and phenomena like correlated parameters, high parameter uncertainty, and low parameter sensitivity can occur. To analyze the impact of individual parameters on model behavior and to enable realistic predictions, various model analysis techniques were developed. Furthermore, such procedures also support the design of experiments tailored to

elucidate currently ill-defined parameters. In the following, the model analysis methods used in the scope of this thesis are introduced.

Parameter sensitivity

A model parameter can be defined as sensitive, if its value has a significant impact on the model simulation, i.e., a change of the parameter value leads to changed dynamics for at least one state variable [260]. The sensitivity of a parameter is, however, not sufficient to derive its identifiability, because correlations between parameters or the usage of redundant parameters could render it unidentifiable. The local sensitivity of a parameter can be determined by perturbing a parameter and evaluating the model response. To that end, the sensitivity coefficient is calculated via

$$S_\theta^M = \frac{\delta M(\gamma)/M(\gamma)}{\delta\theta/\theta} \tag{2.3.4}$$

where θ denotes the perturbed parameter and γ the model output. M represents a specific characteristic of the model output, e.g., the area under the curve of the output, steady states of model variables or frequencies and amplitudes of oscillations. Thus, $\delta M(\gamma)$ quantifies the change of this characteristic in response to a variation of $\delta\theta$ in the evaluated parameter [261]. Another characteristic that is applied regularly is the weighted sum of squared residuals (SSR)

$$\frac{\delta M(\gamma)}{M(\gamma)} \equiv \frac{1}{N_c N_s} \sum_{s,c} \left[\frac{1}{N_t} \sum_t \left(\frac{y_{s,c}(\theta,t) - y_{s,c}(\theta^*,t)}{\sigma_s} \right)^2 \right] \tag{2.3.5}$$

where $y_{s,c}(\theta,t)$ describes the time course of model state s using parameter θ in experimental condition c. This is related to $y_{s,c}(\theta^*,t)$, which describes the simulated time course when parameter θ^* is used. The difference between model outputs is normalized by considering σ_s, which denotes the maximum value of species s in all experimental conditions, and by the number of time points N_t. The individual SSRs for

each condition and species are again normalized with regards to the total number of conditions and species, i.e., N_c and N_s [262].

A low sensitivity coefficient indicates that a model parameter is poorly constrained and likely non-identifiable. Such low sensitivities can be the result of constructing complex representations of processes for which few measurements are available to inform the model. Thus, one has to be careful when constructing large models and consider the available experimental data. Insights obtained from sensitivity analyses can also be used to support experimental design, facilitate a better understanding of the biological mechanisms, and reveal parameter correlations.

Parameter confidence intervals

Mathematical models employed in systems biology regularly contain parameters that show low sensitivities and large uncertainties. However, most models can provide robust predictions despite using some ill-defined parameters [262]. If the exact value and accuracy of parameters rather than model predictions are studied, various theoretical approaches can be employed [260, 263]. In the scope of this thesis, parameter confidence intervals were calculated via bootstrap algorithms to examine the accuracy of model parameters [264]. Bootstrapping relies on random resampling to estimate the properties of an unknown probability distribution. Typically, Monte Carlo sampling is used to generate new random samples of the examined property. The advantage of this method is its simplicity and that it does not require repetition of experiments. However, confidence intervals obtained from bootstrapping can be biased by the initial sample and their calculation can be very time-consuming depending on the underlying complexity of the system.

To assess the confidence intervals of model parameters, we used a Monte Carlo approach to resample data sets randomly based on experimental measurements. In the initial model fit, parameter values θ were estimated by fitting the model to the actual experimental data $y = (x_1, x_2, \ldots, x_n)$, e.g., dynamics of viral RNAs or virus titers. Then, we generated a random sample $y^* = (x_1^*, x_2^*, \ldots, x_n^*)$ considering the original experimental data [264]. For the time series data used in this thesis, we assumed a normal distribution of measurement errors and drew a bootstrap sample from $N(x_i, \sigma_i^2)$, where x_i and σ_i^2 are the mean and standard deviation of the actual measurement. By

refitting the model to y^*, we obtained a different set of parameter values θ^*. Repeating this numerous times yielded a distribution of parameter values, which was used to determine the confidence intervals. Following the percentile method and assuming a significance level α, the confidence interval were calculated from the central interval between the $100 \cdot \dfrac{\alpha}{2}$ and $100 \cdot \left(1 - \dfrac{\alpha}{2}\right)$ percentiles of the parameter distribution obtained via bootstrapping [264].

Akaike information criterion

When developing mathematical models to describe biological processes, various aspects regarding model structure have to be considered, e.g., the size of the model, the complexity of molecule interactions, and the implementation of vaguely described mechanisms. For the comparison of different model compositions and hypotheses, a variety of methods can be employed to quantify the goodness of fit, e.g., the SSR, cross validation, and the predictive least-squares principle (reviewed in [265]). Another approach, which has become more and more common since its formulation in the 1970s and which we also employ in this thesis, is the Akaike information criterion (AIC) [266]. The AIC is based on information theory and compares the quality of fit of models describing a set of data or a process. To that end, it considers the goodness of fit and the complexity of a model at the same time. To avoid overfitting, it applies a penalty that is directly correlated to the number of model parameters. Therefore, it favors simple models that can provide a good representation of a process over large models that achieve slightly better fits.

The AIC is defined as

$$\text{AIC} = -2 \, \log(L(\hat{\theta}|\text{data})) + 2K \tag{2.3.6}$$

where $\log(L(\hat{\theta}|\text{data}))$ denotes the log-likelihood function and K the number of model parameters [266]. Lower values of the AIC imply a better quality of fit. AIC results can also be used further to calculate the model probability w_i, which quantifies the probabilistic chance of model i to provide the best representation of a process or a set of data in the range of 0 to 1 [267].

To calibrate our models, we minimized the SSR of experimental data and model simulations. According to [267], when employing such a least squares estimation and assuming a normal distribution of errors, $\log(L(\hat{\theta}|\text{data}))$ can be approximated using the maximum likelihood estimator $\hat{\sigma}^2$. This is done via

$$\log(L(\theta^*|\text{data})) = -\frac{N_d}{2}(\hat{\sigma}^2) \tag{2.3.7}$$

where N_d describes the amount of available individual measurements. $\hat{\sigma}^2$ itself can also be approximated using the normalized SSR

$$\hat{\sigma}^2 = \frac{\sum_i (\hat{\varepsilon}_i)^2}{N_d} \tag{2.3.8}$$

where $\hat{\varepsilon}_i$ are the residuals estimated from the fitted model. By applying Equations (2.3.7) and (2.3.8) to Equation (2.3.6), we obtain

$$\text{AIC} = N_d \log\left(\frac{\sum_i (\hat{\varepsilon}_i)^2}{N_d}\right) + 2K \tag{2.3.9}$$

which can be used to calculate the AIC.

3. Models and Methods

3.1 Multiscale model of STV infection

The multiscale model of STV infection developed in the scope of this work is based on a model of IAV infection by Heldt *et al.* [38]. This original model links virus replication on the intracellular level with virus propagation on the cell population level by using a segregated population of infected cells. In the scope of this thesis, we introduced new mechanisms that adjust virus-induced apoptosis, virus release, and inhibition of vmRNA synthesis. The model was adapted with these modifications to describe infection dynamics in different MOI regimes and to predict how the effective MOI changes during an infection of cell cultures. Note that in this section parts of the original publication on the multiscale model of STV infection were used [181].

3.1.1 Cell population level

The model of the cell population level combines a set of integro-partial differential equations with a set of ODEs to describe extracellular interactions based on Heldt *et al.* [38]. The implementation of an age-segregated infected cell population enables the simultaneous simulation of the intracellular and cell population level.

Cell populations

$$\frac{dT}{dt} = \mu T - r^{\mathrm{Inf}} T - k_{\mathrm{T}}^{\mathrm{Apo}} T \tag{3.1.1}$$

$$\frac{\partial I}{\partial t} + \frac{\partial I}{\partial \tau} = -\left(k_{\mathrm{T}}^{\mathrm{Apo}} + k_{\mathrm{I}}^{\mathrm{Apo}}\left(\tau\right) \right) I\left(t,\tau\right) \tag{3.1.2}$$

$$\frac{dT_{\mathrm{A}}}{dt} = k_{\mathrm{T}}^{\mathrm{Apo}} T - r^{\mathrm{Inf}} T_{\mathrm{A}} - k^{\mathrm{Lys}} T_{\mathrm{A}} \tag{3.1.3}$$

$$\frac{dI_A}{dt} = \int_0^\infty \left(k_T^{Apo} + k_I^{Apo}(\tau)\right)I(t,\tau)d\tau + r^{Inf}T_A - k^{Lys}I_A \tag{3.1.4}$$

$$\text{with } \mu = \left[\frac{\mu_{Max}}{T_{Max}}\left(T_{Max} - T - \int_0^\infty I(t,\tau)\,d\tau\right)\right]_+ \tag{3.1.5}$$

$$r^{Inf} = F_{Inf}k^{Fus}V^{En}\theta\left((T+T_A)^{-1}\right) \tag{3.1.6}$$

$$\text{with } \theta\left((T+T_A)^{-1}\right) = \begin{cases} (T+T_A)^{-1}, & T+T_A > 0, \\ 0, & T+T_A \leq 0, \end{cases} \tag{3.1.7}$$

On the cell population level, uninfected cells (T), apoptotic uninfected cells (T_A), infected cells (I) and apoptotic infected cells (I_A) are described. Uninfected cells can grow with the specific rate μ, become infected with the rate r^{Inf} and undergo apoptosis with the rate k_T^{Apo}. Cell growth is limited by the maximum specific growth rate μ_{Max} and the maximum cell concentration T_{Max}. Infected cells have a higher rate of apoptosis induction due to intracellular virus replication, which is recognized by the cellular immune system. Depending on the infection age τ of an infected cell, the base apoptosis rate is increased by the rate of virus-induced apoptosis $k_I^{Apo}(\tau)$. Apoptotic cells are lysed with the rate k_{Lys}.

The infection rate r^{Inf} is determined by considering the fusion (k^{Fus}) of the viral envelope with the endosomal membrane performed by virions in endosomes (V^{En}), which will be described later. The fraction of cells successfully infected by fusion of a single virion is given by F_{Inf}. Then, this term is divided by the sum of uninfected cells to split the total infection "capability" between non-apoptotic and apoptotic uninfected cells in Equation (3.1.1) and (3.1.3).

Age-segregated infected cell population

$$I(t,\tau) = \begin{cases} r^{Inf}(t-\tau)T(t-\tau)\exp\left(-\int_0^\tau \left(k_T^{Apo} + k_I^{Apo}(a)\right)da\right), & t > \tau \geq 0, \\ 0, & \tau > t \geq 0, \end{cases} \tag{3.1.8}$$

Following the implementation of an age-segregated population used by Heldt *et al.*, infected cells $I(t,\tau)$ are classified by the infection age τ. At the time of infection t_{I}, infected cells with age zero are generated leading to a boundary condition of $I(t_{\mathrm{I}}, \tau = 0) = r^{\mathrm{Inf}}(t_{\mathrm{I}})T(t_{\mathrm{I}})$. Transforming equation (3.1.2) into an algebraic equation leads to (3.1.8), which represents an infection age density. After each time step dt a new subpopulation of infected cells is created assuming $r^{\mathrm{Inf}}(t)T(t) > 0$. Once infected, these cells are only subject to apoptosis, which occurs with an increasing rate $k_{\mathrm{T}}^{\mathrm{Apo}} + k_{\mathrm{I}}^{\mathrm{Apo}}(\tau)$ depending on the infection age τ. This is calculated by considering the variation of the infected cell apoptosis rate over time during an infection. The integration over the complete state space $\int_{0}^{\infty} I(t,\tau)d\tau$ provides the total number of infected cells.

Infection age-dependent infected cell apoptosis rate

The apoptosis dynamics of infected cells was implemented with the aim to comply with a normal distribution of the survival time of infected cells as indicated by recent experimental data [64] (shown in Figure 4.4). To this end, we employed a logistic function, which can be used to approximate dynamics induced by the cumulative density function of the normal distribution [268], to describe the infection age-dependent cell apoptosis rate

$$k_{\mathrm{I}}^{\mathrm{Apo}}(\tau) = \frac{K_{\mathrm{I}}}{1 + \exp(-v_{\mathrm{Apo}}(\tau - \tau_{\mathrm{Apo}}))} \tag{3.1.9}$$

with K_{I} as the maximum virus-induced apoptosis rate, τ_{Apo} referring to the time after cell infection at which the rate of virus-induced apoptosis reaches its half-maximum and v_{Apo} as a factor that describes the time required from cell infection until the full activation of the apoptosis mechanism. The parameter τ_{Apo} can be directly related to the average μ of the normal distribution and v_{Apo} can be converted to the standard deviation σ of the normal distribution by calculating

$$\sigma = \frac{1.62}{v_{\text{Apo}}} \quad . \tag{3.1.10}$$

Additionally, we tested Gompertz and Hill functions for the description of a delay in apoptosis induction (Figure 4.4) as they can also approximate the cumulative density function of the normal distribution. Finally, we decided to implement a logistic function as it provided the best fit to our experimental data and enabled a comprehensive adaptation to different scenarios including a step-like or smooth as well as an instant or delayed increase of the virus-induced apoptosis rate.

Virus particle release

$$\frac{dV}{dt} = \int_0^\infty r_{\text{Inf}}^{\text{Rel}}(\tau) I(t,\tau) d\tau - k_V^{\text{Deg}} V + \sum_n \left[k_n^{\text{Dis}} V_n^{\text{Att}} - k_{c,n}^{\text{Att}} B_n V \right], \tag{3.1.11}$$

$$\text{with } B_n = B_n^{\text{Tot}} \left(T + T_A \right) - V_n^{\text{Att}} \;, \tag{3.1.12}$$

$$\text{and } k_n^{\text{Dis}} = \frac{k_{c,n}^{\text{Att}}}{k_{c,n}^{\text{Eq}}} \;, \text{n} \in \left\{ \text{Hi}, \text{Lo} \right\} \tag{3.1.13}$$

$$\frac{dV_{\text{tot}}^{\text{Rel}}}{dt} = \int_0^\infty r_{\text{Inf}}^{\text{Rel}}(\tau) I(t,\tau) d\tau \tag{3.1.14}$$

$$\frac{dP_{\text{tot}}^{\text{Rel}}}{dt} = \int_0^\infty r_{\text{Par}}^{\text{Rel}}(\tau) I(t,\tau) d\tau \tag{3.1.15}$$

We consider infectious virions (V), the total number of released infectious virions ($V_{\text{Tot}}^{\text{Rel}}$) and the total number of released virus particles ($P_{\text{Tot}}^{\text{Rel}}$) on the cell population level. Infectious virus particles attach to free binding sites B_n on the cell membrane of uninfected cells with the rate $k_{c,n}^{\text{Att}}$, detach with the rate k_n^{Dis} and degrade over time with the rate k_V^{Deg}. The number of available high-affinity (n = Hi) and low-affinity (n = Lo) binding sites is calculated using the total amount per cell B_n^{Tot}. The detachment rate is determined based on the equilibrium constant $k_{c,n}^{\text{Eq}}$. Infectious virions are released with the rate $r_{\text{Inf}}^{\text{Rel}}(\tau)$ and the total virus release rate is described by the

rate $r_{\text{Par}}^{\text{Rel}}(\tau)$, both of them affected by the infection age τ of a releasing cell. Furthermore, the total amount of infectious virions and virus particles released, which disregard attachment and degradation, are described to represent the cumulative virus titers measured in [64].

Virus entry

The entry of virus particles into an uninfected cell is also described on the cell population level, because it is linked to a version of the intracellular model that neglects virus entry. This enables the simulation of the cell population dynamics while considering the intracellular replication as described in [38].

$$\frac{dV_n^{\text{Att}}}{dt} = k_{c,n}^{\text{Att}} B_n V - \left(k_n^{\text{Dis}} + k^{\text{En}}\right) V_n^{\text{Att}} - \left(r^{\text{Inf}} + r^{\text{Lys}}\right) V_n^{\text{Att}} \tag{3.1.16}$$

$$\frac{dV^{\text{En}}}{dt} = k^{\text{En}} \left(V_{\text{Hi}}^{\text{Att}} + V_{\text{Lo}}^{\text{Att}}\right) - k^{\text{Fus}} V^{\text{En}} - \left(r^{\text{Inf}} + r^{\text{Lys}}\right) V^{\text{En}} \tag{3.1.17}$$

$$r^{\text{Lys}} = k^{\text{Lys}} T_A \, \theta\left((T + T_A)^{-1}\right) \tag{3.1.18}$$

Attached virus particles V_n^{Att} can detach from receptors or perform receptor-mediated endocytosis with the rate k^{En}. Virions in endosomes (V^{En}) fuse with the endosomal membrane with the rate k^{Fus}. The additional removal of these two populations due to infection or cell lysis is covered by the rates r^{Inf} and r^{Lys}, respectively. To describe the impact of lysis on currently attached virions and virions in endosomes, the number of cells undergoing lysis is related to the total amount of uninfected cells.

3.1.2 Intracellular level

The model of the intracellular level comprises a set of ODEs covering essential steps of virus replication shown in Figure 2.2. These include virus entry, nuclear import, replication and transcription of viral RNA, protein synthesis, viral assembly and virus particle release.

Virus entry

The initial step of infection is the binding of virions to SA residues on the cell surface followed by receptor-mediated endocytosis. According to Heldt *et al.* [242], we describe low- and high-affinity binding sites representing divergent binding potential based on experimental data reported by Nunes-Correia *et al.* [269]. Furthermore, the inability of a certain fraction of virus particles to fuse with the endosomal membrane shown in [97] is considered.

$$\frac{dV^{\text{Ex}}}{dt} = k_{Hi}^{\text{Dis}} V_{\text{Hi}}^{\text{Att}} + k_{\text{Lo}}^{\text{Dis}} V_{\text{Lo}}^{\text{Att}} - \left(k_{\text{Hi}}^{\text{Att}} B_{\text{Hi}} + k_{\text{Lo}}^{\text{Att}} B_{\text{Lo}} \right) V^{\text{Ex}} \tag{3.1.19}$$

$$\text{with } B_{\text{n}} = B_{\text{n}}^{\text{Tot}} - V_{\text{n}}^{\text{Att}}, \ \text{n} \in \left\{ \text{Hi}, \text{Lo} \right\} \tag{3.1.20}$$

$$\text{and } k_{\text{n}}^{\text{Dis}} = \frac{k_{\text{n}}^{\text{Att}}}{k_{\text{n}}^{\text{Eq}}}, \ \text{n} \in \left\{ \text{Hi}, \text{Lo} \right\} \tag{3.1.21}$$

$$\frac{dV_{\text{n}}^{\text{Att}}}{dt} = k_{\text{n}}^{\text{Att}} B_{\text{n}} V^{\text{Ex}} - \left(k_{\text{n}}^{\text{Dis}} + k^{\text{En}} \right) V_{\text{n}}^{\text{Att}}, \ \text{n} \in \left\{ \text{Hi}, \text{Lo} \right\} \tag{3.1.22}$$

$$\frac{dV^{\text{En}}}{dt} = k^{\text{En}} \left(V_{\text{Hi}}^{\text{Att}} + V_{\text{Lo}}^{\text{Att}} \right) - \left(k^{\text{Fus}} + k_{\text{Ven}}^{\text{Deg}} \right) V^{\text{En}} \tag{3.1.23}$$

$$\text{with } k_{\text{Ven}}^{\text{Deg}} = \frac{1 - F_{\text{Fus}}}{F_{\text{Fus}}} k^{\text{Fus}}, \ 0 < F_{\text{Fus}} \leq 1 \tag{3.1.24}$$

where extracellular virus particles (V^{Ex}) bind to free binding sites B_{n} on the cell membrane with the rate $k_{\text{n}}^{\text{Att}}$. The total number of high-affinity (n = Hi) and low-affinity (n = Lo) binding sites in given by $B_{\text{n}}^{\text{Tot}}$. Virus particles attached to the cell surface ($V_{\text{n}}^{\text{Att}}$) can either dissociate from these binding sites with the rate $k_{\text{n}}^{\text{Dis}}$ or perform endocytosis with the rate k^{En}. The dissociation of virions is determined via an equilibrium constant k_{n}^{Eq}. Then, the enveloped virus particles (V^{En}) either fuse with the endosomal membrane to release their genome segments into the cytoplasm or are degraded in lysosomes with the rates k^{Fus} and $k_{\text{Ven}}^{\text{Deg}}$, respectively. The balance between virion fusion and degradation is determined using the fraction of fusion-competent virions F_{Fus}.

Virus replication

The vRNPs released into the cytoplasm can enter the nucleus and synthesize cRNA and vmRNA. The cRNA acts as a template for vRNA replication. Both RNAs containing the viral genome are stabilized by binding of RdRp and NP reducing degradation considerably. Subsequent attachment of M1 and NEP induces nuclear export of vRNP complexes. According to the implementation of Heldt *et al.* [242], we assume that all eight genome segments show similar levels of cRNA and vRNA enabling a description via their total number.

$$\frac{dVp^{\text{Cyt}}}{dt} = 8k^{\text{Fus}}V^{\text{En}} - k^{\text{Imp}}Vp^{\text{Cyt}} \tag{3.1.25}$$

$$\frac{dVp^{\text{Nuc}}}{dt} = k^{\text{Imp}}Vp^{\text{Cyt}} + k_{\text{NP}}^{\text{Bind}}P_{\text{NP}}R_{\text{RdRp}}^{\text{V}} - \left(k_{\text{M1}}^{\text{Bind}}P_{\text{M1}} + k_{\text{Rnp}}^{\text{Deg}}\right)Vp^{\text{Nuc}} \tag{3.1.26}$$

$$\frac{dR^{\text{C}}}{dt} = k_{\text{C}}^{\text{Syn}}Vp^{\text{Nuc}} - k_{\text{RdRp}}^{\text{Bind}}P_{\text{RdRp}}R^{\text{C}} - k_{\text{R}}^{\text{Deg}}R^{\text{C}} \tag{3.1.27}$$

$$\frac{dR^{\text{V}}}{dt} = k_{\text{V}}^{\text{Syn}}Cp - k_{\text{RdRp}}^{\text{Bind}}P_{\text{RdRp}}R^{\text{V}} - k_{\text{R}}^{\text{Deg}}R^{\text{V}} \tag{3.1.28}$$

$$\frac{dR_{\text{RdRp}}^{\text{C}}}{dt} = k_{\text{RdRp}}^{\text{Bind}}P_{\text{RdRp}}R^{\text{C}} - k_{\text{NP}}^{\text{Bind}}P_{\text{NP}}R_{\text{RdRp}}^{\text{C}} - k_{\text{RRdRp}}^{\text{Deg}}R_{\text{RdRp}}^{\text{C}} \tag{3.1.29}$$

$$\frac{dR_{\text{RdRp}}^{\text{V}}}{dt} = k_{\text{RdRp}}^{\text{Bind}}P_{\text{RdRp}}R^{\text{V}} - k_{\text{NP}}^{\text{Bind}}P_{\text{NP}}R_{\text{RdRp}}^{\text{V}} - k_{\text{RRdRp}}^{\text{Deg}}R_{\text{RdRp}}^{\text{V}} \tag{3.1.30}$$

$$\frac{dCp}{dt} = k_{\text{NP}}^{\text{Bind}}P_{\text{NP}}R_{\text{RdRp}}^{\text{C}} - k_{\text{Rnp}}^{\text{Deg}}Cp \tag{3.1.31}$$

$$\frac{dVp_{\text{M1}}^{\text{Nuc}}}{dt} = k_{\text{M1}}^{\text{Bind}}P_{\text{M1}}Vp^{\text{Nuc}} - \left(k^{\text{Exp}}P_{\text{NEP}} + k_{\text{Rnp}}^{\text{Deg}}\right)Vp_{\text{M1}}^{\text{Nuc}} \tag{3.1.32}$$

$$\frac{dVp_{\text{M1}}^{\text{Cyt}}}{dt} = k^{\text{Exp}}P_{\text{NEP}}Vp_{\text{M1}}^{\text{Nuc}} - 8r^{\text{Rel}} - k_{\text{Rnp}}^{\text{Deg}}Vp_{\text{M1}}^{\text{Cyt}} \tag{3.1.33}$$

After the vRNPs reach the cytoplasm (Vp^{Cyt}) they can enter the nucleus (Vp^{Nuc}) with the rate k^{Imp}. There, they act as templates for viral replication. cRNA (R^{C}) is transcribed from vRNPs with the rate $k_{\text{C}}^{\text{Syn}}$ and subsequently stabilized by binding viral RdRp (P_{RdRp}) to form intermediate complexes ($R_{\text{RdRp}}^{\text{C}}$) and binding NP ($P_{\text{NP}}$) to form

cRNP (Cp) with the rates $k_{\text{RdRp}}^{\text{Bind}}$ and $k_{\text{NP}}^{\text{Bind}}$, respectively. The produced cRNP is the template for intracellular vRNA transcription. Similar to the cRNA, the newly formed vRNA (R^{V}) is stabilized by binding RdRp and NP forming $R_{\text{RdRp}}^{\text{V}}$ and Vp^{Nuc}, respectively. The naked viral RNAs (cRNA and vRNA) are highly susceptible to degradation, but due to the stabilization the formed complexes are degraded with lower rates ($k_{\text{R}}^{\text{Deg}} > k_{\text{RRdRp}}^{\text{Deg}} > k_{\text{Rnp}}^{\text{Deg}}$). To prepare the vRNP for nuclear export, M1 attaches to it with the rate $k_{\text{M1}}^{\text{Bind}}$ to form a complex ($Vp_{\text{M1}}^{\text{Nuc}}$), which is assumed to be replication incompetent [71-73]. After subsequent binding of NEP (P_{NEP}) the complexes can leave the nucleus. The combination of these two processes is described by the rate r^{Exp}. When the vRNP complexes are exported from the nucleus, they are denoted as $Vp_{\text{M1}}^{\text{Cyt}}$ and travel to the cell membrane. There, the eight viral genomes assemble and perform virus budding, which is conflated into the rate k^{Rel}.

vmRNA transcription and protein synthesis

vmRNAs are transcribed in the nucleus, but the synthesis of viral proteins occurs in the cytoplasm. According to the model by Heldt *et al.* [242], we assume that nuclear vmRNA export can be disregarded and consider vmRNA levels of different genome segments individually. As the exact quantification of viral proteins levels remains a challenge, we still focus on the net production, disregard degradation and assume an equal distribution of structural viral proteins.

$$\frac{dR_i^{\text{M}}}{dt} = \frac{k_{\text{M}}^{\text{Syn}} Vp^{\text{Nuc}}}{8L_i \left(1 + \dfrac{P_{\text{Rdrp}}}{K_{\text{R}}}\right)} - k_{\text{M}}^{\text{Deg}} R_i^{\text{M}}, \quad i = 1,\ldots,8 \tag{3.1.34}$$

$$\frac{dP_{\text{PB1}}}{dt} = \frac{k_{\text{P}}^{\text{Syn}}}{D_{\text{Rib}}} R_2^{\text{M}} - k^{\text{RdRp}} P_{\text{PB1}} P_{\text{PB2}} P_{\text{PA}} \tag{3.1.35}$$

$$\frac{dP_{\text{PB2}}}{dt} = \frac{k_{\text{P}}^{\text{Syn}}}{D_{\text{Rib}}} R_1^{\text{M}} - k^{\text{RdRp}} P_{\text{PB1}} P_{\text{PB2}} P_{\text{PA}} \tag{3.1.36}$$

$$\frac{dP_{\text{PA}}}{dt} = \frac{k_{\text{P}}^{\text{Syn}}}{D_{\text{Rib}}} R_3^{\text{M}} - k^{\text{RdRp}} P_{\text{PB1}} P_{\text{PB2}} P_{\text{PA}} \tag{3.1.37}$$

$$\frac{dP_{\text{RdRp}}}{dt} = k^{\text{RdRp}} P_{\text{PB1}} P_{\text{PB2}} P_{\text{PA}} - k^{\text{Bind}}_{\text{RdRp}} P_{\text{RdRp}} \left(R^{\text{V}} + R^{\text{C}} \right) - \left(N_{P_{\text{RdRp}}} - 8 \right) r^{\text{Rel}} \tag{3.1.38}$$

$$\frac{dP_{\text{NP}}}{dt} = \frac{k^{\text{Syn}}_{\text{P}}}{D_{\text{Rib}}} R^{\text{M}}_5 - \frac{L_{\text{V}}}{N^{\text{Nuc}}_{\text{NP}}} k^{\text{Bind}}_{\text{NP}} P_{\text{NP}} \left(R^{\text{V}}_{\text{RdRp}} + R^{\text{C}}_{\text{RdRp}} \right) - \left(N_{P_{\text{NP}}} - 8 \frac{L_{\text{V}}}{N^{\text{Nuc}}_{\text{NP}}} \right) r^{\text{Rel}} \tag{3.1.39}$$

$$\frac{dP_{\text{M1}}}{dt} = \frac{k^{\text{Syn}}_{\text{P}}}{D_{\text{Rib}}} \left(1 - F_{\text{Spl7}} \right) R^{\text{M}}_7 - \frac{L_{\text{V}}}{N^{\text{Nuc}}_{\text{M1}}} k^{\text{Bind}}_{\text{M1}} P_{\text{M1}} Vp^{\text{Nuc}} - \left(N_{P_{\text{M1}}} - 8 \frac{L_{\text{V}}}{N^{\text{Nuc}}_{\text{M1}}} \right) r^{\text{Rel}} \tag{3.1.40}$$

$$\frac{dP_{\text{NEP}}}{dt} = \frac{k^{\text{Syn}}_{\text{P}}}{D_{\text{Rib}}} F_{\text{Spl8}} R^{\text{M}}_8 - \frac{L_{\text{V}}}{N^{\text{Nuc}}_{\text{NEP}}} k^{\text{Exp}} P_{\text{NEP}} Vp^{\text{Nuc}}_{\text{M1}} - \left(N_{P_{\text{NEP}}} - 8 \frac{L_{\text{V}}}{N^{\text{Nuc}}_{\text{NEP}}} \right) r^{\text{Rel}} \tag{3.1.41}$$

$$\frac{dP_{\text{HA}}}{dt} = \frac{k^{\text{Syn}}_{\text{P}}}{D_{\text{Rib}}} R^{\text{M}}_4 - N_{P_{\text{HA}}} r^{\text{Rel}} \tag{3.1.42}$$

$$\frac{dP_{\text{NA}}}{dt} = \frac{k^{\text{Syn}}_{\text{P}}}{D_{\text{Rib}}} R^{\text{M}}_6 - N_{P_{\text{NA}}} r^{\text{Rel}} \tag{3.1.43}$$

$$\frac{dP_{\text{M2}}}{dt} = \frac{k^{\text{Syn}}_{\text{P}}}{D_{\text{Rib}}} F_{\text{Spl7}} R^{\text{M}}_7 - N_{P_{\text{M2}}} r^{\text{Rel}} \tag{3.1.44}$$

Each of the eight genome segments i encodes for a different vmRNA (R^{M}_{i}). We assume that the transcription of vmRNAs is dependent on the transcription rate $k^{\text{Syn}}_{\text{M}}$, their respective length (L_{i}) and that they are degraded with the rate $k^{\text{Deg}}_{\text{M}}$. We introduced an additional regulatory mechanism that reduces vmRNA synthesis depending on the availability of free RdRp (Equation (3.1.34)), with K_{R} describing the amount of RdRp that has to be available to reduce vmRNA synthesis by half. As Vp^{Nuc} denotes the total number of nuclear vRNP templates, this number has to be divided by eight to obtain the appropriate amount for the transcription of a specific vmRNA. vmRNA is translated into viral proteins P_{i} with a length-dependent rate $k^{\text{Syn}}_{\text{P}}$ in the cytoplasm. More than one ribosome can bind to the vmRNA constituting a polysome, which is considered by applying the average distance between two ribosomes on the vmRNA (D_{Rib}).

The three polymerase subunits PB1, PB2 and PA (P_{PB1}, P_{PB2} and P_{PA}) unite to form the RdRp with the rate k^{RdRp}, which is essential for virus replication. The vmRNAs of

genome segments 7 and 8 undergo splicing, which is incorporated by the factors F_{Spl7} and F_{Spl8} describing the fraction of the corresponding vmRNA encoding for M2 (P_{M2}) and NEP. The proteins RdRp, NP, M1 and NEP play a role during vRNP formation and export, which is considered via the respective number of bound nucleotides for each protein ($N_{\text{NP}}^{\text{Nuc}}$, $N_{\text{M1}}^{\text{Nuc}}$ and $N_{\text{NEP}}^{\text{Nuc}}$) applied to the average vRNA length (L_{V}). Exactly eight RdRps are required for vRNP formation. The surface proteins HA (P_{HA}), NA (P_{NA}) and M2 are only required during virus release and consumed according to their observed amount per virion ($N_{P_{\text{HA}}}$, $N_{P_{\text{NA}}}$ and $N_{P_{\text{M2}}}$). As the determined number of proteins required for vRNP stabilization and export per virion ($N_{P_{\text{RdRp}}}$, $N_{P_{\text{NP}}}$, $N_{P_{\text{M1}}}$ and $N_{P_{\text{NEP}}}$) does not exactly match the quantity required to form eight vRNPs, the excess amount is removed during virus release.

Virus particle release and infectivity of virions

For the description of all processes constituting virus release, a single equation considering all involved components is used. This conflates vRNP transport to the cell membrane, assembly of the correct eight vRNPs and virus budding. Furthermore, we differentiate virions that are able to infect cells successfully from particles that contribute to the total virus titer, but show no infection activity.

$$\frac{dP^{\text{Rel}}}{dt} = r_{\text{Par}}^{\text{Rel}}(\tau) = k^{\text{Rel}} \frac{Vp_{\text{M1}}^{\text{Cyt}}}{Vp_{\text{M1}}^{\text{Cyt}} + 8K_{\text{V}^{\text{Rel}}}} \prod_{j} \frac{P_{j}}{P_{j} + N_{P_{j}} K_{\text{V}^{\text{Rel}}}} \tag{3.1.45}$$

$$\frac{dV^{\text{Rel}}}{dt} = r_{\text{Inf}}^{\text{Rel}}(\tau) = F_{\text{Par}} k^{\text{Rel}} \frac{Vp_{\text{M1}}^{\text{Cyt}}}{Vp_{\text{M1}}^{\text{Cyt}} + 8K_{\text{V}^{\text{Rel}}}} \prod_{j} \frac{P_{j}}{P_{j} + N_{P_{j}} K_{\text{V}^{\text{Rel}}}} \tag{3.1.46}$$

$$\text{with } j \in \{\text{RdRp,HA,NP,NA,M1,M2,NEP}\}$$

$$\frac{dF_{\text{Par}}}{dt} = -k_{\text{Red}}^{\text{Rel}} F_{\text{Par}} \tag{3.1.47}$$

Both the total release of virus particles (P^{Rel}) and the release of infectious virions (V^{Rel}) depend on the availability of vRNPs and viral proteins, which is incorporated similarly to Michaelis-Menten kinetics. Based on this implementation, the virus release rate k^{Rel}

represents the maximum release rate. The parameter $K_{V^{\mathrm{Rel}}}$, which describes the amount of vRNPs or proteins that must be present to reach half of the maximum release rate, acts as a Michaelis-Menten constant. The percentage of infectious virions that are produced is determined by the variable F_{Par}, which is implemented as a first order degradation. A previous experimental study revealed that $F_{\mathrm{Par}}(\tau)$ is decreasing over time [64], which implies that virus particles released during early infection have a higher chance to infect new cells. The rate $k_{\mathrm{Red}}^{\mathrm{Rel}}$ describes the decrease of the fraction of infectious virus particle released. As the understanding of factors influencing the capability of cells to produce infectious particles is still limited [64], we decided to combine such effects in a single parameter.

3.2 Multiscale model of STV and DIP co-infection

The mathematical model of STV and DIP co-infection describes the dynamics of both virus particle species during replication in cells and their spread across a cell population. As we aimed to capture the impact of different MOIs and MODIPs on the infection in detail, we used the multiscale model of STV infection presented in section 3.1 as a foundation. We adapted this model by considering the dynamics of DIPs on the intracellular level based on a model of intracellular DIP replication [257] and expanded dynamics on the cell population level. Note that in this section parts of the original publication on the multiscale model of STV and DIP co-infection were used [125].

3.2.1 Expansion of the cell population level

To implement the impact of DIPs on the infection and spread of a cell population, we introduced DIP-related cell and virus populations to the existing dynamics described in Equation (3.1.1)–(3.1.8).

Cell populations

$$\frac{dT}{dt} = \left(\mu - r_{STV}^{Inf} - r_{DIP}^{Inf} - k_{T}^{Apo} \right) T \tag{3.2.1}$$

$$\frac{dI_{DIP}}{dt} = r_{DIP}^{Inf} T + \left(\mu - r_{STV}^{Inf} - k_{T}^{Apo} \right) I_{DIP} \tag{3.2.2}$$

$$\frac{\partial I_{STV}}{\partial t} + \frac{\partial I_{STV}}{\partial \tau} = -\left[r_{DIP}^{Inf} + k_{I}^{Apo}(\tau) \right] I_{STV}(t, \tau) \tag{3.2.3}$$

$$\frac{\partial I_{CO}}{\partial t} + \frac{\partial I_{CO}}{\partial \tau} = -k_{I}^{Apo}(\tau) I_{CO}(t, \tau) \tag{3.2.4}$$

$$\frac{dT_{A}}{dt} = k_{T}^{Apo} T - \left(r_{STV}^{Inf} + r_{DIP}^{Inf} + k^{Lys} \right) T_{A} \tag{3.2.5}$$

$$\frac{dI_{A}}{dt} = \int_{0}^{\infty} k_{I}^{Apo}(\tau) \left[I_{STV}(t, \tau) + I_{CO}(t, \tau) \right] d\tau + k_{T}^{Apo} I_{DIP} + \left(r_{STV}^{Inf} + r_{DIP}^{Inf} \right) T_{A} - k^{Lys} I_{A} \tag{3.2.6}$$

$$C_{Tot}(t) = T(t) + T_{A}(t) + I_{DIP}(t) + \int_{0}^{\infty} I_{STV}(t, \tau) \, d\tau + \int_{0}^{\infty} I_{CO}(t, \tau) \, d\tau + I_{A}(t) \tag{3.2.7}$$

On the cell population level, the model considers populations of uninfected cells (T), STV-only infected cells (I_{STV}), DIP-only infected cells (I_{DIP}), co-infected cells (I_{CO}), apoptotic uninfected cells (T_{A}), and apoptotic infected cells (I_{A}). STV-only and co-infected cells are considered as age-segregated populations and are classified by their infection age τ. Uninfected cells proliferate with the specific growth rate μ, can become infected by STVs and DIPs with rates r_{STV}^{Inf} and r_{DIP}^{Inf}, respectively, and become apoptotic with the rate k_{T}^{Apo}. Similarly, DIP-only infected cells can grow, become infected by STVs and undergo apoptosis. STV-only infected cells do not proliferate, but can become infected by DIPs and become apoptotic with the virus-induced apoptosis rate $k_{I}^{Apo}(\tau)$. Co-infected cells are also subject to virus-induced apoptosis. Apoptotic uninfected cells can become infected by either STVs or DIPs and undergo cell lysis with the rate k_{Lys}. The same lysis rate applies to apoptotic infected cells. The total amount of viable cells is collected as C_{Tot} in Equation (3.2.7).

The specific growth rate defined by

$$\mu(t) = \left(f_\mu \frac{\mu_{\mathrm{Max}}}{T_{\mathrm{Max}}} \left[T_{\mathrm{Max}} - C_{\mathrm{Tot}}(t) \right] \right)_+ \qquad (3.2.8)$$

$$\text{with } f_\mu = \begin{cases} F_\mu, & \dfrac{V(0) + D(0)}{C_{\mathrm{Tot}}(0)} \geq 6, \\ 1, & \dfrac{V(0) + D(0)}{C_{\mathrm{Tot}}(0)} < 6, \end{cases} \qquad (3.2.9)$$

considers the maximum specific growth rate and cell concentration μ_{Max} and T_{Max}. It is reduced by the factor F_μ if the combined MOI and MODIP exceed a value of 6. This specific value is used based on experimental data showing a reduction in cell growth in very high MODIP scenarios (Figure 4.11B).

Infection rates and superinfection exclusion

The infection rates of cells are separated for STVs and DIPs, resulting in

$$r_{\mathrm{STV}}^{\mathrm{Inf}} = F_{\mathrm{Inf}} k^{\mathrm{Fus}} V^{\mathrm{En}} \theta \left(\left(T + T_{\mathrm{A}} + I_{\mathrm{DIP}} \right)^{-1} \right) \qquad (3.2.10)$$

$$r_{\mathrm{DIP}}^{\mathrm{Inf}} = F_{\mathrm{Inf}} k^{\mathrm{Fus}} D^{\mathrm{En}} \theta \left(\left(T + T_{\mathrm{A}} + \int_0^{\tau_{\mathrm{SIE}}} I_{\mathrm{STV}}(t, \tau) d\tau \right)^{-1} \right) \qquad (3.2.11)$$

$$\text{with } \theta \left(a^{-1} \right) = \begin{cases} a^{-1}, & a > 0, \\ 0, & a \leq 0, \end{cases} \qquad (3.2.12)$$

where STVs and DIPs in endosomes are denoted by V^{En} and D^{En}, respectively. Their amount is related to the fusion rate k^{Fus} and the fraction of cells successfully infected by fusion of a single virion F_{Inf}. To account for the current number of suitable infection targets, this is divided by the total amount of cells that are targeted by either STVs or DIPs. The parameter τ_{SIE} describes the infection age after which STV-only infected cells cannot become re-infected by a DIP.

Uninfected cells T and their apoptotic counterpart T_A can become infected by either STVs or DIPs, however, we assume re-infection of STV- and DIP-only infected cells (I_{STV} and I_{DIP}) is only possible by the opposing virus particle. Additionally, STV-only infected cells are protected from re-infection by DIPs to consider superinfection exclusion, which is mediated by neuraminidase [58]. According to [270], we set the time window for a productive co-infection of STV-only infected cells to $\tau_{SIE} = 3\,\text{h}$ after initial infection. This results in STV-only infected cells that have reached an infection age of $\tau = 3\,\text{h}$ to remain in this state and continuously producing progeny STVs. This implementation prevents DIPs that are produced at later stages to transform all STV-only infected cells to co-infected cells, which would result in an inaccurate description of STV titers.

Furthermore, we assume that STV-only infected cells are not re-infected by STVs, DIP-only infected cells are not re-infected by DIPs, and co-infected cells are not re-infected by either virus particle. This was implemented to prevent the existence of a continuous sink draining virus particles from the system. Lastly, we assume that STVs can infect DIP-only infected cells and convert them to co-infected cells at all times, because they are not capable of replication as they cannot produce progeny RdRp. This would likely result in low levels of neuraminidase, which are not sufficient to prevent re-infection.

Age-segregated infected cell populations

For the model of STV and DIP co-infection we consider age-segregated cell populations similar to the one used in equation (3.1.8) for STV-only and co-infected cells.

$$I_{STV}(t,\tau) = \begin{cases} r_{STV}^{Inf}(t-\tau)\,T(t-\tau)\exp\left(-\int_0^\tau \left(r_{DIP}^{Inf}(a) + k_I^{Apo}(a)\right)da\right), & t > \tau \geq 0, \\ 0, & \tau > t \geq 0, \end{cases} \qquad (3.2.13)$$

$$I_{CO}(t,\tau) = \begin{cases} \left(r_{STV}^{Inf}(t-\tau)\,I_{DIP}(t-\tau) + r_{DIP}^{Inf}(t-\tau)\int_0^{\tau_{SIE}} I_{STV}(t-\tau,a)\,da\right)\exp\left(-\int_0^\tau k_I^{Apo}(a)da\right), & t > \tau \geq 0, \\ 0, & \tau > t \geq 0, \end{cases}$$

$$(3.2.14)$$

These algebraic equations can be derived from Equations (3.2.3) and (3.2.4) providing the infection age density for both species. Upon infection at time t_I, corresponding cells with age zero emerge. This leads to boundary condition of $I_{STV}(t_I, \tau = 0) = r_{STV}^{Inf}(t_I)T(t_I)$ and $I_{CO}(t_I, \tau = 0) = r_{STV}^{Inf}(t_I)I_{DIP}(t_I) + r_{DIP}^{Inf}(t_I)I_{STV}(t_I)$ for STV-only and co-infected cells, respectively. Both types of populations are subject to virus-induced apoptosis, however, STV-only infected cells can also still become infected by DIPs.

The rate of virus-induced apoptosis in Equation (3.1.9) has been slightly modified to

$$k_I^{Apo}(\tau) = k_T^{Apo} + \frac{K_I}{1 + \exp(-v_{Apo}(\tau - \tau_{Apo}))} \tag{3.2.15}$$

taking into account the base apoptosis rate k_T^{Apo}.

Virus particle release

Infectious STVs (V) and DIPs (D) can theoretically be released from both STV-only and co-infected cells. DIP-only infected cells are assumed to not release any virus particles. Therefore, we obtain the following release dynamics

$$\frac{dV}{dt} = \int_0^\infty \left[r_{STV,I_{STV}}^{Rel}(\tau)I_{STV}(t,\tau) + r_{STV,I_{CO}}^{Rel}(\tau)I_{CO}(t,\tau) \right] d\tau - k_V^{Deg}V + \sum_n \left(k_n^{Dis}D_n^{Att} - k_{c,n}^{Att}B_n^V V \right) \tag{3.2.16}$$

$$\frac{dD}{dt} = \int_0^\infty \left[r_{DIP,I_{STV}}^{Rel}(\tau)I_{STV}(t,\tau) + r_{DIP,I_{CO}}^{Rel}(\tau)I_{CO}(t,\tau) \right] d\tau - k_V^{Deg}D + \sum_n \left(k_n^{Dis}D_n^{Att} - k_{c,n}^{Att}B_n^D D \right) \tag{3.2.17}$$

$$\text{with } B_n^V = B_n^{Tot}\left(T + T_A + I_{DIP} \right) - V_n^{Att} , \tag{3.2.18}$$

$$B_n^D = B_n^{Tot}\left(T + T_A + \int_0^{\tau_{SIE}} I_{STV}(t,\tau)\, d\tau \right) - D_n^{Att} \tag{3.2.19}$$

$$\text{and } k_n^{Dis} = \frac{k_{c,n}^{Att}}{k_{c,n}^{Eq}} , \, n \in \{Hi, Lo\} \tag{3.2.20}$$

where STVs and DIPs attach to their free binding sites on the cell membrane with the rate $k_{c,n}^{Att}$. We assume STVs do not re-infect STV-only and co-infected cells, while DIPs do not re-infect DIP-only and co-infected cells. This limits the potential binding sites for

the two different virus particles, i.e., B_n^V and B_n^D, as described in Equations (3.2.18) and (3.2.19). Attached STVs (V_n^{Att}) and DIPs (D_n^{Att}) can detach from binding sites with the rate k_n^{Dis} based on the equilibrium constant $k_{c,n}^{Eq}$. Additionally, they are degraded with the rate k_V^{Deg} which is applied to both STVs and DIPs. The rates $r_{i,j}^{Rel}(\tau)$ describe virus particle release of $i \in \{STV, DIP\}$ particles from $j \in \{I_{STV}, I_{CO}\}$ cells.

For the description of experimental data, we also consider the total amounts of released STVs (V_{Tot}^{Rel}), DIPs (D_{Tot}^{Rel}), and the total number of released virus particles (P_{Tot}^{Rel})

$$\frac{dV_{Tot}^{Rel}}{dt} = \int_0^\infty \left[r_{STV,I_{STV},Tot}^{Rel}(\tau) I_{STV}(t,\tau) + r_{STV,I_{CO},Tot}^{Rel}(\tau) I_{CO}(t,\tau) \right] d\tau \tag{3.2.21}$$

$$\frac{dD_{Tot}^{Rel}}{dt} = \int_0^\infty \left[r_{DIP,I_{STV},Tot}^{Rel}(\tau) I_{STV}(t,\tau) + r_{DIP,I_{CO},Tot}^{Rel}(\tau) I_{CO}(t,\tau) \right] d\tau \tag{3.2.22}$$

$$\frac{dP_{Tot}^{Rel}}{dt} = \frac{dV_{Tot}^{Rel}}{dt} + \frac{dD_{Tot}^{Rel}}{dt} \tag{3.2.23}$$

Virus entry

$$\frac{dV_n^{Att}}{dt} = k_{c,n}^{Att} B_n^V V - \left(k_n^{Dis} + k^{En} \right) V_n^{Att} - \left(r_{STV}^{Inf} + r_{STV}^{Lys} \right) V_n^{Att} \tag{3.2.24}$$

$$\frac{dD_n^{Att}}{dt} = k_{c,n}^{Att} B_n^D D - \left(k_n^{Dis} + k^{En} \right) D_n^{Att} - \left(r_{DIP}^{Inf} + r_{DIP}^{Lys} \right) D_n^{Att} \tag{3.2.25}$$

$$\frac{dV^{En}}{dt} = k^{En} \left(V_{Hi}^{Att} + V_{Lo}^{Att} \right) - k^{Fus} V^{En} - \left(r_{STV}^{Inf} + r_{STV}^{Lys} \right) V^{En} \tag{3.2.26}$$

$$\frac{dD^{En}}{dt} = k^{En} \left(D_{Hi}^{Att} + D_{Lo}^{Att} \right) - k^{Fus} D^{En} - \left(r_{DIP}^{Inf} + r_{DIP}^{Lys} \right) D^{En} \tag{3.2.27}$$

$$r_{STV}^{Lys} = k^{Lys} T_A \theta \left(\left(T + T_A + I_{DIP} \right)^{-1} \right) \tag{3.2.28}$$

$$r_{DIP}^{Lys} = k^{Lys} T_A \theta \left(\left(T + T_A + \int_0^\infty I_{STV}(t,\tau) d\tau \right)^{-1} \right) \tag{3.2.29}$$

Attached STVs and DIPs undergo endocytosis with the rate k^{En} and virus particles in endosomes fuse with the endosomal membrane with the rate k^{Fus}. During cell infection and lysis, virus particles that are attached to binding sites and inside of endosomes are also removed from the system according to the infection and lysis rates ($r_{\text{STV}}^{\text{Lys}}$ and $r_{\text{DIP}}^{\text{Lys}}$). The lysis rates are determined by relating the uninfected apoptotic cells undergoing lysis to the amount of cells having STVs or DIPs attached or in endosomes in Equations (3.2.28) and (3.2.29).

3.2.2 Consideration of individual genome segments during replication

To implement DIPs on the intracellular level, we decided to account for individual genome segments separately based on Laske and Heldt *et al.* [257]. Furthermore, we introduced additional vRNA and vmRNA regulation mechanisms to capture experimental data. Accordingly, the dynamics of intracellular replication changes as described in the following. Note that we did not introduce kinetic rates specific for DIP infection and replication, but use the same ones that apply to STVs.

Virus entry

To account for DIPs explicitly, species of extracellular DIPs (D^{Ex}), attached DIPs ($D_{\text{n}}^{\text{Att}}$) and DIPs in endosomes (D^{En}) were introduced analogous to STVs in Equations (3.1.19)–(3.1.23). Additionally, the calculation of available binding sites in Equation (3.1.20) was changed to

$$B_{\text{n}} = B_{\text{n}}^{\text{Tot}} - V_{\text{n}}^{\text{Att}} - D_{\text{n}}^{\text{Att}}, \ \text{n} \in \{\text{Hi}, \text{Lo}\} \tag{3.2.30}$$

as both STVs and DIPs can bind to the same sites.

Virus replication

The replication of the eight STV genome segments and the DI segment, which we implemented as a truncated version of segment 1, is considered separately. Therefore, Equation (3.1.25) was changed to

$$\frac{dV^{\mathrm{Cyt}}}{dt} = k^{\mathrm{Fus}}V^{\mathrm{En}} - k^{\mathrm{Imp}}V^{\mathrm{Cyt}} \tag{3.2.31}$$

and the DIP version

$$\frac{dD^{\mathrm{Cyt}}}{dt} = k^{\mathrm{Fus}}D^{\mathrm{En}} - k^{\mathrm{Imp}}D^{\mathrm{Cyt}} \tag{3.2.32}$$

was implemented, so that instead of the total number of vRNPs the amount of viral genome complexes in the cytoplasm are described. STV complexes (V^{Cyt}) are composed of the eight FL segments and the DIP complex (D^{Cyt}) contains a DI segment 1 in place of FL segment 1.

To consider the genome segments imported by STVs and DIPs, nuclear vRNPs ($Vp_{\mathrm{k}}^{\mathrm{Nuc}}$) are defined as

$$\frac{dVp_{\mathrm{i}}^{\mathrm{Nuc}}}{dt} = k^{\mathrm{Imp}}(V^{\mathrm{Cyt}} + D^{\mathrm{Cyt}}) + k_{\mathrm{NP}}^{\mathrm{Bind}}P_{\mathrm{NP}}R_{\mathrm{RdRp,i}}^{\mathrm{V}} - \left(k_{\mathrm{M1}}^{\mathrm{Bind}}P_{\mathrm{M1}} + k_{\mathrm{Rnp}}^{\mathrm{Deg}}\right)Vp_{\mathrm{i}}^{\mathrm{Nuc}} \tag{3.2.33}$$

$$\text{for i} = 2,\ldots,8$$

$$\frac{dVp_{1}^{\mathrm{Nuc}}}{dt} = k^{\mathrm{Imp}}V^{\mathrm{Cyt}} + k_{\mathrm{NP}}^{\mathrm{Bind}}P_{\mathrm{NP}}R_{\mathrm{RdRp,1}}^{\mathrm{V}} - \left(k_{\mathrm{M1}}^{\mathrm{Bind}}P_{\mathrm{M1}} + k_{\mathrm{Rnp}}^{\mathrm{Deg}}\right)Vp_{1}^{\mathrm{Nuc}} \tag{3.2.34}$$

$$\frac{dVp_{9}^{\mathrm{Nuc}}}{dt} = k^{\mathrm{Imp}}D^{\mathrm{Cyt}} + k_{\mathrm{NP}}^{\mathrm{Bind}}P_{\mathrm{NP}}R_{\mathrm{RdRp,9}}^{\mathrm{V}} - \left(k_{\mathrm{M1}}^{\mathrm{Bind}}P_{\mathrm{M1}} + k_{\mathrm{Rnp}}^{\mathrm{Deg}}\right)Vp_{9}^{\mathrm{Nuc}} \tag{3.2.35}$$

where the FL segments are denoted by $\mathrm{i} = 1,\ldots,8$ and the DI segment as $\mathrm{i} = 9$.

To account for a growth advantage of DI RNAs over their FL counterparts, which is theorized to originate from a reduced segment length, the synthesis of DI cRNA was implemented based on [257] as

$$\frac{dR_9^C}{dt} = (1 + F_{\text{Adv}}) k_C^{\text{Syn}} V p_9^{\text{Nuc}} - \left(k_{\text{RdRp}}^{\text{Bind}} P_{\text{RdRp}} + k_R^{\text{Deg}} \right) R_9^C \qquad (3.2.36)$$

where the factor F_{Adv} describes the advantage during DI cRNA synthesis. Additionally, the synthesis of FL cRNAs is described individually for each segment.

The synthesis of viral RNA was adapted based on experimental findings showing reduced vRNA levels in high MODIP infections [125]. Equation (3.1.28) was modified to account for each genome segment individually

$$\frac{dR_i^V}{dt} = k_V^{\text{Syn}} C p_i - \left(k_{\text{RdRp}}^{\text{Bind}} P_{\text{RdRp}} + k_R^{\text{Deg}} \right) R_i^V \qquad (3.2.37)$$

and the vRNA synthesis rate k_V^{Syn} is affected by the MODIP-to-MOI ratio via the factor $f_{\text{D,V}}(t_I)$

$$k_V^{\text{Syn}} = \frac{K_V}{f_{\text{D,V}}(t_I)} \qquad (3.2.38)$$

with

$$f_{\text{D,V}}(t_I) = \begin{cases} v_1 \left(\dfrac{D(t_I)}{V(t_I)} \right)^{v_2}, & \dfrac{D(t_I)}{C_{\text{Tot}}(t_I)} \geq F_{\text{MODIP}}, \\ 1, & \dfrac{D(t_I)}{C_{\text{Tot}}(t_I)} < F_{\text{MODIP}}, \end{cases} \qquad , f_{\text{D,V}}(t_I) \geq 1 \qquad (3.2.39)$$

where K_V denotes the maximum vRNA synthesis rate and t_I describes the time point at which a cell became infected. The parameters v_1 and v_2 describe the effect of the MODIP-to-MOI ratio $\dfrac{D(t_I)}{V(t_I)}$ on the parameter $k_V^{\text{Syn}}(t_I)$. To calculate the MODIP-to-MOI ratio, the extracellular concentrations of STVs ($V(t_I)$) and DIPs ($D(t_I)$) at the time of infection are utilized. If the MODIP is above a threshold value F_{MODIP} when a cell is

infected, vRNA synthesis is reduced. Based on experimental data [125], we determined this value to be in the range of 10^{-3} to 3. For model prediction in section 4.3.2, we assumed a value of $F_{\text{MODIP}} = 10^{-3}$.

The stabilization and formation of vRNP-M1-complexes is constructed similar to Equations (3.1.29)–(3.1.32), but considers each segment i = 1,...,9 separately. Accounting for the competition between FL and DI segment 1 during virion packaging, the formation of segment-specific complexes of vRNPs, which are covered later in this section, was implemented. These are generated from cytoplasmic vRNPs, which changes their dynamics to

$$\frac{dVp_{\text{M1,i}}^{\text{Cyt}}}{dt} = k^{\text{Exp}}P_{\text{NEP}}Vp_{\text{M1,i}}^{\text{Nuc}} - k_{\text{Rnp}}^{\text{Deg}}Vp_{\text{M1,i}}^{\text{Cyt}} - k^{\text{Cplx}}\left(Vp_{\text{M1,1}}^{\text{Cyt}} + Vp_{\text{M1,9}}^{\text{Cyt}}\right)\prod_{g=2,\ldots,8}Vp_{\text{M1,g}}^{\text{Cyt}} \quad (3.2.40)$$

$$\text{for } i = 2,\ldots,8$$

$$\frac{dVp_{\text{M1,1}}^{\text{Cyt}}}{dt} = k^{\text{Exp}}P_{\text{NEP}}Vp_{\text{M1,1}}^{\text{Nuc}} - k_{\text{Rnp}}^{\text{Deg}}Vp_{\text{M1,1}}^{\text{Cyt}} - k^{\text{Cplx}}Vp_{\text{M1,1}}^{\text{Cyt}}\prod_{g=2,\ldots,8}Vp_{\text{M1,g}}^{\text{Cyt}} \quad (3.2.41)$$

$$\frac{dVp_{\text{M1,9}}^{\text{Cyt}}}{dt} = k^{\text{Exp}}P_{\text{NEP}}Vp_{\text{M1,9}}^{\text{Nuc}} - k_{\text{Rnp}}^{\text{Deg}}Vp_{\text{M1,9}}^{\text{Cyt}} - k^{\text{Cplx}}Vp_{\text{M1,9}}^{\text{Cyt}}\prod_{g=2,\ldots,8}Vp_{\text{M1,g}}^{\text{Cyt}} \quad (3.2.42)$$

where the rate of complex formation is described by k^{Cplx}.

Viral transcription and protein synthesis

vmRNA transcription was already implemented using a segment-specific implementation in the multiscale model of STV infection. However, experimental data showed a clear difference in the accumulation of genome segments. Therefore, we modified Equation (3.1.34) to

$$\frac{dR_{\text{i}}^{\text{M}}}{dt} = f_{\text{M}}\frac{k_{\text{M}}^{\text{Syn}}Vp_{\text{i}}^{\text{Nuc}}}{L_{\text{i}}\left(1 + \dfrac{P_{\text{Rdrp}}}{K_{\text{R}}}\right)} - k_{\text{M}}^{\text{Deg}}R_{\text{i}}^{\text{M}} \quad (3.2.43)$$

$$\text{with } f_{\text{M}} = \begin{cases} F_{\text{M}}, & i \in \{1,2,3,9\}, \\ 1, & i \in \{4,\ldots,8\}, \end{cases} \quad (3.2.44)$$

where, the factor f_{M} incorporates the assumption that RdRp-related segments, i.e., FL segments 1 to 3 as well as the DI segment 1, are transcribed at a lower rate than FL segments 4 to 8.

The viral protein dynamics in Equation (3.1.35)–(3.1.44) were modeled as described in Laske and Heldt *et al.* [257], which changes the usage of proteins for virus release. The release of STVs and DIPs removes HA, NA, M1 and M2 from the protein pool, however, no additional RdRp, NP and NEP is required for virus budding.

Furthermore, the model accounts for the transcription of vmRNA in DIP-only infected cells as experiments showed significant accumulation despite very low MOIs and few co-infections [125]. To describe these dynamics, we implemented primary viral transcription events, discussed in [62, 271, 272], for DIP-only infected cells on the population level. Therefore, we assume that the vRNAs entering the nucleus during initial infection enable the production of large amounts of vmRNA. However, as we used a DIP with a deletion in a genome segment related to RdRp, the replication of vRNA cannot take place. We implemented the primary vmRNA transcription in DIP-only infected cells similar to Equation (3.2.43) as

$$\frac{dR_{\mathrm{i},I_{\mathrm{DIP}}}^{\mathrm{M}}}{dt} = f_{\mathrm{M}} \frac{k_{\mathrm{M}}^{\mathrm{Syn}}}{L_{\mathrm{i}}} \frac{D(t_{\mathrm{I}})}{C_{\mathrm{Tot}}(t_{\mathrm{I}})} - k_{\mathrm{M}}^{\mathrm{Deg}} R_{\mathrm{i},I_{\mathrm{DIP}}}^{\mathrm{M}} \quad , \mathrm{i} = 2,...,9 \tag{3.2.45}$$

Here, the templates for transcription in an individual cell $\dfrac{D(t_{\mathrm{I}})}{C_{\mathrm{Tot}}(t_{\mathrm{I}})}$ are the DIPs provided at the time of initial infection t_{I}. The inhibition of vmRNA synthesis by RdRp is not applied in these equations, because we used a DIP containing a deletion in segment 1 encoding for PB2. However, the segment-specific regulation of vmRNA transcription mediated by f_{M} is still considered.

Complex formation and virus particle release

After release from the nucleus vRNPs travel to the cellular membrane and assemble to create either STVs or DIPs. For the co-infection model the formation of STV ($V_{\mathrm{Cplx}}^{\mathrm{Cyt}}$) and DIP ($D_{\mathrm{Cplx}}^{\mathrm{Cyt}}$) complexes containing eight vRNPs, i.e., seven FL vRNPs of segment 2 to 8 and either FL segment 1 or DI segment 1, prior to virus particle release was implemented.

$$\frac{dV_{\mathrm{Cplx}}^{\mathrm{Cyt}}}{dt} = k^{\mathrm{Cplx}} V p_{\mathrm{M1,1}}^{\mathrm{Cyt}} \prod_{g=2,\dots,8} V p_{\mathrm{M1,g}}^{\mathrm{Cyt}} - r_{\mathrm{STV,Tot}}^{\mathrm{Rel}} - k_{\mathrm{Rnp}}^{\mathrm{Deg}} V_{\mathrm{Cplx}}^{\mathrm{Cyt}} \tag{3.2.46}$$

$$\frac{dD_{\mathrm{Cplx}}^{\mathrm{Cyt}}}{dt} = k^{\mathrm{Cplx}} V p_{\mathrm{M1,9}}^{\mathrm{Cyt}} \prod_{g=2,\dots,8} V p_{\mathrm{M1,g}}^{\mathrm{Cyt}} - r_{\mathrm{DIP,Tot}}^{\mathrm{Rel}} - k_{\mathrm{Rnp}}^{\mathrm{Deg}} D_{\mathrm{Cplx}}^{\mathrm{Cyt}} \tag{3.2.47}$$

$$\frac{dV_{\mathrm{Tot}}^{\mathrm{Rel}}}{dt} = r_{\mathrm{STV,Tot}}^{\mathrm{Rel}}(\tau) = k^{\mathrm{Rel}} \frac{V_{\mathrm{Cplx}}^{\mathrm{Cyt}}}{V_{\mathrm{Cplx}}^{\mathrm{Cyt}} + D_{\mathrm{Cplx}}^{\mathrm{Cyt}} + K_{V^{\mathrm{Rel}}}} \prod_{j} \frac{P_j}{P_j + N_{P_j} K_{V^{\mathrm{Rel}}}} \tag{3.2.48}$$

$$\frac{dD_{\mathrm{Tot}}^{\mathrm{Rel}}}{dt} = r_{\mathrm{DIP,Tot}}^{\mathrm{Rel}}(\tau) = k^{\mathrm{Rel}} \frac{D_{\mathrm{Cplx}}^{\mathrm{Cyt}}}{V_{\mathrm{Cplx}}^{\mathrm{Cyt}} + D_{\mathrm{Cplx}}^{\mathrm{Cyt}} + K_{V^{\mathrm{Rel}}}} \prod_{j} \frac{P_j}{P_j + N_{P_j} K_{V^{\mathrm{Rel}}}} \tag{3.2.49}$$

$$\frac{dV^{\mathrm{Rel}}}{dt} = r_{\mathrm{STV}}^{\mathrm{Rel}}(\tau) = F_{\mathrm{Par}} k^{\mathrm{Rel}} \frac{V_{\mathrm{Cplx}}^{\mathrm{Cyt}}}{V_{\mathrm{Cplx}}^{\mathrm{Cyt}} + D_{\mathrm{Cplx}}^{\mathrm{Cyt}} + K_{V^{\mathrm{Rel}}}} \prod_{j} \frac{P_j}{P_j + N_{P_j} K_{V^{\mathrm{Rel}}}} \tag{3.2.50}$$

$$\frac{dD^{\mathrm{Rel}}}{dt} = r_{\mathrm{DIP}}^{\mathrm{Rel}}(\tau) = F_{\mathrm{Par}} k^{\mathrm{Rel}} \frac{D_{\mathrm{Cplx}}^{\mathrm{Cyt}}}{V_{\mathrm{Cplx}}^{\mathrm{Cyt}} + D_{\mathrm{Cplx}}^{\mathrm{Cyt}} + K_{V^{\mathrm{Rel}}}} \prod_{j} \frac{P_j}{P_j + N_{P_j} K_{V^{\mathrm{Rel}}}} \tag{3.2.51}$$

$$\text{with } \frac{dF_{\mathrm{Par}}}{dt} = -k_{\mathrm{Red}}^{\mathrm{Rel}} F_{\mathrm{Par}} \tag{3.2.52}$$

$$\text{and } j \in \{\mathrm{HA,NA,M1,M2}\}$$

where $r_{\mathrm{STV,Tot}}^{\mathrm{Rel}}$ and $r_{\mathrm{DIP,Tot}}^{\mathrm{Rel}}$ describe the rate of total STV and DIP release, respectively. Additionally, the virus particle complexes can degrade. The total number of released STVs and DIPs is represented by $V_{\mathrm{Tot}}^{\mathrm{Rel}}$ and $D_{\mathrm{Tot}}^{\mathrm{Rel}}$, which are calculated similar to Equation (3.1.45). Virion release is determined by the relative availability of STV and DIP complexes maintaining a maximum rate of overall virus particle release described by k^{Rel}. As in the model of STV infection introduced in section 3.1, we consider that

only a certain fraction of virus particles is capable of successful replication. This is implemented via F_{Par}, which describes the fraction of infectious virions released (FIVR), enabling the description of the amount of infectious STVs (V^{Rel}) and DIPs (D^{Rel}) released during infection.

3.3 Model simulation and analysis

3.3.1 Set-up and initialization of the intracellular and cell population sub-models

Multiscale model of STV infection

For the simulation of the model of STV infection, the intracellular and cell population model were decoupled according to Heldt *et al.* [38] to reduce computational burden. Therefore, it was assumed that processes on the cell population level do not affect intracellular dynamics. This enabled the separate simulation of the different levels providing a significant reduction of complexity. For this approach, two versions of the intracellular model were established: a complete and a reduced version. The complete model is used to simulate the dynamics of virus entry, replication and release in an infected cell. The reduced intracellular model, which neglects virus entry and considers an already infected cell with a set of eight vRNPs in the cytoplasm, is used to calculate the infection age-dependent release rates of infected cells, i.e., $r_{\text{Inf}}^{\text{Rel}}(\tau)$ and $r_{\text{Par}}^{\text{Rel}}(\tau)$. Then, these rates are utilized in Equations (3.1.11), (3.1.14) and (3.1.15) for the simulation of the cell population level, which covers virus entry to compensate for the reduced intracellular model.

The initial amount of virus particles used for the complete intracellular model, i.e., $V^{\text{Ex}}(0)$, is based on the MOI applied for infection. When the MOI is below one, a minimum of one virion infecting a cell is assumed, because we do not consider infections by incomplete virus particles. Accordingly, the reduced intracellular model, which neglects virus entry, is initiated with

$$Vp^{\text{Cyt}}(0) = 8\frac{\text{molecules}}{\text{virion}} F_{\text{Fus}} V^{\text{Ex}}(0) .$$ (3.3.1)

The expression $Vp^{\text{Cyt}}(0)$ in the reduced intracellular model represents the amount of vRNPs that reach the cytoplasm after $V^{\text{Ex}}(0)$ virus particles have infected a cell. We assume that at least one full set of vRNP infects a cell resulting in a minimum of $Vp^{\text{Cyt}}(0) = F_{\text{Fus}} \cdot 8 \text{ molecules}$.

Multiscale model of co-infection

To simulate the multiscale model of co-infection, we reconsidered the assumption that events on the cell population level do not affect intracellular dynamics, which enabled the uncoupling of the two levels. The proportion of STVs to DIPs during infection can significantly change cell-specific yields and high DIP concentrations can suppress STV replication [125]. Therefore, we decided that the current concentrations of STVs and DIPs should be considered when cells are infected or a co-infection occurs. In the multiscale model of co-infection, the intracellular and cell population sub-models are still linked via the infection age-dependent release rates $r_{\text{STV}}^{\text{Rel}}(\tau)$ and $r_{\text{DIP}}^{\text{Rel}}(\tau)$. However, these are not calculated by the now obsolete reduced intracellular model, but the complete intracellular model is simulated considering the current concentrations of STVs and DIPs on the cell population level. Consequently, cells infected at distinct time points show different replication and release dynamics. This new approach increased computational burden considerably, but it enables the description of infections with highly dynamic STV and DIP concentrations.

To simulate the intracellular model, we apply the concentrations of available virus particles calculated on the cell population level as initial conditions. Therefore, the number of free, attached and enveloped STVs ($V(t_{\text{I}})$, $V_{\text{n}}^{\text{Att}}(t_{\text{I}})$, $V^{\text{En}}(t_{\text{I}})$) and DIPs ($D(t_{\text{I}})$, $D_{\text{n}}^{\text{Att}}(t_{\text{I}})$, $D^{\text{En}}(t_{\text{I}})$) per amount of cells that can still be infected at time of infection t_{I} is converted to $V^{\text{Ex}}(0)$, $V_{\text{n}}^{\text{Att}}(0)$, $V^{\text{En}}(0)$, $D^{\text{Ex}}(0)$, $D_{\text{n}}^{\text{Att}}(0)$, $D^{\text{En}}(0)$ on the intracellular level, respectively. Additionally, we assume that a minimum of one full STV or DIP is required for infection and that a cell counts as infected in the moment a virus

genome reaches its cytoplasm. To that end, $V^{\mathrm{Cyt}}(0)$ is set to 1 for STV-only infected cells and both $V^{\mathrm{Cyt}}(0)$ and $D^{\mathrm{Cyt}}(0)$ are set to 1 for co-infected cells for the simulation of the intracellular model. When simulating replication and release in STV-only infected cells, all DIP-related initial conditions are set to 0.

Furthermore, we assume that an infected cell does not release partial virus particles, but has a minimum release of one complete STV or DIP. Therefore, all values in the infection age-dependent release rates $r_{\mathrm{STV}}^{\mathrm{Rel}}(\tau)$, $r_{\mathrm{STV,Tot}}^{\mathrm{Rel}}(\tau)$, $r_{\mathrm{DIP}}^{\mathrm{Rel}}(\tau)$, and $r_{\mathrm{DIP,Tot}}^{\mathrm{Rel}}(\tau)$ lower than 1 are set to 0. With this assumption, we also introduce a delay between cell infection and virus particle release. Additionally, the disproportionately fast spreading of infections in low MOI conditions is prevented.

3.3.2 Model simulation, calibration and prediction

Model simulation, parameter fitting, model prediction and visualization of results was performed with MATLAB® (R2017a, version 9.2.0.556344, The MathWorks, Inc.) on a Linux-based system.

Simulation

The intracellular and cell population dynamics were simulated using different approaches for the STV infection model and the model of STV and DIP co-infection. The intracellular sub-models (Equations (3.1.19)–(3.1.47), Equations (3.2.30)–(3.2.52)) and experimental data were managed with the Systems Biology Toolbox 2 developed by Schmidt and Jirstrand [273]. The ODEs were solved numerically with the CVODE routine from SUNDIALS [274]. Cell population dynamics were calculated using Euler's method with a step size of $dt = 0.05\,\mathrm{h}$ for the model of STV infection. For the co-infection model, a larger step size of $dt = 0.1\,\mathrm{h}$ was used. In case this step size led to rapidly oscillating behavior, e.g., when the concentration of uninfected cells reached values close to zero, it was reduced to $dt = 0.02\,\mathrm{h}$. Integrals present in the ODEs were calculated by using Equation (3.1.8) instead of $I(t,\tau)$ for the model of STV infection or Equations (3.2.13) and (3.1.14) instead of $I_{\mathrm{STV}}(t,\tau)$ and $I_{\mathrm{CO}}(t,\tau)$,

respectively, for the co-infection model. To this end, the rectangle method was used to approximate results using the same step sizes as described before.

For the STV infection model, confidence intervals in Table 4.2 were determined by bootstrapping [264] based on the standard deviations obtained from three independent experiments [64, 181].

The confidence intervals for the model of STV and DIP co-infection shown in Table 4.3 were calculated by bootstrapping considering a 55% error for qPCR measurements and a 40% error for cell population data based on experiments from [64]. Additionally, an error of 40% for the infectious STV titer was applied based on test runs using the plaque assay. The local sensitivities for all model parameters shown in Table B.3 were calculated based on Heldt *et al.* [242].

Parameter estimation

For the multiscale model of STV infection, estimation was performed with the fSSm algorithm for global stochastic optimization [275]. Measurements comprised vRNA, cRNA and vmRNA dynamics of genome segment 5 on the intracellular level. On the cell population level, infectious and total virus titers as well as fractions of cells in different states of infection and apoptosis were determined [64, 181].

Parameter estimation for the multiscale model of co-infection was performed using the evolutionary optimization algorithm CMA-ES [276]. Here, experimental data consisted of vRNA and vmRNA dynamics of FL segment 1, DI segment 1 and FL segment 5 on the intracellular level. On the cell population level, the infectious STV titer, total STV and DIP titers, as well as fractions of cells in different states of infection and apoptosis were determined [125].

Optimal sets of model parameters were estimated by simultaneously fitting the intracellular and cell population sub-models to the respective experimental data. During calibration, individual estimation steps were evaluated by normalizing errors to their corresponding maximum measurement value. Then, the sum of errors for the intracellular and cell population level were divided by the number of measurements and summed up to indicate the goodness of fit. The first measured data point was applied as an offset to the simulated values of viral RNAs to accommodate for a background signal in the real-time RT-qPCR experiments.

The optimal model parameters used for the simulation of the STV infection model are presented in Tables A.2 and A.3. For the STV and DIP co-infection model, they are provided in Tables B.1 and B.2.

Model prediction

In order to predict virus release dynamics for MOI 10^{-4} and 3 with the model of STV infection in section 4.1.2, parameters fitted to experimental data measured in infections with MOI 73 were used. However, the initial value of the FIVR, which was estimated to be $F_{\mathrm{Par}}(0) = 0.034$, was modified based on large differences in the measurements of infectious virus particles between low and high MOI conditions (Figures 4.5 and 4.8). For the simulation of infections at MOI 10^{-4} and 3 we applied a $F_{\mathrm{Par}}(0) = 0.26$, which was determined by testing a range of values from 0 to 1 to find an optimum for both conditions (Figure 4.9).

For the prediction of infectious and total virus release for various MOI and MODIP conditions with the multiscale model of co-infection, the initial conditions of STVs and DIPs on the cell population level were adjusted to the appropriate values considering a viable cell concentration of $T(0) = 2.2 \times 10^{6} \ \mathrm{cells/mL}$. For the evaluation of the impact of the replication advantage of DI cRNA on STV and DIP release, we varied the parameter F_{Adv} in a range from 0 to 3.2 around its estimated value (0.32). This modified parameter was then applied for simulation using different MOI and MODIP conditions. The initial conditions and adjusted parameters used for the model predictions presented in section 4.3.1 are listed in Table A.1.

4. Results and Discussion

4.1 Multiscale model of STV replication and spread

The application and analysis of multiscale models combining intracellular virus replication and spreading of virions on the cell population level is a powerful tool to provide a systems-level understanding of virus infection in general and IAV infection in particular. An often-overlooked aspect is the MOI, which affects infection dynamics, time scales during virus propagation and process yields. Therefore, we developed a multiscale model of STV replication and spread in cell cultures that describes a wide range of MOI conditions providing a comprehensive representation of STV infection. In the first part of this section, we focus on high MOI infections and move towards low MOI conditions in the second part.

4.1.1 Dynamics of a one-step STV infection for high MOI conditions

As a basis for the development of our model, we employed a previously published model of IAV infection in animal cell cultures by Heldt *et al.* [38] and modified various aspects to enable the description of a STV infection in high MOI conditions. An overview of the considered reactions during STV replication and spread is depicted in Figure 4.1. Note that in this section major parts of the original publication on the multiscale model of STV infection were used [181].

The original model by Heldt *et al.* [38] combines intracellular virus replication with virus propagation on the cell population level. On the intracellular level, various steps of STV replication including viral RNA synthesis, viral protein translation, and STV release are described in detail. The cell population level comprises population kinetics of uninfected cells, infected cells, apoptotic cells, and free virions (infectious STVs). The two levels of viral infection are linked by connecting the intracellular dynamics to a segregated population of infected cells. This segregation considers the time passed

since cells were infected, i.e., the infection age τ. The release of STVs from an infected cell, which is calculated by the intracellular sub-model, is dependent on the infection age and assigned to the segregated infected cell population. Thus, the intracellular and cell population level of STV infection can be simulated simultaneously.
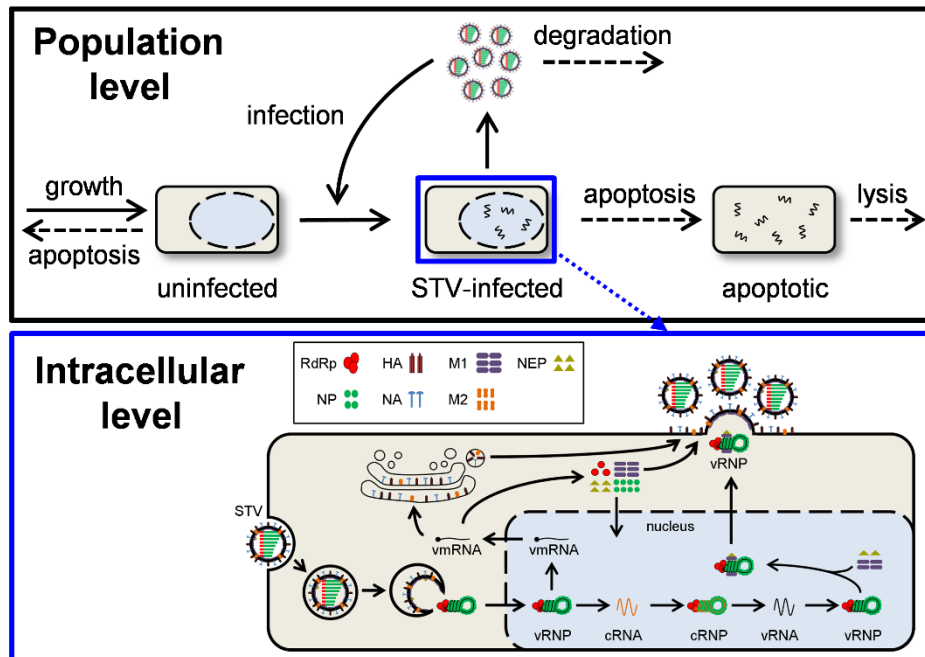
Figure 4.1.: Scheme of the multiscale model of STV infection. (Top) The population level of infection describes growth and apoptosis of uninfected cells, their infection by STVs, virus-induced apoptosis of infected cells and the lysis of apoptotic cells. STVs are released from infected cells. (Bottom) Virus entry, nuclear import, viral RNA and protein synthesis, nuclear export and progeny virion release in infected cells is described by an intracellular model of virus infection. Figure adapted from [38].

One-step high MOI infection

For the calibration of the original model, measurements from two separate experiments, which were performed at a high MOI for the intracellular STV replication dynamics and a low MOI for the cell population dynamics, were used. Furthermore, in a recent publication, STV replication dynamics on the intracellular and cell population level were analyzed for MDCKadh cells using high MOI conditions [64]. To that end, an MOI of 10 plaque forming units (PFU) per cell was used. However, the resulting

virus titers were determined by the $TCID_{50}$ assay. To utilize data for virus input and production that were measured with the same assay for model calibration, the initial MOI was determined again via the $TCID_{50}$ assay, which resulted in an MOI of about 73. This high virus load was employed to induce a single-cycle infection and resulted in a rapid infection of cells. Consequently, all cells are infected in a confined time frame leading to homogeneous cell infection ages. This enabled a profound investigation of the intracellular infection dynamics as cells in similar stages of infection were observed, rather than a mixture of cells at highly different levels of progression. A recalibration of the original model to measurements provided by this newer study showed mixed results. While levels of viral cRNA, vRNA and STV release could be reproduced, cell population and vmRNA dynamics (Figure 4.2) differed considerably from the experimental data.

Additionally, model predictions performed with the original model fitted for high MOI measurements from [64] did not capture viral release dynamics observed in new infection experiments performed at lower MOIs (Figure 4.3) [181]. Therefore, we decided to augment the original model to enable the description of STV infection dynamics for a wider range of MOI conditions, e.g., for the low MOI regimes used in cell culture-based influenza vaccine production.

Infection age-dependent apoptosis dynamics

First, we focused on the description of cell population dynamics during the STV infection of MDCKadh cell cultures. On the cell population level, the model considers uninfected cells, infected cells and apoptotic cells of both cell populations. Previous measurements of a STV infection of MDCKadh cells in high MOI conditions showed that apoptotic cells start to accumulate about 16 hours post infection (hpi) [64]. To describe this delay, which is not considered in the original model (Figure 4.4A–B), we adjusted the apoptosis rate of infected cells (Equation (3.1.9)). The original model assumed an exponential distribution of the survival time of infected cells, which was implemented by a stepwise increase of the apoptosis rate to a fixed value after infection [64]. In a previous study, Holder *et al.* suggested that normal distributions are well suited to describe the time which cells spend in a specific state [277]. However, to
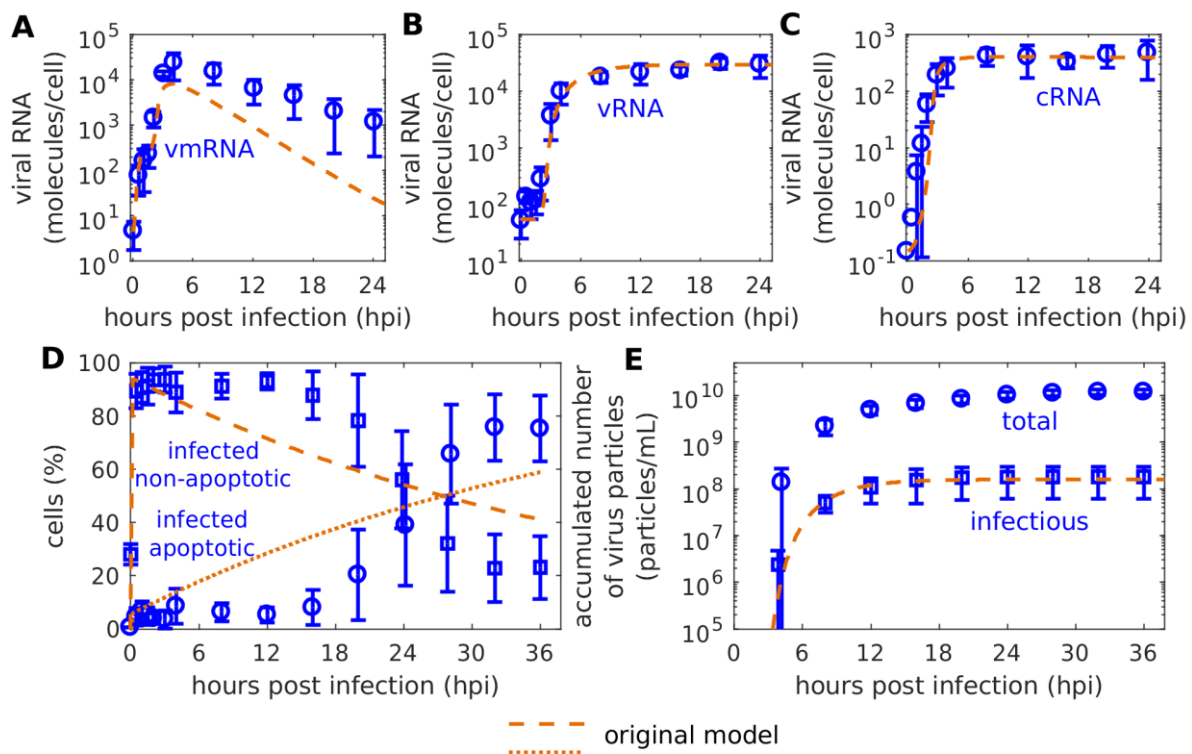
Figure 4.2.: Model fit of the original multiscale model to infection dynamics on the intracellular and cell population level. Curves depict the fits of the original model to (A-C) cell-specific viral RNA of genome segment 5, (D) cell population and (E) virus titer measurements obtained in MDCKadh cell-culture infections with influenza A/PR/8/34 (H1N1) at an MOI of 73 based on $TCID_{50}$ [64]. Symbols represent the mean and error bars the standard deviation of three independent experiments. Figure adapted from Rüdiger *et al.* [181].

introduce an infection age-dependent apoptosis rate, the cumulative density function of the normal distribution is required. This cumulative density function utilizes the Gauss error function and does not have a closed analytical form of estimation [268]. Therefore, we considered other approaches capable of approximating dynamics induced by a normal distribution while still being easy to handle. To that end, we used a logistic function, Hill kinetics, and a Gompertz function, based on their capacity to introduce sigmoid dynamics. All of these functions described the time course of virus-induced apoptosis relatively well (Figure 4.4A–B).

Finally, we decided to employ a logistic function to describe the apoptosis rate of
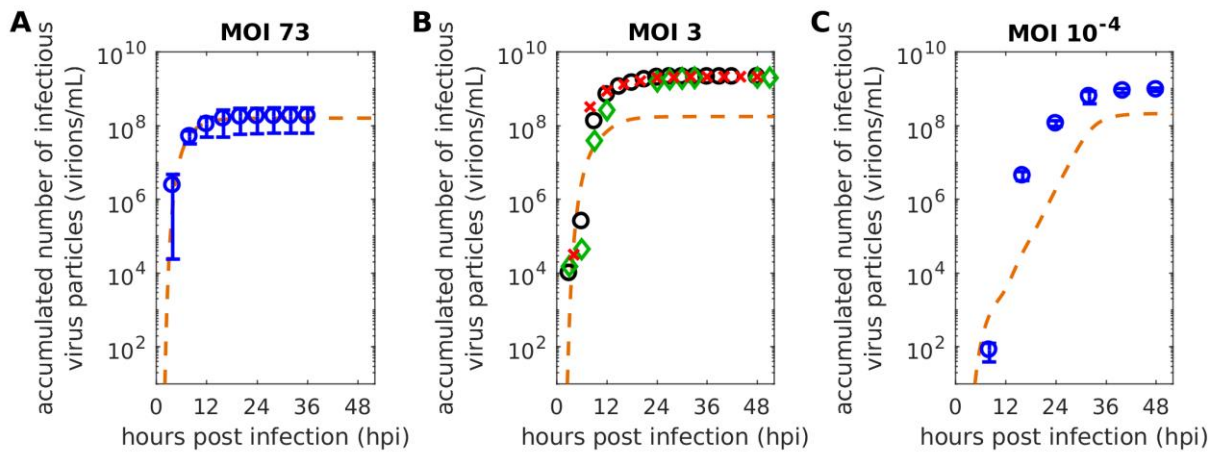
Figure 4.3.: The original multiscale model cannot reproduce virus particle release dynamics for different infection conditions. Curves depict model simulations of infectious virus particles released during MDCKadh cell infections with influenza A/PR/8/34 (H1N1) generated by the original multiscale model of Heldt *et al.* [38]. Results for MOI 73 were adapted from [64], experiments for MOI 3 and 10^{-4} were conducted following the same protocol [181]. Infections at MOI 73 and MOI 3 were performed with an influenza A/PR/8/34 strain from the National Institute for Biological Standards and Control (NIBSC); for the infection at MOI 10^{-4}, an influenza A/PR/8/34 strain from the Robert Koch Institute (RKI) was used. Symbols represent the accumulated number of infectious virus particles quantified by the TCID$_{50}$ assay. (A+C) Error bars indicate standard deviations of three independent experiments, time courses of three individual experiments in (B) are shown separately (O, $\Diamond$, X). Model parameters were fitted to experimental results obtained with (A) an MOI of 73 [64]. Relevant initial conditions in (B+C) were adjusted to the respective infection conditions. Figure taken from Rüdiger *et al.* [181].

infected cells (Equation (3.1.9)) as it provides two benefits. The logistic function allowed the best fit of the experimental data and, in contrast to a Hill kinetic, the introduced parameters can be readily interpreted. In this scenario, τ_{Apo} describes the time after cell infection at which the rate of virus-induced apoptosis reaches its half-maximum and ν_{Apo} denotes a factor that represents the time required from cell infection
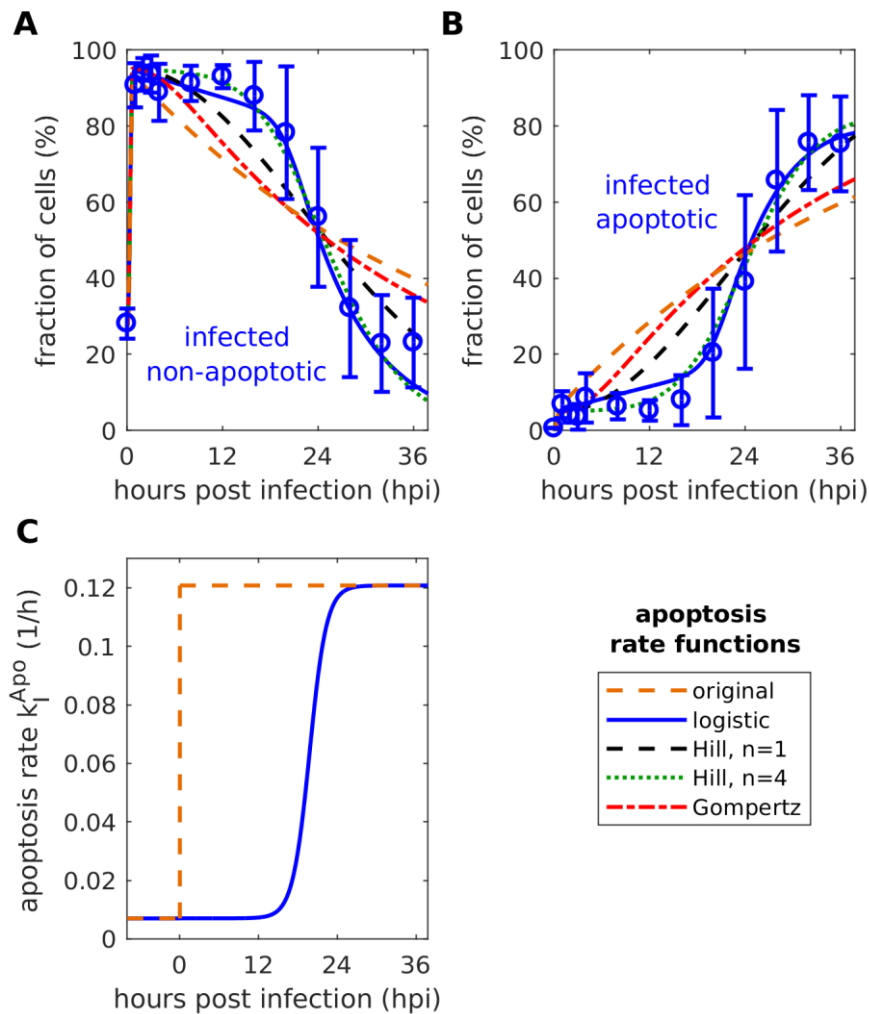
Figure 4.4.: Logistic apoptosis rate enables reproduction of cell population dynamics. Model fits to cell population measurements from MDCKadh cell cultures infected with influenza A/PR/8/34 (H1N1) at an MOI of 73 [64]. Mean percentage values of (A) infected, non-apoptotic and (B) infected, apoptotic cells from three independent experiments are shown. Curves represent simulations of the original model [38] and the extended multiscale model with different implementations of the infection age-dependent apoptosis rate. (C) Comparison of infected, non-apoptotic cell apoptosis rate dynamics using a stepwise (original model, [38]) and logistically increasing virus-induced apoptosis rate $k_{\mathrm{T}}^{\mathrm{Apo}}$. Hours post infection in (A) and (B) refer to the time passed since the cell culture was infected while in (C) it corresponds to the individual infection time point of a cell. Figure adapted from Rüdiger *et al.* [181].

until the full activation of the apoptosis mechanism. Figure 4.4C shows the difference between both scenarios. The original model uses an apoptosis rate that instantly increases after cell infection while the extended model establishes a delayed, gradually increasing rate. Hence, the implementation of an infection age-dependent rate of virus-induced apoptosis enables a better description of cell population dynamics observed in a single-cycle STV infection of MDCKadh cells (Figure 4.4A–B) [64].

Release of infectious and non-infectious STVs

Next, we extended the original model to consider the number of infectious STVs (determined by infectivity assays, e.g., TCID$_{50}$) and the total number of STVs (determined by the HA assay) separately. This characteristic was not accounted for in the original model, which solely focused on "virions" (infectious STVs). However, the concentration of total STVs holds valuable information for influenza virus production as it correlates with process yields for manufacturing of inactivated vaccines. Accordingly, we implemented the total STV release of an individual infected cell (Equation (3.1.45)) and defined the release of infectious STVs as a fraction of the overall release (Equation (3.1.46)). As shown in [64], virus titer measurements indicate that the ratio of infectious to total STV release is not constant over the course of infection. In MDCKadh cell cultures infected with influenza A/PR/8/34 at an MOI of 73, the initial FIVR was about 4% and decreased to about 0.3% over time (Figure 4.5A). As a result, most virions released during late infection were non-infectious. The variable $F_{\mathrm{Par}}(\tau)$ (Equation (3.1.47)) describes the FIVR by an infected cell at a certain infected cell age τ. Generally, the FIVR represents factors that affect the capability of progeny STVs to infect cells productively. Plausible effects that may influence this capability are the accumulation of DIPs or limited precursors for viral protein and RNA synthesis due to a rapid virus replication. The dynamics of F_{Par} is defined as a first order degradation to reproduce the observation that infected cells release higher percentages of infectious STVs immediately after infection compared to later time points (Figure 4.5A).
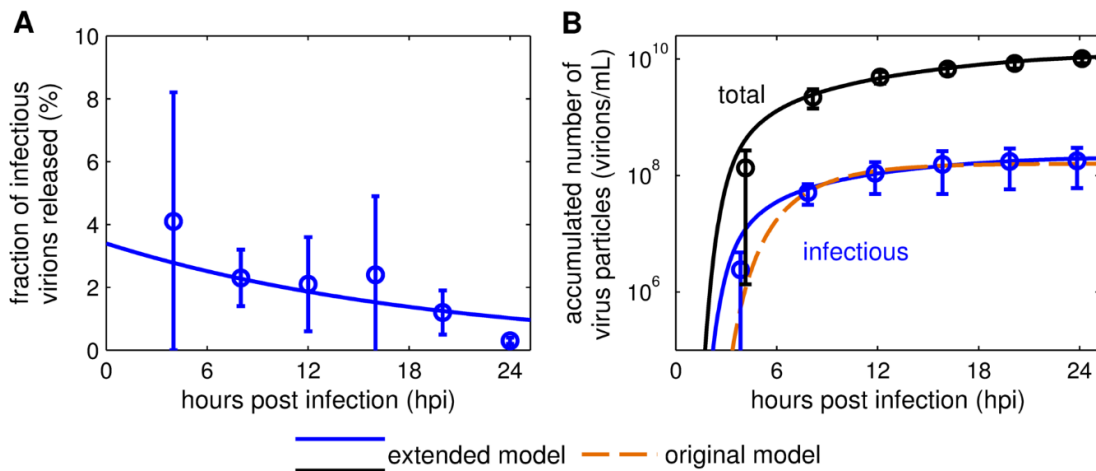
Figure 4.5.: Relation of infectious to total virus particles released. (A) The fraction of infectious virions released, (B) the accumulated number of infectious and total virus particles were taken from three individual experiments performed in [64]. In brief, MDCKadh cells were infected with influenza A/PR/8/34 (H1N1) at an MOI of 73. Cumulative viral titers were determined by TCID$_{50}$ assay and HA assay, respectively. The solid lines represent the model fit to the data with the extended model, (B) the dashed line depicts the model fit with the original model [38]. Figure taken from Rüdiger *et al.* [181].

Using this infection age-dependent variable, the model captures both infectious and overall STVs released by an individual infected cell (Figure 4.5B). To describe the total amount of STVs on the population level, we introduced the variable P_{tot}^{Rel} (Equation (3.1.15)), which can be correlated to IAV production yields. Thus, these model extensions enable the description of both the cell-specific yield and overall viral titers during IAV production in cell cultures.

RdRp-related inhibition of vmRNA production

The final step of model extension was to take details of intracellular vmRNA dynamics into account. After implementation of the aforementioned changes, the description of vmRNA dynamics still showed deviations from the measurements (Figure 4.6A, dotted line). While the initial accumulation of vmRNA and the resulting peak could be captured, its following degradation could not be fully reproduced. Previous

experimental studies of IAV infection in high MOI conditions indicated that a complete shutdown of vmRNA synthesis occurs at about 6 hpi [59]. The original model did not describe such a rapid shutdown and vmRNA synthesis continued during late infection (Figure 4.6B). To capture such dynamics, another extension of the mathematical model, i.e., the inhibition of vmRNA synthesis, was required.
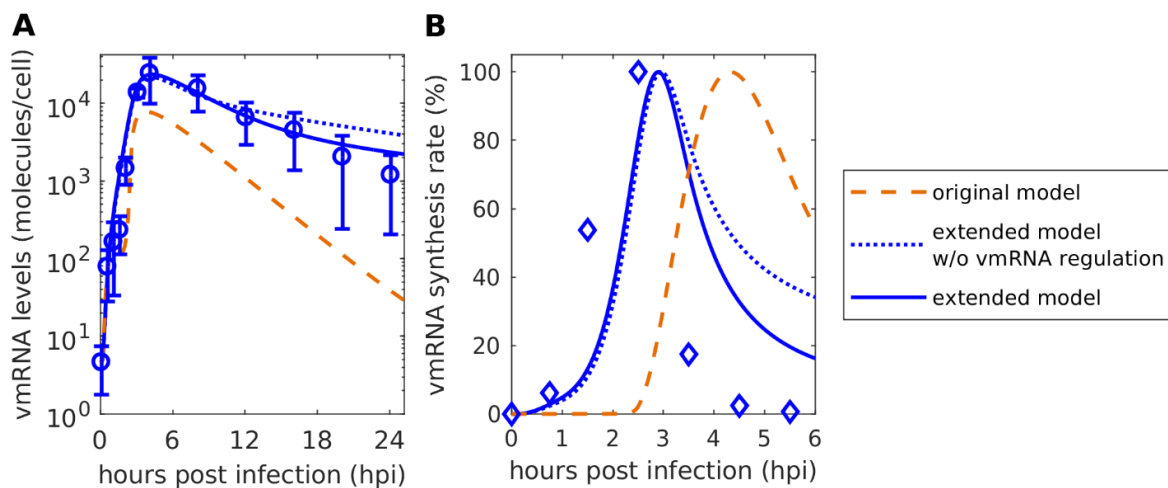
Figure 4.6.: Implementation of an inhibition of vmRNA synthesis improves description of vmRNA dynamics. (A) Model fits to genome segment 5 vmRNA measurements of MDCKadh cultures infected with influenza A/PR/8/34 (H1N1) at an MOI of 73 based on $TCID_{50}$ [64]. Error bars indicate standard deviations of three individual experiments. (B) Percentage of the vmRNA synthesis rate for different model versions, experimental data were adapted from [59]. In short, adherent BHK-21 cells were infected by IAV (Wisconsin strain) at 10 to 20 PFU per cell. Figure adapted from Rüdiger *et al.* [181].

To keep kinetics simple, we implemented an inhibition of vmRNA synthesis by free RdRp (Equation (3.1.34)). This indirect approach was employed as the inclusion of a separate state variable for Pol II without corresponding measurements for parameter estimation would have unnecessarily increased model complexity. As before, accounting for this mechanism in the extended model of STV infection improved the fit to measurements for an MOI of 73, which is affirmed by a lower sum of squared residuals and the AIC [266] (Table 4.1). Furthermore, the extended model with

inhibition of the vmRNA synthesis allowed a more precise description of vmRNA levels at time points later than 12 hpi (Figure 4.6A) and the simulated vmRNA synthesis rate showed dynamics similar to previous studies [59] (Figure 4.6B).

Table 4.1.: Evaluation of the model fits performed for the extended model of STV infection with and without inhibition of vmRNA synthesis.

	extended model w/o inhibition of vmRNA synthesis	extended model
SSR	1.96	1.88
AIC	-437.2	-440.4

SSR: sum of squared residuals (error of each variable normalized to the respective maximum measurement value); AIC: Akaike information criterion

Model calibration

The extended model of STV infection containing the adjusted dynamics for infected cell apoptosis, STV release, and inhibition of vmRNA synthesis was calibrated to published measurements from STV infections of MDCKadh cells performed at an MOI of 73 [64]. Experimental data of the intracellular level (viral RNA dynamics) and the cell population level (cell population dynamics and cumulative virus titers) were utilized. The cumulative virus titer measurements show the amount of STVs produced since the previous sampling time point, but provide no information about the degradation of virus particles. The multiscale model was fit to both data sets simultaneously.

Model simulation is in good agreement with the experimental data on both the intracellular and the cell population level (Figure 4.7). In particular, the early accumulation of vmRNA and cRNA can be captured closely. However, the extended model underestimates the level of vRNA between 3 to 8 hpi (Figure 4.7). The cell population dynamics, i.e., the fast progress of cell infection and initiation of virus-induced apoptosis, are described well. All cells are infected at 1 hpi due to the high MOI conditions and infected cells start to undergo apoptosis around 16 hpi. The model slightly overestimates the onset of STV release on the population level, but reproduces later measurements for infectious and total STV concentrations. The delay between cell infection and first virus release at MOI 73 constitutes roughly 3 h (Figure 4.5B),

indicating that the high viral load results in a fast uptake and intracellular replication of STVs.

Table 4.2.: Parameters estimated from the experimental data in Figure 4.7.

Parameter	Value	Unit	Confidence interval (95%)[a]
$F_{\mathrm{Par}}(0)$	3.4×10^{-2}	–	$(1.8 - 17.0) \times 10^{-2}$
$k_{\mathrm{T}}^{\mathrm{Apo}}$	7×10^{-3}	h^{-1}	$(1.4 - 11.4) \times 10^{-3}$
$k_{\mathrm{M1}}^{\mathrm{Bind}}$	9×10^{-7}	moluecules$^{-1} \cdot h^{-1}$	$(2.9 - 34.2) \times 10^{-7}$
$k_{\mathrm{M}}^{\mathrm{Deg}}$	0.33	h^{-1}	$0.12 - 1.35$
$k_{\mathrm{V}}^{\mathrm{Deg}}$	1.15×10^{-2}	h^{-1}	$(0.23 - 2.15) \times 10^{-2}$
k^{Fus}	0.31	h^{-1}	$0.21 - 0.40$
K_{I}	0.11	h^{-1}	$0.08 - 0.29$
k^{Lys}	9.4×10^{-3}	h^{-1}	$(1.9 - 35) \times 10^{-3}$
K_{R}	1.1×10^{7}	molecules	$(0.1 - 5.7) \times 10^{7}$ [b]
k^{Rel}	1270	virions$\cdot h^{-1}$	$917 - 2210$
$k_{\mathrm{Red}}^{\mathrm{Rel}}$	0.05	h^{-1}	$0.001 - 0.25$ [b]
$k_{\mathrm{C}}^{\mathrm{Syn}}$	0.8	h^{-1}	$0.4 - 1.7$
$k_{\mathrm{M}}^{\mathrm{Syn}}$	1.8×10^{5}	nucleotides$\cdot h^{-1}$	$(0.9 - 3.4) \times 10^{5}$
$k_{\mathrm{V}}^{\mathrm{Syn}}$	8.4	h^{-1}	$5.2 - 12.9$
$K_{\mathrm{V^{Rel}}}$	1250	virions	$92 - 4600$
τ_{Apo}	19.8	h	$16.7 - 23.7$
ν_{Apo}	0.77	h^{-1}	$0.30 - 3.82$

[a] 95% confidence intervals were determined from the $Q_{0.025}$ and $Q_{0.975}$ quantiles of 2000 bootstrap iterations [264].

[b] Estimates reached lower and upper bootstrap parameter bounds.
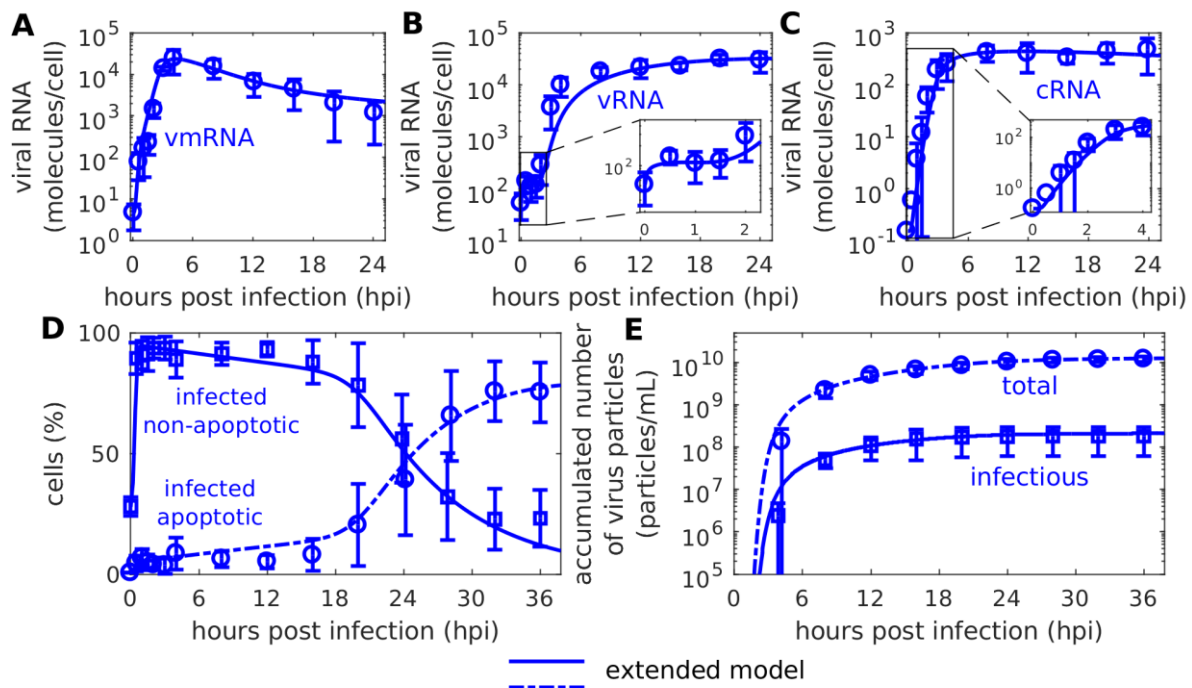
Figure 4.7.: The extended multiscale model of STV infection captures viral dynamics on the intracellular and cell population level. Curves depict the fits of the extended model of STV infection to (A-C) cell-specific viral RNAs of genome segment 5, (D) cell population and (E) virus titer measurements obtained in MDCKadh cell-culture infections with influenza A/PR/8/34 (H1N1) at an MOI of 73 based on $TCID_{50}$ [64]. Symbols represent the mean and error bars the standard deviation of three independent experiments. The extended model of STV infection includes an adjusted apoptosis rate and takes into account the fraction of infectious virions released as well as an additional mechanism for inhibition of vmRNA synthesis. Figure adapted from Rüdiger *et al.* [181].

4.1.2 Description of infection dynamics for low and medium MOI conditions

In order to investigate the predictive power of the extended model calibrated for MOI 73 measurements [64], we challenged it with virus titer measurements obtained from MDCKadh cell infections performed at MOI 10^{-4} and 3 [181].

Initial prediction for low MOI infections

First, we simulated the infection dynamics of different MOI conditions by changing the initial STV concentration on the cell population level. Unfortunately, this approach did not result in satisfying predictions (Figure 4.8, solid lines). While the total STV concentration for an infection at MOI 3 based on $TCID_{50}$ could be described (Figure 4.8B), other measurements differed significantly from model simulations in both dynamics and magnitude of STV release. Additionally, we observed clear differences in the FIVR dynamics between simulations and low MOI measurements. In experiments performed at MOI 3 and 10^{-4} (based on $TCID_{50}$), the FIVR initially shows considerably higher values (Figure 4.8A and 4.8D) than at MOI 73 (Figure 4.5A). This indicates that cells infected at lower MOIs have a significantly higher ratio of infectious to non-infectious STVs released than cells infected at a high MOI.

Consequently, to improve the model prediction, we adjusted the initial FIVR $F_{Par}(0)$ for low MOI conditions. To only introduce a single new $F_{Par}(0)$ for the low MOI conditions we tested different values and their effect on model predictions for MOI 3 and 10^{-4} based on $TCID_{50}$ (Figure 4.9). We determined an optimal value at $F_{Par}(0) = 0.26$, which provided the best description of the FIVR for both low MOI conditions (Figure 4.8A and 4.8D). As a result, the model predictions for virus release using the adjusted initial condition are in good agreement with the two experiments performed at lower MOIs (Figure 4.8). In particular, the time delay before cells start to release considerable amounts of STVs, which is heavily dependent on the MOI conditions, can be described well. Thus, by considering the influence of a critical initial condition, i.e., $F_{Par}(0)$, during influenza virus infection our model captures the viral release dynamics of both high and lower MOI infections in MDCKadh cell cultures.
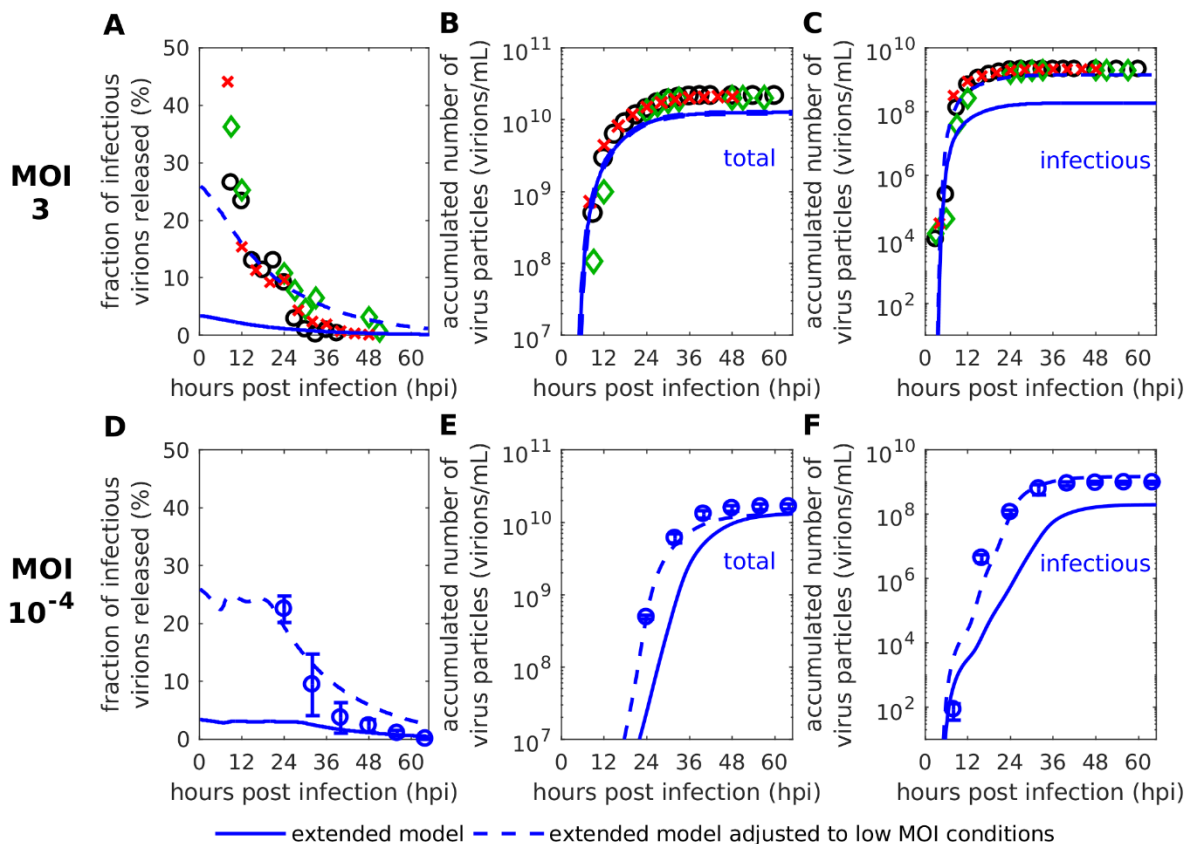
Figure 4.8.: Model predictions of viral titers in low MOI conditions. The mathematical model fitted to measurements obtained from MDCKadh cell infections at an MOI of 73 (Figure 4.7) was used to reproduce results of experiments performed at (A-C) MOI 3 and (D-F) MOI 10^{-4} based on $TCID_{50}$. Symbols represent measurements of MDCK cell infections with influenza A/PR/8/34 (H1N1) obtained from NIBSC (A-C) and RKI (D-F). (A+D) Description of the fraction of infectious virions released with different initial conditions. Model prediction for total (B+E) and infectious STVs (C+F) released. Error bars in (D-F) indicate standard deviations of three individual experiments. Solid lines depict simulations of the extended model of STV infection with initial virus concentrations adapted to the respective MOI. Dashed lines represent simulations of the extended model of STV infection with an additional change to the initial conditions to adjust for low MOI scenarios, i.e., by increasing the initial fraction of infectious virions released. Figure taken from Rüdiger *et al.* [181].
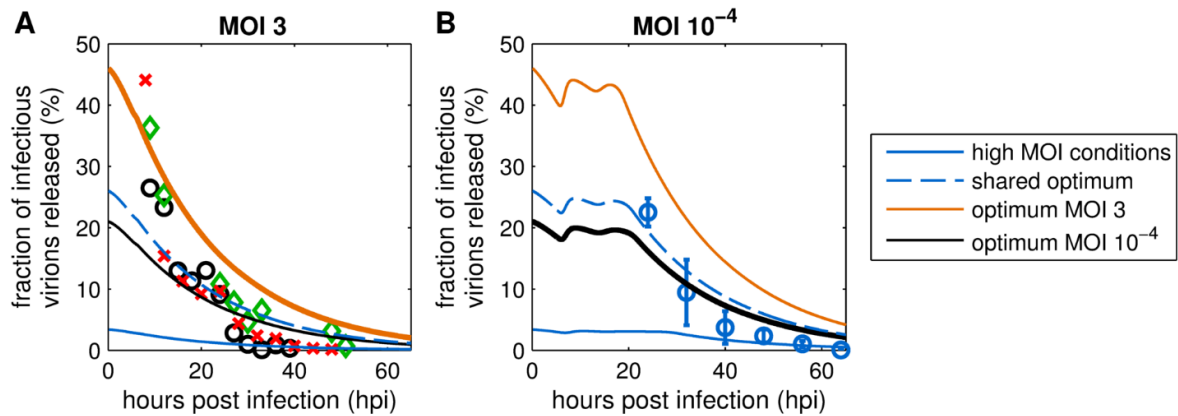
Figure 4.9.: Optimization of the initial fraction of infectious virions released in low MOI conditions. Simulation of the extended model of STV infection with an MOI of (A) 3 and (B) 10^{-4} based on TCID$_{50}$ using different initial FIVRs. Various initial FIVRs were tested for their ability to improve the model prediction for virus release dynamics in low MOI infections. Simulation results were evaluated based on their deviation to the experimental data and showed different optima at MOI 3 ($F_{\text{Par}}(0) = 0.46$) and MOI 10^{-4} ($F_{\text{Par}}(0) = 0.21$). The shared optimum ($F_{\text{Par}}(0) = 0.26$) was determined by summing up deviations of both MOI 3 and 10^{-4} to obtain the initial FIVR resulting in the lowest error. Figure taken from Rüdiger *et al.* [181].

4.1.3 Discussion

The dynamics of IAV infections can vary greatly depending on the initial MOI, which affects time scales of propagation, virus yields and the infectivity of released virions. Different scenarios, i.e., natural infections, vaccine production or antiviral treatment, are initialized at or progress to highly different MOIs. To cover these scenarios at the intracellular and cell population level, we introduced MOI-dependent apoptosis dynamics into a previously published multiscale model of IAV infection. To capture experimental data from a high MOI infection closely, we further implemented a mechanism of vmRNA regulation and differentiate between infectious and non-infectious virions. The subsequent prediction of virus titers generated in low MOI conditions was enabled by increasing the FIVR in such scenarios, which may be related to the impact of DIPs.

Description of STV infection for a wide MOI range

In contrast to the original multiscale model established by Heldt *et al.* [38], the extended model of STV infection was calibrated to measurements of intracellular and cell population dynamics from the same experiment [64]. The high MOI infection conditions used in these experiments enabled the observation of STV replication and propagation on both scales. We used these measurements for parameter estimation and the resulting model simulation showed good agreement with the experimental data (Figure 4.7). Viral RNA dynamics and the percentage of cells in different states of infection and apoptosis were captured closely. However, between 3 and 8 hpi, model simulations underestimated the level of intracellular vRNA. Previous experimental studies also identified an accumulation of vRNA in this time frame [38, 63], which cannot be fully reproduced by the current model implementation.

The three viral RNA species of IAV are highly interconnected, because vRNA serves as the template for vmRNA and cRNA replication. The underestimation of one viral RNA species indicated that an additional layer of regulation, which could support earlier vRNA accumulation without affecting the other species, might exist. Such a regulation could concern nuclear export processes of viral proteins, the depletion of precursors for viral RNA and protein synthesis impeding further replication or an increased degradation of vRNPs that enter the cytoplasm for release.

Logistic virus-induced apoptosis kinetics mediate a normal distribution of infected cell survival times

The crucial step to reproduce infection dynamics in MDCKadh cell cultures for high MOI conditions was the description of apoptotic processes. In general, apoptosis is induced in infected cells as a defense mechanism aiming to reduce progeny virion release [278]. In infected cells, viral RNA and protein synthesis progress rapidly, which leads to an accumulation of viral molecules. This is detected by the cell and, as a reaction, apoptotic processes are induced that initiate the controlled death of the cell to prevent further virus spread.

In the original model [38], the apoptosis of infected cells was described by a fixed rate (Figure 4.4C), which resulted in an exponential distribution of the survival time of infected cells. However, experimental data of infected cells and their transition to an

apoptotic state indicated a normal distribution of cell survival time (Figure 4.4A–B) [64], which was discussed previously by Holder *et al.* [277]. To accommodate these characteristics, we implemented a logistic function (Equation (3.1.9)) for the description of apoptosis induction in infected cells. Logistic functions can approximate the dynamics described by the cumulative density function of the normal distribution and are relatively simple to apply [268]. Other approximation functions exist, which can provide an even closer representation of the normal distribution. However, these functions are more complex than the logistic function and not required to describe the experimental data. This approximation of a normally distributed survival time of infected cells enabled the reproduction of the apoptosis dynamics measured in high MOI influenza A infection experiments [64]. Additionally, by utilizing a logistic function, we introduced a delay before significant amounts of cells undergo apoptosis, which was experimentally observed until 16 hpi (Figure 4.4). This delay is represented by the newly introduced parameter τ_{Apo}, which describes the time frame until apoptotic processes can be detected in an infected cell by a respective assay. Therefore, a low value for τ_{Apo} indicates that the cell can induce a fast response to the infection.

However, viruses have developed mechanisms to interfere with the host cell apoptosis to prolong virus production [278]. Thus, the parameter τ_{Apo} could also show how well a virus is adapted to the host cell. The delayed apoptosis induction described in our extended model is similar to the cell death dynamics during HIV infection described in [279]. In this study, a piecewise-defined function that includes a specific time delay was utilized to achieve an effect similar to the one resulting from the use of a logistic function in our model. Nevertheless, dynamics of influenza-induced cell death is not only highly strain-dependent [280], but also depends on the specific assay performed to monitor apoptosis. Therefore, different approaches could be required based on the respective scenario and applied assays.

Infectious and non-infectious STVs

Infected cells release infectious and non-infectious progeny STVs, which can be determined via $TCID_{50}$ and HA assay results, respectively. The ratio of released infectious STVs to the total amount of STVs released, which is described by the

introduced variable F_{Par} (Equation (3.1.47)), is a measure for the efficiency of virus replication in cell culture. The highest FIVR occurs during early infection, which is crucial to enable fast virus spreading before host defense mechanisms, i.e., apoptotic processes or the cellular immune response, may interfere. Over time, the FIVR decreases and during later stages of infection non-infectious STVs are released predominantly (Figure 4.5A). An experimental study [64] identified that during late infection (starting at around 20 hpi) the morphology of released virus particles changes, leading to more deformed or broken particles. This observation was linked to decreasing cell viability, the detachment of infected MDCKadh cells and nuclear fragmentation indicating apoptotic processes in the infected cells. In addition, cellular metabolism is affected heavily by virus replication at later stages of infection [281]. Furthermore, the FIVR differed significantly between low and high MOI cultivations. For low MOI conditions, a considerably increased FIVR was observed (Figures 4.5A, 4.8A and 4.8D). In particular, during experiments performed at an MOI of 10^{-4} based on TCID_{50}, the FIVR maintained a value above 20% until 24 hpi. This dynamics can be explained by the continuous infection of cells, which results in a constant supply of newly infected cells contributing with a high initial FIVR to the release characteristics. Overall, the differences in viral release between low and high MOI infections have a significant impact on the infectious virus titer and the propagation of infections on the cell population level (Figure 4.3). Although various factors influence the efficiency of virus replication and release, the presence of DIPs in high MOI seed virus and their accumulation over the time course of infection most likely play a key role regarding the observed disparity. Further support for a connection between the FIVR and DIP interference is provided by the correlation of DIP accumulation with the decrease of infectious STV release, which was observed in experiments performed at an MOI of 3 based on TCID_{50} [181]. However, the influence DIPs exert on the molecular level of virus replication is still not fully understood.

MOI impact on vmRNA accumulation

Another intriguing effect of different MOI conditions is their impact on vmRNA dynamics. In high MOI conditions, vmRNA accumulates rapidly (Figure 4.6A), reaches a distinct peak around 4 hpi, and declines thereafter. Various studies showed similar

findings in high MOI IAV infections in different cell lines [59, 60, 63]. In contrast, low MOI scenarios induce a considerably slower accumulation with less pronounced peaks around 8 hpi [38, 282, 283]. The fast accumulation in high MOI infections is most likely induced by the increased amount of available templates, i.e., vRNAs. The subsequent shutdown of vmRNA synthesis is mediated by the export of vRNAs from the nucleus, which occurs around 4 hpi in high MOI experiments [64].

However, the first iteration of our extended model of STV infection, which was modified by an adjusted apoptosis rate and the newly introduced FIVR, could not describe adequately the shutdown of vmRNA replication and its degradation (Figure 4.6). Model simulations showed considerable levels of remaining vmRNA transcription until late infection (Figure 4.6B). To also reproduce the drop of vmRNA levels after 4 hpi, the rate of vmRNA degradation ($k_{\mathrm{M}}^{\mathrm{Deg}} = 0.6$) was calibrated to a value twice as high as determined previously [242]. Moreover, the dynamics of vmRNA degradation was still not captured fully (Figure 4.6A). Thus, we implemented an interaction between viral and host cell mechanisms that was reported recently by Rodriguez *et al.* [65] and Martínez-Alonso *et al.* [66]. They showed that the binding of free viral RdRp to Pol II leads to the degradation of the latter, which is proposed as a method for inhibiting host gene expression. In addition, this mechanism would impede vmRNA transcription, which depends on Pol II activity, and provides an explanation for the observed shutdown. After implementation of this interaction, the extended model is in good agreement with the vmRNA dynamics during a high MOI infection (Figure 4.6A). Additionally, the vmRNA degradation rate estimated for the extended model is consistent with previous results ($k_{\mathrm{M}}^{\mathrm{Deg}} = 0.3$). These findings indicate that the RdRp-mediated degradation of Pol II not only inhibits host gene expression, but may also play a role in the downregulation of the vmRNA synthesis.

Summary

We have developed a mathematical multiscale model of STV infection in animal cell cultures that describes a wide range of infection conditions. In contrast to previous models, we explicitly considered the infection age of a cell regarding apoptotic processes and the release of infectious STVs, which enables the description of both high and low MOI scenarios relevant for basic research and vaccine production.

Models that describe wide ranges of applied MOI conditions could also benefit research on other viruses, e.g., plant viruses, in which the MOI is theorized to have an impact on virus evolution [284]. Furthermore, this model can be used to examine specific steps in the IAV life cycle in relation to the maximum virus yield or regarding measures to intervene with viral spread *in vivo* efficiently. Given available experimental data, the model could be used to describe infections in tissues and organs at the within-host scale, which show strong fluctuation in the spatiotemporal MOI. Additionally, the multiscale model presented here is well suited to predict and optimize process performance of IAV production in cell cultures and provides a solid framework for further analysis of MOI-dependent virus infections in general.

4.2 Multiscale model of STV and DIP co-infection

DIPs are virus particles with an incomplete genome that can propagate during co-infection with their corresponding STV impeding the replication of STVs in the process. The balance between STV and DIP production heavily depends on the concentrations of both virus species during initial infection. To investigate how the MOI and the MODIP affect the production of DIPs and the interference with STV replication, we developed a multiscale model of STV and DIP co-infection. In the first part of this section, we expand the multiscale model of STV infection by including DIP dynamics. Then, we augment the model to capture experimental results for a large range of MOIs and MODIPs with a single set of parameters.

4.2.1 Including DIPs in the multiscale model

Following the basic implementation of the model of STV infection covered in section 4.1, we introduced DIP-related species on the cell population level. The adjustment of the intracellular dynamics was based on Laske and Heldt *et al.* [257]. In contrast to this model, our model considers a specific DIP with a deletion on segment 1, which is referred to as DI244. An overview of the reactions considered during virus

replication and spread is depicted in Figure 4.10. Note that in this section major parts of the original publication on the multiscale model of STV and DIP co-infection were used [125].

Incorporation of DIP dynamics during virus replication and propagation

To consider DIPs on the cell population level, we introduced cells infected only by DIPs (I_{DIP}) and co-infected cells (I_{CO}) to the existing uninfected (T), STV-only infected (I_{STV}), uninfected apoptotic (T_A) and infected apoptotic cells (I_A) (Figure 4.10, Equations (3.2.1)-(3.2.7)). Cells infected only by STVs release progeny STVs and are capable to produce progeny DIPs due to *de novo* generation. As the emergence of new DIPs from STV-only infected cells is mostly relevant for continuous cultivations and plays a minor role in batch cultivations, we disregarded it when developing the multiscale model of STV and DIP co-infection focusing on infections in batch experiments. We assumed that cells infected only by DIPs and no STV are incapable to produce progeny virions, because they cannot produce the PB2 required to form the RdRp, which is critical for virus replication. Therefore, all intracellular processes for DIP-only infected cells, including virus entry, replication and release, were neglected for initial model development. Co-infected cells release both progeny STVs and DIPs. In accordance with the description of STV-only infected cells (Equation (3.2.3), co-infected cells were represented as an age-segregated population $I_{CO}(t,\tau)$ (Equation (3.2.4)). Additionally, DIPs themselves (D) as well as their different binding and endocytosis states, i.e., attached DIPs (D_n^{Att}) and DIPs in endosomes (D^{En}), were implemented analogous to STV particles (Equations (3.2.16)–(3.2.20) and (3.2.24)–(3.2.29)).

The model of the intracellular level was adjusted to consider a separate replication for each genome segment according to Laske and Heldt *et al.* [257]. Therefore, state variables of cRNA- and vRNA-related components were described individually for the eight FL segments and DI segment 1. Additionally, we adapted the model structure slightly in accordance with specific assumptions used in the multiscale model of STV infection (Equations (3.1.1)–(3.1.47)). To that end, we modified the STV and DIP
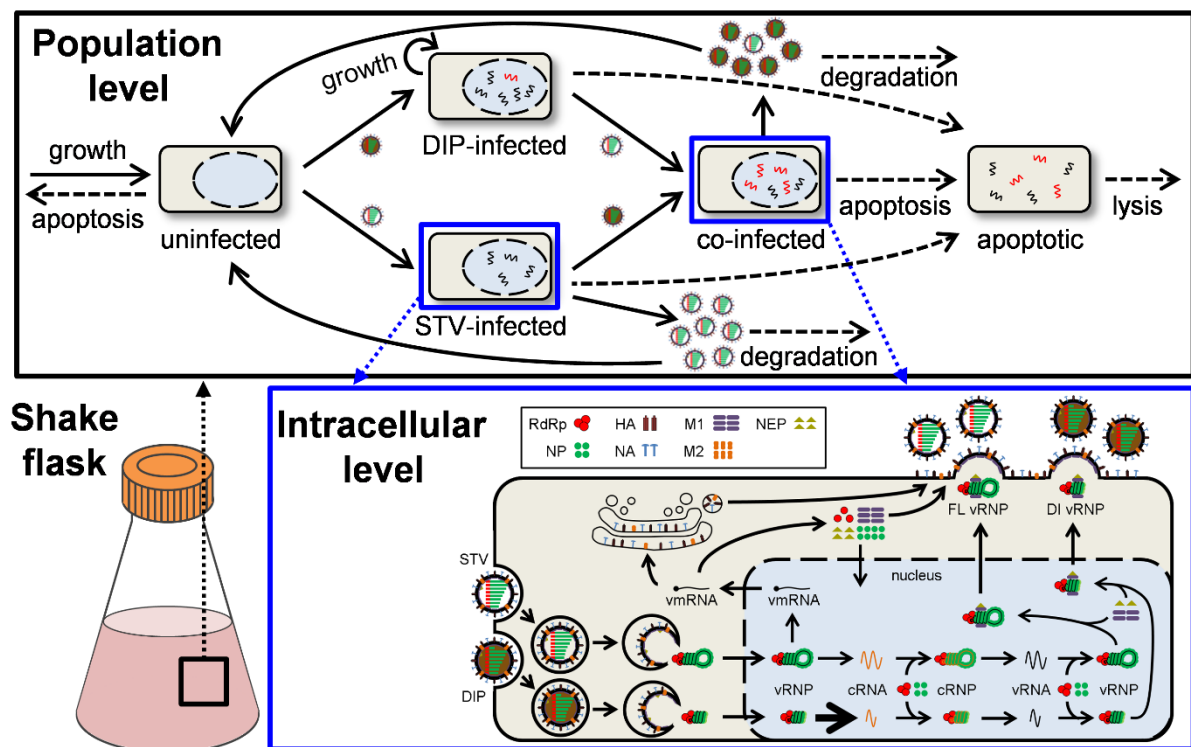
Figure 4.10.: Schematic depiction of the multiscale STV and DIP co-infection model. (Top) The population level of infection describes growth and apoptosis of uninfected cells, their infection by either STVs or DIPs, the growth and apoptosis of DIP-only infected cells, the co-infection of STV-only infected and DIP-only infected cells, virus-induced apoptosis of STV-only and co-infected cells, and the lysis of apoptotic cells. STVs are released from STV-only infected and co-infected cells, DIPs are only released from co-infected cells and both are cleared via virus degradation. (Bottom) Virus entry, nuclear import, viral RNA and protein synthesis, nuclear export and progeny virion release in STV-only infected and co-infected cells is simulated using the same intracellular model. Figure adapted from Rüdiger and Pelz *et al.* [125].

release kinetics by implementing a maximum release rate of infected cells (Equations (3.2.48)-(3.2.51)).

The model of the intracellular level was adjusted to consider a separate replication for each genome segment according to Laske and Heldt *et al.* [257]. Therefore, state variables of cRNA- and vRNA-related components were described individually for the eight FL segments and DI segment 1. Additionally, we adapted the model structure slightly in accordance with specific assumptions used in the multiscale model of STV

infection (Equations (3.1.1)–(3.1.47)). To that end, we modified the STV and DIP release kinetics by implementing a maximum release rate of infected cells (Equations (3.2.48)-(3.2.51)).

Changes to the general simulation approach

The FIVR (F_{Par}) by infected cells was crucial in the development of the multiscale model of STV infection as it determined how rapidly an infection can spread when low MOI concentrations are used [181]. For the purpose of predicting virus titers for different MOI conditions, the FIVR had to be adjusted for application as it showed a reduced value for high MOI ($F_{\mathrm{Par}} = 0.034$) compared to low MOI scenarios ($F_{\mathrm{Par}} = 0.26$). As mentioned in section 4.1, this variation was likely induced due to the impact of DIPs, which affect STV replication more strongly in high MOI conditions. For the development of our model of STV and DIP co-infection, we employed a single value for the FIVR as the interference of DIPs was implemented in the model itself.

To take into account the specific impact of the MOI and MODIP conditions as well as their dynamics over time, we adapted our simulation approach to re-evaluate the initial conditions for newly infected cells based on the current concentration of STVs and DIPs in the cell culture. While this increases computational burden, it considers the dynamic changes of MOI and MODIP during infection.

Model calibration

The experimental data used for the calibration of the multiscale model of STV and DIP co-infection were obtained from infections of MDCKsus cells with a seed virus adapted specifically to these cells [125]. The resulting infections showed significantly faster dynamics compared to the measurements from MDCKadh cell infections used for the development of the multiscale model of STV infection [64]. Therefore, a re-evaluation of various process parameters that may have been affected by this change was required. Additionally, the co-infection model was adapted to utilize infectious STV titer measurements obtained via plaque assay (PFU/mL) instead of the previously used TCID$_{50}$ assay [107] that typically results in slightly higher titers.
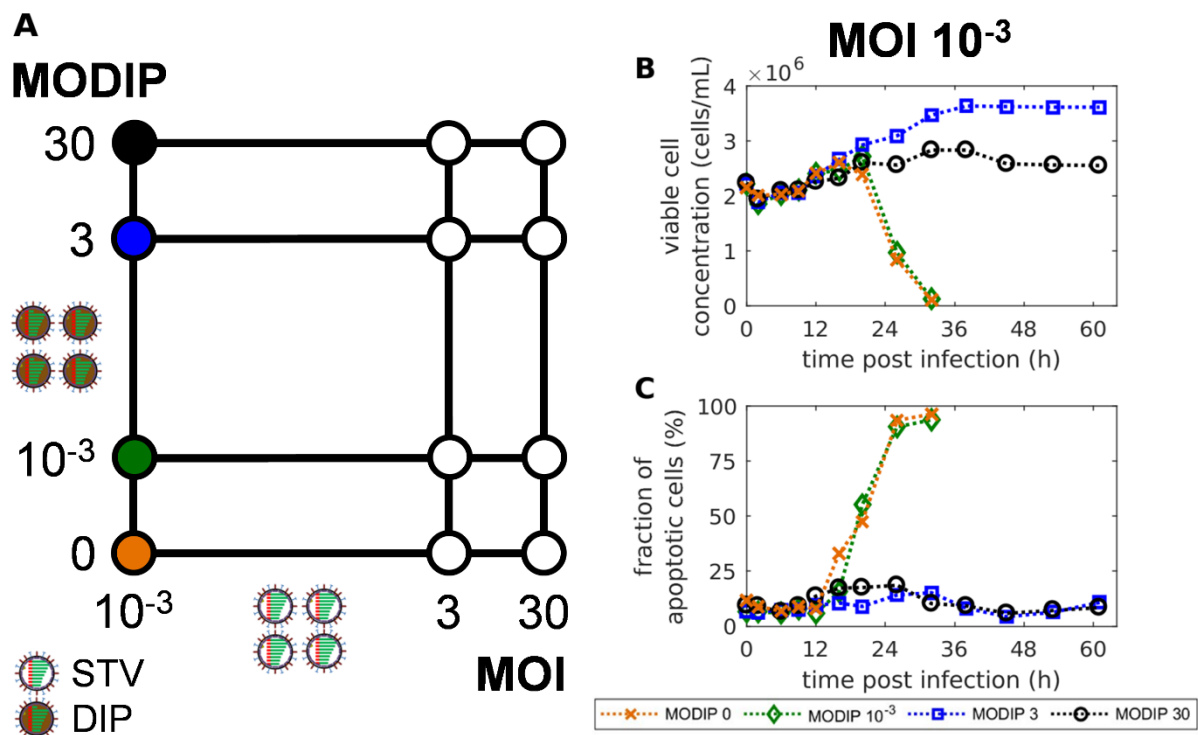
Figure 4.11.: Addition of DIPs can prevent virus-induced apoptosis and protect MDCKsus cells from STV infection. (A) Schematic depiction of the 12 different MOI and MODIP conditions used for infection experiments. (B) Viable cell concentration and (C) the fraction of apoptotic cells for infections with MOI 10^{-3} and MODIPs of 0, 10^{-3}, 3 and 30. Figure taken from Rüdiger and Pelz *et al.* [125].

The basic model of STV and DIP co-infection was calibrated to the intracellular and cell population data obtained from MDCKsus cell infections using 12 different infection conditions (Figures 4.10 and 4.11) performed in [125]. Measurements from the intra- and extracellular level were utilized simultaneously for parameter estimation.

For the majority of fitted conditions, model simulations capture the general dynamics of the observed infection dynamics (Figure 4.12). In particular, FL vmRNA and DI vRNA are represented well. Additionally, the prevention of virus replication and a strong reduction of STV titers for a low MOI of 10^{-3} combined with high MODIPs of 3 and 30 can be achieved (Figure 4.12C and 4.12L). These two infection conditions will from here on be referred to as L3 (MOI 10^{-3} + MODIP 3) and L30 (MOI 10^{-3} + MODIP 30). However, in other infection conditions, model simulations show large
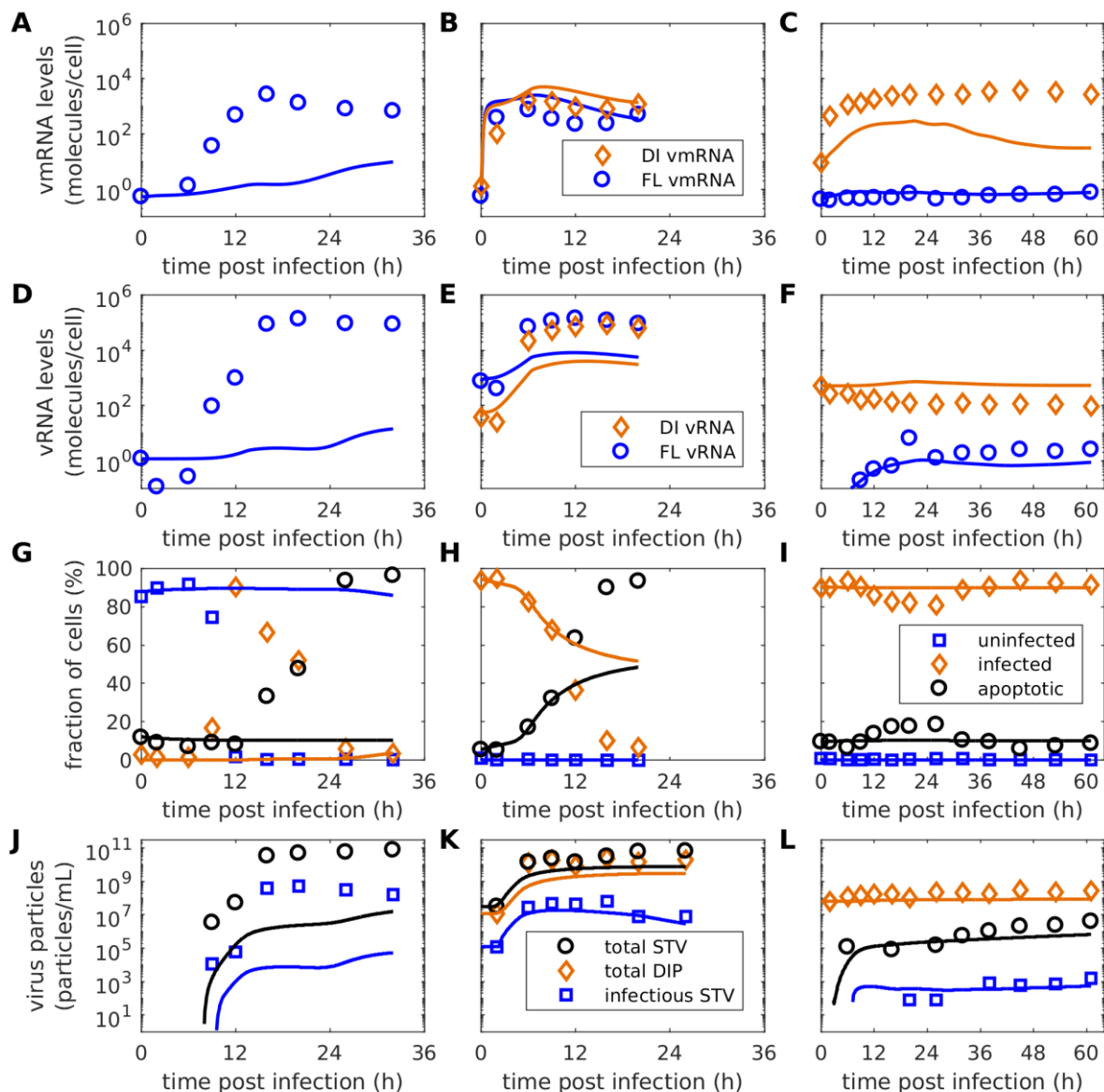
Figure 4.12.: The basic co-infection model fails to describe virus replication and propagation dynamics for all infection conditions. Curves represent model simulations of the basic co-infection model calibrated to (A-C) cell-specific vmRNA, (D-F) cell-specific vRNA, (G-I) cell population and (J-L) virus titer data measured in MDCKsus cell cultures infected with different amounts of influenza A/PR/8/34 (H1N1) and DIPs (DI244). Results from MOIs and MODIPs of 10^{-3} and 0 (first column), 30 and 3 (second column), 10^{-3} and 30 (third column) are shown. The basic model describes STV and DIP replication and propagation based on Rüdiger *et al.* [181] and Laske and Heldt *et al.* [257] without considering additional model adaptations. Figure adapted from Rüdiger and Pelz *et al.* [125].

deviations to the measured values. The exact levels of intracellular and population measurements cannot be captured for the majority of experiments. Especially in low MOI conditions, large deviations for the observed intracellular properties are apparent (Figure 4.12A,D,G,J). In comparison, measurements from experiments using higher MOIs are described more closely, but still do not allow for a complete representation of the infection process. Therefore, we were not able to obtain a single set of parameters describing all measured dynamics simultaneously. Most likely, this is due to the inherent complexity of the interaction of STVs and DIPs during infection. In sum, we established a mathematical multiscale model of STV and DIP co-infection by taking into account DIP replication and spreading on the intracellular and cell population level, respectively, to describe the infection dynamics observed in infection experiments (Figure 4.11). However, estimating a single set of parameters that describes all infection conditions could not be achieved with this basic model.

4.2.2 Capturing various MOI and MODIP conditions using a single set of parameters

To address the observed discrepancies between the basic model of STV and DIP co-infection and the dynamics observed during infections of animal cell cultures with different MOIs and MODIPs, we implemented several targeted changes to the model equations.

Segment-specific vmRNA transcription

First, we addressed the discrepancies observed between the levels of the vmRNAs of FL segment 1, DI segment 1 and FL segment 5 (Figure 4.13A). Although the overall dynamics of vmRNA accumulation could be captured, the levels of FL and DI segment 1 vmRNA were overestimated, while the levels of FL segment 5 vmRNA were underestimated. As described in section 2.1.3, segments encoding for proteins of RdRp, i.e., segment 1 to 3, were shown to accumulate to significantly lower levels than segments 4 to 8 [60, 61, 126]. Therefore, we decided to implement this effect by a simple parameter f_{M} that reduces vmRNA transcription in polymerase segments

including DI segment 1 (Equation (3.2.44)). This clearly improved the description of the experimental data compared to the basic model and enabled the representation of the different levels of accumulated vmRNA (Figures 4.13B and B.4–B.6).
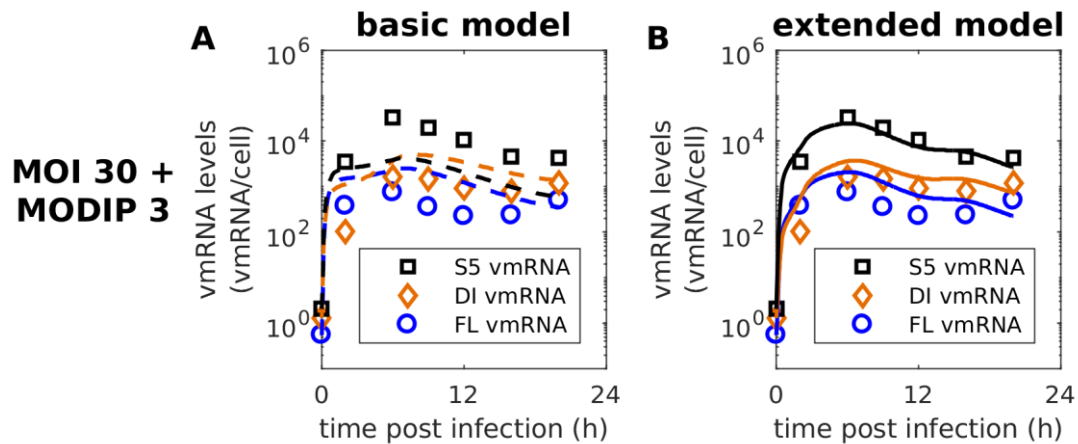
Figure 4.13.: Segment-specific vmRNA transcription enables close description of the differences between accumulation and degradation dynamics. Dynamics of vmRNA for segment 5, FL segment 1 and DI segment 1 using MOI 30 and MODIP 3. Dashed lines show model simulations of the basic co-infection model fitted to experimental data, solid lines depict simulations of the extended co-infection model calibrated to the same measurements. Figure adapted from Rüdiger and Pelz *et al.* [125].

Primary vmRNA transcription in DIP-only infected cells

Another significant deviation between the simulation of the basic model and the experimental data could be observed for the levels of DI segment 1 and FL segment 5 vmRNA for low MOI, high MODIP conditions L3 and L30 (Figure 4.11B). In these scenarios, DI segment 1 and FL segment 5 vmRNAs still accumulated to considerable numbers, although nearly all infected cells should have been infected with a DIP but no STV as a helper virus. We assumed initially that cells just infected by DIPs do not produce any viral RNAs. Yet, previous IAV infection studies showed that the "primary transcription" of vmRNAs by incoming parental vRNAs leads to significant intracellular vmRNA levels [62, 271, 272].

To implement this hypothesis, we used a modified version of the intracellular equation describing vmRNA kinetics (Equation (3.2.43)) for DIP-only infected cells. In this simplified equation (Equation (3.2.45)), the negative feedback induced by RdRp is removed, because cells infected only by DI244 cannot synthesize functional PB2, which is essential for RdRp formation. Furthermore, the primary transcription now depends on the raw input of vRNP templates per cell from the initial infection. Using this simple description, we can describe the level of vmRNA accumulation in L30 closely (Figures 4.14B and B.4–B.6). For L3, the combination of primary transcription and the regular vmRNA generation in co-infected cells also describes the initial plateau and the subsequent increase.
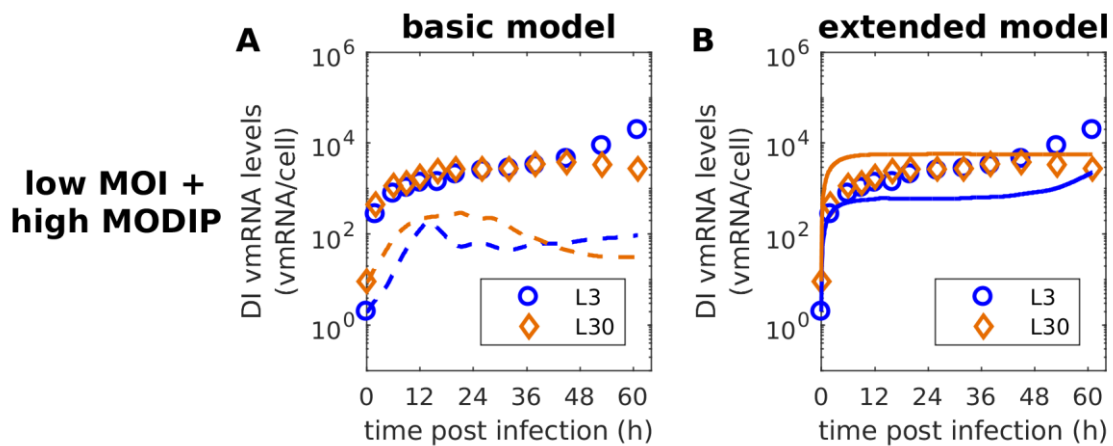
Figure 4.14.: Primary transcription enables representation of vmRNA accumulation in low MOI, high MODIP conditions. Accumulation of viral DI vmRNA for conditions L3 (MOI 10^{-3} and MODIP 3) and L30 (MOI 10^{-3} and MODIP 30). Dashed lines show model simulations of the basic co-infection model fitted to experimental data, solid lines depict simulations of the extended co-infection model calibrated to the same measurements. Figure adapted from Rüdiger and Pelz *et al.* [125].

Reduction of vRNA synthesis in high MODIP conditions

Then, we focused on the vRNA dynamics, which were not represented completely (Figure 4.12). To that end, we fixed every model parameter except k_V^{Syn}, which describes the rate of vRNA synthesis, and calibrated the model to the experimental data. Thus, we identified that k_V^{Syn} was estimated to very similar values for low initial

DIP concentrations, i.e., MODIP 0 and 10^{-3}, but showed a clear reduction when MODIP 3 and 30 were used for infection (Figure 4.15). Specifically, we observed a direct relation of the parameter value to the applied ratio of MODIP to MOI. Consequently, we introduced a dependency of the parameter k_V^{Syn} on the used MODIP-to-MOI ratio during infection (Equation (3.2.38)). Fortunately, this modification to the model did not only enable the description of STV and DIP co-infection for all conditions using a single set of parameters, but also improved the description of the experimental data considerably (Figures B.2–B.9).
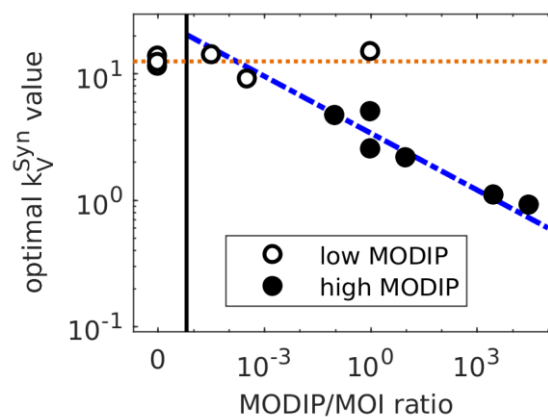
Figure 4.15.: MODIP-to-MOI ratio-dependent vRNA synthesis rate. Estimated values for the parameter k_V^{Syn} describing vRNA synthesis for different infection scenarios based on the applied MODIP-to-MOI ratio. The orange dotted line depicts the average k_V^{Syn} value for low MODIP infections (empty circles) and the blue dash-dotted line represents the dependency of k_V^{Syn} on the MODIP-to-MOI ratio for high MODIP conditions (full circles). The vertical black line separates infections only using STVs from infections with MODIP > 0. Figure adapted from Rüdiger and Pelz *et al.* [125].

Effect of high MOI conditions on cell growth

Additionally, we considered that the cell growth observed for low MOI, high MODIP conditions L3 and L30 was reduced with a higher MODIP (Figure 4.11B). Therefore, we introduced a factor f_μ that lowers the specific cell growth rate during infection

depending on the initial DIP concentration (Equation (3.2.9)). While the fraction of apoptotic cells did not increase when infected with a large quantity of DIPs (Figure 4.11C), they nevertheless showed an impaired cell growth. By using this additional factor, we were able to describe the differing growth dynamics for conditions L3 and L30 (Figure 4.16).
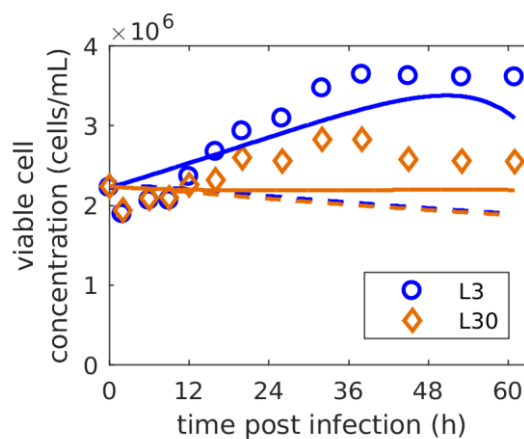
Figure 4.16.: Reduction of the specific cell growth rate for very high MODIP conditions. Dynamics of the viable cell concentration for low MOI, high MODIP conditions L3 and L30. Dashed lines show model simulations of the basic co-infection model fitted to experimental data, solid lines depict simulations of the extended co-infection model calibrated to the same measurements. Figure adapted from Rüdiger and Pelz *et al.* [125].

Final model calibration

Finally, the extended model of STV and DIP co-infection was fitted to measurements from all 12 different combinations of MOI and MODIP conditions (Table 4.3). Experimental data of infected MDCKsus cells from the intracellular and cell population level were utilized simultaneously for model calibration. Model simulations capture experimental data on the intracellular and cell population level closely (Figures 4.17 and B.2–B.9). In contrast to the basic co-infection model, low and high MOI scenarios can be described using a single set of parameters. Furthermore, the effects of STV suppression for low MOI, high MODIP conditions L3 and L30 can be reproduced well (Figure 4.17L).
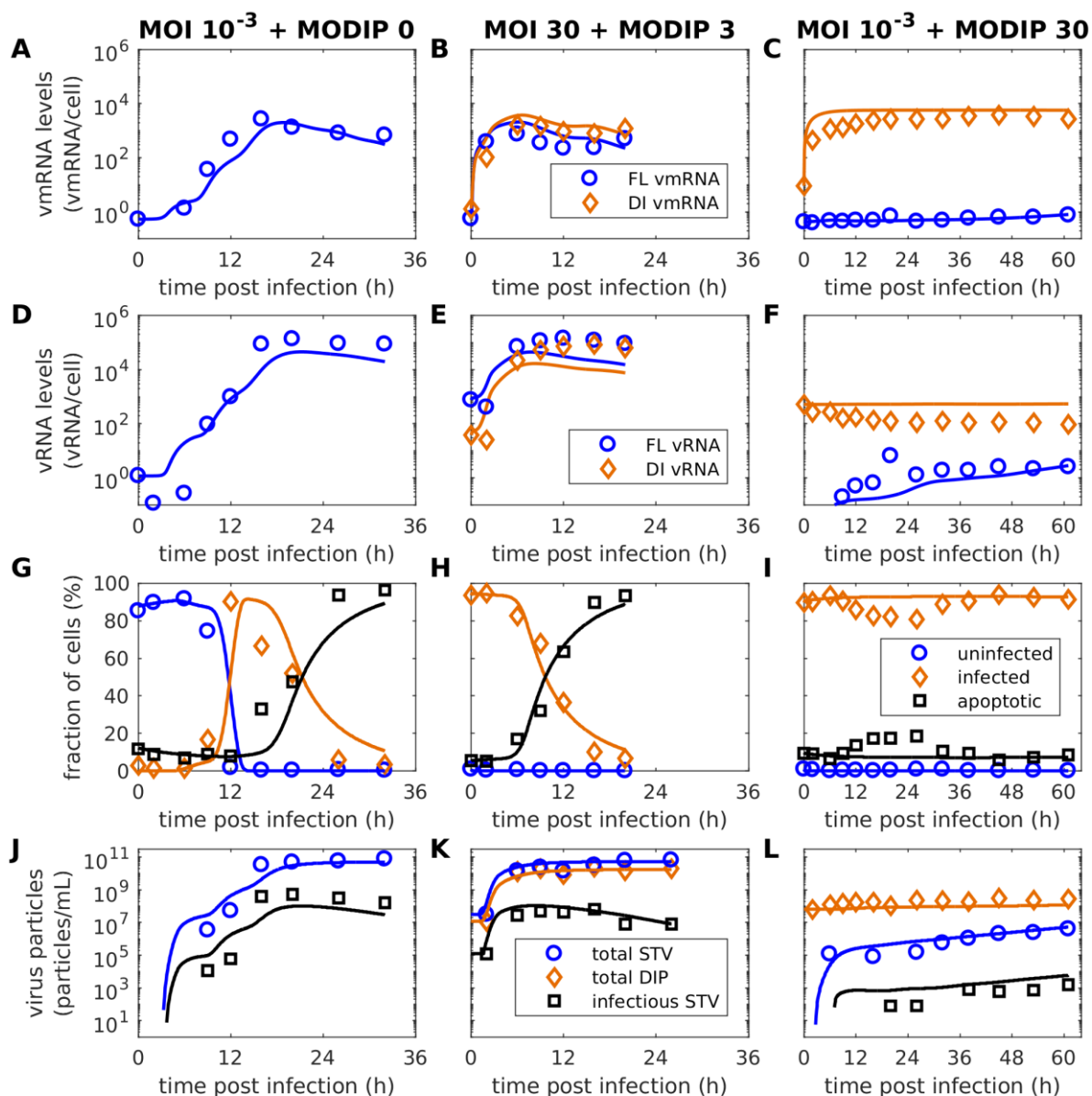
Figure 4.17.: The extended co-infection model captures infection dynamics on the intracellular and cell population level for all measured infection conditions. Curves depict simulations of the extended co-infection model fitted to (A-C) cell-specific vmRNA, (D-F) cell-specific vRNA, (G-I) cell population and (J-L) extracellular virus titers measured in MDCKsus cell cultures infected with different amounts of influenza A/PR/8/34 (H1N1) and defective interfering particles (DI244). Results for MOI 10^{-3} and MODIP 0 (first column), 30 and 3 (second column), and 10^{-3} and 30 (third column) are shown. The figures presenting cell population dynamics (G-I) show fits to uninfected non-apoptotic, infected non-apoptotic, as well as the sum of uninfected and infected apoptotic cells. The extended co-infection model is based on

Rüdiger *et al.* [181] and Laske and Heldt *et al.* [257], but additionally considers primary transcription of vmRNA, segment-specific vmRNA production, a reduced vRNA synthesis for high MODIP conditions and a DIP-induced reduction of cell growth. Simulation results for all other infection conditions are shown in Figures B.2–B.9. Figure adapted from Rüdiger and Pelz *et al.* [125].

On the intracellular level, the balance between vRNA and vmRNA can be captured for the majority of infection conditions. However, in a few scenarios DI vmRNA is overestimated, i.e., when an MOI of 3 is applied (Figure B.5E-H), and vRNA levels are slightly underestimated (Figures B.7–B.9). On the extracellular level, viral titers and cell population dynamics are captured well for all conditions (Figures B.2 and B.3). The infection of uninfected cells, virus-induced apoptosis dynamics and the protection of cells in L3 and L30 are described closely. Additionally, the proportion of infectious and total STV as well as total DIP titers are captured in all scenarios. However, the levels of infectious STV and total DIP concentration in the supernatant is underestimated when using a very low MOI and MODIP (Figure B.2A–B).

The extended co-infection model comprises 132 ODEs and 73 parameters (basic co-infection model: 130 ODEs, 68 parameters). For 8 out of 12 experiments fitted, the extended co-infection model showed lower values for the AIC (Table B.4) and is, therefore, preferable [266]. This applies, in particular, for MOI 10^{-3} combined with a low MODIP, where the experimental data could not be described using the basic model (Figure 4.12). Furthermore, for high MOI combined with high MODIP conditions the data is fitted better by the extended co-infection model. Overall, while the basic co-infection model displays a certain advantage to describe some infection conditions, the extended co-infection model is able to capture all conditions simultaneously.

Table 4.3.: Parameters estimated from the experimental data in Figures B.2–B.9.

Parameter	Value	Unit	Confidence interval (95%)[a]
$F_{Par}(0)$	3.6×10^{-3}	–	$(0.3 - 48.9) \times 10^{-3}$
F_{Adv}	0.32	–	$0.07 - 0.84$
F_M	0.12	–	$0.006 - 0.53$
F_μ	0.63	–	$0.2 - 1$
k_T^{Apo}	1.18×10^{-2}	h^{-1}	$(0.1 - 1.3) \times 10^{-2}$
k^{Fus}	58.3	h^{-1}	$9.5 - 258.8$
K_I	0.27	h^{-1}	$0.05 - 0.35$
k^{Lys}	0.16	h^{-1}	$0.02 - 0.5$
K_R	7.8×10^3	molecules	$(1.1 - 30.9) \times 10^3$
k_{Red}^{Rel}	4.1×10^{-4}	h^{-1}	$(0.7 - 16.1) \times 10^{-4}$
k^{Rel}	6.15×10^3	virions · h^{-1}	$(0.9 - 19.3) \times 10^3$
K_V	20.1	h^{-1}	$4.7 - 78.5$
$K_{V^{Rel}}$	1.8	virions	$0.3 - 6.8$
τ_{Apo}	6.65	h	$5.0 - 18.0$
v_1	5.2	–	$2.0 - 47.7$
v_2	0.1	–	$0.002 - 0.23$ [b]

[a] 95% confidence intervals were obtained from the Q0.025 and Q0.975 quantiles of 1250 bootstrap iterations [264].

[b] Estimates reached lower bootstrap parameter bounds.

4.2.3 Discussion

IAV infection is a highly complex process that shows different dynamics depending on the initially applied virus concentrations. The addition of DIPs further increases the complexity of these processes making a description of the overall infection dynamics challenging. For the development of our multiscale model of STV and DIP co-infection, we introduced DIP related populations to the model. For the estimation of model parameters, we used data from 12 experiments performed using different infection conditions for infecting animal cell cultures. Based on these data, we were able to calibrate the model to describe all observed dynamics using a single set of parameters.

Development of the initial model of co-infection

The experiments performed at different initial MOI and MODIP conditions showed diverse infection dynamics. By expanding the multiscale model of STV infection, we aimed to capture these dynamics considering the impact of DIPs. However, this first attempt did not allow describing the dynamics in all observed conditions. While some scenarios could be reproduced closely, for others the infection progress could not be represented. The structure of the initially developed model of co-infection was capable to describe each individual scenario if the model parameters were calibrated solely to the corresponding experimental data. However, to obtain a single set of parameters capable of reproducing the full range of experimental results, some modifications were necessary.

This inability to find a parameter set that describes all experimental data simultaneously was likely due to underlying dependencies inherent to the system described. These could only be observed by covering such a wide range of infection conditions with the experiments, but required an extension of the model. While most observed properties develop linearly when increasing the input of STVs or DIPs, some infection conditions induce divergent behavior of specific properties. An example are the DI vRNA levels, which show a direct relation neither to the MOI nor to the MODIP [125]. However, they seem to increase towards equimolar levels of STVs and DIPs. Additionally, vmRNA levels of the observed segments, i.e., FL segment 1, DI segment 1 and FL segment 5, achieve similar values in simulations performed with the initial model implementation. In contrast, the experimental data show significant differences between the three observed vmRNAs [125].

Model extension

To enable the description of the dynamics of STV and DIP co-infection dynamics in a wide range of MOI and MODIP conditions using a single set of parameters, we extended the initially developed basic model. Therefore, various steps of viral RNA regulation and the growth of cells in high MODIP conditions were modified.

Specifically, we introduced an internal regulation between vmRNA segments, i.e., a lower transcription rate for segments encoding for RdRp-related proteins compared to structural proteins, as observed in previous IAV replication studies [60, 61, 126].

Interestingly, for infection conditions using equimolar amounts of STVs and DIPs, the DI segment 1 vmRNA levels are exactly in between FL segment 1 and 5 vmRNA levels (Figure 4.13B). This indicates that due to the replication advantage of DIPs their vmRNA levels can exceed their STV counterpart. Nevertheless, they do not reach the levels of segment 5 and potentially other segments.

Furthermore, co-infection experiments showed that cells infected only by DIPs are able to produce high concentrations of vmRNA for scenarios with very few co-infections, i.e., low MOI conditions [125]. A baseline level of vmRNA for DI segment 1 and FL segment 5 was detected, which correlates with a primary transcription mediated only by the infecting DIP. However, since FL segment 1 vmRNA encoding for a subunit of RdRp is defective (DI244), the replication of vRNA and with that the amplification of the viral genome did not occur. A highly interesting aspect in this regard is, if cells are capable to perform vRNA replication in case that they are solely infected by DIPs with deletions in segments not encoding for RdRp. In a recent study, Phan *et al*. [126] investigated the levels of viral RNAs during infection for two different defective influenza viruses in A549 cells. One of them was lacking FL segment 2, which encodes for a subunit of RdRp, and showed an accumulation of vmRNA but no replication of vRNA similar to the experimental results for condition L30. An infection with the second virus, which was lacking FL segment 4 encoding for the structural protein hemagglutinin, resulted in vRNA and vmRNA levels similar to a wild-type infection. This indicates that the *de novo* synthesis of RdRp is critical for virus replication, while the genome-bound RdRp provided by virions entering during initial infection is sufficient for vmRNA transcription.

The extended co-infection model was calibrated simultaneously to measurements on the intracellular and cell population level and was able to capture the observed dynamics closely (Figures B.2–B.9). An important factor to capture all infection dynamics was the introduction of an MODIP-to-MOI ratio-dependent rate of vRNA synthesis resulting in a reduction of vRNA levels in the presence of high DIP concentrations. Experimental data clearly demonstrated that higher MODIPs lead to a reduction of vRNA levels (Figures B.7 and B.9). This interaction could describe a "self-interference" that has been reported previously [136, 258] and was also predicted by mathematical modeling [257]. Specifically, due to high DIP levels, the viral replication

is restricted and, thus, the amplification of both STVs and DIPs is affected. However, the exact mechanism of this effect and which factors could support such a reduction cannot be clarified using a mathematical model. Our hypothesis regarding the underlying interactions is that virus replication is limited due to a strong competition for viral proteins caused by high DIP concentrations. If DI genomes occupy most RdRp, the transcription of FL vmRNA could be reduced significantly and fewer functional viral proteins would be synthesized. This would ultimately lead to a reduction of viral replication for both STVs and DIPs. To elucidate such interdependencies, further experiments focusing on the effect of high DIP levels on viral RNA replication are required.

***De novo* generation and expansion towards continuous cultivation**

For the development of the model of co-infection and the description of the experimental data, we disregarded the *de novo* generation of DIPs. In the experiments used for model calibration, no progeny DIP production was detected for initial MODIPs of 0. When using higher MODIPs, the measured DIP titers are most likely related to the initially provided DIPs and not to substantial *de novo* generation. Therefore, the description of this process was neglected.

The effects of DIP *de novo* generation are more prominent when using a different cultivation system, i.e., a continuous process with a constant supply of uninfected cells [183, 184]. Over time, DIPs generated *de novo* can accumulate and affect vaccine production. The multiscale model of co-infection can also be applied to the continuous cultivation of cell cultures subject to IAV infection. To that end, the *de novo* generation of DIPs could be easily implemented. This process would be introduced as an additional output of STV-only infected cells and could be adjusted to a theoretical or experimentally determined rate. Furthermore, the constant addition of fresh uninfected cells and the removal of bioreactor contents could be implemented in the model. After introducing these changes, the co-infection model developed in this thesis could also provide a solid framework for the simulation of infection dynamics for continuous processes in vaccine production.

Interferon response

The multiscale model of co-infection presented in this section describes the interference of DIPs with the replication of the STV in MDCKsus cells. However, the innate immune response induced by DIPs was shown to play a major role for their therapeutic effect [152] initiating antiviral activity against influenza B virus [142], pneumovirus [143] and SARS-CoV-2 [144]. In particular, DIPs could also improve the defense against STVs by other means than interfering during viral replication. To evaluate such effects, a different biological system than the MDCKsus cells used to generate experimental results for the calibration of the co-infection model should be used. While MDCK cells generally show a strong IFN response following STV infection, the subsequently produced myxovirus resistance protein 1 shows a lack of activity against the human IAV due to its canine origin [285]. Moreover, it was reported that the added trypsin, which is necessary for the cleavage of hemagglutinin, leads to a proteolytic degradation of IFN [286]. Thus, MDCK cells provide a powerful platform to observe IAV infection dynamics, but are not suited to evaluate the complete virus-induced immune response.

Summary

The multiscale co-infection model developed combines STV infection with DIP replication at the intracellular and cell population level. This enabled the estimation of model parameters related to general IAV infection and DIP interference. Additionally, this allowed the reproduction of infection dynamics in highly different MOI and MODIP scenarios. The multiscale model of STV and DIP co-infection provides a solid foundation to describe the impact of DIPs in infections with viruses in general and to evaluate their potential for antiviral therapy. Such a mechanistic model could also be implemented into models describing between-host kinetics to predict how DIPs affect the epidemic scale of virus propagation. To that end, the inclusion of an immune response, especially the activation of the IFN system, is required.

4.3 Model prediction

Following the development and calibration of the two multiscale models described in the previous two sections, we utilized them to predict specific aspects of infection. To enable robust predictions via model simulations, we focused on obtaining a single set of parameters for each model that was capable of capturing a wide range of infection conditions. Using these models, we predicted the dynamics of MOI and MODIP during infection as well as how cells are infected over time. Additionally, we provide estimations for required MODIP-to-MOI ratios for DIP production and antiviral application of DIPs.

4.3.1 STV infection in highly different MOI conditions

Prediction of the changes to the MOI during infection

In section 4.1, we presented and discussed the multiscale model of STV infection, which could reproduce infectious and total STV titers in three different infection conditions. In addition to viral titers, the model is able to predict various processes on the intracellular and cell population level during the STV infection of cell cultures in different MOI conditions. As an example, we simulated the fraction of cells infected and the ratio of infectious STV to non-infected cells (the effective MOI) over the time course of virus infection at MOIs of 73, 3 and 10^{-4} (Figure 4.18). The effective MOI can change considerably over the progress of infection and determines how many virions enter a cell at a specific time point influencing virus replication and release. For MOI 73, cells are infected rapidly until 1 hpi and the effective MOI increases instantly. Simulations with an MOI of 3 result in a slower progress of infection that shows two peaks indicating a second infection wave starting around 4 hpi. Here, the effective MOI stays constant up to 4 hpi and then increases until all cells are infected. Overall, most cells in infections performed at initial MOIs of 73 and 3 are infected at similar effective MOIs.
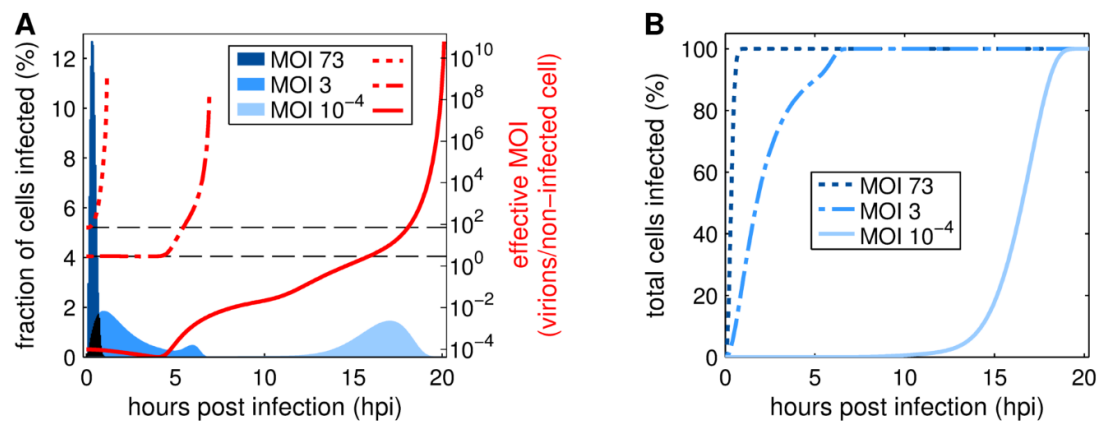
Figure 4.18.: Progress of cell infection and the effective MOI over the time course of IAV infection. Cell culture infections were simulated with initial MOIs of 73, 3 and 10^{-4} based on $TCID_{50}$. (A) Bars depict the amount of cells newly infected in the respective time frame (1 bar = 0.05 h). Dotted, dash-dotted and solid lines represent the current effective MOI based on the number of infectious virus particles and the remaining non-infected cells in the culture. The horizontal dashed lines highlight effective MOIs of 3 and 73. (B) Curves show the cumulative frequency of cell infections for simulations performed at MOI 73, 3 and 10^{-4}. Figure taken from Rüdiger *et al.* [181].

The simulation of an infection performed at an initial MOI of 10^{-4} shows very different results. The infection progress is delayed considerably and the model prediction suggests that most cell infections occur not before 15 hpi. Additionally, the effective MOI decreases until 4 hpi and only then starts to increase gradually. The effective MOI rises in multiple steps showing larger increases around 4, 11 and 17 hpi. This strong variation of the effective MOI during the process induces very different infection scenarios for cells infected at different time points. Additionally, the majority of cell infections, i.e., around 66%, occur at an effective MOI of 3 or higher, despite the low initial MOI.

Amount and origins of infecting virus particles

We can further employ the model of STV infection to predict the timing and proportion of single- and multiple-hit infections in different scenarios (Figure 4.19). Depending on the effective MOI at the current time, different amounts of virus particles can infect cells in the same time window. This is relevant for specific infection events, e.g., the

interference of DIPs during infection or the reassortment of different IAV species during a co-infection. Even a ratio of 1:1 for STV and DIP or two different IAV species would not affect the cells if only single-hit infections occur and co-infections are prevented.
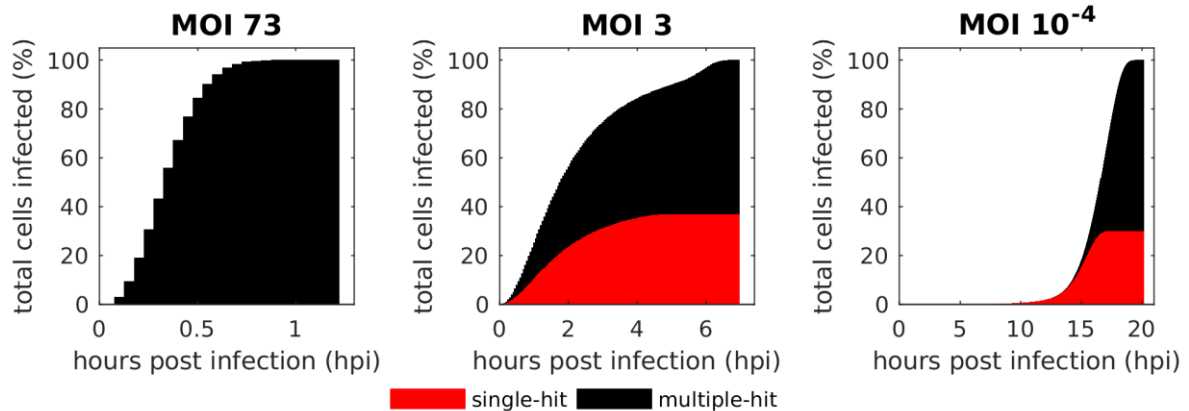
Figure 4.19.: Distribution of single- and multiple-hit infections in different MOI conditions. Cell culture infections were simulated with initial MOIs of 73, 3 and 10^{-4} based on $TCID_{50}$. Bars depict the amount of cells newly infected by a single or multiple virions in the respective time frame (1 bar = 0.05 h).

Model prediction for different scenarios, i.e., MOI 10^{-4}, 3 and 30, shows distinct infection profiles. Infections under very high MOI conditions result only in multiple-hit infections. MOI 3 and 10^{-4} show similar ratios between single- and multiple-hit infections with about 33% of cells infected by one virus particle. Interestingly, using an MOI of 10^{-4} leads to even more multiple-hit infections than an MOI of 3. Furthermore, the timing of infections is different. For MOI 3, cells are infected by a mixture of single- and multiple-hit infections right from the start. After 4.5 hpi, only multiple-hit infections occur. In contrast, MOI 10^{-4} results in almost exclusively single-hit infections until 14 hpi. Then, both types of infection occur until 17 hpi. At later time points, only multiple-hit infections take place. These results show how susceptible different infection scenarios are to co-infection-related effects such as DIP interference. Thus, high MOI infections are always affected by these events while low MOI infections are not affected until late time points. When using medium MOIs, the impact of such effects is likely reduced, but they could still influence infection and production results.

Lastly, we examined the origin of the infecting virus particles, i.e., if they were provided by the virus seed or produced during the infection, for the scenarios predicted above (Figure 4.20). This distinction indicates which factor is more relevant for the production of clean IAV yields containing low DIP levels, the quality of the seed virus or the rate of DIP *de novo* generation.
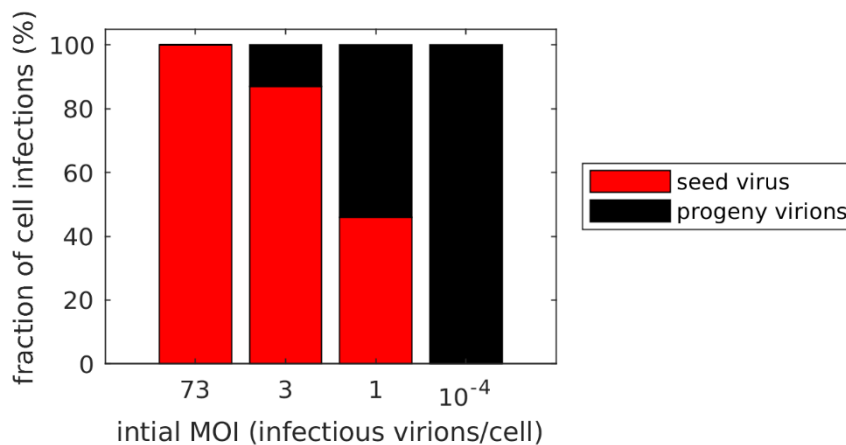
Figure 4.20.: Origin of virus particles infecting cells in different MOI conditions.
Cell culture infections were simulated with initial MOIs of 73, 3 and 10^{-4} based on $TCID_{50}$. Bars depict the percentages of cells infected by either virions from the seed virus or progeny virus particles that were generated during the infection.

Model simulations predict that the initial MOI directly correlates to the split between infections by seed or progeny virions. When using an MOI of 73, practically all cells are infected by virions from the seed virus. An MOI of 3 leads to around 10% of infections mediated by progeny virions, while an MOI of 10^{-4} induces almost exclusively progeny virion infections. Furthermore, the model predicts that an MOI of 1 would lead to a nearly even split between infections by virions from the seed virus and progeny virions. Thus, the reduction of the MOI increases the portion of infections mediated by progeny virions.

In summary, the multiscale model of STV infection predicts a rapid, uniform infection in high MOI conditions and a delayed progress of infection with variations in the effective MOI (multiple waves) in a low MOI scenario. Furthermore, the majority of all cells is infected at effective MOIs above 1, regardless of the initial MOI. However, the

initial MOI influences if these infection are mediated by virions from the seed virus (high MOIs) or progeny virus particles (low MOIs).

4.3.2 STV and DIP co-infection in a wide range of infection scenarios

To evaluate STV and DIP production in different infection conditions, we simulated the virus particle release for a wide range of MOIs and MODIPs. We aimed to identify optimal infection conditions for the successful suppression of STV propagation and the generation of large DIP quantities. These two scenarios are especially relevant regarding the production of DIPs for antiviral therapy and their potential application against STV infection.

Prediction of an optimal DIP-to-STV ratio for inhibition
Generally, high doses of DIPs are required for strong inhibition of STV infection (Figure 4.21A). However, low doses of DIPs can show an inhibiting effect when the MOI is significantly lower than the MODIP. Our simulations predict that using MODIP-to-MOI ratios of 1:1 enables a reduction of infectious STV titers by a factor of 10 compared to a DIP-free infection. To induce a strong reduction of infectious virus titers, i.e., by at least four orders of magnitude, a ratio of 10^4:1 is required.

Our model predicts that the highest DIP amount can be produced using large quantities of both MOI and MODIP during infection (Figure 4.21B). However, this would require a lot of virus seed material for infection, rendering this option unattractive for large scale DIP manufacturing. Very good yields could also be achieved by lower virus input, i.e., an MOI of 0.01 and an MODIP of 0.25, which reaches over 50% of the predicted maximum DIP production using a 150 times lower seed virus concentrations for infection. In general, applying slightly higher DIP than STV concentrations during infection resulted in the best results for DIP production.
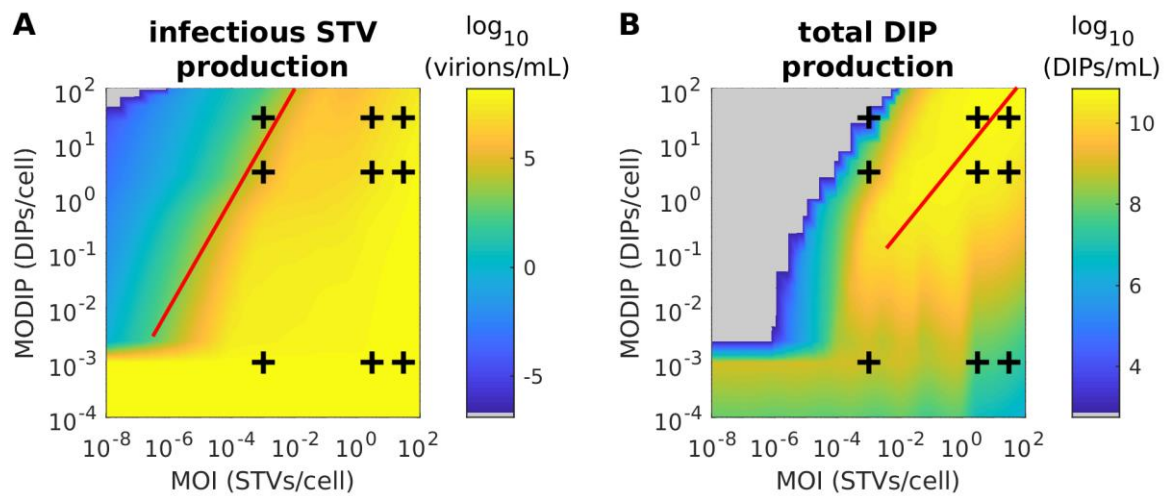
Figure 4.21.: STV infection suppression and DIP production are strongly affected by the infection conditions. Infections of MDCKsus cells were simulated with the multiscale model of STV and DIP co-infection using MOIs and MODIPs in the range of 10^{-8}–10^2 and 10^{-4}–10^2, respectively. The predicted concentrations of (A) infectious STVs and (B) total DIPs at 48 hpi determine the color of the heat map. The experimentally observed infection scenarios (+) are depicted. The solid red line indicates (A) an MODIP-to-MOI ratio of 10^4:1 and (B) the optimal multiplicity ratios for DIP production. For the switch between regular and reduced vRNA synthesis for low and high initial DIP concentrations a threshold value of $F_{\mathrm{MODIP}} = 10^{-3}$ was used. Grey areas indicate that no production of either STVs or DIPs occurs. Figure adapted from Rüdiger and Pelz *et al.* [125].

Impact of the replication advantage on virus titers

Furthermore, we investigated the effect of the intracellular parameter F_{Adv}, which describes the replication advantage of DI cRNA over its FL counterpart, on infectious STV inhibition and DIP propagation. For an MODIP of 10^{-3}, no significant impact of this parameter on infectious STV titers could be determined (Figure 4.22). When combining high STV and DIP concentrations, an increase of the parameter F_{Adv} could lead to decreased infectious STV titers. A reduction of the replication advantage would in turn lead to improved STV production in this scenario. The release of DIPs could be improved when the parameter F_{Adv} is increased, however, after reaching an optimal value the model predicts a decrease for higher values (Figure 4.22). For equimolar

virus particle concentrations, i.e., when both MOI and MODIP are either 10^{-3} or 30, this optimal value regarding DIP production is $F_{\text{Adv}} = 1.8$. Using MOI 30 and MODIP 10^{-3}, $F_{\text{Adv}} = 2.5$ is predicted to be optimal for DIP production.
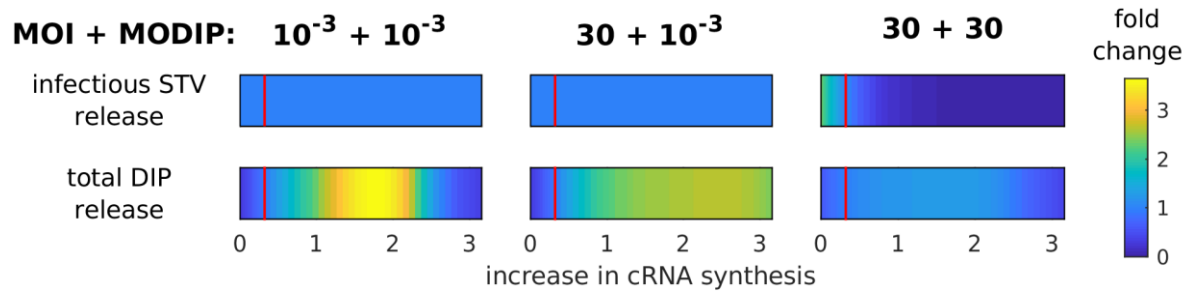

Figure 4.22.: The replication advantage affects DIP production in low MODIP conditions. The predicted fold-change for yields of infectious STVs and total DIPs at 24 hpi depending on a reduction or increase in the replication advantage of DI cRNAs over their FL counterpart is presented. The parameter F_{Adv} was varied in the range of 0 to 1000% of its estimated value. The vertical red line indicates the replication advantage estimated during model calibration, i.e., $F_{\text{Adv}} = 0.32$. Figure adapted from Rüdiger and Pelz *et al.* [125].

Prediction of the effective MOI and MODIP in different infection conditions

Next to STV suppression and DIP production, we were also interested in the impact of different infection conditions on the dynamics of the effective MOI and MODIP. Thus, we predicted how the ratio between infecting particles and potential target cells changes in the infection conditions used for model calibration. Note that for the simulation results depicted in Figure 4.23, we assumed that the system is already initialized with infected cells according to the Poisson distribution considering to the initial MOI and MODIP. Therefore, the bars shown relate to the infections of the remaining and newly produced cells. For all combinations using an MOI of 3 or 30, the progress of cell infection and the dynamics of the effective MOI showed profiles similar to Figure 4.18. Following a rapid infection of cells, the effective MOI increased to values above 10^{10} (Figure 4.23). If an initial MODIP of 3 or 30 was chosen together with high MOIs, the same dynamics could be observed for the effective MODIP. High MOIs

combined with low MODIPs show an initial decrease of the effective MODIP, which starts to increase 2 hpi.
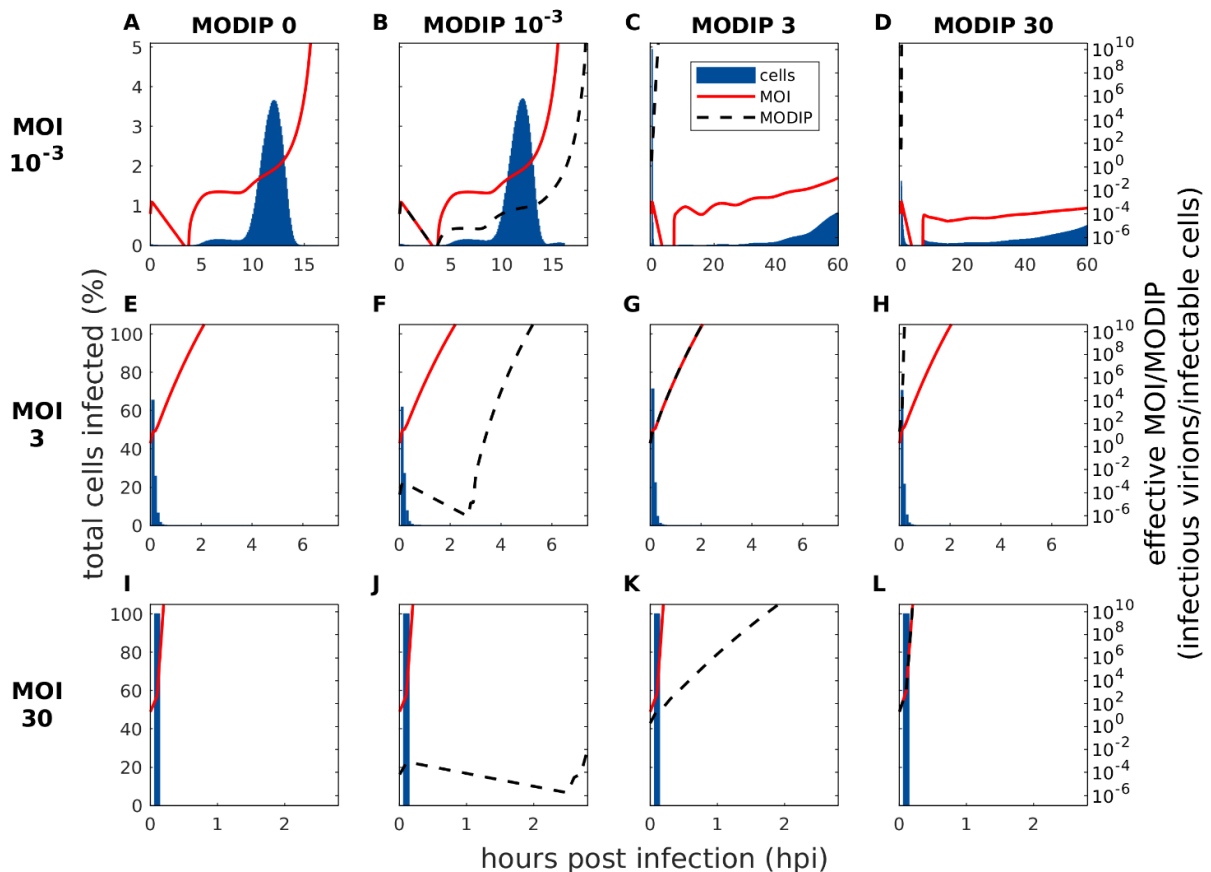
Figure 4.23.: Progress of cell infections, the effective MOI and the effective MODIP over the time course of STV and DIP co-infection. Cell culture infections were simulated with initial MOIs and MODIPs corresponding to the experimental conditions the co-infection model was fitted to. Bars depict the amount of cells newly infected in the respective time frame (1 bar = 0.05 h).The solid and dashed lines represent the current effective MOI and MODIP, respectively, based on the number of infectious virus particles and the remaining non-infected cells in the culture.

Using a low MOI and no DIPs for infection, the model predicts dynamics similar to the simulation of the multiscale model of STV infection (Figure 4.18). The infection is delayed and progresses in multiple waves. In contrast to the multiscale model of STV infection, the majority of infections occur at effective MOIs below 1. While the results

in Figure 4.18 showed that only 33% of cells are infected at low MOIs, the co-infection model predicts that 66% are infected at an effective MOI lower than 1. This is likely caused by the overall faster infection dynamics in the MDCKsus cells used to calibrate the co-infection model compared to the MDCKadh cells applied for the multiscale model of STV infection.

An analogous result was obtained for a combination of low MOI and MODIP. Here, the effective MOI increased as in an infection without DIPs and the effective MODIP followed a similar trajectory 4–6 h later. However, after an initial decrease for both multiplicities, the effective MOI rises to values around 10^{-2} at 4 hpi while the effective MODIP only reaches these levels at 14 hpi. Furthermore, an additional infection wave can be observed at 15 hpi. This is induced by progeny DIPs, which start to accumulate at 12 hpi and lead to co-infections of already STV-infected cells. Due to this small portion of co-infected cells, the model is able to achieve high levels of DIP production despite a low initial MODIP. However, the absolute level of DIP production in infection performed with MOI and MODIP 10^{-3} cannot be reached (Figure B.2B).

The simulation of low MOIs and high MODIPs leads to a fast initial infection wave, which causes the MODIP to increase to high levels as cells that can be infected by DIPs are depleted. The MOI declines until 7 hpi and only then increases to levels around 10^{-4}. Although it keeps rising for the next 50 h, the MOI never reaches high values. However, steadily replicating DIP-only infected cells are constantly infected by the few available STVs to produce co-infected cells. The amount of these co-infections increases until 60 hpi and may lead to all cells becoming co-infected if the infection is prolonged further.

Infection profiles in different infection conditions

When investigating the distribution of single- and multiple-hit infections that emerge using different infection conditions, the addition of DIPs creates more possibilities than before. Cells can become infected by one STV or DIP, by multiple STVs or DIPs, or be subject to a co-infection. We predicted the related profiles for the infection conditions used for model calibration and examine which types of infections occur at which time (Figure 4.24). The relation of the different infection types determines if STV can

replicate freely, DIPs can propagate due to the support of the STV, or virus replication is severely reduced for both viral species.
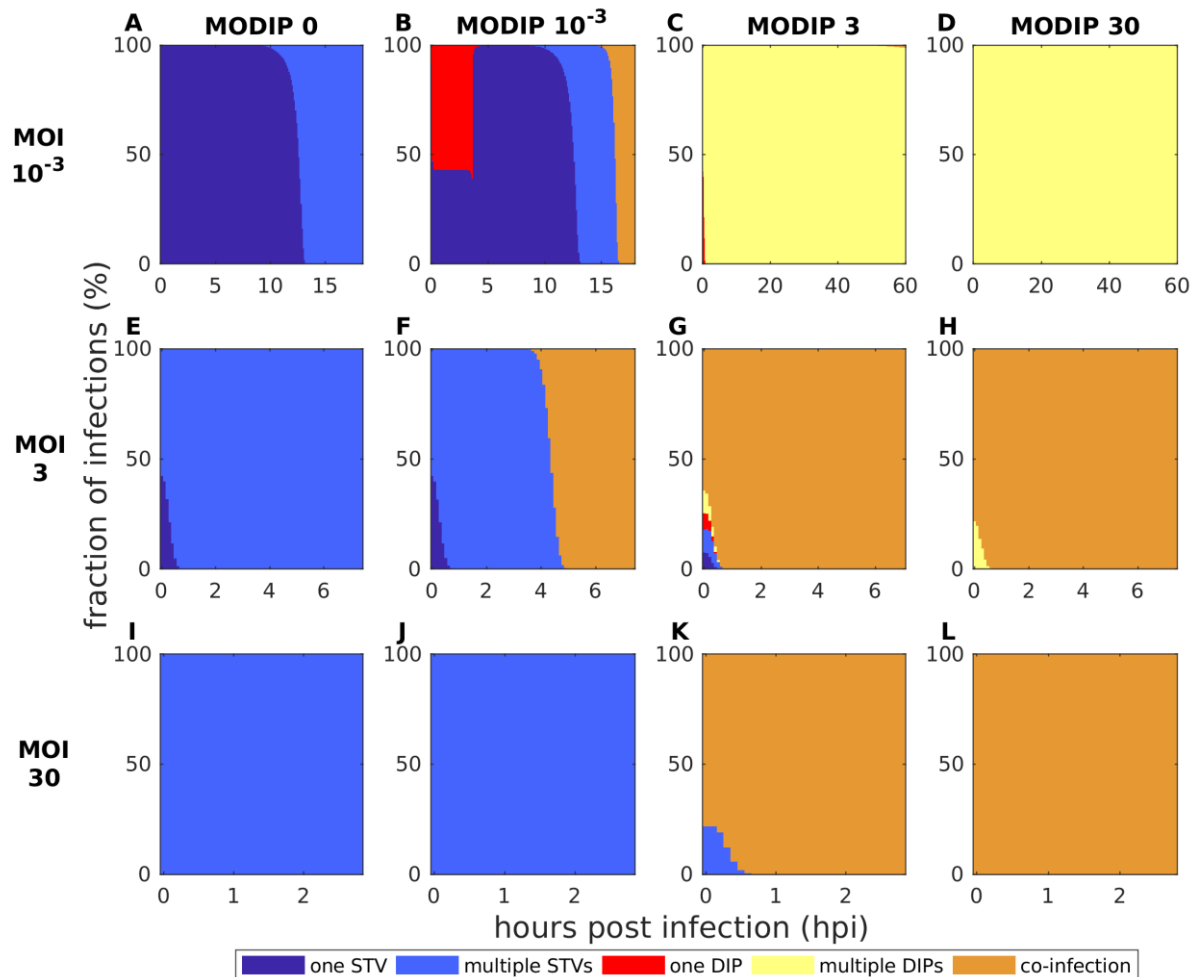
Figure 4.24.: Distribution of single- and multiple-hit infections in different MOI and MODIP conditions. Cell culture infections were simulated with initial MOIs and MODIPs corresponding to the experimental conditions the co-infection model was fitted to. The distribution of infections mediated by one or multiple STVs, one or multiple DIPs or both is shown for each time point of infection. The height of the individual bars shows the share each scenario represents of all infections occurring in the respective time frame (1 bar = 0.05 h). The magnitude of infections is not represented, but can be observed in Figure 4.23.

For infections with an initial MOI of 30, cells are infected either by multiple STVs (Figure 4.24I–J) or mostly by co-infection (Figure 4.24K–L) depending on the MODIP. When reducing the MOI to 3, more diverse infection profiles can be obtained. Adding no DIPs leads to a few single-hit STV infections at the start, but the vast majority consists of multiple-hit STV infections (Figure 4.24E). The behavior of MOI 3 and MODIP 10^{-3} is similar initially, but after 4 hpi most infections are co-infections by STV and DIPs (Figure 4.24F). Therefore, if infections occur in this time frame, they are co-infections. However, this applies to very few infections as shown in Figure 4.23F. Using an equimolar MOI and MODIP of 3, all different types of infection can occur in the initial phase, i.e., infections by one or multiple STVs or DIPs, but most infections are still co-infections (Figure 4.24G). An infection using MOI 3 and MODIP 30 showed similar dynamics, but only multiple-hit DIP infections and co-infections occur.

Low MOI conditions differ strongly depending on the applied MODIP. When adding an MODIP of 30, multiple-hit DIP infections are performed almost exclusively (Figure 4.24D). However, a very small portion of co-infections, i.e., 0.03%, was predicted towards the end. Combining a low MOI and an MODIP of 3, model simulations predict that at the start some single-hit DIP infection can occur (Figure 4.24C). After that, multiple-hit DIP infections constitute the majority of infections. However, after 50 hpi, co-infections by the slowly accumulating progeny STV can capture a small share of the overall infections. When infecting only with a low MOI and no DIPs, an initial phase of single-hit STV infections transitions towards multiple-hit STV infections (Figure 4.24A) as already observed for the multiscale model of STV infection in Figure 4.18. The most varied infection profile, which consists of four distinct phases, was predicted for an equimolar MOI and MODIP of 10^{-3} (Figure 4.24B). First, a mixture of single-hit STV and DIP infections can occur until about 4 hpi. Then, the increasing effective MOI leads to a phase of single-hit STV infections until 10 hpi. As the MOI continues to increase, the infections transition to mostly multiple-hit STV infections until 15 hpi. Lastly, the MODIP also increases to significant levels, which causes the majority of infection to be co-infections.

Taken together, the multiscale model of STV and DIP co-infection predicts that an MODIP-to-MOI ratio of about 10^4:1 has to be used to restrict STV production and spreading significantly. For the production of large DIP quantities, an equimolar MOI

and MODIP are preferable. To improve both the suppression of STV release and the production of DIPs, an increase of the replication advantage of DI cRNAs should be considered. Lastly, the evaluation of the effective multiplicities (MOI and MODIP) during infection and the infection profiles of cells provides additional insights into the infection dynamics of STVs and DIPs in different infection conditions.

4.3.3 Discussion

In the previous subsections, we have developed two multiscale models that capture experimental data obtained from cell culture infections performed for highly different MOIs and MODIPs. The focus during their calibration was to obtain a single set of parameters that can describe all observed infection dynamics. This enables the prediction of non-observable properties, e.g., the changes of the effective MOI during an infection or the amount of multiple-hit infections, and of the infection dynamics for other infection conditions.

Impact of the number of infecting virions

Model predictions performed with the multiscale model of STV infection show that the MOI heavily affects the progress of IAV infection in cell cultures. The higher the MOI, the faster cells are infected and the earlier virus particles are released. Additionally, the initial MOI affects the dynamics of the effective MOI resulting in highly different scenarios regarding the amount and the origin of infecting virions. In high MOI conditions, all cells are infected by the initially available virions in a single infection wave (Figure 4.18). In addition, such infections are with near certainty multiple-hit infections (Figure 4.19). Simulations of an infection at MOI 3, however, show two different scenarios. Until 4 hpi cells are infected at an effective MOI that results in around 50% chance of inducing multiple-hit infections (Figure 4.19). In a second infection wave, starting at 4 hpi, virions begin to infect cells at increasing effective MOIs leading to a higher probability of multiple-hit infection. After 5 hpi, all cells are infected by multiple virions until no uninfected cells remain.

Predictions of infection dynamics for low MOI conditions (10^{-4}) show variations in the effective MOI that span 14 orders of magnitude (Figure 4.18). Using the model of STV infection enabled detailed analyses regarding such a scenario. Simulations show that the effective MOI progresses in three infection waves starting at 0, 4 and 11 hpi. In the first 13 hpi, virions infect uninfected cells mostly in single-hit infections (Figure 4.18). Until 4 hpi, these infections are performed exclusively by virions from the seed virus. From 4 to 13 hpi, first and second generation progeny virions induce additional infection waves, in which still mostly single-hit infections occur as the effective MOI stays below one (Figure 4.19). Finally, the effective MOI increases steadily, so that 16 hpi mostly multiple-hit infections are induced. Interestingly, model prediction with the multiscale model of STV infection predict that over 60% of all cell infections occur after 16 hpi (Figure 4.18). Thus, the majority of cells is infected by multiple virions even using low initial MOI conditions.

Surprisingly, the model predicts that during an infection at MOI 3 slightly more cells are infected by a single-hit infection compared to MOI 10^{-4}. With an initial MOI of 3, more infections are occurring in a phase when the chance of a single-hit infection is reasonably high, i.e., around 50% for MOI 3. Thus, 37% of cells are infected by a single virion using an MOI of 3. The highest value of single-hit infections over the whole infection time could be achieved by an MOI of 2 with a value of 48%. Therefore, if the aim of a future study were the induction of the maximum number of single-hit infections, an MOI 2 would be preferable.

Altogether, this indicates that in both low and high MOI conditions mostly multiple-hit infections occur. However, during the initial phase of a low MOI infection single-hit infections are induced predominantly.

Implications for DIP interference based on the initial MOI

Furthermore, the model predictions generated with the multiscale model of STV infection provide interesting implications for the interference of DIPs with infectious virions for different MOI conditions. With this model, we only considered STVs and not DIPs, but the predictions can still be applied to evaluate the potential impact of DIPs that may reside in the seed virus or are generated *de novo* during infection. As the preparation of large quantities of completely DIP-free IAV seed virus material is

challenging and costly, most seed viruses contain DIPs. There are different approaches to limit the fraction of contained DIPs, however, typically virus seeds are not DIP-free.

In our simulations, the majority of cells are infected by multiple virions, regardless of the MOI. Such conditions favor DIP replication as they increase the chance of co-infections by DIPs and infectious virions. Therefore, it could be argued that even low MOI conditions do not prevent DIP interference, but only postpone it to later infection stages (Figure 4.18). However, there is an important distinction between different MOI conditions regarding the seed virus.

In high MOI conditions, all cells undergo multiple-hit infections by virions exclusively from the seed virus (Figure 4.20). Therefore, the amount of DIPs contained in the seed virus determines the severity of interference. To achieve a low impact of DIPs in high MOI conditions a "clean" seed virus with very low DIP content is required. This is in particular relevant for experimental studies aiming for one-step virus growth to avoid artifacts. However, even for studies in small-scale cultures or laboratory scale bioreactors, the quality of the seed virus should be controlled carefully to avoid misinterpretation of experimental findings. Infections with an MOI of 3 result in a majority of cells becoming infected by virions from the seed virus. If one aims to achieve a case in which half of all cell infections are mediated by seed virions and the other half by progeny virions, an MOI of 1 can be applied (Figure 4.20).

In low MOI conditions relevant for cell culture-based influenza vaccine production, virions from the seed virus infect cells almost exclusively in single-hit infections preventing DIP interference and replication at early cultivation time. In later infection stages, progeny virions of the second to third generation nevertheless induce multiple-hit infections. Thus, the amount of DIPs generated *de novo* [257] during progeny virion production has a higher impact on the extent of interference with virus yields and the DIP content of the seed virus only plays a minor role. Altogether, DIPs always affect the replication of IAV regardless of the initial MOI. However, in low MOI conditions the interference has a lower impact and is postponed until later infection stages.

Altogether, this indicates that cells in high MOI conditions are infected exclusively by the seed virus, while in low MOI cultivations cells are infected almost exclusively by progeny virions. Using an MOI of 1 can generate a mixture of both scenarios.

Optimal MOI and MODIP conditions to prevent STV and support DIP production

Model simulations performed with the STV and DIP co-infection model predict that an MODIP-to-MOI ratio of at least 10^4:1 is required to reduce STV titers by over four orders of magnitude and enable a suppression of STV infection in MDCKsus cells (Figure 4.21). In line with our model prediction, recent infection experiments in mice using varying STV and DIP concentrations provided similar results [18, 19]. In these studies, the complete protection induced by DIP administration was lost when reducing the MODIP-to-MOI ratio from 3.4×10^4:1 to 3.4×10^3:1 and from 4.4×10^4:1 to 2.2×10^4:1, respectively.

Furthermore, the wide range of infection conditions reproduced by our model simulations enables a comprehensive evaluation of the effect of MOI and MODIP on virus production. In a recent study, Martin and Harris *et al.* [234] showed that the MOI strongly affects dynamics of STV replication in adherent MDCK cells. They observed higher virus titers and an earlier onset of virus particle release with increasing MOIs. In contrast, simulations from our STV and DIP co-infection model, as well as the experimental data that the model was calibrated to, do not support these findings. The experiments resulting in the highest concentrations of infectious and total STV were using low MOI conditions [125] and model simulations showed similar results for low and high MOIs (Figure 4.21A). Previously, experimental results supporting higher viral titers in low MOI conditions have been reported for MDCKadh cells [179, 180].

Regarding the cell culture-based production of DIPs, the model predicts that for the generation of large DIP amounts relatively low concentrations of virus material are sufficient for infection. As long as STVs and DIPs are provided in more or less equimolar concentrations and the initial MODIP is kept above 0.1, DIP production achieves high levels (Figure 4.21B). Overall, the maximum DIP titers can be obtained using an equimolar STV and DIP input (Figures B.2G and B.2L). This indicates that the ratio between MOI and MODIP might play a larger role than the total virus input for optimal DIP production conditions. Generally, DIP production was highest when slightly more DIPs were provided.

However, even if regular DIP production is improved by choosing the optimal MOI and MODIP conditions, a recently developed process using a modified cell line may provide a better alternative. In their study, Bdeir *et al.* [178] modified MDCK cells to stably

express the IAV protein PB2. When these so-called MDCK-PB2 cells are infected by a DIP containing a defective viral genome segment 1 encoding for PB2, e.g., DI244, the DIP can replicate without a STV acting as a helper virus. The missing genomic information, which normally results in the lack of PB2, can be compensated by the host cell and the DIP is able to replicate. Virus production in MDCK-PB2 cells was not compromised by the modification and high DIP titers could be achieved [141]. An additional benefit is the absence of STVs, which do not have to be removed from the product to obtain pure DIPs for antiviral application. Therefore, the usage of a modified cell line like MDCK-PB2 may be preferable to the conventional production of DIPs using STVs to provide the missing viral proteins.

Optimal dose for therapeutic application

For infections in humans, about 0.6 to 3 infectious units were reported for airborne transmissions [18]. Extrapolating the required MODIP-to-MOI ratio derived from our model predictions, the administration of 3×10^4 DIPs, e.g., via a nasal spray, could be sufficient to limit infection spread severely. However, as the preferred target tissues of IAV in humans do not correspond to a well-mixed cultivation system, the administration of higher doses is likely necessary. If we assume that the respiratory tract comprises about 4×10^8 cells [218] and that at least an MODIP of 10^{-1} should be achieved to induce strong infection suppression at such low MOIs, 4×10^7 DIPs would be required for a strong inhibiting effect. This amount of DIPs would also theoretically protect against up to 4000 infectious units, which is 1300 times the airborne infectious dose. However, if we consider an advanced infection already subject to strong virus replication, high MOI conditions would be prevalent. Assuming MOIs of 1 or above, at least 4×10^{12} DIPs would be necessary to achieve a strong inhibition according to our predicted MODIP-to-MOI ratio. Most likely, the application of such high DIP doses would not be reasonable due to safety concerns. Therefore, the use of DIP preparations shows the biggest promise shortly after infection or for prophylaxis. Previous *in vivo* experiments, which administered DIPs to mice at varying times before and after infection, support this hypothesis [287].

Impact of the replication advantage

An additional factor that affects the balance between STV and DIP production in co-infected cell populations is the replication advantage of DI over FL genomes [113]. By using an optimal factor for this advantage, which is implemented as an increased synthesis rate of DI cRNA over its FL counterpart in our model, up to 3.6 times more total DIPs could be generated in model simulations (Figure 4.22). Furthermore, model predictions suggest a more prominent replication advantage could also improve STV titer reduction in high virus concentration scenarios. A potential strategy to obtain DIPs with higher advantages over the STV is the selection of strongly accumulating DIPs from long-term continuous bioreactor cultivations [121]. Such DIPs consistently replicated at high levels indicating an increased advantage over their competition, i.e., other emerging DIPs.

Impacts of effective MOI and MODIP

Predictions of effective MOIs and MODIPs show that using an initial MOI of 3 or above induces a fast infection of MDCKsus cells. This implies that the change of these multiplicities over time does not have a large impact on the infection. Cells are infected in a confined time window with effective MOIs and MODIPs similar to the initially applied values. However, when applying a low MOI of 10^{-3}, cells are infected over a longer period of time. Thus, cells are infected under highly different conditions at the start of the infection compared to later phases.

Using a low MOI and a low MODIP, the infection progresses in multiple waves starting at 0, 4, 9 and 13 hpi (Figure 4.23B). Initially, the effective multiplicities behave similarly, but after the first infected cells start to produce progeny virions, the effective MOI always stays at least two logs above the effective MODIP. At the start of the infection, only single-hit infections by either a STV or a DIP occur, which prevents the replication of DIPs (Figure 4.24B). Even after 15 hpi, when most cells were already infected, the effective MODIP only reaches a value around 10^{-2}. Therefore, the vast majority of infections occurs with low MODIPs. However, the MOI changes drastically over time resulting in low MOI infections during the early phase, i.e., until about 12 hpi, but high MOI infections thereafter.

The combination of a low MOI with high MODIPs leads to constantly ongoing infections until 60 hpi. At the start, cells are infected rapidly by DIPs and the effective MODIP increases as the number of cells that are not already infected by a DIP decreases. The effective MOI drops as the initially available STVs infect cells inducing co-infections. These co-infected cells produce a small number of progeny STVs that can then infect DIP-only infected cells. This propagation continues until the end of the cultivation and the effective MOI increases in multiple waves, which start around 7, 16, 27, 40, 50 hpi for initial MODIPs of 3 and 30. The amount of infections by these progeny STVs produced in co-infected cells increases over time and may show even higher levels if the cultivation would have continued after 60 hpi. For a combination of MOI 10^{-3} and MODIP 3, the model predicts that the effective MOI would reach values above 1 at 65 hpi. Therefore, an increasing number of co-infections would occur leading to apoptosis and cell death, which indicates that the protection provided by an initial MODIP of 3 may be lost after 65 hpi. For an initial MODIP of 30, an effective MOI above 1 would be achieved at 118 hpi indicating a prolonged phase of protection from virus-induced apoptosis.

When observing the occurrence of single- and multiple-hit infections in different MOI and MODIP conditions, the distribution of scenarios does not show a large variety in most cases. When high MOIs and MODIPs are provided, mostly multiple-hit infections, which either are mediated by STVs, DIPs or in co-infections by both virus particles, are performed (Figure 4.24C-L). When both multiplicities are set to 3, co-infections represent the majority of infections. However, the remaining infectious are divided between single- and multiple-hit infections by only STVs or DIPs (Figure 4.24G). The largest shift between the types of infection can be observed for a combination of MOI and MODIP 10^{-3}. Here, the model predicts a slow start with a mixture of STV and DIP single-hit infections. Then, as the effective MOI increases, only single-hit followed by only multiple-hit infections by STVs occur. During later phases when the MODIP starts to increase, co-infections can take place. However, as shown in Figure 4.23B, only very few infections occur in this last phase, so that co-infections still represent a minority of infection types in this scenario. These co-infections lead to the production of progeny DIPs to achieve medium DIP titers in the model simulations, despite the non-optimal conditions for DIP replication. However, the surprisingly high DIP titers

measured in an experiment using these infection conditions could not be reached (Figure B.2) [125].

Limits of model prediction using infection condition-dependent parameters

To enable the description of infection dynamics measured in experiments performed at highly different MOIs and/or MODIPs, we introduced specific infection condition-dependent parameters in the models developed in this thesis.

For the multiscale model of STV infection, we implemented the FIVR, which was reduced for MOI 73 compared to the lower MOIs 10^{-4} and 3 enabling the description of observed virus titers. The change in the FIVR was introduced, because the model of STV infection calibrated to experiments from MOI 73 infections was not capable to capture the results obtained for lower MOIs. By increasing the initial FIVR from $F_{\mathrm{Par}}(0) = 0.034$ to $F_{\mathrm{Par}}(0) = 0.26$, the infectious STV titers in low MOI condition could be described. It is likely, that MOI conditions above 73 and below 10^{-4} could also be captured with the corresponding FIVR. However, for MOI values between 3 and 73, the correct FIVR is not deducible from the experimental data and model predictions may not be reliable. Between these two MOI values, the FIVR is transitioning from a high to a low value. We theorized that this is caused by DIP interference and that the increased chance of multiple-hit infections, which would lead to STV and DIP co-infections, is responsible for a reduction in infectious STV release. Therefore, an MOI that results in a high number of multiple-hit infections and in which even small fraction of DIPs contained in the seed virus are amplified to sufficient levels could determine the characteristics of this transition. To define this transition in more detail, follow-up experiments are required. However, an adjustment of the FIVR to different infection conditions was not required for the STV and DIP co-infection model indicating that this effect can be completely described by including DIPs in the model.

For the model of STV and DIP co-infection, we adjusted the rate of vRNA synthesis, which was constant for low MODIP conditions and reduced for higher MODIPs, and the specific cell growth rate, which was reduced for high viral loads. The change of the specific growth rate was introduced to capture the experimental data and only affects infections using high MOIs and/or MODIPs. As all cells are productively infected and cease to grow shortly after the start of the cultivation when high MOIs are applied,

there is only one scenario where this is relevant, i.e., low MOI and high MODIP conditions. This scenario does not strongly affect model prediction, because infection is strongly inhibited.

On the other hand, the adjustment of the vRNA synthesis rate is based on the MODIP-to-MOI ratio and adapts to the current virus concentrations during infection. However, the switch between the regular and a reduced rate, which is determined by the parameter F_{MODIP}, could not be exactly defined. Based on the performed experiments, we could determine that this reduction was prevalent when an MODIP of at least 3 was applied, but not when an MODIP of 10^{-3} was used. Therefore, in the range between 10^{-3} and 3, the impact first appears and increases with the used MODIP-to-MOI ratio. It is likely that this reduction of vRNA synthesis is related to the occurrence of co-infections, which implies that DIPs have to be present in a large enough portion of infected cells. To confirm the exact value at which this reduction starts to impact virus replication, follow-up experiments are required.

For the prediction shown in Figure 4.21 we used an F_{MODIP} of 10^{-3} to show a wide range of the impact of vRNA synthesis reduction on STV production. A potentially higher value of F_{MODIP} would lead to an increase of STV and DIP titers in very low MOIs and MODIPs between 10^{-3} and 3. This would, however, not affect the predicted MODIO-to-MOI ratio of 10^{4}:1 for potent STV inhibition, but imply that for successful STV suppression MODIPs below 3 may not be sufficient. DIP production would also be affected for infection conditions in the specified range if the value of F_{MODIP} is increased. However, the maximum DIP titers achieved are not affected by this change.

Summary

We have developed two mathematical multiscale models that capture a wide range of experimental data. These models enabled the prediction of IAV infection dynamics and the analysis of how these are impacted by the amount of initially provided virus particles. We employed these models to estimate the dynamics of the effective MOI and MODIP, the distribution of single- and multiple-hit infections and the production of progeny STVs and DIPs. Furthermore, we predicted that a ratio of DIPs to STVs of at least 10^{4}:1 is required for the potent inhibition of IAV infection. Additionally, model

predictions show that low initial STV and DIP concentrations provided at roughly equimolar levels are preferable for DIP production. Lastly, we observed the importance of seed virus quality and the impact of *de novo* generation for infection, which is relevant for experimental set-up and vaccine production. An important next step to enable the prediction of *in vivo* infection dynamics is the implementation of an immune response. Furthermore, virus spreading in tissues on a 2D or 3D level should be considered. However, for a reliable model calibration, experiments quantifying the immune response and the spread of infections in tissues using relevant infection scenarios need to be performed.

5. Conclusion

The general target of this thesis was the development of a mathematical model of STV infection and DIP replication at the intracellular and cell population level that explicitly considers the initial MOI and MODIP conditions. These multiplicities strongly influence infection outcomes and understanding their impact is a key factor to uncover virus-host interactions and the dynamics of IAV infection as well as mechanisms of DIP interference. With the models developed in this thesis, we explored various mechanisms of viral RNA regulation to capture a wide range of experimental data closely. Furthermore, we used these models to predict how infection dynamics are affected by varying amounts of STV and DIP input and the optimal MOI-to-MODIP ratio to limit infection spread. The co-infection model is well calibrated to optimize cell culture-based DIP production and provides a solid basis for the analysis of DIP application strategies for prophylaxis and treatment of IAV infections.

Multiscale model of STV infection

With the aim to capture IAV infection dynamics on the intracellular and cell population level measured simultaneously in a high MOI experiment, we employed a previously published multiscale model of infection. However, to capture the observed dynamics fully, a model extension was required. By considering a logistic function for the description of infected cell apoptosis, the transition of cells to an apoptotic state could be captured closely. Additionally, we analyzed the impact of a regulatory feedback on vmRNA production mediated by RdRp. Model fitting results comparing this hypothesis with an implementation without this feedback suggest that its inclusion is favorable. After applying these changes, the model could capture infection dynamics observed in high MOI experiments closely and was capable to describe both infectious and non-infectious virus titers.

Then, we challenged the model with virus titer measurements obtained from experiments using lower MOIs and model simulations could not describe the dynamics and magnitude of virus production. Here, we identified the FIVR as a critical parameter. While its value was estimated to be very low for the high MOI experiment, the

application of lower MOIs resulted in an increased production of infectious STVs. Therefore, we increased its value, which enabled the successful description of virus titers in the other conditions. This indicates that for low MOI infections a significantly larger portion of produced STVs is infectious. A likely cause for this difference is the effect of DIPs during virus replication. In high MOI conditions, all cells are infected by multiple virus particles, which strongly increases the impact of DIP interference. At an intermediate MOI of 3, such a strong reduction of virus titers could not be observed. This suggests that there might be a balance between single- and multiple-hit infections at which infectious virus particle production is not affected.

Multiscale model of STV and DIP co-infection

In the second part of this work, we based our modeling efforts on experimental data specifically tailored to identify the interactions between STVs and DIPs during IAV infection. Therefore, 12 different MOI and MODIP conditions were used for infection of MDCKsus cell cultures, which resulted in a large set of observed infection dynamics. To implement the impact of DIPs on STV infection, we expanded our previously developed multiscale model to consider DIP replication and propagation. To that end, this model introduces an age-segregated population of cells co-infected by STVs and DIPs, which also considers the dynamics of competition between the two virus particles during intracellular replication. As the initial implementation of this model did not capture all observed infection conditions with a single set of parameters, we extended the model by considering additional mechanisms of regulation that could be identified in the experimental data. To that end, the regulation of vRNA and vmRNA represented crucial processes which were adjusted in the model to enable a close description of intracellular infection dynamics. In particular, the implementation of an MODIP-to-MOI ratio-dependent vRNA synthesis rate was required to capture all conditions simultaneously. This dependence on the multiplicity ratio implies that the balance between the initially provided STVs and DIPs affects intracellular replication. However, this effect is not necessarily induced during vRNA synthesis and could be related to other factors, such as anti-proliferative or cytopathic effects. A further elucidation of such mechanisms cannot be achieved by mathematical modeling, but requires biological experiments exploring specific details of virus co-infections.

Model fitting suggest that the DI genomes provided by DI244 replicate 30% faster than their FL counterparts. Previously, higher replication advantages were assumed for DIPs due to the large differences in genome segment length. However, very high advantages would lead to a strong imbalance towards defective genomes during co-infection, which would reduce overall replication and propagation affecting DIPs themselves. DIPs that were shown to accumulate successfully to high levels during virus infections are more likely to have achieved a balance with the STV supporting moderate advantages. Artificially created DIPs may provide higher replication advantages, but due to an excessive restriction of virus replication, they could prevent their own propagation. This could reduce their overall therapeutic potential, because the amplification of the defective genomes, which is an important part of antiviral DIP activity, could be reduced severely. However, the optimal strategy for DIP application is still a topic of research and different types of DIPs need to be considered.

Prediction of infections in different MOI and MODIP conditions

We applied the multiscale model of STV infection to predict the dynamics of the effective MOI during the course of an infection in different conditions. Model simulation results show that low MOI infections progress in multiple waves and the cells are infected at MOIs ranging over 14 orders of magnitude. This suggests that during later stages of infection most cells are infected with high MOIs, even if the infection itself is initiated with few virus particles. Furthermore, it enables the prediction of the distribution of single- and multiple-hit infections over the course of a complete cell culture infection. This shows that when infecting with a low MOI, multiple-hit infections only become relevant during later stages and the initial infection activity is driven by single-hit infections. Additionally, the origin of the infecting virus particles is different for low and high MOI conditions. In higher MOI conditions, cells are infected exclusively by virions from the seed virus. In lower MOI conditions, progeny virus particles mediate most infections. This has interesting implications for vaccine production in regards to the necessity of the generation of clean seed viruses or if the *de novo* generation of DIPs affects virus yields.

In order to study the impact of different MOI and MODIP conditions, we simulated a wide range of multiplicity combinations to study the optimal conditions to reduce STV

propagation and to improve DIP production. The best conditions to generate DIPs in co-infections were determined to be roughly equimolar concentrations of STVs and DIPs, if multiplicities above 10^{-2} were used. Furthermore, we studied the impact of the replication advantage in co-infections and found that it mostly affects DIP production, which can be improved using an optimal advantage. However, when the advantage is increased further, DIP production is reduced. Model simulations suggest that to interfere severely with STV production, the ratio between STVs and DIPs is the critical factor rather than the absolute number of DIPs. An MODIP-to-MOI ratio of 10^4:1 was predicted to induce a reduction of STV titers by four logs when applying DI244. Taken together, our model predictions show how the conditions for cell infections change dynamically over time and the models can be used to estimate the DIP input required for antiviral application.

Summary

We have developed two mathematical multiscale models of IAV infection that consider the initial MOI and MODIP conditions and their dynamics during infection. These models provide insights into virus replication and propagation as well as how they are impacted by varying STV and DIP inputs. In contrast to previous models of virus infection, the models presented here capture a wide range of data measured on the intracellular and cell population level from multiple experiments performed in different conditions using only a single set of parameters. This enabled a robust prediction of not experimentally identifiable infection mechanisms and the system dynamics in other conditions. Model simulations predict how different MOI conditions affect the origin and number of virions infecting cells at different times after infection of a cell culture. Additionally, the co-infection model predicts the MODIP-to-MOI ratio required for significant IAV suppression that could be applied for antiviral therapy. Taken together, the models presented here support a comprehensive understanding of IAV infection as well as the interactions between STVs and DIPs during co-infection providing a solid platform for the optimization of vaccine manufacturing, DIP production, and DIP application for therapeutic use.

6. Outlook

The mathematical multiscale models developed in this thesis closely describe a wide range of measurements obtained from *in vitro* experiments performed in highly different infection conditions. We focused on identifying a single set of parameters that is capable to capture all conditions simultaneously supporting the predictive power of these models. Thus, we could identify the impact of the infection conditions on model parameters and overall infection dynamics. Going forward, we think it is essential to develop models that can describe the effects of different conditions on a system to represent its characteristics accurately. Otherwise, only a snapshot of a system can be captured and crucial properties may be missed, e.g., due to artifacts induced for individual conditions. The ability to create such condition-sensitive models relies on data availability, which is quite challenging for *in vivo* infections compared to *in vitro* experiments. However, models describing *in vivo* infection dynamics would benefit from the calibration of uniform parameter sets for different conditions as it could improve model analysis and prediction.

Applying the multiscale models developed here to *in vivo* infections could show great promise for the description of virus propagation in tissues or even animals and humans. To that end, an expansion of the models towards the second or third dimension would be required. Furthermore, tissue cells do not correspond to a well-mixed system, but are arranged in specific patterns and might be covered by mucosa. These differences have to be considered for modeling of such systems. Moreover, high-resolution data for intracellular dynamics during *in vivo* infections is, unfortunately, not readily available. This impedes a calibration of detailed virus infection models describing *in vivo* systems. Additionally, the immune response of the host should be considered in such scenarios as it plays a crucial role during infections. Our multiscale models were calibrated using data from infections of MDCK cells, which produce a myxovirus resistance protein 1 in response to an infection that does not shows an activity against human IAV due to its canine origin. To inform the model regarding processes mediated by the immune system, a different cell line, e.g., A549 cells of human origin, might be suited better to provide detailed experimental data. Furthermore, the immune response

to DIP infection has been shown as an important factor for the antiviral properties of DIPs. Therefore, to describe their therapeutic effects in animals or humans accurately, the incorporation of the immune response to DIP infection is required.

Another potential application for our multiscale models is the combination with epidemiological models that describe between-host transmission of virus particles. Such overarching models could account for the competition and spreading of different virus strains based on the properties of their intracellular replication. Additionally, they could be employed to estimate the impact of specific mutations, which result in altered virus protein functionality, on virus competition and their potential to induce dangerous epi- and pandemics. Furthermore, such models could provide insights regarding the effect of therapeutic interventions in a population, e.g., the treatment of certain groups of people with larger social circles or a higher risk for severe outcomes, and provide support for the optimal distribution of antivirals to combat infection spread.

The description of the intracellular level of virus replication could benefit from incorporating experimental data describing the dynamics of virus proteins during infection. Especially during STV and DIP co-infection, the limitation of specific viral proteins was proposed to impact interference significantly. Additionally, DIPs can have defects on different genome segments, which introduces various ways the viral protein balance can be affected. Furthermore, viral protein data may support the evaluation of semi-infectious virus particles that contain less than the full eight genome segments and cannot provide the complete set of required proteins. The impact of such particles is currently not well understood and could be investigated by mathematical modeling. Another aspect of virus infection is the impact of host cell factors, which may play a large role for virus production. This is especially relevant for the engineering of cell lines for vaccine production. Modeling could support the design of such cells by predicting the importance of different factors. However, the availability of experimental data regarding relevant host cell factors during IAV infection is still a bottleneck that needs to be considered for such a model extension.

The multiscale model of STV and DIP co-infection considers changing virus concentrations during an infection, which affect the intracellular dynamics of cells infected at different time points. This is especially relevant for DIP interference, because the number of infecting STVs and DIPs determines the balance between the

accumulation of functional and defective genome segments. Additionally, for the description of a continuous IAV production set-up, in which virus titers generally show oscillations, such an implementation is necessary. However, by considering different MOIs and MODIPs on the intracellular level of infection, the computational burden is increased quite substantially and parameter estimation requires more resources. For future applications, a strategy to reduce these requirements would be beneficial. A potential approach would be the pre-simulation of intracellular infection dynamics for different MOI and MODIP conditions. However, this would not benefit testing different parameter sets. Furthermore, the inherent heterogeneity observed in IAV infections could also be considered in the model by transitioning to a stochastic implementation. However, to inform such a stochastic model, specific single-cell experiments observing intracellular dynamics in individual cells would be required. Additionally, the consideration of individual cell infection dynamics in such a large system consisting of millions of cells would again lead to large computational efforts. A potential solution to that problem is the application of a hybrid simulation approach, which uses a stochastic implementation when molecule numbers are low but can switch to a deterministic representation when molecule numbers increase above a certain threshold. Overall, the development of potentially more efficient simulation approaches and powerful computational hardware may provide a large boost to the ability to model complex systems in the future. This could support the solution of the aforementioned issues and enable detailed infection models that consider stochastic effects and the highly dynamic nature of virus infections.

As proven in the past two years in response to the newly emerged SARS-CoV2, mathematical modeling can greatly benefit the societal response to a pandemic. Following the current trajectory of global events, such undertakings may become highly relevant in regards to other viruses and especially influenza virus in the near future. Therefore, it is of utmost importance to further develop and improve our current models and understanding of virus infection to prepare us for the challenges we are facing.

List of Figures

List of Tables

List of Publications

Research articles

Rüdiger D*, Kupke SY, Laske T, Zmora P, Reichl U. Multiscale modeling of influenza A virus replication in cell cultures predicts infection dynamics for highly different infection conditions. PLOS Computational Biology. 2019;15(2):e1006819.

Contribution: Conceptualization, Formal analysis, Methodology, Software, Validation, Visualization, Writing – original draft, Writing – review & editing

Rüdiger D*, Pelz L*, Hein MD, Kupke SY, Reichl U. Multiscale model of defective interfering particle replication for influenza A virus infection in animal cell culture. PLOS Computational Biology. 2021;17(9):e1009357.

Contribution: Conceptualization, Formal analysis, Investigation, Methodology, Software, Validation, Visualization, Writing – original draft, Writing – review & editing

Pelz L*, **Rüdiger D***, Dogra T*, Alnaji FG, Genzel Y, Brooke CB, Kupke SY, Reichl U. Semi-continuous propagation of influenza A virus and its defective interfering particles: analyzing the dynamic competition to select candidates for antiviral therapy. Journal of Virology. 2021;95(24):e0117421.

Contribution: Conceptualization, Formal analysis, Investigation, Visualization, Writing – review & editing

Conference paper

Rüdiger D*, Kupke SY, Reichl U. A multiscale model of influenza A virus replication covering highly different infection conditions in cell cultures. IFAC-PapersOnLine, 2018;51(19):32-33.

Contribution: Conceptualization, Formal analysis, Investigation, Methodology, Software, Validation, Visualization, Writing – original draft, Writing – review & editing

* first author

Supervised theses

Karina Pál. Intracellular Stochastic Modelling of Influenza A Virus and DIP Replication. Master Thesis. Faculty of Science and Technology, NOVA University of Lisbon. 2018.

Carolina Pontes. Modeling of influenza A virus infection dynamics subjected to OP7 interference. Master Thesis. Faculty of Science and Technology, NOVA University of Lisbon. 2021.

Talks

Rüdiger D, Kupke SY, Zmora P, Reichl U. Multiscale model of influenza virus infection predicts viral release dynamics in cell cultures for a wide range of infection conditions. 3rd Workshop on Virus Dynamics. Heidelberg, Germany. 2017.

Rüdiger D, Laske T, Kupke SY, Reichl U. Multiscale model of DIP interference and production during influenza A virus infection in animal cell culture. 4th Workshop on Virus Dynamics. Paris, France. 2019.

Rüdiger D, Pelz L, Hein MD, Kupke SY, Reichl U. Multiscale model of DIP replication and its effects on influenza A virus infection in animal cell culture. Society for Mathematical Biology 2020 Annual Meeting. 2020.

Pelz L, **Rüdiger D**, Alnaji FG, Genzel Y, Brooke CB, Kupke SY, Reichl U. Evolution and selection of influenza a virus defective interfering particles in a semi-continuous production system for the use as antiviral. 7th ESWI Influenza Conference. 2020.

Rüdiger D, Pelz L, Hein MD, Kupke SY, Reichl U. Multiscale model of influenza A virus and defective interfering particle co-infection in animal cell culture. 5th Workshop on Virus Dynamics. 2021.

Posters

Rüdiger D, Heldt, FS, Kupke SY, Reichl U. Stochastic multiscale modeling of influenza virus production in cell cultures. 6th Foundations of Systems Biology in Engineering, Magdeburg, Germany. 2016.

Rüdiger D, Kupke SY, Reichl U. A multiscale model of influenza A virus replication covering highly different infection conditions in cell cultures. 7th Foundations of Systems Biology in Engineering, Oak Brook, Illinois, USA. 2018.

Rüdiger D, Laske T, Kupke SY, Reichl U. A multiscale model of defective interfering particle replication. 8th Foundations of Systems Biology in Engineering, Valencia, Spain. 2019.

Pelz L, **Rüdiger D**, Alnaji FG, Genzel Y, Brooke CB, Kupke SY, Reichl U. Semi-continuous propagation of influenza A virus and its defective interfering particles - analyzing the dynamic competition to select antiviral candidates. 30th Annual Meeting of the Society for Virology. 2021.

Bibliography

1. Global, regional, and national age-sex specific all-cause and cause-specific mortality for 240 causes of death, 1990-2013: a systematic analysis for the Global Burden of Disease Study 2013. Lancet (London, England). 2015;385(9963):117-71.
2. Worldometer. Coronavirus Worldwide Graphs. 2021 [cited 18 November 2021]. Available from: https://www.worldometers.info/coronavirus/worldwide-graphs/.
3. Piret J, Boivin G. Pandemics Throughout History. Front Microbiol. 2020;11:631736.
4. Taubenberger JK, Morens DM. 1918 Influenza: the mother of all pandemics. Emerg Infect Dis. 2006;12(1):15-22.
5. LePan N, Routley N, Schell H. Visualizing the History of Pandemics. 2020 [cited 18 August 2021]. Available from: https://www.visualcapitalist.com/history-of-pandemics-deadliest/.
6. Potter CW. A history of influenza. J Appl Microbiol. 2001;91(4):572-9.
7. Webster RG. Wet markets--a continuing source of severe acute respiratory syndrome and influenza? Lancet (London, England). 2004;363(9404):234-6.
8. Petrova VN, Russell CA. The evolution of seasonal influenza viruses. Nat Rev Microbiol. 2018;16(1):47-60.
9. Wright PF, Neumann G, Kawaoka Y. Orthomyxoviruses. In: Fields BN, Knipe DM, editors. Fields Virology: Wolters Kluwer Lippincott Williams & Wilkins; 2013. p. 1186-243.
10. CDC. Avian Influenza in Birds. 2017 [cited 18 August 2021]. Available from: https://www.cdc.gov/flu/avianflu/avian-in-birds.htm.
11. Chen X, Liu S, Goraya MU, Maarouf M, Huang S, Chen J-L. Host Immune Response to influenza A Virus Infection. Front Immunol. 2018;9.
12. Iuliano AD, Roguski KM, Chang HH, Muscatello DJ, Palekar R, Tempia S, et al. Estimates of global seasonal influenza-associated respiratory mortality: a modelling study. The Lancet. 2018;391(10127):1285-300.
13. OECD. Influenza vaccination rates. 2021 [cited 05 August 2021]. Available from: https://www.oecd-ilibrary.org/social-issues-migration-health/influenza-vaccination-rates/indicator/english_e452582e-en.
14. Williams JH, Dawson A. Prioritising access to pandemic influenza vaccine: a review of the ethics literature. BMC medical ethics. 2020;21(1):40.
15. Lackenby A, Thompson CI, Democratis J. The potential impact of neuraminidase inhibitor resistant influenza. Current opinion in infectious diseases. 2008;21(6):626-38.
16. Imai M, Yamashita M, Sakai-Tagawa Y, Iwatsuki-Horimoto K, Kiso M, Murakami J, et al. Influenza A variants with reduced susceptibility to baloxavir isolated from Japanese patients are fit and transmit through respiratory droplets. Nat Microbiol. 2020;5(1):27-33.
17. Dimmock NJ, Easton AJ. Defective Interfering Influenza Virus RNAs: Time To Reevaluate Their Clinical Potential as Broad-Spectrum Antivirals? J Virol. 2014;88(10):5217-27.

18. Dimmock N, Easton A. Cloned Defective Interfering Influenza RNA and a Possible Pan-Specific Treatment of Respiratory Virus Diseases. Viruses. 2015;7(7):3768-88.

19. Hein MD, Kollmus H, Marichal-Gallardo P, Püttker S, Benndorf D, Genzel Y, et al. OP7, a novel influenza A virus defective interfering particle: production, purification, and animal experiments demonstrating antiviral potential. Appl Microbiol Biotechnol. 2021;105(1):129-46.

20. Beauchemin CAA, Handel A. A review of mathematical models of influenza A infections within a host or cell culture: lessons learned and challenges ahead. BMC Public Health. 2011;11 Suppl 1:S7-S.

21. Bubar KM, Reinholt K, Kissler SM, Lipsitch M, Cobey S, Grad YH, et al. Model-informed COVID-19 vaccine prioritization strategies by age and serostatus. Science. 2021;371(6532):916-21.

22. Shaw ML, Palese P. Orthomyxoviridae. In: Fields BN, Knipe DM, editors. Fields Virology. I: Wolters Kluwer Lippincott Williams & Wilkins; 2013. p. 1151-85.

23. Dou D, Revol R, Östbye H, Wang H, Daniels R. Influenza A Virus Cell Entry, Replication, Virion Assembly and Movement. Front Immunol. 2018;9:1581-.

24. Lamb RA, Krug RM. Orthomyxoviridae: the viruses and their replication. In: Knipe DM, Howley PM, editors. Fields Virology: Lippincott Williams & Wilkins; 2001. p. 1487-531.

25. Calder LJ, Wasilewski S, Berriman JA, Rosenthal PB. Structural organization of a filamentous influenza A virus. Proc Natl Acad Sci U S A. 2010;107(23):10685-90.

26. Dadonaite B, Vijayakrishnan S, Fodor E, Bhella D, Hutchinson EC. Filamentous influenza viruses. J Gen Virol. 2016;97(8):1755-64.

27. Heldt FS. Mathematical Models of Influenza A Virus Infection: From Intracellular Replication to Virus Growth in Cell Populations: Faculty of Process and Systems Engineering, Otto von Guericke University Magdeburg; 2015.

28. Moeller A, Kirchdoerfer RN, Potter CS, Carragher B, Wilson IA. Organization of the influenza virus replication machinery. Science. 2012;338(6114):1631-4.

29. Fodor E. The RNA polymerase of influenza A virus: mechanisms of viral transcription and replication. Acta Virol. 2013;57(2):113-22.

30. Fodor E, te Velthuis AJW. Structure and Function of the Influenza Virus Transcription and Replication Machinery. Cold Spring Harbor Perspectives in Medicine. 2019;10(9):a038398-a.

31. Shaw ML, Stone KL, Colangelo CM, Gulcicek EE, Palese P. Cellular proteins in influenza virus particles. PLoS Pathog. 2008;4(6):e1000085-e.

32. Compans RW, Content J, Duesberg PH. Structure of the ribonucleoprotein of influenza virus. J Virol. 1972;10(4):795-800.

33. Noda T, Sagara H, Yen A, Takada A, Kida H, Cheng RH, et al. Architecture of ribonucleoprotein complexes in influenza A virus particles. Nature. 2006;439(7075):490-2.

34. Noda T, Murakami S, Nakatsu S, Imai H, Muramoto Y, Shindo K, et al. Importance of the 1+7 configuration of ribonucleoprotein complexes for influenza A virus genome packaging. Nat Commun. 2018;9(1):54-.

35. Vasin AV, Temkina OA, Egorov VV, Klotchenko SA, Plotnikova MA, Kiselev OI. Molecular mechanisms enhancing the proteome of influenza A viruses: an overview of recently discovered proteins. Virus Res. 2014;185:53-63.

36. Huang TS, Palese P, Krystal M. Determination of influenza virus proteins required for genome replication. J Virol. 1990;64(11):5669-73.

37. Dawson WK, Lazniewski M, Plewczynski D. RNA structure interactions and ribonucleoprotein processes of the influenza A virus. Briefings in Functional Genomics. 2017;17:402-14.

38. Heldt FS, Frensing T, Pflugmacher A, Gröpler R, Peschel B, Reichl U. Multiscale modeling of influenza A virus infection supports the development of direct-acting antivirals. PLoS Comput Biol. 2013;9(11):e1003372-e.

39. Luo M. Influenza Virus Entry. In: Rossmann MG, Rao VB, editors. Viral Molecular Machines: Springer US; 2012. p. 201-21.

40. Lamb RA. The Structure, Function, and Pathobiology of the influenza A and B Virus Ion Channels. Cold Spring Harbor Perspectives in Medicine. 2020;10(11):a038505-a.

41. Hutchinson EC, Fodor E. Transport of the Influenza Virus Genome from Nucleus to Nucleus. Viruses. 2013;5(10):2424-46.

42. Cros JF, Palese P. Trafficking of viral genomic RNA into and out of the nucleus: influenza, Thogoto and Borna disease viruses. Virus Res. 2003;95(1-2):3-12.

43. Boulo S, Akarsu H, Ruigrok RWH, Baudin F. Nuclear traffic of influenza virus proteins and ribonucleoprotein complexes. Virus Res. 2007;124(1-2):12-21.

44. Bui M, Whittaker G, Helenius A. Effect of M1 protein and low pH on nuclear transport of influenza virus ribonucleoproteins. J Virol. 1996;70(12):8391-401.

45. Martin K, Helenius A. Nuclear transport of influenza virus ribonucleoproteins: the viral matrix protein (M1) promotes export and inhibits import. Cell. 1991;67(1):117-30.

46. Martin K, Helenius A. Transport of incoming influenza virus nucleocapsids into the nucleus. J Virol. 1991;65(1):232-44.

47. Whittaker G, Bui M, Helenius A. Nuclear trafficking of influenza virus ribonuleoproteins in heterokaryons. J Virol. 1996;70(5):2743-56.

48. Babcock HP, Chen C, Zhuang X. Using single-particle tracking to study nuclear trafficking of viral genes. Biophys J. 2004;87(4):2749-58.

49. Elton D, Digard P, Tiley L, Ortin J. Structure and function of the influenza virus RNP. In: Y. Kawaoka (ed.), Influenza Virology: Current Topics. Hethersett, United Kingdom: Caister Academic Press; 2006. p. 1-36.

50. Engelhardt OG, Smith M, Fodor E. Association of the influenza A virus RNA-dependent RNA polymerase with cellular RNA polymerase II. J Virol. 2005;79(9):5812-8.

51. Eisfeld AJ, Neumann G, Kawaoka Y. At the centre: influenza A virus ribonucleoproteins. Nat Rev Microbiol. 2014;13(1):28-41.

52. Poon LL, Pritlove DC, Fodor E, Brownlee GG. Direct evidence that the poly(A) tail of influenza A virus mRNA is synthesized by reiterative copying of a U track in the virion RNA template. J Virol. 1999;73(4):3473-6.

53. Zheng H, Lee HA, Palese P, García-Sastre A. Influenza A virus RNA polymerase has the ability to stutter at the polyadenylation site of a viral RNA template during RNA replication. J Virol. 1999;73(6):5240-3.

54. York A, Fodor E. Biogenesis, assembly, and export of viral messenger ribonucleoproteins in the influenza A virus infected cell. RNA Biol. 2013;10(8):1274-82.

55. Yángüez E, Nieto A. So similar, yet so different: selective translation of capped and polyadenylated viral mRNAs in the influenza virus infected cell. Virus Res. 2011;156(1-2):1-12.

56. Hutchinson EC, Fodor E. Nuclear import of the influenza A virus transcriptional machinery. Vaccine. 2012;30(51):7353-8.

57. Nayak DP, Hui EK-W, Barman S. Assembly and budding of influenza virus. Virus Res. 2004;106(2):147-65.

58. Huang IC, Li W, Sui J, Marasco W, Choe H, Farzan M. Influenza A virus neuraminidase limits viral superinfection. J Virol. 2008;82(10):4834-43.

59. Shapiro GI, Gurney T, Krug RM. Influenza virus gene expression: control mechanisms at early and late times of infection and nuclear-cytoplasmic transport of virus-specific RNAs. J Virol. 1987;61(3):764-73.

60. Hatada E, Hasegawa M, Mukaigawa J, Shimizu K, Fukuda R. Control of influenza virus gene expression: quantitative analysis of each viral RNA species in infected cells. J Biochem. 1989;105(4):537-46.

61. Enami M, Fukuda R, Ishihama A. Transcription and replication of eight RNA segments of influenza virus. Virology. 1985;142(1):68-77.

62. Cheung TK, Poon LL. Biology of influenza a virus. Annals of the New York Academy of Sciences. 2007;1102:1-25.

63. Kawakami E, Watanabe T, Fujii K, Goto H, Watanabe S, Noda T, et al. Strand-specific real-time RT-PCR for distinguishing influenza vRNA, cRNA, and mRNA. J Virol Methods. 2011;173(1):1-6.

64. Frensing T, Kupke SY, Bachmann M, Fritzsche S, Gallo-Ramirez LE, Reichl U. Influenza virus intracellular replication dynamics, release kinetics, and particle morphology during propagation in MDCK cells. Appl Microbiol Biotechnol. 2016;100(16):7181-92.

65. Rodriguez A, Pérez-González A, Nieto A. Influenza virus infection causes specific degradation of the largest subunit of cellular RNA polymerase II. J Virol. 2007;81(10):5315-24.

66. Martínez-Alonso M, Hengrung N, Fodor E. RNA-Free and Ribonucleoprotein-Associated Influenza Virus Polymerases Directly Bind the Serine-5-Phosphorylated Carboxyl-Terminal Domain of Host RNA Polymerase II. J Virol. 2016;90(13):6014-21.

67. Resa-Infante P, Jorba N, Coloma R, Ortín J. The influenza virus RNA synthesis machine: Advances in its structure and function. RNA Biol. 2011;8(2):207-15.

68. Neumann G, Hughes MT, Kawaoka Y. Influenza A virus NS2 protein mediates vRNP nuclear export through NES-independent interaction with hCRM1. EMBO J. 2000;19(24):6751-8.

69. Paterson D, Fodor E. Emerging roles for the influenza A virus nuclear export protein (NEP). PLoS Pathog. 2012;8(12):e1003019-e.

70. Akarsu H, Burmeister WP, Petosa C, Petit I, Müller CW, Ruigrok RWH, et al. Crystal structure of the M1 protein-binding domain of the influenza A virus nuclear export protein (NEP/NS2). EMBO J. 2003;22(18):4646-55.

71. Zvonarjev AY, Ghendon YZ. Influence of membrane (M) protein on influenza A virus virion transcriptase activity in vitro and its susceptibility to rimantadine. J Virol. 1980;33(2):583-6.

72. Hankins RW, Nagata K, Kato A, Ishihama A. Mechanism of influenza virus transcription inhibition by matrix (M1) protein. Res Virol. 1990;141(3):305-14.

73. Watanabe K, Handa H, Mizumoto K, Nagata K. Mechanism for inhibition of influenza virus RNA polymerase activity by matrix protein. J Virol. 1996;70(1):241-7.

74. Nasser EH, Judd AK, Sanchez A, Anastasiou D, Bucher DJ. Antiviral activity of influenza virus M1 zinc finger peptides. J Virol. 1996;70(12):8639-44.

75. Perez DR, Donis RO. The matrix 1 protein of influenza A virus inhibits the transcriptase activity of a model influenza reporter genome in vivo. Virology. 1998;249(1):52-61.

76. Baudin F, Petit I, Weissenhorn W, Ruigrok RW. In vitro dissection of the membrane and RNP binding activities of influenza virus M1 protein. Virology. 2001;281(1):102-8.

77. Mänz B, Brunotte L, Reuther P, Schwemmle M. Adaptive mutations in NEP compensate for defective H5N1 RNA replication in cultured human cells. Nat Commun. 2012;3:802-.

78. Brunotte L, Flies J, Bolte H, Reuther P, Vreede F, Schwemmle M. The Nuclear Export Protein of H5N1 Influenza A Viruses Recruits Matrix 1 (M1) Protein to the Viral Ribonucleoprotein to Mediate Nuclear Export. J Biol Chem. 2014;289(29):20067-77.

79. Zhang J, Pekosz A, Lamb RA. Influenza virus assembly and lipid raft microdomains: a role for the cytoplasmic tails of the spike glycoproteins. J Virol. 2000;74(10):4634-44.

80. Leser GP, Lamb RA. Influenza virus assembly and budding in raft-derived microdomains: a quantitative analysis of the surface distribution of HA, NA and M2 proteins. Virology. 2005;342(2):215-27.

81. Schroeder C, Heider H, Möncke-Buchner E, Lin T-I. The influenza virus ion channel and maturation cofactor M2 is a cholesterol-binding protein. Eur Biophys J. 2005;34(1):52-66.

82. Eisfeld AJ, Kawakami E, Watanabe T, Neumann G, Kawaoka Y. RAB11A is Essential for Influenza Genome Transport to the Plasma Membrane. J Virol. 2011;85(13):6117-26.

83. Amorim MJ, Bruce EA, Read EKC, Foeglein A, Mahen R, Stuart AD, et al. A Rab11 and microtubule dependent mechanism for cytoplasmic transport of influenza A virus vRNA. J Virol. 2011;85(9):4143-56.

84. Hutchinson EC, von Kirchbach JC, Gog JR, Digard P. Genome packaging in influenza A virus. J Gen Virol. 2010;91(Pt 2):313-28.

85. Noda T, Kawaoka Y. Structure of influenza virus ribonucleoprotein complexes and their packaging into virions. Rev Med Virol. 2010;20(6):380-91.

86. Fournier E, Moules V, Essere B, Paillart J-C, Sirbat J-D, Cavalier A, et al. Interaction network linking the human H3N2 influenza A virus genomic RNA segments. Vaccine. 2012;30(51):7359-67.

87. Fournier E, Moules V, Essere B, Paillart J-C, Sirbat J-D, Isel C, et al. A supramolecular assembly formed by influenza A virus genomic RNA segments. Nucleic Acids Res. 2012;40(5):2197-209.

88. Gavazzi C, Yver M, Isel C, Smyth RP, Rosa-Calatrava M, Lina B, et al. A functional sequence-specific interaction between influenza A virus genomic RNA segments. Proc Natl Acad Sci U S A. 2013;110(41):16604-9.

89.   Nakatsu S, Sagara H, Sakai-Tagawa Y, Sugaya N, Noda T, Kawaoka Y. Complete and Incomplete Genome Packaging of Influenza A and B Viruses. mBio. 2016;7(5).
90.   Rossman JS, Lamb RA. Influenza virus assembly and budding. Virology. 2011;411(2):229-36.
91.   Chen BJ, Leser GP, Morita E, Lamb RA. Influenza virus hemagglutinin and neuraminidase, but not the matrix protein, are required for assembly and budding of plasmid-derived virus-like particles. J Virol. 2007;81(13):7111-23.
92.   Rossman JS, Lamb RA. Viral Membrane Scission. Annu Rev Cell Dev Biol. 2013;29(1):551-69.
93.   Ghorbani A, Ngunjiri JM, Lee CW. Influenza A Virus Subpopulations and Their Implication in Pathogenesis and Vaccine Development. Annual review of animal biosciences. 2020;8:247-67.
94.   Huang AS, Baltimore D. Defective viral particles and viral disease processes. Nature. 1970;226(5243):325-7.
95.   Nayak DP, Chambers TM, Akkina RK. Defective-interfering (DI) RNAs of influenza viruses: origin, structure, expression, and interference. Curr Top Microbiol Immunol. 1985;114:103-51.
96.   Raj A, van Oudenaarden A. Nature, nurture, or chance: stochastic gene expression and its consequences. Cell. 2008;135(2):216-26.
97.   Stegmann T, Schoen P, Bron R, Wey J, Bartoldus I, Ortiz A, et al. Evaluation of viral membrane fusion assays. Comparison of the octadecylrhodamine dequenching assay with the pyrene excimer assay. Biochemistry. 1993;32(42):11330-7.
98.   Schelker M, Mair CM, Jolmes F, Welke R-W, Klipp E, Herrmann A, et al. Viral RNA Degradation and Diffusion Act as a Bottleneck for the influenza A Virus Infection Efficiency. PLoS Comput Biol. 2016;12(10):e1005075-e.
99.   Heldt FS, Kupke SY, Dorl S, Reichl U, Frensing T. Single-cell analysis and stochastic modelling unveil large cell-to-cell variability in influenza A virus infection. Nat Commun. 2015;6:8938-.
100. Ngunjiri JM, Sekellick MJ, Marcus PI. Clonogenic assay of type a influenza viruses reveals noninfectious cell-killing (apoptosis-inducing) particles. J Virol. 2008;82(6):2673-80.
101. Marcus PI, Ngunjiri JM, Sekellick MJ. Dynamics of biologically active subpopulations of influenza virus: plaque-forming, noninfectious cell-killing, and defective interfering particles. J Virol. 2009;83(16):8122-30.
102. Diefenbacher M, Sun J, Brooke CB. The parts are greater than the whole: the role of semi-infectious particles in influenza A virus biology. Current Opinion in Virology. 2018;33:42-6.
103. Brooke CB, Ince WL, Wrammert J, Ahmed R, Wilson PC, Bennink JR, et al. Most influenza A virions fail to express at least one essential viral protein. J Virol. 2013;87(6):3155-62.
104. Virology -- A Laboratory Manual. Burleson FG, Chambers TM, Wiedebrauk DL, editors: Academic Press Inc.; 1992.
105. Hierholzer JC, Killington RA. Virus Isolation and Quantitation. In: Brian W. J. Mahy and Hillar O. Kangro (ed.), Virology Methods Manual. San Diego, CA: Academic Press Inc.; 1996. p. 25-46.

106. Burleson FG, Chambers TM, Wiedebrauk DL. Hemagglutination assay. In: Virology -- A Laboratory Manual. San Diego, CA: Academic Press; 1992. p. 86-92.

107. Genzel Y, Reichl U. Vaccine production -- state of the art and future needs in upstream processing. In: Poertner R, editor. Animal Cell Biotechnology: Methods and Protocols: Humana Press; 2007. p. 457-73.

108. Henle W, Henle G. Interference of inactive virus with the propagation of virus of influenza. Science. 1943;98(2534):87-9.

109. von Magnus P. Propagation of the PR8 strain of influenza A virus in chick embryos. II. The formation of incomplete virus following inoculation of large doses of seed virus. Acta Pathol Microbiol Scand. 1951;28(3):278-93.

110. von Magnus P. Incomplete forms of influenza virus. Adv Virus Res. 1954;2:59-79.

111. Saira K, Lin X, DePasse JV, Halpin R, Twaddle A, Stockwell T, et al. Sequence analysis of in vivo defective interfering-like RNA of influenza A H1N1 pandemic virus. J Virol. 2013;87(14):8064-74.

112. Huang AS. Defective interfering viruses. Annu Rev Microbiol. 1973;27:101-17.

113. Marriott AC, Dimmock NJ. Defective interfering viruses and their potential as antiviral agents. Rev Med Virol. 2010;20(1):51-62.

114. Frensing T. Defective interfering viruses and their impact on vaccines and viral vectors. Biotechnol J. 2015;10(5):681-9.

115. Gould PS, Easton AJ, Dimmock NJ. Live Attenuated Influenza Vaccine contains Substantial and Unexpected Amounts of Defective Viral Genomic RNA. Viruses. 2017;9(10):296-.

116. Breen M, Nogales A, Baker S, Martínez-Sobrido L. Replication-Competent Influenza A Viruses Expressing Reporter Genes. Viruses. 2016;8(7):179-.

117. Alnaji FG, Brooke CB. Influenza virus DI particles: Defective interfering or delightfully interesting? PLoS Pathog. 2020;16(5):e1008436-e.

118. Alnaji FG, Holmes JR, Rendon G, Vera JC, Fields CJ, Martin BE, et al. Sequencing Framework for the Sensitive Detection and Precise Mapping of Defective Interfering Particle-Associated Deletions across Influenza A and B Viruses. J Virol. 2019;93(11).

119. Jennings PA, Finch JT, Winter G, Robertson JS. Does the higher order structure of the influenza virus ribonucleoprotein guide sequence rearrangements in influenza viral RNA? Cell. 1983;34(2):619-27.

120. Davis AR, Nayak DP. Sequence relationships among defective interfering influenza viral RNAs. Proc Natl Acad Sci U S A. 1979;76(7):3092-6.

121. Pelz L, Rüdiger D, Dogra T, Alnaji FG, Genzel Y, Brooke CB, et al. Semi-continuous propagation of influenza A virus and its defective interfering particles: analyzing the dynamic competition to select candidates for antiviral therapy. J Virol. 2021:Jvi0117421.

122. Kupke SY, Riedel D, Frensing T, Zmora P, Reichl U. A Novel Type of Influenza A Virus-Derived Defective Interfering Particle with Nucleotide Substitutions in Its Genome. J Virol. 2019;93(4):e01786-18.

123. Vignuzzi M, López CB. Defective viral genomes are key drivers of the virustextendashhost interaction. Nat Microbiol. 2019;4(7):1075-87.

124. Genoyer E, López CB. The Impact of Defective Viruses on Infection and Immunity. Annu Rev Virol. 2019;6(1):547-66.

125. Rüdiger D, Pelz L, Hein MD, Kupke SY, Reichl U. Multiscale model of defective interfering particle replication for influenza A virus infection in animal cell culture. PLoS Comput Biol. 2021;17(9):e1009357.

126. Phan T, Fay EJ, Lee Z, Aron S, Hu WS, Langlois RA. Segment-specific kinetics of mRNA, cRNA and vRNA accumulation during influenza infection. J Virol. 2021;95(10).

127. Akkina RK, Chambers TM, Nayak DP. Expression of defective-interfering influenza virus-specific transcripts and polypeptides in infected cells. J Virol. 1984;51(2):395-403.

128. Duhaut SD, McCauley JW. Defective RNAs inhibit the assembly of influenza virus genome segments in a segment-specific manner. Virology. 1996;216(2):326-37.

129. Odagiri T, Tominaga K, Tobita K, Ohta S. An amino acid change in the non-structural NS2 protein of an influenza A virus mutant is responsible for the generation of defective interfering (DI) particles by amplifying DI RNAs and suppressing complementary RNA synthesis. J Gen Virol. 1994;75 (Pt 1):43-53.

130. Widjaja I, de Vries E, Rottier PJM, de Haan CAM. Competition between Influenza A Virus Genome Segments. PLoS One. 2012;7(10):e47529-e.

131. Odagiri T, Tashiro M. Segment-specific noncoding sequences of the influenza virus genome RNA are involved in the specific competition between defective interfering RNA and its progenitor RNA segment at the virion assembly step. J Virol. 1997;71(3):2138-45.

132. Duhaut SD, Dimmock NJ. Defective segment 1 RNAs that interfere with production of infectious influenza A virus require at least 150 nucleotides of 5' sequence: evidence from a plasmid-driven system. J Gen Virol. 2002;83(Pt 2):403-11.

133. Giachetti C, Holland JJ. Vesicular stomatitis virus and its defective interfering particles exhibit in vitro transcriptional and replicative competition for purified L-NS polymerase molecules. Virology. 1989;170(1):264-7.

134. Chanda PK, Chambers TM, Nayak DP. In vitro transcription of defective interfering particles of influenza virus produces polyadenylic acid-containing complementary RNAs. J Virol. 1983;45(1):55-61.

135. Boergeling Y, Rozhdestvensky TS, Schmolke M, Resa-Infante P, Robeck T, Randau G, et al. Evidence for a Novel Mechanism of Influenza Virus-Induced Type I Interferon Expression by a Defective RNA-Encoded Protein. PLoS Pathog. 2015;11(5):e1004924-e.

136. Sekellick MJ, Marcus PI. Viral interference by defective particles of vesicular stomatitis virus measured in individual cells. Virology. 1980;104(1):247-52.

137. Stauffer-Thompson KA, Rempala GA, Yin J. Multiple-hit inhibition of infection by defective interfering particles. J Gen Virol. 2009;90(Pt 4):888-99.

138. Vasilijevic J, Zamarreño N, Oliveros JC, Rodriguez-Frandsen A, Gómez G, Rodriguez G, et al. Reduced accumulation of defective viral genomes contributes to severe outcome in influenza virus infected patients. PLoS Pathog. 2017;13:e1006650-e.

139. Ke R, Aaskov J, Holmes EC, Lloyd-Smith JO. Phylodynamic Analysis of the Emergence and Epidemiological Impact of Transmissible Defective Dengue Viruses. PLoS Pathog. 2013;9(2):e1003193-e.

140. Dimmock NJ, Beck S, McLain L. Protection of mice from lethal influenza: evidence that defective interfering virus modulates the immune response and not virus multiplication. J Gen Virol. 1986;67 (Pt 5):839-50.

141. Hein MD, Arora P, Marichal-Gallardo P, Winkler M, Genzel Y, Pöhlmann S, et al. Cell culture-based production and in vivo characterization of purely clonal defective interfering influenza virus particles. BMC Biol. 2021;19(1):91.

142. Scott PD, Meng B, Marriott AC, Easton AJ, Dimmock NJ. Defective interfering influenza A virus protects in vivo against disease caused by a heterologous influenza B virus. J Gen Virol. 2011;92(9):2122-32.

143. Easton AJ, Scott PD, Edworthy NL, Meng B, Marriott AC, Dimmock NJ. A novel broad-spectrum treatment for respiratory virus infections: Influenza-based defective interfering virus provides protection against pneumovirus infection in vivo. Vaccine. 2011;29(15):2777-84.

144. Rand U, Kupke SY, Shkarlet H, Hein MD, Hirsch T, Marichal-Gallardo P, et al. Antiviral Activity of Influenza A Virus Defective Interfering Particles against SARS-CoV-2 Replication In Vitro through Stimulation of Innate Immunity. Cells. 2021;10(7).

145. Laborda P, Wang SY, Voglmeir J. Influenza Neuraminidase Inhibitors: Synthetic Approaches, Derivatives and Biological Activity. Molecules (Basel, Switzerland). 2016;21(11).

146. Omoto S, Speranzini V, Hashimoto T, Noshi T, Yamaguchi H, Kawai M, et al. Characterization of influenza virus variants induced by treatment with the endonuclease inhibitor baloxavir marboxil. Sci Rep. 2018;8(1):9633.

147. Killip MJ, Fodor E, Randall RE. Influenza virus activation of the interferon system. Virus Res. 2015;209:11-22.

148. Noble S, McLain L, Dimmock NJ. Interfering vaccine: a novel antiviral that converts a potentially virulent infection into one that is subclinical and immunizing. Vaccine. 2004;22(23-24):3018-25.

149. Baum A, García-Sastre A. Differential recognition of viral RNA by RIG-I. Virulence. 2011;2(2):166-9.

150. Rehwinkel J, Tan CP, Goubau D, Schulz O, Pichlmair A, Bier K, et al. RIG-I detects viral genomic RNA during negative-strand RNA virus infection. Cell. 2010;140(3):397-408.

151. te Velthuis AJW, Long JC, Bauer DLV, Fan RLY, Yen H-L, Sharps J, et al. Mini viral RNAs act as innate immune agonists during influenza virus infection. Nat Microbiol. 2018;3(11):1234-42.

152. López CB. Defective viral genomes: critical danger signals of viral infections. J Virol. 2014;88:8720-3.

153. Thomas F, Magill TP. Vaccination of Human Subjects with Virus of Human Influenza. Exp Biol Med. 1936;33(4):604-6.

154. Shaw A. New technologies for new influenza vaccines. Vaccine. 2012;30(33):4927-33.

155. Hannoun C. The evolving history of influenza viruses and influenza vaccines. Expert Rev Vaccines. 2013;12(9):1085-94.

156. Cox MMJ, Patriarca PA, Treanor J. FluBlok, a recombinant hemagglutinin influenza vaccine. Influenza Other Respir Viruses. 2008;2(6):211-9.

157. Treanor JJ, Campbell JD, Brady RC, Keitel WA, Drame M, Jain VK, et al. Rapid Licensure of a New, Inactivated Influenza Vaccine in the United States. Human Vaccines. 2005;1(6):239-44.

158. Doroshenko A, Halperin SA. Trivalent MDCK cell culture-derived influenza vaccine Optaflutextregistered (Novartis Vaccines). Expert Rev Vaccines. 2009;8(6):679-88.

159. Verbeke R, Lentacker I, De Smedt SC, Dewitte H. Three decades of messenger RNA vaccine development. Nano Today. 2019;28:100766.

160. Feldman RA, Fuhr R, Smolenov I, Mick Ribeiro A, Panther L, Watson M, et al. mRNA vaccines against H10N8 and H7N9 influenza viruses of pandemic potential are immunogenic and well tolerated in healthy adults in phase 1 randomized clinical trials. Vaccine. 2019;37(25):3326-34.

161. Freyn AW, Ramos da Silva J, Rosado VC, Bliss CM, Pine M, Mui BL, et al. A Multi-Targeting, Nucleoside-Modified mRNA Influenza Virus Vaccine Provides Broad Protection in Mice. Mol Ther. 2020;28:1569-84.

162. Moderna. Moderna Announces First Participant Dosed in Phase 1/2 Study of Its Quadrivalent Seasonal Flu mRNA Vaccine. 2021 [cited 15 July 2021]. Available from: https://investors.modernatx.com/news-releases/news-release-details/moderna-announces-first-participant-dosed-phase-12-study-its.

163. Yamayoshi S, Kawaoka Y. Current and future influenza vaccines. Nature Medicine. 2019;25(2):212-20.

164. Milián E, Kamen AA. Current and emerging cell culture manufacturing technologies for influenza vaccines. Biomed Res Int. 2015;2015:504831.

165. Perdue ML, Arnold F, Li S, Donabedian A, Cioce V, Warf T, et al. The future of cell culture-based influenza vaccine production. Expert Rev Vaccines. 2011;10(8):1183-94.

166. Blume S. A Brief History of Polio Vaccines. Science. 2000;288(5471):1593-4.

167. Brands R, Visser J, Medema J, Palache AM, van Scharrenburg GJ. Influvac: a safe Madin Darby Canine Kidney (MDCK) cell culture-based influenza vaccine. Dev Biol Stand. 1999;98:93-100.

168. Lee M-S, Hu AY-C. A cell-based backup to speed up pandemic influenza vaccine production. Trends Microbiol. 2012;20(3):103-5.

169. Hegde NR. Cell culture-based influenza vaccines: A necessary and indispensable investment for the future. Human Vaccines & Immunotherapeutics. 2015;11(5):1223-34.

170. Tree JA, Richardson C, Fooks AR, Clegg JC, Looby D. Comparison of large-scale mammalian cell culture systems with egg culture for the production of influenza virus A vaccine strains. Vaccine. 2001;19(25-26):3444-50.

171. Ru AL, Jacob D, Transfiguracion J, Ansorge S, Henry O, Kamen AA. Scalable production of influenza virus in HEK-293 cells for efficient vaccine manufacturing. Vaccine. 2010;28(21):3661-71.

172. Price PM, Reichelderfer CF, Johansson BE, Kilbourne ED, Acs G. Complementation of recombinant baculoviruses by coinfection with wild-type virus facilitates production in insect larvae of antigenic proteins of hepatitis B virus and influenza virus. Proc Natl Acad Sci U S A. 1989;86(5):1453-6.

173. Genzel Y, Behrendt I, Rödig J, Rapp E, Kueppers C, Kochanek S, et al. CAP, a new human suspension cell line for influenza virus production. Appl Microbiol Biotechnol. 2012;97(1):111-22.

174. Pau MG, Ophorst C, Koldijk MH, Schouten G, Mehtali M, Uytdehaag F. The human cell line PER.C6 provides a new manufacturing system for the production of influenza vaccines. Vaccine. 2001;19:2716-21.

175. Genzel Y, Reichl U. Continuous cell lines as a production system for influenza vaccines. Expert Rev Vaccines. 2009;8(12):1681-92.

176. Gröner A, Vorlop J. Patent WO 1997/037000: Animal cells and processes for the replication of influenza viruses (Chiron Behring GmbH & Co). 1997.

177. Rubio AP, Eiros JM. Cell culture-derived flu vaccine: Present and future. Human Vaccines & Immunotherapeutics. 2018;14(8):1874-82.

178. Bdeir N, Arora P, Gärtner S, Hoffmann M, Reichl U, Pöhlmann S, et al. A system for production of defective interfering particles in the absence of infectious influenza A virus. PLoS One. 2019;14(3):e0212757-e.

179. Isken B, Genzel Y, Reichl U. Productivity, apoptosis, and infection dynamics of influenza A/PR/8 strains and A/PR/8-based reassortants. Vaccine. 2012;30(35):5253-61.

180. Aggarwal K, Jing F, Maranga L, Liu J. Bioprocess optimization for cell culture based influenza vaccine production. Vaccine. 2011;29(17):3320-8.

181. Rüdiger D, Kupke SY, Laske T, Zmora P, Reichl U. Multiscale modeling of influenza A virus replication in cell cultures predicts infection dynamics for highly different infection conditions. PLoS Comput Biol. 2019;15(2):1-22.

182. Lee CW. Reverse genetics of influenza virus. Methods Mol Biol. 2014;1161:37-50.

183. Frensing T, Heldt FS, Pflugmacher A, Behrendt I, Jordan I, Flockerzi D, et al. Continuous influenza virus production in cell culture shows a periodic accumulation of defective interfering particles. PLoS One. 2013;8(9):e72288-e.

184. Tapia F, Laske T, Wasik MA, Rammhold M, Genzel Y, Reichl U. Production of Defective Interfering Particles of Influenza A Virus in Parallel Continuous Cultures at Two Residence Times - Insights From qPCR Measurements and Viral Dynamics Modeling. Front Bioeng Biotechnol. 2019;7:275-.

185. Perelson AS. Modelling viral and immune system dynamics. Nat Rev Immunol. 2002;2(1):28-36.

186. Elowitz MB, Levine AJ, Siggia ED, Swain PS. Stochastic gene expression in a single cell. Science. 2002;297(5584):1183-6.

187. Srivastava R, You L, Summers J, Yin J. Stochastic vs. deterministic modeling of intracellular viral kinetics. J Theor Biol. 2002;218(3):309-21.

188. Dolgov SV, Savostyanov DV. Alternating Minimal Energy Methods for Linear Systems in Higher Dimensions. SIAM Journal on Scientific Computing. 2014;36(5):A2248-A71.

189. Kazeev V, Khammash M, Nip M, Schwab C. Direct solution of the Chemical Master Equation using quantized tensor trains. PLoS Comput Biol. 2014;10(3):e1003359.

190. Gillespie DT. A general method for numerically simulating the stochastic time evolution of coupled chemical reactions. Journal of Computational Physics. 1976;22(4):403-34.

191. Gillespie DT. Stochastic simulation of chemical kinetics. Annu Rev Phys Chem. 2007;58:35-55.

192. Cao Y, Gillespie DT, Petzold LR. Efficient step size selection for the tau-leaping simulation method. J Chem Phys. 2006;124(4):044109-.

193. Lecca P, Bagagiolo F, Scarpa M. Hybrid deterministic/stochastic simulation of complex biochemical systems. Mol Biosyst. 2017;13(12):2672-86.
194. Ahmadian M, Tyson JJ, Peccoud J, Cao Y. A hybrid stochastic model of the budding yeast cell cycle. NPJ Syst Biol Appl. 2020;6(1):7.
195. Beauchemin C, Samuel J, Tuszynski J. A simple cellular automaton model for influenza A viral infections. J Theor Biol. 2005;232(2):223-34.
196. Lin H, Shuai JW. A stochastic spatial model of HIV dynamics with an asymmetric battle between the virus and the immune system. New J Phys. 2010;12(4):043051-.
197. Akpinar F, Inankur B, Yin J. Spatial-Temporal Patterns of Viral Amplification and Interference Initiated by a Single Infected Cell. J Virol. 2016;90(16):7552-66.
198. Bauer AL, Beauchemin CAA, Perelson AS. Agent-based modeling of host-pathogen systems: The successes and challenges. Inf Sci. 2009;179(10):1379-89.
199. Murray JM, Goyal A. In silico single cell dynamics of hepatitis B virus infection and clearance. J Theor Biol. 2015;366:91-102.
200. Madrahimov A, Helikar T, Kowal B, Lu G, Rogers J. Dynamics of influenza virus and human host interactions during infection and replication cycle. Bull Math Biol. 2013;75(6):988-1011.
201. Haseltine EL, Rawlings JB, Yin J. Dynamics of viral infections: incorporating both the intracellular and extracellular levels. Comput Chem Eng. 2005;29(3):675-86.
202. Müller T, Dürr R, Isken B, Schulze-Horsel J, Reichl U, Kienle A. Distributed modeling of human influenza A virus-host cell interactions during vaccine production. Biotechnol Bioeng. 2013;110(8):2252-66.
203. Dropkin G. COVID-19 UK Lockdown Forecasts and R (0). Frontiers in public health. 2020;8:256.
204. Smith AM, Perelson AS. Influenza A virus infection kinetics: quantitative data and models. Wiley Interdiscip Rev Syst Biol Med. 2011;3(4):429-45.
205. Perelson AS, Neumann AU, Markowitz M, Leonard JM, Ho DD. HIV-1 dynamics in vivo: virion clearance rate, infected cell life-span, and viral generation time. Science. 1996;271(5255):1582-6.
206. Perelson A, Nelson P. Mathematical Analysis of HIV-1 Dynamics in Vivo. SIAM Rev. 1999;41(1):3-44.
207. De Boer RJ, Perelson AS. Target cell limited and immune control models of HIV infection: a comparison. J Theor Biol. 1998;190(3):201-14.
208. Kirschner D, Webb GF, Cloyd M. Model of HIV-1 disease progression based on virus-induced lymph node homing and homing-induced apoptosis of CD4+ lymphocytes. J Acquir Immune Defic Syndr. 2000;24(4):352-62.
209. Rong L, Perelson AS. Modeling HIV persistence, the latent reservoir, and viral blips. J Theor Biol. 2009;260(2):308-31.
210. Wang S, Rong L. Stochastic population switch may explain the latent reservoir stability and intermittent viral blips in HIV patients on suppressive therapy. J Theor Biol. 2014;360C:137-48.
211. Alizon S, Magnus C. Modelling the Course of an HIV Infection: Insights from Ecology and Evolution. Viruses. 2012;4(10):1984-2013.

212. Rosenbloom DIS, Hill AL, Rabi SA, Siliciano RF, Nowak MA. Antiretroviral dynamics determines HIV evolution and predicts therapy outcome. Nat Med. 2012;18(9):1378-85.

213. Iwami S, Koizumi Y, Ikeda H, Kakizoe Y. Quantification of viral infection dynamics in animal experiments. Front Microbiol. 2013;4:264-.

214. Chatterjee A, Smith PF, Perelson AS. Hepatitis C viral kinetics: the past, present, and future. Clin Liver Dis. 2013;17(1):13-26.

215. Bernhauerová V, Rezelj VV, Vignuzzi M. Modelling Degradation and Replication Kinetics of the Zika Virus In Vitro Infection. Viruses. 2020;12(5):547-.

216. Brugnano L, Iavernaro F, Zanzottera P. A multiregional extension of the SIR model, with application to the COVID-19 spread in Italy. Mathematical methods in the applied sciences. 2020.

217. Lloyd AL. The dependence of viral parameter estimates on the assumed viral life cycle: limitations of studies of viral load data. Proc Biol Sci. 2001;268(1469):847-54.

218. Baccam P, Beauchemin C, Macken CA, Hayden FG, Perelson AS. Kinetics of influenza A virus infection in humans. J Virol. 2006;80(15):7590-9.

219. Larson EW, Dominik JW, Rowberg AH, Higbee GA. Influenza virus population dynamics in the respiratory tract of experimentally infected mice. Infect Immun. 1976;13(2):438-47.

220. Bocharov GA, Romanyukha AA. Mathematical model of antiviral immune response. III. Influenza A virus infection. J Theor Biol. 1994;167(4):323-60.

221. Saenz RA, Quinlivan M, Elton D, Macrae S, Blunden AS, Mumford JA, et al. Dynamics of influenza virus infection and pathology. J Virol. 2010;84(8):3974-83.

222. Tridane A, Kuang Y. Modeling the interaction of cytotoxic T lymphocytes and influenza virus infected epithelial cells. Math Biosci Eng. 2010;7(1):171-85.

223. Handel A, Longini IM, Antia R. Towards a quantitative understanding of the within-host dynamics of influenza A infections. J R Soc Interface. 2010;7(42):35-47.

224. Beauchemin CAA, McSharry JJ, Drusano GL, Nguyen JT, Went GT, Ribeiro RM, et al. Modeling amantadine treatment of influenza A virus in vitro. J Theor Biol. 2008;254(2):439-51.

225. Zitzmann C, Kaderali L. Mathematical Analysis of Viral Replication Dynamics and Antiviral Treatment Strategies: From Basic Models to Age-Based Multi-Scale Modeling. Front Microbiol. 2018;9.

226. Perelson AS, Rong L, Hayden FG. Combination antiviral therapy for influenza: predictions from modeling of human infections. J Infect Dis. 2012;205(11):1642-5.

227. Kamal MA, Gieschke R, Lemenuel-Diot A, Beauchemin CAA, Smith PF, Rayner CR. A Drug-Disease Model Describing the Effect of Oseltamivir Neuraminidase Inhibition on Influenza Virus Progression. Antimicrob Agents Chemother. 2015;59(9):5388-95.

228. Quirouette C, Younis NP, Reddy MB, Beauchemin CAA. A mathematical model describing the localization and spread of influenza A virus infection within the human respiratory tract. PLoS Comput Biol. 2020;16(4):e1007705.

229. Dobrovolny HM, Reddy MB, Kamal MA, Rayner CR, Beauchemin CAA. Assessing mathematical models of influenza infections using features of the immune response. PLoS One. 2013;8(2):e57088-e.
230. Möhler L, Flockerzi D, Sann H, Reichl U. Mathematical model of influenza A virus production in large-scale microcarrier culture. Biotechnol Bioeng. 2005;90(1):46-58.
231. Schulze-Horsel J, Schulze M, Agalaridis G, Genzel Y, Reichl U. Infection dynamics and virus-induced apoptosis in cell culture-based influenza vaccine production-Flow cytometry and mathematical modeling. Vaccine. 2009;27(20):2712-22.
232. Sidorenko Y, Schulze-Horsel J, Voigt A, Reichl U, Kienle A. Stochastic population balance modeling of influenza virus replication in vaccine production processes. Chem Eng Sci. 2008;63(1):157-69.
233. Sidorenko Y, Voigt A, Schulze-Horsel J, Reichl U, Kienle A. Stochastic population balance modeling of influenza virus replication in vaccine production processes. II. Detailed description of the replication mechanism. Chem Eng Sci. 2008;63(8):2299-304.
234. Martin BE, Harris JD, Sun J, Koelle K, Brooke CB. Cellular co-infection can modulate the efficiency of influenza A virus production and shape the interferon response. PLoS Pathog. 2020;16(10):e1008974.
235. Yin J, Redovich J. Kinetic Modeling of Virus Growth in Cells. Microbiol Mol Biol Rev. 2018;82(2).
236. Dee KU, Hammer DA, Shuler ML. A model of the binding, entry, uncoating, and RNA synthesis of Semliki Forest virus in baby hamster kidney (BHK-21) cells. Biotechnol Bioeng. 1995;46(5):485-96.
237. Dee KU, Shuler ML. A mathematical model of the trafficking of acid-dependent enveloped viruses: application to the binding, uptake, and nuclear accumulation of baculovirus. Biotechnol Bioeng. 1997;54(5):468-90.
238. Reddy B, Yin J. Quantitative intracellular kinetics of HIV type 1. AIDS Res Hum Retroviruses. 1999;15(3):273-83.
239. Yin L, Xu S, Cheng J, Zheng D, Limmon GV, Leung NHN, et al. Spatiotemporal quantification of cell dynamics in the lung following influenza virus infection. J Biomed Opt. 2013;18(4):046001-.
240. Sidorenko Y, Reichl U. Structured model of influenza virus replication in MDCK cells. Biotechnol Bioeng. 2004;88(1):1-14.
241. Bazhan SI, Kashevarova NA, Khlebodarova TM, Likhoshvaĭ VA, Kolchanov NA. A mathematical model of the intracellular reproduction of the influenza virus. (in Russian). Biofizika. 2009;54:1066-80.
242. Heldt FS, Frensing T, Reichl U. Modeling the intracellular dynamics of influenza virus replication to understand the control of viral RNA synthesis. J Virol. 2012;86(15):7806-17.
243. Haseltine EL, Yin J, Rawlings JB. Implications of decoupling the intracellular and extracellular levels in multi-level models of virus growth. Biotechnol Bioeng. 2008;101(4):811-20.
244. Murillo LN, Murillo MS, Perelson AS. Towards multiscale modeling of influenza infection. J Theor Biol. 2013;332:267-90.

245. Sattenspiel L, Dimka J, Orbann C. Using cultural, historical, and epidemiological data to inform, calibrate, and verify model structures in agent-based simulations. Math Biosci Eng. 2019;16(4):3071-93.
246. Handel A, Brown J, Stallknecht D, Rohani P. A multi-scale analysis of influenza A virus fitness trade-offs due to temperature-dependent virus persistence. PLoS Comput Biol. 2013;9(3):e1002989-e.
247. Guedj J, Neumann AU. Understanding hepatitis C viral dynamics with direct-acting antiviral agents due to the interplay between intracellular replication and cellular infection dynamics. J Theor Biol. 2010;267(3):330-40.
248. Guedj J, Dahari H, Rong L, Sansone ND, Nettles RE, Cotler SJ, et al. Modeling shows that the NS5A inhibitor daclatasvir has two modes of action and yields a shorter estimate of the hepatitis C virus half-life. Proc Natl Acad Sci U S A. 2013;110(10):3991-6.
249. Smale S. On the differential equations of species in competition. J Math Biol. 1976;3(1):5-7.
250. Sprott JC, Wildenberg JC, Azizi Y. A simple spatiotemporal chaotic Lotka–Volterra model. Chaos, Solitons & Fractals. 2005;26(4):1035-43.
251. Bangham CR, Kirkwood TB. Defective interfering particles: effects in modulating virus growth and persistence. Virology. 1990;179(2):821-6.
252. Szathmáry E. Co-operation and defection: playing the field in virus dynamics. J Theor Biol. 1993;165(3):341-56.
253. Kirkwood TB, Bangham CR. Cycles, chaos, and evolution in virus cultures: a model of defective interfering particles. Proc Natl Acad Sci U S A. 1994;91(18):8685-9.
254. Stauffer-Thompson KA, Yin J. Population dynamics of an RNA virus and its defective interfering particles in passage cultures. Virol J. 2010;7:257-.
255. Liao LE, Iwami S, Beauchemin CAA. (In)validating experimentally derived knowledge about influenza A defective interfering particles. J R Soc Interface. 2016;13(124):20160412-.
256. Zwart MP, Pijlman GP, Sardanyés J, Duarte J, Januário C, Elena SF. Complex dynamics of defective interfering baculoviruses during serial passage in insect cells. J Biol Phys. 2013;39(2):327-42.
257. Laske T, Heldt FS, Hoffmann H, Frensing T, Reichl U. Modeling the intracellular replication of influenza A virus in the presence of defective interfering RNAs. Virus Res. 2016;213:90-9.
258. Akpinar F, Timm A, Yin J. High-Throughput Single-Cell Kinetics of Virus Infections in the Presence of Defective Interfering Particles. J Virol. 2016;90(3):1599-612.
259. Meir M, Harel N, Miller D, Gelbart M, Eldar A, Gophna U, et al. Competition between social cheater viruses is driven by mechanistically different cheating strategies. Science advances. 2020;6(34).
260. Raue A, Kreutz C, Maiwald T, Bachmann J, Schilling M, Klingmüller U, et al. Structural and practical identifiability analysis of partially observed dynamical models by exploiting the profile likelihood. Bioinformatics. 2009;25(15):1923-9.
261. van Riel NAW. Dynamic modelling and analysis of biochemical networks: mechanism-based models and model-based experiments. Brief Bioinform. 2006;7(4):364-74.

262. Gutenkunst RN, Waterfall JJ, Casey FP, Brown KS, Myers CR, Sethna JP. Universally sloppy parameter sensitivities in systems biology models. PLoS Comput Biol. 2007;3(10):1871-8.

263. Joshi M, Seidel-Morgenstern A, Kremling A. Exploiting the bootstrap method for quantifying parameter confidence intervals in dynamical systems. Metab Eng. 2006;8(5):447-55.

264. Efron B, Tibshirani R. Bootstrap Methods for Standard Errors, Confidence Intervals, and Other Measures of Statistical Accuracy. Statistical Science. 1986;1(1):pp. 54-75-.

265. Ding J, Tarokh V, Yang Y. Model Selection Techniques: An Overview. IEEE Signal Processing Magazine. 2018;35(6):16-34.

266. Akaike H. A new look at the statistical model identification. IEEE Transactions on Automatic Control. 1974;19(6):716-23.

267. Burnham KP, Anderson DR. Multimodel inference - understanding AIC and BIC in model selection. SOCIOLOGICAL METHODS & RESEARCH. 2004;33(2):261-304.

268. Bowling SR, Khasawneh MT, Kaewkuekool S, Cho BR. A logistic approximation to the cumulative normal distribution. Journal of Industrial Engineering and Management; Vol 2, No 1 (2009). 2009.

269. Nunes-Correia I, Ramalho-Santos J, Nir S, de Lima MCP. Interactions of influenza virus with cultured cells: detailed kinetic modeling of binding and endocytosis. Biochemistry. 1999;38(3):1095-101.

270. Dou D, Hernández-Neuta I, Wang H, Östbye H, Qian X, Thiele S, et al. Analysis of IAV Replication and Co-infection Dynamics by a Versatile RNA Viral Genome Labeling Method. Cell Reports. 2017;20:251-63.

271. Bean WJ, Jr., Simpson RW. Primary transcription of the influenza virus genome in permissive cells. Virology. 1973;56(2):646-51.

272. Hay AJ, Lomniczi B, Bellamy AR, Skehel JJ. Transcription of the influenza virus genome. Virology. 1977;83(2):337-55.

273. Schmidt H, Jirstrand M. Systems Biology Toolbox for MATLAB: a computational platform for research in systems biology. Bioinformatics. 2006;22(4):514-5.

274. Cohen SD, Hindmarsh AC. CVODE, a stiff/nonstiff ODE solver in C. Computers in Physics. 1996;10(2):138-43.

275. Egea JA, Rodriguez-Fernandez M, Banga JR, Marti R. Scatter search for chemical and bio-process optimization. J Global Optim. 2007;37(3):481-503.

276. Hansen N, Ostermeier A. Completely Derandomized Self-Adaptation in Evolution Strategies. Evolutionary Computation. 2001;9(2):159-95.

277. Holder BP, Beauchemin CAA. Exploring the effect of biological delays in kinetic models of influenza within a host or cell culture. BMC Public Health. 2011;11 Suppl 1:S10.

278. Thomson BJ. Viruses and apoptosis. International journal of experimental pathology. 2001;82(2):65-76.

279. Nelson PW, Gilchrist MA, Coombs D, Hyman JM, Perelson AS. An age-structured model of hiv infection that allows for variations in the production rate of viral particles and the death rate of productively infected cells. Math Biosci Eng. 2004;1(2):267-88.

280. Mohsin MA, Morris SJ, Smith H, Sweet C. Correlation between levels of apoptosis, levels of infection and haemagglutinin receptor binding interaction of

various subtypes of influenza virus: does the viral neuraminidase have a role in these associations. Virus Res. 2002;85(2):123-31.

281. Ritter JB, Wahl AS, Freund S, Genzel Y, Reichl U. Metabolic effects of influenza virus infection in cultured animal cells: Intra- and extracellular metabolite profiling. BMC Syst Biol. 2010;4:61.

282. Rosenberger CM, Podyminogin RL, Askovich PS, Navarro G, Kaiser SM, Sanders CJ, et al. Characterization of innate responses to influenza virus infection in a novel lung type I epithelial cell model. J Gen Virol. 2014;95(Pt 2):350-62.

283. Liu X, Zhao Z, Xu C, Sun L, Chen J, Zhang L, et al. Cyclophilin A restricts influenza A virus replication through degradation of the M1 protein. PLoS One. 2012;7(2):e31063-e.

284. González-Jara P, Fraile A, Canto T, García-Arenal F. The multiplicity of infection of a plant virus varies during colonization of its eukaryotic host. J Virol. 2009;83(15):7487-94.

285. Seitz C, Frensing T, Höper D, Kochs G, Reichl U. High yields of influenza A virus in Madin-Darby canine kidney cells are promoted by an insufficient interferon-induced antiviral state. J Gen Virol. 2010;91(Pt 7):1754-63.

286. Seitz C, Isken B, Heynisch B, Rettkowski M, Frensing T, Reichl U. Trypsin promotes efficient influenza vaccine production in MDCK cells by interfering with the antiviral host response. Appl Microbiol Biotechnol. 2012;93(2):601-11.

287. Dimmock NJ, Rainsford EW, Scott PD, Marriott AC. Influenza Virus Protecting RNA: an Effective Prophylactic and Therapeutic Antiviral. J Virol. 2008;82(17):8570-8.

288. Arava Y, Wang Y, Storey JD, Liu CL, Brown PO, Herschlag D. Genome-wide analysis of mRNA translation profiles in Saccharomyces cerevisiae. Proc Natl Acad Sci U S A. 2003;100(7):3889-94.

289. Robb NC, Jackson D, Vreede FT, Fodor E. Splicing of influenza A virus NS1 mRNA is independent of the viral NS1 protein. J Gen Virol. 2010;91(Pt 9):2331-40.

290. Spirin AS. Ribosome structure and protein biosynthesis: Benjamin/Cummings Pub. Co., Advanced Book Program, Menlo Park, CA; 1986.

291. Wakefield L, Brownlee GG. RNA-binding properties of influenza A virus matrix protein M1. Nucleic Acids Res. 1989;17(21):8569-80.

292. Portela A, Digard P. The influenza virus nucleoprotein: a multifunctional RNA-binding protein pivotal to virus replication. J Gen Virol. 2002;83(Pt 4):723-34.

Appendix A

Model of STV infection

Here, we report the initial conditions and model parameters employed to simulate the multiscale model of STV infection. Furthermore, the correlation between the decrease of the FIVR and the accumulation of DIPs in an infection performed using an MOI of 3 are presented.

Table A.1.: Initial conditions for the multiscale model of STV infection.

MOI condition	Figure	Sub model	Non-zero initial conditions
MOI 73	Figure 4.4, 4.5, 4.6, 4.7, 4.18 (dotted)	intracellular model	$V^{\text{Ex}}(0) = 73$ virions $F_{\text{Par}}(0) = 3.4 \times 10^{-2}$
		reduced intracellular model	$Vp^{\text{Cyt}}(0) = 297.84$ molecules $F_{\text{Par}}(0) = 3.4 \times 10^{-2}$
		extracellular model	$T(0) = 4.24 \times 10^{5}$ cells / mL $T_{\text{A}}(0) = 2.63 \times 10^{4}$ cells / mL $I(0) = 1.75 \times 10^{5}$ cells / mL $I_{\text{A}}(0) = 3.53 \times 10^{3}$ cells / mL $V(0) = 3.1 \times 10^{7}$ virions / mL

MOI condition	Figure	Sub model	Non-zero initial conditions
MOI 3	Fig 4.8A-C (dashed), 4.18 (dash-dotted)	intracellular model	$V^{\text{Ex}}(0) = 3$ virions $F_{\text{Par}}(0) = 0.26$
		reduced intracellular model	$Vp^{\text{Cyt}}(0) = 12.24$ molecules $F_{\text{Par}}(0) = 0.26$
		extracellular model	$T(0) = 5.99 \times 10^5$ cells / mL $T_{\text{A}}(0) = 0$ cells / mL $I(0) = 0$ cells / mL $I_{\text{A}}(0) = 0$ cells / mL $V(0) = 1.8 \times 10^6$ virions / mL
MOI 10^{-4}	Fig 4.8D-F (dashed), 4.18 (solid)	intracellular model	$V^{\text{Ex}}(0) = 1$ virion $F_{\text{Par}}(0) = 0.26$
		reduced intracellular model	$Vp^{\text{Cyt}}(0) = 8$ molecules $F_{\text{Par}}(0) = 0.26$
		extracellular model	$T(0) = 5.99 \times 10^5$ cells / mL $T_{\text{A}}(0) = 0$ cells / mL $I(0) = 0$ cells / mL $I_{\text{A}}(0) = 0$ cells / mL $V(0) = 59.9$ virions / mL

**Table A.2.:** Parameters of the intracellular model of STV infection.

Parameter	Value	Unit	Source
$B_{\text{Hi}}^{\text{Tot}}$	150	sites	[269]
$B_{\text{Lo}}^{\text{Tot}}$	1000	sites	[269]
D_{Rib}	160	nucleotides	[288]
F_{Fus}	0.51	–	[242]
F_{Spl7}	0.02	–	based on ratio of M2 to M1
F_{Spl8}	0.125	–	[289]
$k_{\text{Hi}}^{\text{Att}}$	8.09×10^{-2}	site$^{-1}\cdot$h^{-1}	adjusted to data in reference [269]
$k_{\text{Lo}}^{\text{Att}}$	4.55×10^{-4}	site$^{-1}\cdot$h^{-1}	adjusted to data in reference [269]
$k_{\text{M1}}^{\text{Bind}}$	1.09×10^{-6}	moluecules$^{-1}\cdot$h^{-1}	model fit in Figure 4.7
$k_{\text{NP}}^{\text{Bind}}$	3.01×10^{-4}	moluecules$^{-1}\cdot$h^{-1}	[242]
$k_{\text{RdRp}}^{\text{Bind}}$	1	moluecules$^{-1}\cdot$h^{-1}	[242]
$k_{\text{M}}^{\text{Deg}}$	0.63	h^{-1}	model fit in Figure 4.7
$k_{\text{R}}^{\text{Deg}}$	36.36	h^{-1}	[242]
$k_{\text{Rnp}}^{\text{Deg}}$	0.09	h^{-1}	[242]
$k_{\text{RRdRp}}^{\text{Deg}}$	4.25	h^{-1}	[242]
k^{En}	4.8	h^{-1}	[242]
$k_{\text{Hi}}^{\text{Eq}}$	1.13×10^{-2}	sites^{-1}	[269]
$k_{\text{Lo}}^{\text{Eq}}$	8.33×10^{-5}	sites^{-1}	[269]
k^{Fus}	0.31	h^{-1}	model fit in Figure 4.7
k^{Imp}	6	h^{-1}	[48]
K_{R}	1.1×10^{7}	molecules	model fit in Figure 4.7
k^{RdRp}	1	moluecules$^{-2}\cdot$h^{-1}	assuming rapid complex formation
k^{Rel}	1270	virions$\cdot$h^{-1}	model fit in Figure 4.7
$k_{\text{Red}}^{\text{Rel}}$	5.17×10^{-2}	h^{-1}	model fit in Figure 4.7
$k_{\text{C}}^{\text{Syn}}$	0.9	h^{-1}	model fit in Figure 4.7
$k_{\text{M}}^{\text{Syn}}$	1.73×10^{5}	nucleotides$\cdot$h^{-1}	model fit in Figure 4.7
$k_{\text{P}}^{\text{Syn}}$	64800	nucleotides$\cdot$h^{-1}	[290]
$k_{\text{V}}^{\text{Syn}}$	8.33	h^{-1}	model fit in Figure 4.7
$K_{\text{V}^{\text{Rel}}}$	1250	virions	model fit in Figure 4.7
L_1	2320	nucleotides	[24]
L_2	2320	nucleotides	[24]
L_3	2211	nucleotides	[24]
L_4	1757	nucleotides	[24]

Parameter	Value	Unit	Source
L_5	1540	nucleotides	[24]
L_6	1392	nucleotides	[24]
L_7	1005	nucleotides	[24]
L_8	868	nucleotides	[24]
L_V	1700	nucleotides	based on reference [24]
$N_{P_{RdRp}}$	45	molecules·virion^{-1}	[24]
$N_{P_{HA}}$	500	molecules·virion^{-1}	[24]
$N_{P_{NP}}$	1000	molecules·virion^{-1}	[24]
$N_{P_{NA}}$	100	molecules·virion^{-1}	[24]
$N_{P_{M1}}$	3000	molecules·virion^{-1}	[24]
$N_{P_{M2}}$	40	molecules·virion^{-1}	[24]
$N_{P_{NEP}}$	165	molecules·virion^{-1}	[24]
N_{M1}^{Nuc}	200	nucleotides	[291]
N_{NEP}^{Nuc}	1700	nucleotides	adjusted to data in reference [292]
N_{NP}^{Nuc}	24	nucleotides	[292]

Table A.3.: Parameters of the cell population model of STV infection.

Parameter	Value	Unit	Source
μ_{Max}	0.03	h^{-1}	[231]
$B_{\text{Hi}}^{\text{Tot}}$	150	sites·cell^{-1}	[269]
$B_{\text{Lo}}^{\text{Tot}}$	1000	sites·cell^{-1}	[269]
F_{Inf}	1	cells·virion^{-1}	[38]
K_{I}	0.11	h^{-1}	model fit in Figure 4.7
$k_{\text{T}}^{\text{Apo}}$	6.97×10^{-3}	h^{-1}	model fit in Figure 4.7
$k_{\text{c,Hi}}^{\text{Att}}$	3.32×10^{-8}	mL·sites^{-1}·h^{-1}	adjusted to data in reference [269]
$k_{\text{c,Lo}}^{\text{Att}}$	1.85×10^{-10}	mL·sites^{-1}·h^{-1}	adjusted to data in reference [269]
$k_{\text{V}}^{\text{Deg}}$	1.15×10^{-2}	h^{-1}	model fit in Figure 4.7
k^{En}	4.8	h^{-1}	[242]
$k_{\text{c,Hi}}^{\text{Eq}}$	4.48×10^{-9}	mL·sites^{-1}	[269]
$k_{\text{c,Lo}}^{\text{Eq}}$	3.32×10^{-11}	mL·sites^{-1}	[269]
k^{Fus}	0.31	h^{-1}	model fit in Figure 4.7
k^{Lys}	9.34×10^{-3}	h^{-1}	model fit in Figure 4.7
T_{Max}	1×10^{6}	cells·mL^{-1}	maximum cell concentration observed in control flasks
τ_{Apo}	19.8	h	model fit in Figure 4.7
ν_{Apo}	0.76	h^{-1}	model fit in Figure 4.7
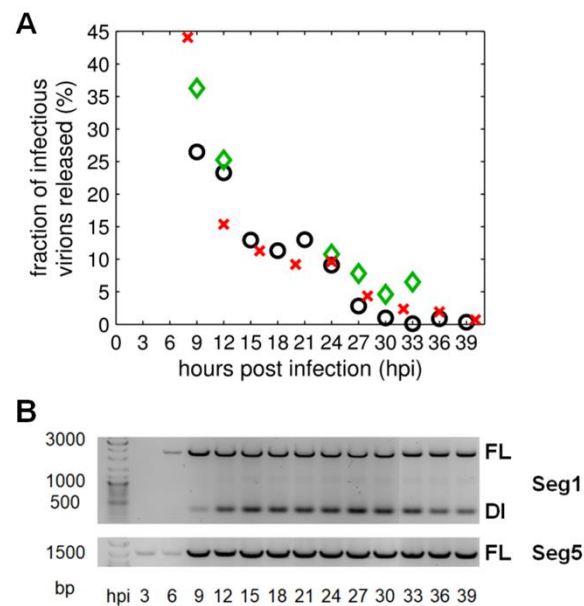
Figure A.1.: Correlation of the accumulation of DIPs and the reduction of infectious virus particles released. (A) Percentage of infectious virus particles released compared to the total number of virions released based on $TCID_{50}$ and HA assay results. Time course data of three individual experiments for an infection at MOI 3 are shown. (B) Samples of one time series (A, circles) were analyzed via segment-specific RT-PCR to reveal intracellular accumulation of viral RNAs. FL and DI RNAs are depicted for segment 1. Segment 5 FL RNA is shown as a control. Figure taken from Rüdiger *et al.* [181].

Appendix B

STV and DIP co-infection model

Here we report all model parameters used to simulate the multiscale model of STV and DIP co-infection. Furthermore, the calculated parameter sensitivities as well as the AIC results for a comparison of the basic and extended co-infection model are presented. Lastly, the full model fitting results for all experimental data measured in 12 different infection conditions are provided.

B.1 Model parameters and model analysis

Table B.1.: Parameters of the intracellular STV and DIP co-infection model.

Parameter	Value	Unit	Source
$B_{\text{Hi}}^{\text{Tot}}$	150	sites	[269]
$B_{\text{Lo}}^{\text{Tot}}$	1000	sites	[269]
D_{Rib}	160	nucleotides	[288]
F_{Adv}	0.32	–	model fit in Figures B.2–B.9
F_{Fus}	0.51	–	[242]
F_{M}	0.12	–	model fit in Figures B.2–B.9
F_{MODIP}	1.1×10^{-3}	virion·cell^{-1}	vRNA synthesis reduction only observed for MODIPs > 10^{-3}
F_{Spl7}	0.02	–	[38]
F_{Spl8}	0.125	–	[289]
$k_{\text{Hi}}^{\text{Att}}$	8.09×10^{-2}	site^{-1}·h^{-1}	[38]
$k_{\text{Lo}}^{\text{Att}}$	4.55×10^{-4}	site^{-1}·h^{-1}	[38]
$k_{\text{M1}}^{\text{Bind}}$	1×10^{-7}	molecules^{-1}·h^{-1}	model fit in Figures B.2–B.9
$k_{\text{NP}}^{\text{Bind}}$	3.01×10^{-4}	molecules^{-1}·h^{-1}	[242]
$k_{\text{RdRp}}^{\text{Bind}}$	1	molecules^{-1}·h^{-1}	[242]
k^{Cplx}	1	molecules^{-7}·h^{-1}	[257]
$k_{\text{M}}^{\text{Deg}}$	0.33	h^{-1}	[242]
$k_{\text{R}}^{\text{Deg}}$	36.36	h^{-1}	[242]

Parameter	Value	Unit	Source
$k_{\text{Rnp}}^{\text{Deg}}$	0.09	h^{-1}	[242]
$k_{\text{RRdRp}}^{\text{Deg}}$	4.25	h^{-1}	[242]
k^{En}	4.8	h^{-1}	[242]
$k_{\text{Hi}}^{\text{Eq}}$	1.13×10^{-2}	sites^{-1}	[269]
$k_{\text{Lo}}^{\text{Eq}}$	8.33×10^{-5}	sites^{-1}	[269]
k^{Fus}	58.3	h^{-1}	model fit in Figures B.2–B.9
k^{Imp}	6	h^{-1}	[48]
K_{R}	7.8×10^3	molecules	model fit in Figures B.2–B.9
k^{RdRp}	1	molecules^{-2}·h^{-1}	[38]
k^{Rel}	6.15×10^3	virions·h^{-1}	model fit in Figures B.2–B.9
$k_{\text{Red}}^{\text{Rel}}$	4.1×10^{-4}	h^{-1}	model fit in Figures B.2–B.9
$k_{\text{C}}^{\text{Syn}}$	0.9	h^{-1}	[181]
$k_{\text{M}}^{\text{Syn}}$	1.73×10^5	nucleotides·h^{-1}	[181]
$k_{\text{P}}^{\text{Syn}}$	64800	nucleotides·h^{-1}	[290]
K_{V}	20.1	h^{-1}	model fit in Figures B.2–B.9
$K_{\text{V}^{\text{Rel}}}$	1.8	virions	model fit in Figures B.2–B.9
L_1	2320	nucleotides	[24]
L_2	2320	nucleotides	[24]
L_3	2211	nucleotides	[24]
L_4	1757	nucleotides	[24]
L_5	1540	nucleotides	[24]
L_6	1392	nucleotides	[24]
L_7	1005	nucleotides	[24]
L_8	868	nucleotides	[24]
L_9	373	nucleotides	extrapolated from DI segment vRNA and cRNA length
$L_{\text{V},1}$	2341	nucleotides	[24]
$L_{\text{V},2}$	2341	nucleotides	[24]
$L_{\text{V},3}$	2233	nucleotides	[24]
$L_{\text{V},4}$	1778	nucleotides	[24]
$L_{\text{V},5}$	1565	nucleotides	[24]
$L_{\text{V},6}$	1413	nucleotides	[24]
$L_{\text{V},7}$	1027	nucleotides	[24]
$L_{\text{V},8}$	890	nucleotides	[24]
$L_{\text{V},9}$	395	nucleotides	[287]

Parameter	Value	Unit	Source
$N_{P_{\text{HA}}}$	500	molecules·virion^{-1}	[24]
$N_{P_{\text{NA}}}$	100	molecules·virion^{-1}	[24]
$N_{P_{\text{M1}}}$	3000	molecules·virion^{-1}	[24]
$N_{P_{\text{M2}}}$	40	molecules·virion^{-1}	[24]
$N_{\text{M1}}^{\text{Nuc}}$	200	nucleotides	[291]
$N_{\text{NP}}^{\text{Nuc}}$	24	nucleotides	[292]
v_1	5.2	–	model fit in Figures B.2–B.9
v_2	0.1	–	model fit in Figures B.2–B.9

Table B.2.: Parameters of the cell population model of STV and DIP co-infection.

Parameter	Value	Unit	Source
μ_{Max}	0.03	h^{-1}	[231]
$B_{\text{Hi}}^{\text{Tot}}$	150	sites·cell^{-1}	[269]
$B_{\text{Lo}}^{\text{Tot}}$	1000	sites·cell^{-1}	[269]
F_{Inf}	1	cells·virion^{-1}	[38]
F_μ	0.63	-	model fit in Figures B.2–B.9
K_{I}	0.27	h^{-1}	model fit in Figures B.2–B.9
$k_{\text{T}}^{\text{Apo}}$	1.2×10^{-2}	h^{-1}	model fit in Figures B.2–B.9
$k_{\text{c,Hi}}^{\text{Att}}$	3.32×10^{-8}	mL·sites^{-1}·h^{-1}	[38]
$k_{\text{c,Lo}}^{\text{Att}}$	1.85×10^{-10}	mL·sites^{-1}·h^{-1}	[38]
$k_{\text{V}}^{\text{Deg}}$	0.2	h^{-1}	adjusted to infectious titer reduction observed in experiments
k^{En}	4.8	h^{-1}	[242]
$k_{\text{c,Hi}}^{\text{Eq}}$	4.48×10^{-9}	mL·sites^{-1}	[269]
$k_{\text{c,Lo}}^{\text{Eq}}$	3.32×10^{-11}	mL·sites^{-1}	[269]
k^{Fus}	58.3	h^{-1}	model fit in Figures B.2–B.9
k^{Lys}	0.16	h^{-1}	model fit in Figures B.2–B.9
T_{Max}	1×10^7	cells·mL^{-1}	maximum cell concentration observed in control flasks
τ_{Apo}	6.65	h	model fit in Figures B.2–B.9
v_{Apo}	1.7	h^{-1}	fixed to value inducing a normal distribution

Table B.3.: Sensitivity of model parameters on the intracellular and cell population level of the STV and DIP co-infection model.

Parameter	Local sensitivity (%), intracellular model output	Local sensitivity (%), cell population model output
B_{Hi}^{Tot}	3.0×10^{-6}	2.4×10^{-6}
B_{Lo}^{Tot}	1.0×10^{-7}	1.2×10^{-7}
D_{Rib}	1.5×10^{-4}	1.0×10^{-5}
F_{Adv}	2.5×10^{-4}	1.3×10^{-4}
F_{Fus}	3.5×10^{-5}	1.9×10^{-5}
F_M	2.3×10^{-4}	1.0×10^{-5}
F_{Spl7}	2.1×10^{-7}	6.4×10^{-9}
F_{Spl8}	2.5×10^{-6}	9.2×10^{-7}
k_{Hi}^{Att}	1.4×10^{-7}	6.3×10^{-8}
k_{Lo}^{Att}	2.2×10^{-8}	2.5×10^{-8}
k_{M1}^{Bind}	7.4×10^{-5}	1.5×10^{-5}
k_{NP}^{Bind}	6.0×10^{-6}	2.8×10^{-6}
k_{RdRp}^{Bind}	1.4×10^{-7}	6.8×10^{-8}
k^{Cplx}	2.3×10^{-11}	2.7×10^{-12}
k_M^{Deg}	2.0×10^{-5}	1.1×10^{-6}
k_R^{Deg}	1.7×10^{-7}	8.3×10^{-8}
k_{Rnp}^{Deg}	8.4×10^{-5}	1.9×10^{-5}
k_{RRdRp}^{Deg}	1.4×10^{-5}	2.3×10^{-6}
k^{En}	4.9×10^{-6}	3.9×10^{-6}
k_{Hi}^{Eq}	3.3×10^{-7}	1.6×10^{-7}
k_{Lo}^{Eq}	1.9×10^{-8}	2.2×10^{-8}
k^{Fus}	1.7×10^{-7}	3.2×10^{-7}
k^{Imp}	5.8×10^{-7}	2.8×10^{-7}
K_R	5.0×10^{-5}	5.5×10^{-6}
k^{RdRp}	3.9×10^{-11}	2.2×10^{-11}
k^{Rel}	1.4×10^{-4}	2.4×10^{-4}
k_{Red}^{Rel}	1.8×10^{-9}	1.2×10^{-9}
k_C^{Syn}	9.9×10^{-4}	3.5×10^{-4}
k_M^{Syn}	9.3×10^{-5}	1.0×10^{-5}
k_P^{Syn}	1.5×10^{-4}	1.0×10^{-5}
K_V	2.9×10^{-3}	1.0×10^{-3}
$K_{V^{Rel}}$	2.9×10^{-9}	1.0×10^{-9}

Parameter	Local sensitivity (%), intracellular model output	Local sensitivity (%), cell population model output
L_1	2.7×10^{-4}	9.9×10^{-6}
L_2	9.5×10^{-5}	2.2×10^{-6}
L_3	7.9×10^{-11}	3.4×10^{-11}
L_4	1.6×10^{-11}	4.3×10^{-12}
L_5	9.7×10^{-4}	1.9×10^{-5}
L_6	2.0×10^{-11}	4.9×10^{-12}
L_7	4.9×10^{-4}	1.5×10^{-5}
L_8	2.5×10^{-6}	9.1×10^{-7}
L_9	2.9×10^{-5}	1.1×10^{-11}
$L_{V,1}$	1.6×10^{-5}	2.6×10^{-7}
$L_{V,2}$	2.3×10^{-5}	3.2×10^{-7}
$L_{V,3}$	2.1×10^{-5}	2.9×10^{-7}
$L_{V,4}$	1.4×10^{-5}	1.9×10^{-7}
$L_{V,5}$	1.1×10^{-5}	1.4×10^{-7}
$L_{V,6}$	8.6×10^{-6}	1.2×10^{-7}
$L_{V,7}$	4.5×10^{-6}	6.2×10^{-8}
$L_{V,8}$	3.4×10^{-6}	4.7×10^{-8}
$L_{V,9}$	1.1×10^{-6}	4.1×10^{-9}
$N_{P_{HA}}$	1.5×10^{-11}	3.7×10^{-12}
$N_{P_{NA}}$	1.5×10^{-11}	4.0×10^{-12}
$N_{P_{M1}}$	2.3×10^{-4}	3.8×10^{-6}
$N_{P_{M2}}$	2.7×10^{-11}	1.2×10^{-11}
N_{M1}^{Nuc}	5.4×10^{-7}	3.5×10^{-10}
N_{NP}^{Nuc}	8.2×10^{-4}	1.0×10^{-5}
v_1	2.1×10^{-3}	8.1×10^{-4}
v_2	1.6×10^{-3}	6.8×10^{-4}
μ_{Max}	8.2×10^{-6}	1.5×10^{-5}
F_{Inf}	3.3×10^{-4}	1.7×10^{-4}
F_μ	1.6×10^{-6}	4.4×10^{-6}
K_I	1.0×10^{-3}	3.4×10^{-4}
k_T^{Apo}	3.0×10^{-6}	2.0×10^{-5}
$k_{c,Hi}^{Att}$	2.6×10^{-6}	2.3×10^{-6}

Parameter	Local sensitivity (%), intracellular model output	Local sensitivity (%), cell population model output
$k_{c,Lo}^{Att}$	3.8×10^{-9}	3.2×10^{-9}
k_V^{Deg}	4.1×10^{-6}	2.9×10^{-5}
$k_{c,Hi}^{Eq}$	7.7×10^{-7}	9.1×10^{-7}
$k_{c,Lo}^{Eq}$	9.3×10^{-10}	7.8×10^{-10}
k^{Lys}	4.1×10^{-5}	4.5×10^{-5}
T_{Max}	1.2×10^{-6}	1.3×10^{-6}
τ_{Apo}	1.6×10^{-3}	8.5×10^{-4}
v_{Apo}	5.0×10^{-7}	1.0×10^{-6}

Table B.4.: Evaluation of model fits performed for the basic and the extended STV and DIP co-infection model for individual infection conditions.

Condition		SSR		AIC	
MOI	MODIP	Basic model	Extended model	Basic model	Extended model
10^{-3}	0	2.0×10^1	6.6×10^0	11.8	**-90.3**
10^{-3}	10^{-3}	2.6×10^1	1.4×10^1	-21.3	**-100.9**
10^{-3}	3	1.6×10^1	2.1×10^1	**-282.8**	-231.1
10^{-3}	30	3.4×10^1	2.9×10^2	**-142.9**	236.8
3	0	1.6×10^1	4.5×10^0	18.2	**-85.4**
3	10^{-3}	6.0×10^1	8.5×10^1	**96.0**	129.7
3	3	1.1×10^2	3.2×10^1	155.5	**15.2**
3	30	4.1×10^2	1.4×10^2	295.1	**172.8**
30	0	1.7×10^1	8.7×10^0	20.6	**-35.7**
30	10^{-3}	1.9×10^1	1.9×10^2	**-4.2**	214.6
30	3	2.4×10^1	1.3×10^1	-12.8	**-80.4**
30	30	7.3×10^1	3.7×10^1	106.1	**29.6**

SSR: sum of squared residuals (errors of each variable were normalized to the respective maximum measurement value);

AIC: Akaike information criterion
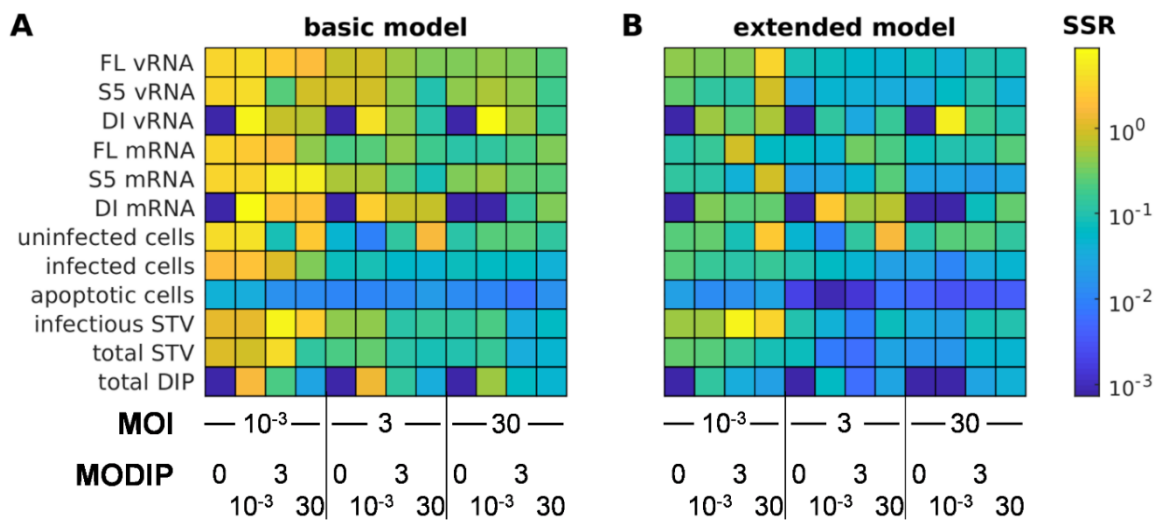
Figure B.1.: Model extension significantly improves description of experimental measurements. The sum of squared residuals for each individual measured property is depicted. Logarithmic errors of each variable were normalized to the respective maximum measurement value. The (A) basic model and the (B) extended model were calibrated to a wide range of experimental data. Measured properties include vRNA and vmRNA of FL segment 1, DI segment 1 and S5, the concentration of uninfected, infected and apoptotic cells, total and STV titers as well as DIP titers. Figure taken from Rüdiger and Pelz *et al.* [125].

B.2 Complete model fitting results
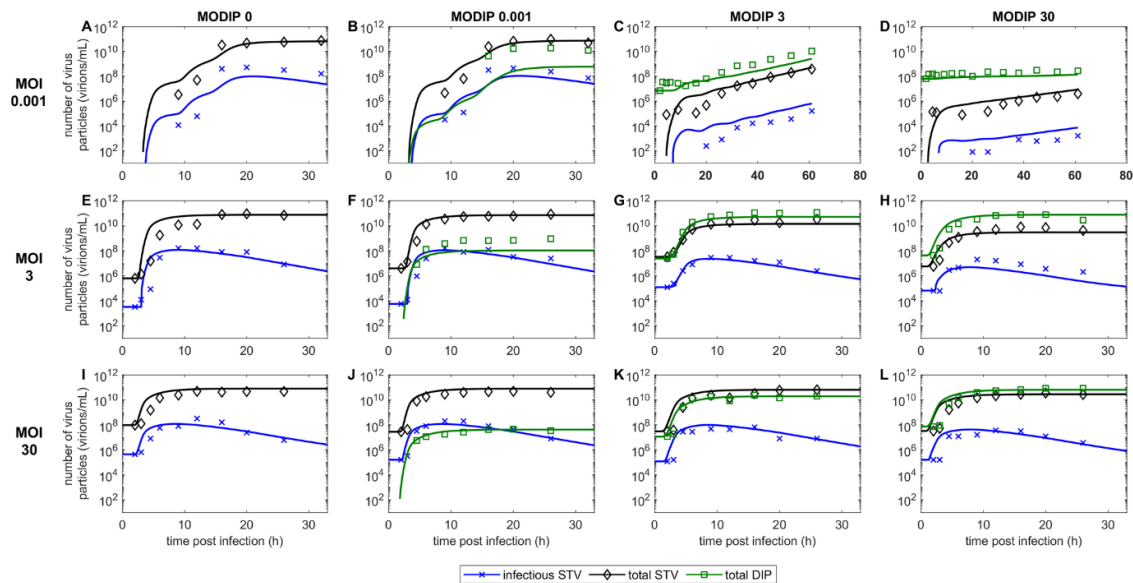
Figure B.2.: Experimental data and model simulations for virus titers. Model fits to measurements of the infectious STV titer, the total amount of STVs and the total amount of DIPs for MDCKsus infections with MOI 10^{-3}, 3 and 30 using different MODIPs. Figure taken from Rüdiger and Pelz *et al.* [125].
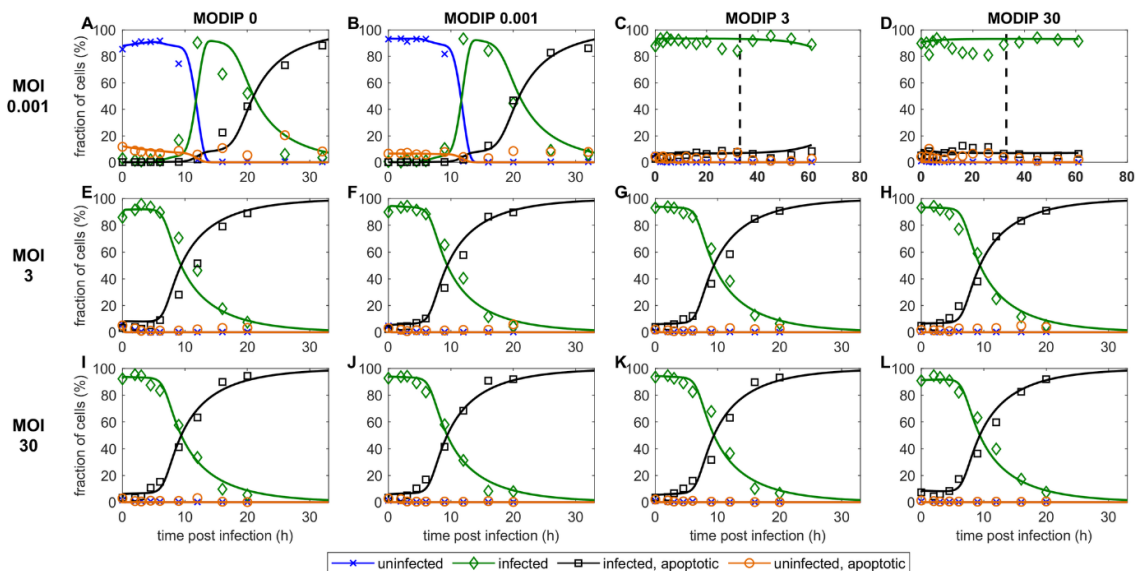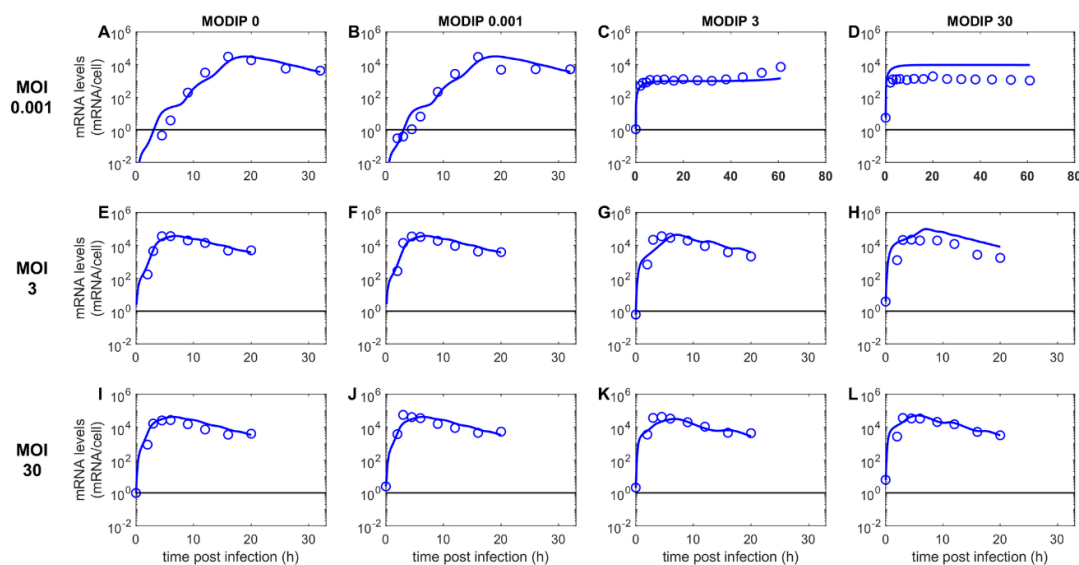

Figure B.3.: Experimental data and model simulations for cell populations. Model fits to measurements of the fraction of uninfected, uninfected and apoptotic, infected, infected and apoptotic cells for MDCKsus infections with MOI 10^{-3}, 3 and 30 using different MODIPs. Figure taken from Rüdiger and Pelz *et al.* [125].
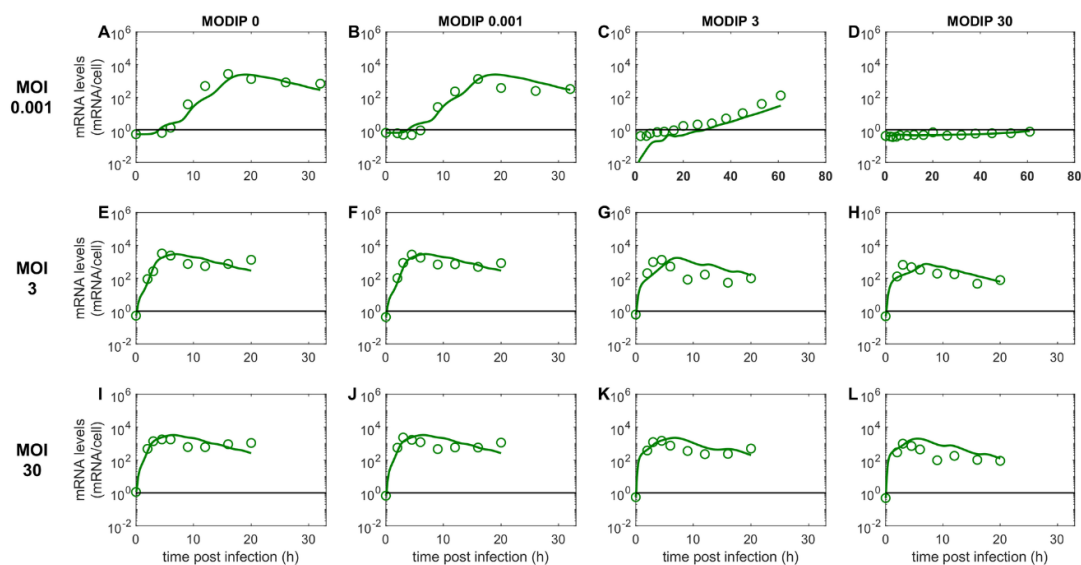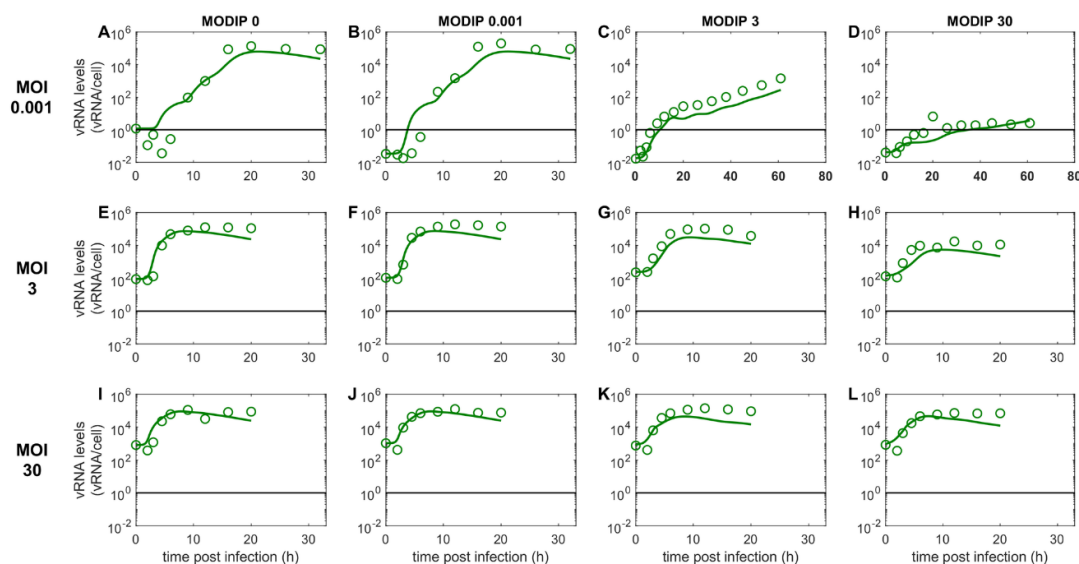
Figure B.4.: Experimental data and model simulations for FL vmRNA dynamics.
Model fits to measurements of the intracellular levels of FL vmRNA for MDCKsus infections with MOI 10^{-3}, 3 and 30 using different MODIPs. Figure taken from Rüdiger and Pelz *et al*. [125].
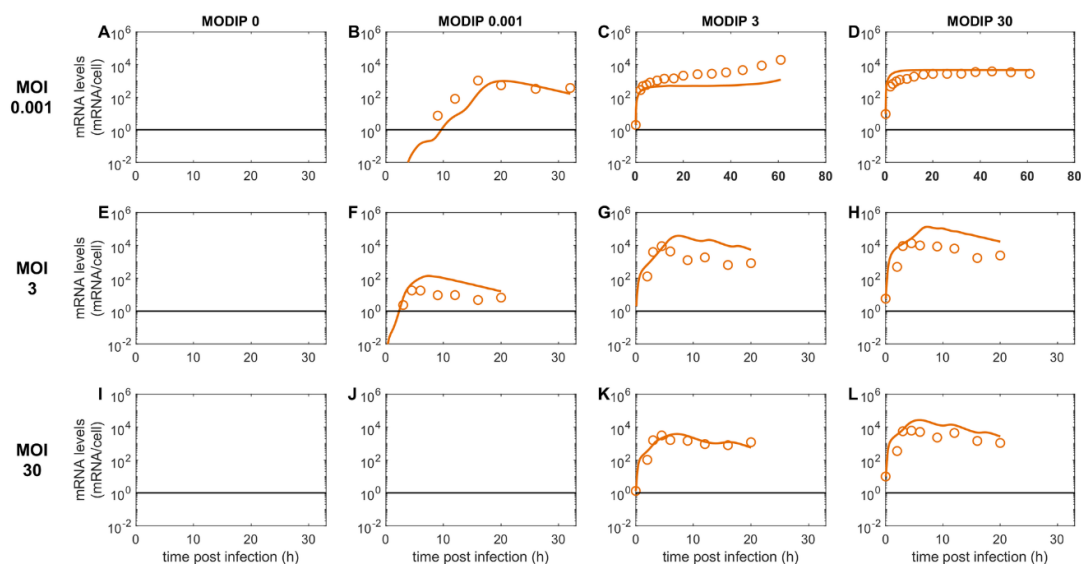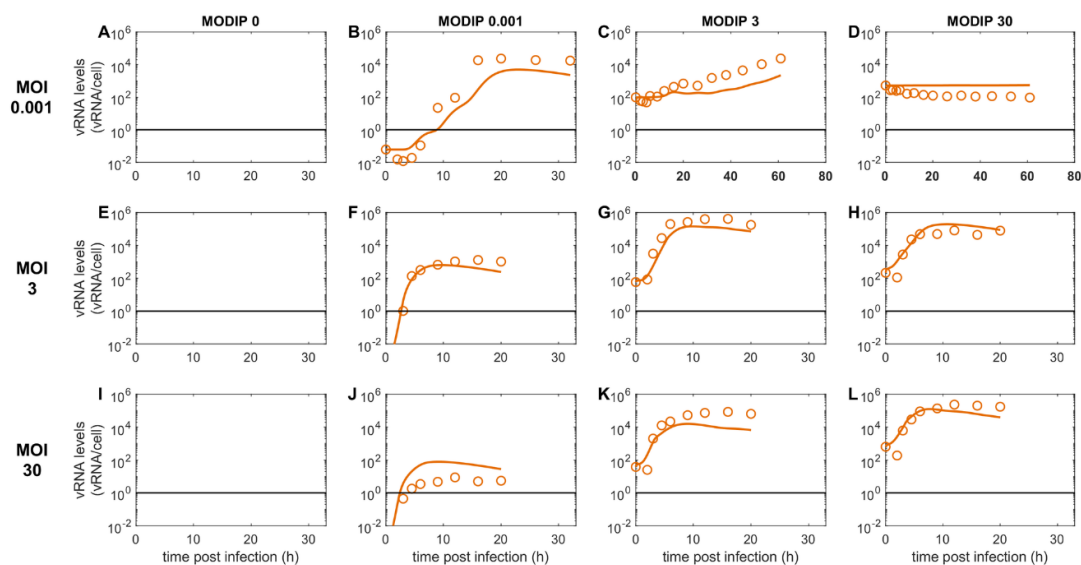

Figure B.5.: Experimental data and model simulations for DI vmRNA dynamics.
Model fits to measurements of the intracellular levels of DI vmRNA for MDCKsus infections with MOI 10^{-3}, 3 and 30 using different MODIPs. Figure taken from Rüdiger and Pelz *et al*. [125].
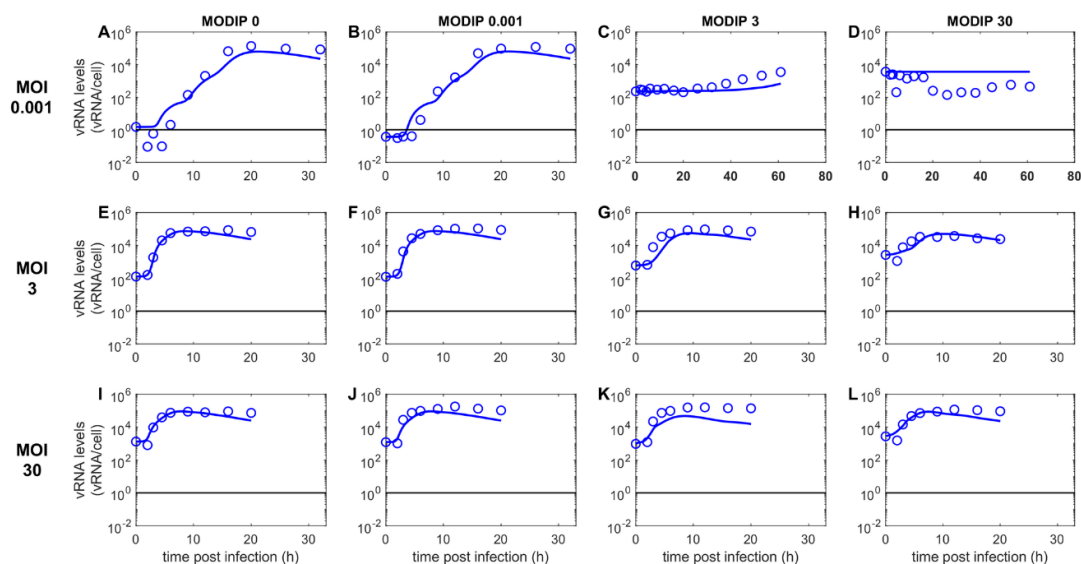
Figure B.6.: Experimental data and model simulations for segment 5 vmRNA dynamics. Model fits to measurements of the intracellular levels of segment 5 vmRNA for MDCKsus infections with MOI 10^{-3}, 3 and 30 using different MODIPs. Figure taken from Rüdiger and Pelz *et al.* [125].

Figure B.7.: Experimental data and model simulations for FL vRNA dynamics. Model fits to measurements of the intracellular levels of FL vRNA for MDCKsus infections with MOI 10^{-3}, 3 and 30 using different MODIPs. Figure taken from Rüdiger and Pelz *et al.* [125].

Figure B.8.: Experimental data and model simulations for DI vRNA dynamics. Model fits to measurements of the intracellular levels of DI vRNA for MDCKsus infections with MOI 10^{-3}, 3 and 30 using different MODIPs. Figure taken from Rüdiger and Pelz *et al.* [125].

Figure B.9.: Experimental data and model simulations for segment 5 vRNA dynamics. Model fits to measurements of the intracellular levels of segment 5 vRNA for MDCKsus infections with MOI 10^{-3}, 3 and 30 using different MODIPs. Figure taken from Rüdiger and Pelz *et al.* [125].